Effects of Combined Zr and Mn Additions on the Microstructure and Properties of AA2198 Sheet

A thesis submitted to The University of Manchester for the degree of
Doctor of Philosophy
in the Faculty of Engineering and Physical Sciences

2010

DIMITRIOS TSIVOULAS

SCHOOL OF MATERIALS

Contents

Final word count: 73,923

List of Tables

List of Figures

Abstract

The effect of individual and combined zirconium and manganese additions have been compared for an AA2198 6 mm thick sheet in T351 temper regarding their influence primarily on recrystallisation resistance and secondly on fracture toughness and overageing resistance. A complete characterisation of the dispersoid distributions was carried out for a deeper understanding of the effects of the Al_3Zr and $Al_{20}Cu_2Mn_3$ particles, involving studying their formation from the as-cast and homogenised stage.

The most important finding in this work was the lower recrystallisation resistance in the alloy containing 0.1 wt%Zr + 0.3 wt%Mn compared to that containing only 0.1 wt%Zr. This result was rather unexpected, if one considers the opposite microsegregation patterns of Zr and Mn during casting, which leads to dispersoids occupying the majority of the grains' volume and minimising dispersoid-free zones that could be potential sites for nucleation of recrystallisation. The other two alloys with dispersoid additions 0.05 wt%Zr + 0.3 wt%Mn and 0.4 wt%Mn, were partially and fully recrystallised respectively in the rolled T351 condition.

Equally important in this work, was the observation that the opposite microsegregation trend of Zr and Mn sufficed to restrict grain growth in unrecrystallised areas. The 0.1Zr-0.3Mn alloy exhibited the lowest grain size of all alloys, both in the T351 temper and after annealing at 535°C for up to 144 hours. The reason for this was the combined action of $Al_{20}Cu_2Mn_3$ dispersoids and Mn solute in the regions where the Zr concentration was low (i.e. near the grain boundaries), which offered additional pinning pressure to those areas compared to the 0.1Zr alloy.

The lower recrystallisation resistance of the 0.1Zr-0.3Mn alloy was explained on the grounds of two main factors. The first was the lower subgrain size and hence stored energy within bands of $Al_{20}Cu_2Mn_3$ dispersoids, which increased the driving force for recrystallisation in these regions. The second was the interaction between Zr and Mn that led to a decrease in the Al_3Zr number density and pinning pressure. Since Zr was the dominant dispersoid family in terms of inhibiting recrystallisation, inevitably this alloy became more prone to recrystallisation. The Al_3Zr pinning pressure was found to be much lower especially within bands of $Al_{20}Cu_2Mn_3$ dispersoids. The detrimental effect of the Mn addition on the Al_3Zr distribution was proven not to result from the dissolution of Zr within Mn-containing phases, and several other phases, at the grain interior and also in grain boundaries. The observed effect could not be precisely explained at this stage.

Concerning mechanical properties, the 0.1Zr alloy exhibited the best combination of properties in the Kahn tear tests for fracture toughness. Further, it had a higher overageing resistance compared to the 0.1Zr-0.3Mn alloy.

As an overall conclusion from this work, considering all the studied properties here that are essential for damage tolerant applications, the addition of 0.1 wt%Zr to the AA2198 6 mm thick sheet was found to be superior to that of the combined addition of 0.1 wt%Zr + 0.3 wt%Mn.

Publications from this thesis

The following paper was derived from the experimental work undertaken during this PhD project. A poster was presented at "THERMEC 2009" in Berlin, Germany, where it was also published in the conference's proceedings and in an associated journal.

- D. Tsivoulas, P. B. Prangnell, C. Sigli, B. Bès, "Effects of combined Zr and Mn additions on dispersoid formation and recrystallisation behaviour of 2198 alloy sheet", *Advanced Materials Research*, **89-91** (2010) 568-573

Several more publications are in preparation and will be published after the completion of the thesis.

Declaration

I hereby declare that no portion of the work referred to in this thesis has been submitted in support of an application for another degree or qualification of this or any other university or other institute of learning.

Copyright statement

i. The author of this thesis (including any appendices and/or schedules to this thesis) owns certain copyright or related rights in it (the "Copyright") and he has given The University of Manchester certain rights to use such Copyright, including for administrative purposes.

ii. Copies of this thesis, either in full or in extracts and whether in hard or electronic copy, may be made **only** in accordance with the Copyright, Designs and Patent Act 1988 (as amended) and regulations issued under it or, where appropriate, in accordance with licensing agreements which the University has from time to time. This page must form part of any such copies made.

iii. The ownership of any certain Copyright, patents, designs, trade marks and other intellectual property (the "Intellectual Property") and any reproductions of copyright works in the thesis, for example graphs and tables ("Reproductions"), which may be described in this thesis, may not be owned by the author and may be owned by third parties. Such Intellectual Property Rights and Reproductions cannot and must not be made available for use without the prior written permission of the owner(s) of the relevant Intellectual Property Rights and/or Reproductions.

iv. Further information on the conditions under which disclosure, publication and commercialisation of this thesis, the Copyright and any Intellectual Property and/or Reproductions described in it may take place is available in the University IP Policy (see http://www.campus.manchester.ac.uk/medialibrary/policies/intellectual-property.pdf), in any relevant Thesis restriction declarations deposited in the University Library, The University Library's regulations (see http://www.manchester.ac.uk/library/aboutus/regulations) and in The University's policy on presentation of Theses.

Acknowledgements

The author would like to express his gratitude to a large number of people for their contribution towards the completion of this thesis.

First of all, I would like to thank my good friend and colleague Dr Dimitrios Bakavos, whose input to my work and life has been manifold throughout these years, but mainly for recommending me as a suitable candidate for this PhD project. Also for his help with the TEM at the start of my PhD, the training on the SAXS measurements in my first year, all the tips on lab work that saved me precious time and for being there to listen and give me useful advice when I had felt overwhelmed on certain occasions.

I would also like to express my appreciation to my supervisor Professor Philip Prangnell, firstly for the trust he showed me by allocating this important project to me and secondly for the large amounts of time he has spent on it since its start. Our frequent meetings and his invaluable recommendations on my work have made it possible to produce some high quality results and extend my knowledge in more depth in the field of metallurgy. I would also like to thank him for his moral support during certain periods when the project was going through some difficult phases and also for the financial support at the end of the third year.

I would like to thank my family for their support throughout all these years, my father Nikolaos who has made it possible for me to get to this point and to whom I owe everything I have achieved so far and my brother Christodoulos. I will always cherish the love that my extended family and family friends showed me every time I was travelling back and forth to the UK.

Not to forget Dr Christophe Sigli and Dr Bernard Bès of Alcan Centre de Recherches de Voreppe for their critical role in this project with the provision of the materials, suggestions for further research during our meetings in Voreppe and, generally, for their aid with all my enquiries.

I am really grateful to Professor Pete Bate for his very useful advice on recrystallisation and textures and also to Professor John Humphreys for the fruitful discussions on recrystallisation and on the use of the Vmap software.

The contribution of the following people is also greatly acknowledged; Mr Ian Brough for all the advice and assistance with SEM and EBSD and for maintaining the Sirion microscope at a perfect condition, Mr Michael Faulkner for the SEM training and for the SEM/EDX measurements, Dr Yan Huang for his priceless help and advice on EBSD, Dr Kuvasani Govender for her aid with the TEM and the training on the Tecnai microscope, Dr Teruo Hashimoto for his very useful tips on EELS and for providing me with general information on the use of TEM, Dr Alan Harvey for his help and training with the TEM, Dr David Plant and Dr John Charnock from the School of Earth, Atmospheric and Environmental Sciences for their help with the electron microprobe measurements, and Professor Paul Midgley and Dr Juan-

Carlos Hernandez-Garrido from the Electron Microscopy Group in the Department of Materials at the University of Cambridge who spent a lot of time in carrying out, as well as analysing, the electron tomography measurements at their facilities. Not to forget, the guys at the workshop who have been extremely helpful and prepared mechanical test samples rapidly whenever I needed them.

Finally, I need to highlight my good fortune for having shared an office with all these great characters that have made my life more interesting during all these years and especially my good friend in there, Dr Kasra Sotoudeh, who has helped me numerous times with fruitful discussions on my results.

The author wishes to thank LATEST, the University of Manchester EPSRC Light Alloys Portfolio Partnership (EP/D029201/1), and Alcan CRV for the financial support to this project.

List of Abbreviations

AA	aluminium alloy
BF	bright field
BSE	backscatter electron
CRV	Centre de Recherches de Voreppe
DC	direct chill
DF	dark field
DP	diffraction pattern
DRX	dynamic recrystallisation
EBSD	electron backscatter diffraction
ECAP	equal channel angular pressing
ECD	equivalent circular diameter
EDX	energy dispersive x-ray
EELS	electron energy loss spectroscopy
FC	full constraints
FCC	face-centred cubic
FEG	field emission gun
FSW	friction stir welding
GB	grain boundary
GP	Guinier-Preston
HAADF	high angle annular dark field
HAGB	high angle grain boundary
HRTEM	high resolution transmission electron microscopy
LAGB	low angle grain boundary
NC	no constraints
ND	normal direction
ODF	orientation distribution function
PFZ	precipitate free zone
ppm	parts per million
PSN	particle stimulated nucleation
RC	relaxed constraints
RD	rolling direction
RT	room temperature
SCC	stress corrosion cracking
SE	secondary electron
SEM	scanning electron microscopy/microscope
SIBM	strain induced boundary migration
SS	solid solution
ST	solution treatment
STEM	scanning transmission electron microscopy/microscope
TD	transverse direction
TEM	transmission electron microscopy/microscope
UIE	unit initiation energy

UPE	unit propagation energy
UTE	unit total energy
V_f	volume fraction
WDS	wavelength dispersive spectrometer

To my mother…

…who is no longer with us

CHAPTER 1: Introduction

1.1 Evolution of Al-Li alloys

Al-Li alloys are employed mainly for aerospace applications, since they offer an impressive combination of specific mechanical properties, due to their lower density and high performance, compared to other types of Al alloys. They have attracted considerable interest over the last few decades, especially at periods when fuel prices had risen significantly, thus promoting the development of new products to reduce the overall cost of aircraft operation by weight saving. An equally important reason for their evolution is the constant demand for more efficient aircraft structures by the aircraft manufacturers. One of the principal drawbacks for the delay in the deployment of these materials has been their extremely high cost, which can reach 3-5 times that of conventional Al alloys. Hence the use of these materials was confined to applications where weight savings are far more essential than cost cutting, such as military aircraft and space vehicles [1].

Although Li-containing Al alloys have been studied and patented since the 1920s [1-4], it was only three decades later that their commercialisation became possible with the production of the AA2020 alloy. The ever-increasing demands of the military aircraft manufacturers from the end of the 2nd World War onwards, led to the development of the 1st generation of Al-Li alloys (1945-late 1960s) [4]. They were based on the Al-Li-Cu system but only had limited applications, such as on the US Navy RA-5C Vigilante aircraft [2, 4]. A range of similar alloys (e.g. AA1420, AA1421), some of which contained Sc as a dispersoid-former element, were developed in the Soviet Union for use also in military aircraft [5, 6].

The 2nd generation of Al-Li alloys (late 1970s-mid 1980s) resulted from the fuel crisis in 1973 and the demand for lighter aerospace structures [2]. These alloys had Li contents above 2 wt% in order to reduce weight to the maximum possible extent [4]. The main strategy was to directly substitute existing Al alloys in aircraft with new Li-containing ones, such as the AA2090, AA2091 and AA8090. The alloys to be replaced were the medium/high strength 2014-T6, the damage tolerant 2024-T3, the high strength AA7075-T6 and the stress corrosion resistant AA7075-T73 [2-4, 6]. As with the previous Al-Li generation, similar alloys were produced in parallel in the Soviet Union (e.g. AA1430, AA1440) [4].

Since a high Li content brings about a deterioration in several critical properties, as a direct result of the precipitation of the metastable δ' and equilibrium δ phases [7], a 3rd generation of Al-Li alloys was designed from the early 1980s onwards with a much lower Li content (1.0-1.8 wt%) [4]. This family of alloys is based on the Al-Cu-Li system and are targeted for damage tolerant applications, especially in the military and aerospace sectors [8]. Besides their higher Cu:Li ratios, compared to the 2nd generation alloys, they also have a different strengthening phase; T_1 instead of δ'. Some examples of the first alloys of this type that were developed are the Weldalite 049, AA2094, AA2095, AA2098 and AA2195, while recently, design improvements have led to the introduction of even more damage tolerant alloys, such as the AA2050, AA2196, AA2198, AA2099 and AA2199. Fig. 1.1 shows a composition map containing selected alloys from the 2nd and 3rd generations.

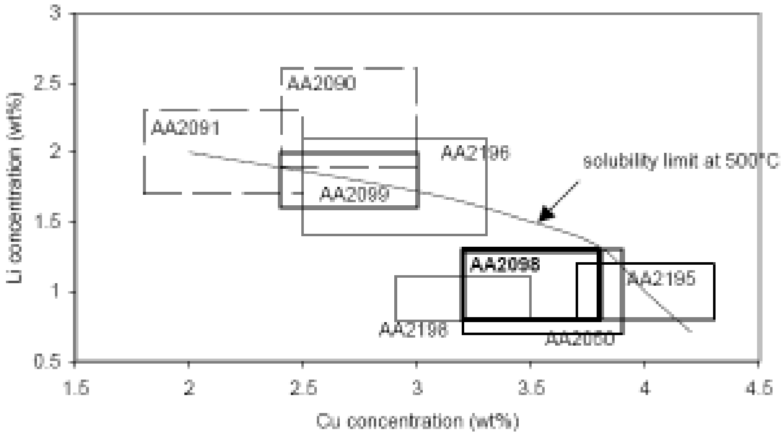

Fig. 1.1: Cu and Li contents of selected alloys of the 2nd and 3rd Al-Li generations [8].

1.2 Design philosophy

The reason for the decrease in Li content in the current generation of commercial alloys, such as the AA2198, can be clearly understood simply by looking at the binary Al-Li phase diagram in Fig. 1.2, where the solvus line of the $\alpha+\delta'$ phase field has also been included. This shows that if the Li content is chosen to be up to 1 wt%, precipitation of the metastable δ' phase will be prevented upon ageing below the α solvus line [9]. This particular phase is detrimental to fracture toughness. The discontinuity in the δ' phase field represents a miscibility gap which leads to local ordering of a possible Li-rich GP zone formation on quenching from the solution treatment (ST) temperature [2].

A detailed study of the Al-Cu-Li phase diagram is vital both for alloy design and selection of the solution treatment temperature. Concerning the former consideration, the alloy needs to be designed so as to yield the most effective combination of strengthening precipitates during ageing. The isothermal phase diagram sections in Fig. 1.3a illustrate the resulting precipitates for various composition ranges as a function of heat treatment temperature and Cu, Li content, for a fixed Al concentration which is equal to that of the AA2195 alloy, typically close to 94 wt%.

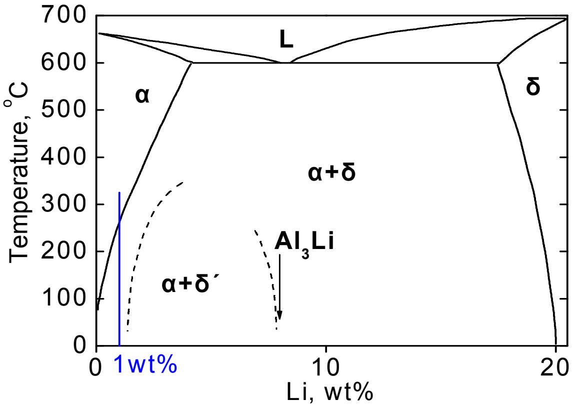

Fig. 1.2: The Al-Li phase diagram demonstrating the exact position of the Li content for the AA2198 alloy relevant to the solubility limits of the metastable δ' phase [2].

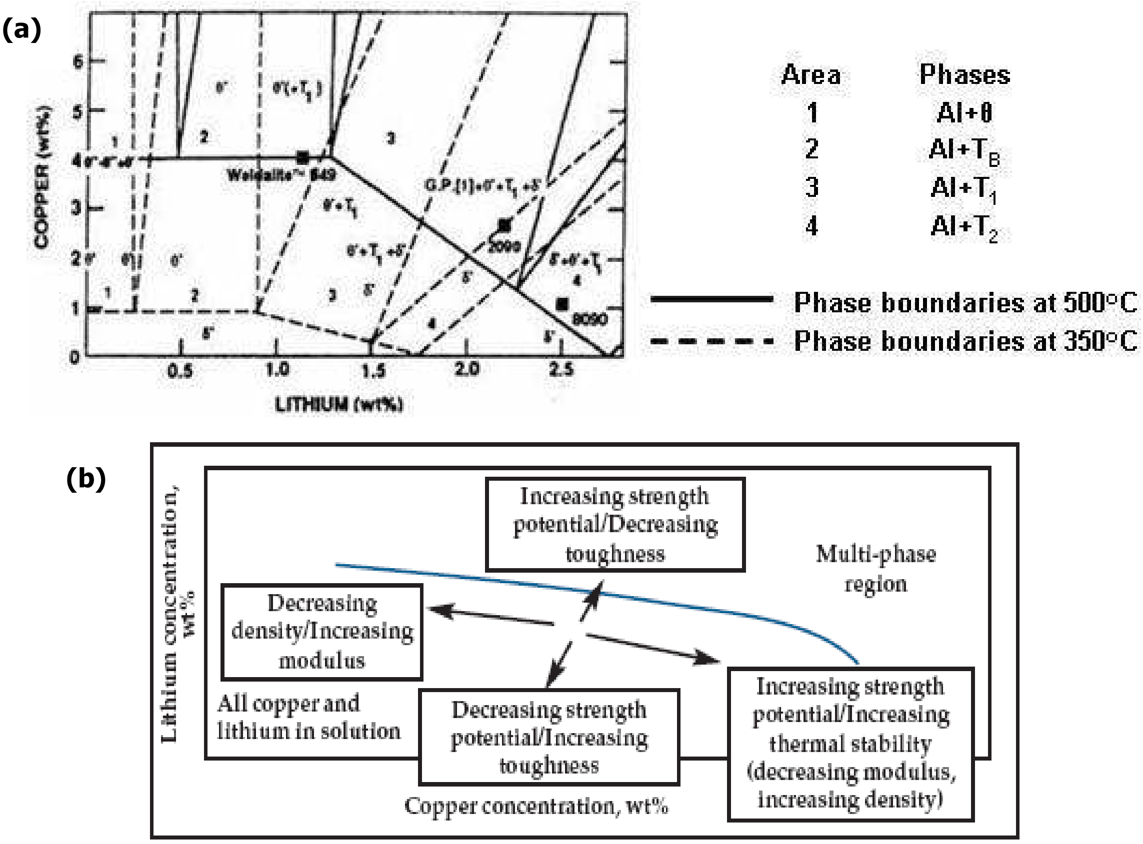

Fig. 1.3: a) Phase boundaries in the Al-rich corner of the Al-Cu-Li ternary phase diagram, with an Al content equal to that of the AA2195 alloy (~94 wt%) [10]. **b)** Mechanical property map relative to the Li and Cu concentrations in Al-Cu-Li alloys [11].

In Fig. 1.3a the AA2198 alloy which contains 1 wt% Li, 3 wt% Cu and 95 wt% Al, slightly higher than the AA2195, is seen to lay within the region of the T_1 phase at 350°C (designated by the dashed lines). At lower ageing temperatures (i.e. below 200°C) it is expected to lie within the θ'+T_1 region. A similar isopleth constructed for the present system would show a similar trend for the resulting phases and the final microstructure of AA2198 at a lower ageing temperature and would only consist of T_1 and θ'. Experimental investigations on the AA2198, carried out at SIMAP-INP in Grenoble by another group working on the same materials provided by Alcan CRV, have verified that the precipitates present after ageing at 155°C are mainly T_1 together with a small amount of θ' [12].

Since an alloy's microstructure is in direct relation to its final mechanical properties, a property map, such as that shown in Fig. 1.3b is vital for an engineer when designing a new alloy. Alloy chemistry plays a critical role in the strengthening precipitates which, depending on their nature, subsequently affect the deformation mechanisms and thus the resulting mechanical properties. In Al-Cu-Li alloys, the Cu/Li ratio is of primary importance for the material's design. High Li and low Cu contents lead to a weight reduction and an increase in elastic modulus. Increasing the Cu content promotes strengthening due to precipitation of fine Cu-containing phases, which change from θ' to T_1 when also increasing the Li content. The negative side-effect of a high Cu content is the inevitable increase in density. The blue curve in Fig. 1.3b indicates the solubility limit at 500°C, which is a typical solution treatment temperature in Al-Cu-Li alloys [8].

To select the most appropriate ST temperature for an alloy with a composition similar to the AA2198 (3.86 at% Li), the Al-Cu-Li phase diagram has to be employed. From Fig. 1.4, it is obvious that the temperature range for ST is approximately between 505°C and 540°C. The equilibrium phases resulting from slow cooling of the melt would be T_B and T_1. Nevertheless, quenching after the solution heat treatment ensures that no second phases will form on cooling. This fact justifies why the ST temperature, as well as the annealing temperature for recrystallisation kinetics experiments, have been chosen within this region.

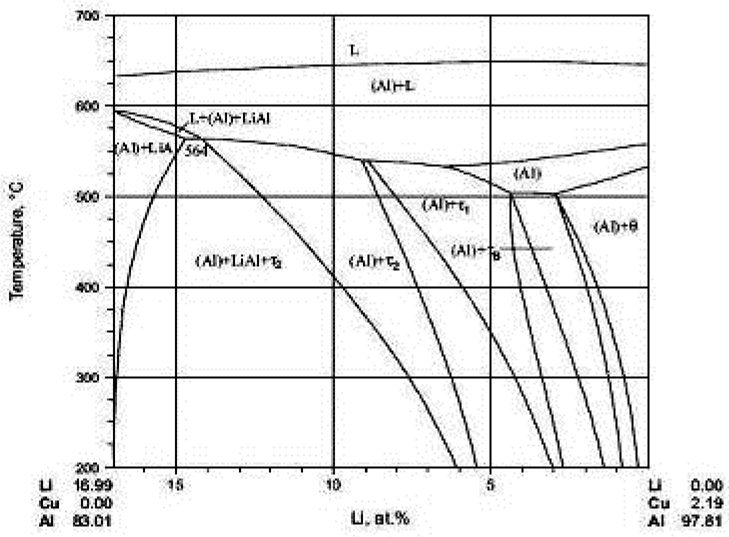

Fig. 1.4: Vertical section of the ternary Al-Cu-Li phase diagram at 95 wt% Al [13].

1.3 Grain structure control by dispersoids

The future generations of aerospace alloys will benefit from the in-depth understanding of the grain refining mechanisms in conjunction with clarifying the dispersoid behaviour during formation and processing. The ability to control the grain structures of wrought Al products is crucial since many of the final material properties are affected. The effects of grain structure control on the most important material properties are briefly discussed below.

- *Grain size hardening* is favoured by a small grain size according to the Hall-Petch relationship: $\sigma = \sigma_o + k_1 d^{-m}$ (1-1)
  where σ is the yield stress, σ_o is the lattice yield stress, k_1 is a strengthening coefficient of the grain boundaries for a given material, d is the grain size and m an experimental exponent whose value depends on the material [5].
- *Recrystallisation resistance* is lower for fine-grained alloys because GBs can act as recrystallisation nuclei [14].
- *Texture* can be controlled through the amount of recrystallisation allowed to occur, as the new grains might have random orientations [4].
- *Anisotropy of mechanical properties* is higher when a strong texture exists [4, 15].
- *Slip homogenisation* is aided by a smaller grain size since the slip line length and stress concentrations at GBs are decreased [16].
- *Ductility and fracture toughness* are higher for smaller grain sizes due to the change in fracture mode from intergranular to transgranular, while strong textures have the same effect as well [2, 16].
- *Superplasticity* is favoured by a small grain size and grain coarsening can be prevented by precipitation of strongly pinning particles [17].

Although zirconium and manganese are commonly added together in commercial high strength aluminium alloys to increase their damage tolerance by enhancing the grain size hardening effect and inhibiting recrystallisation, there has been no systematic study so far to understand the microstructural features of this simultaneous addition. This is the actual purpose of the current thesis. The known advantage of the coexistence of Zr- and Mn-dispersoids is the presence of particles almost in all areas of a grain, hence minimising dispersoid-free volumes which could act as recrystallisation nucleation sites [18]. This phenomenon occurs due to the inverse segregation trends during casting of the two elements of interest and is illustrated in Fig. 1.5, where zirconium segregates to the dendrite centres while manganese segregates near the dendrite edges [19]. The ultimate aim is the limitation of grain growth and improvement of recrystallisation resistance due to the inhibition of the grain boundary migration by the dispersoids, or by the additional amount of solute in that region [18].

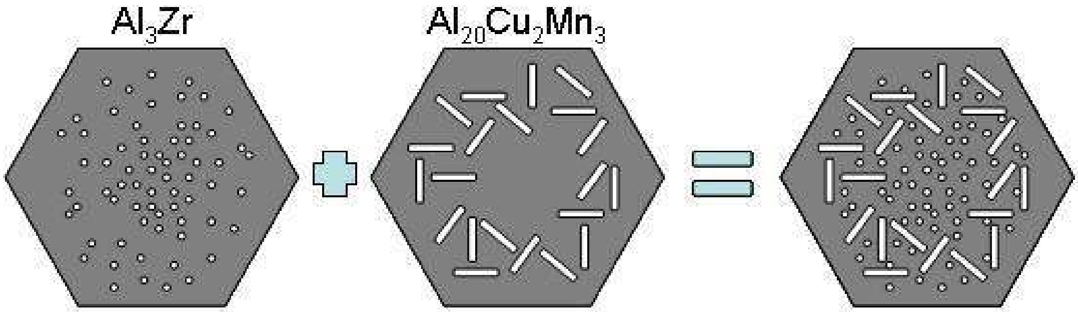

Fig. 1.5: Schematic diagram of the idealised spatial distribution of Al_3Zr and $Al_{20}Cu_2Mn_3$ dispersoids within model hexagonal grains. The opposite segregation patterns of the two phases lead to minimisation of dispersoid-depleted areas when both of them are present.

1.4 Properties and applications of Li-containing alloys

Al-Li alloys have been extensively reviewed in the past, either in articles dedicated solely to these alloys [1-3, 7, 16, 20-22], or as part of articles or books on aerospace materials [5, 6, 8, 23-26]. Thus both the advantages and the shortcomings of Li addition are well-known. One gap identified in the literature so far, is the lack of a review paper on the latest variants of the 3rd generation alloys. However, this is natural since these materials are still under development and not enough data has been published by the manufacturing companies yet due to confidentiality issues.

In brief, the two most significant benefits from the addition of Li are weight reduction and increase in stiffness. Li has an extremely low density (0.534 g/cm^3), so each 1 wt% in solid solution in Al leads to a decrease in alloy density by 0.08 g/cm^3 (~3%) [2]. In the same manner, the Young's modulus increases by approximately 3 GPa for every 1 wt% Zr, as reported by Martin [2], or by approximately 5-6%, as reported in various reviews [1, 5-7, 9, 20, 25, 27]. It has also been claimed that the maximum weight reduction can increase from 10% to 18% if a structure of Al-Li alloys is designed to be thinner than one of conventional alloys but without any loss in strength, due to the higher specific stiffness of these materials [3]. Other properties that show improvement are strength, low temperature mechanical properties, fatigue crack growth and stress corrosion cracking resistance (SCC) [2, 3, 6, 22].

On the other hand, several significant problems can be encountered and this was especially true in the first two generations of Al-Li alloys. Namely:

- *Low mechanical properties in the S-T and S-L directions* of thick plates (especially fracture toughness but also SCC) [3, 6, 22, 25].
- *High degree of anisotropy* due to strong crystallographic texture in unrecrystallised products (in-plane and through-thickness) [4, 22, 25].
- *Strain localisation/crack turning* due to particles sheared by dislocations (aids fatigue crack growth resistance but lowers fracture toughness) [2-4, 16, 22, 25].

- *Necessity for cold-work before ageing*, which does not facilitate the fabrication of complex-shaped products with high strength [4, 6].
- *Poor thermal stability* of certain alloys (owing to δ' precipitation) [21, 22, 25].
- *Intergranular fracture* due to precipitation of δ and T_1 phases on GBs, which leads to microvoid formation around them [2, 5, 16, 22].
- *PFZs near the GBs* due to δ' dissolution and Li diffusion towards the boundaries where subsequently δ phase is formed [5, 16].
- *Presence of impurities* such as Fe, Si, Na, K, Ca, S and H_2, which cause embrittlement [3, 5, 16, 20, 28, 29].
- *Inadequate high temperature properties* [2].
- *Recycling issues* since Al-Li scrap needs to be dried, de-oiled and separated from that of conventional Al alloys [6, 25, 30].

Most of the afore-mentioned problems have been overcome in the current generation of Al-Li alloys via minimising the volume fraction of δ' precipitates, elemental additions, or appropriate thermomechanical processing. In order to be able to effectively control an alloy's microstructure and overcome the problems met, one should have a deep understanding of the requirements for each property that the material is targeted to possess. Several references exist in the literature where assessments of all the necessary properties for commercialisation of aerospace Al alloys are set out [2, 3, 22, 23, 26]. Table 1.1 lists typical applications of the majority of Li-containing alloys found in the literature so far.

1.5 Future research on Al-Li alloys

The future of Al-Li products in aerospace structures seems bright as Lequeu [11] of Alcan Aerospace mentions in a recent article, since trade studies showed that they are beneficial compared to composite materials. The objectives under which the 2nd generation alloys were developed have been finally achieved and the most recent variants of the 3rd generation Al-Li alloys have directly substituted for the conventional high performance 2xxx and 7xxx alloys on various aircraft parts. Nevertheless, in order to maintain and extend their application in aircraft, a strategy needs to be followed consisting of optimised material utilisation, superior alloy performance, utilisation of new technologies and implementation of new designs [8]. The overall goal is to produce an acceptable balance of properties along with minimising cost.

Table 1.1: Existing and potential aerospace applications of Al-Li alloys (potential applications at the time of publication of the corresponding reference are denoted by *).

Alloy	Form	Application	Ref.
1420	sheet, plate, extrusion, forging	Soviet military aircraft, MIG-25 Foxbat (similar applications to 2020 alloy)	[2, 4-6]
1421	sheet, plate, extrusion, forging	Soviet military aircraft	[4]
1430	—	similar applications to 2091 alloy	[4]
1440	—	similar applications to 8090 alloy	[4]
1450	—	similar applications to 2090 alloy	[4]
1460	—	similar applications to 2090 alloy	[4]
2020	plate	wing skins in A-5A and RA-5C Vigilante bomber aircraft	[2, 4]
2050	plate	*damage tolerant components in commercial airframes, *FSW wing ribs, structural parts in Airbus A350	[8, 31]
2050-T84	plate	*wing skins, *spars, *floor beams, *non-critical parts, *various fittings in the aircraft, lower wing reinforcement in Airbus A380	[31, 32]
2090	sheet	AgustaWestland EH101 helicopter, lower wing skins, fuselage panels and doors and cargo floor area in McDonell Douglas C-17 airlifter craft, high damage tolerance and fracture toughness products, *fuselage skins, *internal structures, *fairings, *nacelles, *fan casings, *access doors, *slats, *storage racks	[2, 3, 25, 26]
	extrusion	cargo floor area in McDonell Douglas C-17 airlifter craft, *upper/lower wing skins, *fuselage skins, *internal structures, *fairings, *nacelles, *fan casings, *access doors, *slats, *storage racks	[3, 26]
2090-T62	sheet	flooring sections in McDonell Douglas C-17 airlifter craft, seats	[1, 25]
2090-T81	plate	thin sections, *cryogenic tankage of booster systems	[1, 4]
2090-T83	sheet	flooring sections in McDonell Douglas C-17 airlifter craft, thin sections, upper stringers, flaps, upper wings, access doors, slats, spoilers, frames	[1, 3, 4, 25]
2090-T84	sheet	wing leading edges in Airbus A330/A340, European Fighter Aircraft prototypes, thin sections, spoilers, slats, leading edges, flaps, bulkheads	[1, 3, 4]
2090-T86	extrusion	thin sections, flooring sections in McDonell Douglas C-17 airlifter craft, ducts, seal tracks, cargo tracks	[1, 3, 4]
2091	sheet	AgustaWestland EH101 helicopter, lower wing skins, fuselage panels and doors, *fuselage skins, *internal structures, *fairings, *nacelles, *fan casings, *access doors, *slats, *storage racks	[3, 25]
2091-T3	sheet	*Fokker 100 fuselage access doors	[3]
2091-T8	plate	fuselage frames and skins, flaps, doors	[1]
2091-T8X	plate	medium strength for space applications	[4]
2091-T84	sheet	*fuselage sections in Airbus A340 commercial aircraft, lower stringers, bulkheads	[1, 3]
2091-T851	sheet	seats	[1]
2094	plate	—	[4]
2095	plate	aerospace launch vehicles, cryogenic tanks	[4, 33]
2096	plate	—	[4]
2097	plate	fighter aircraft bulkhead, aircraft sections requiring high fatigue resistance	[4, 26]

2098-T82	plate	fuselage components in F-16 fighter aircraft	[31]
2099-T8E77	plate	*internal structure (e.g. wing ribs)	[22]
2099-T83	extrusion	crossbeams, seat rails, false rails, cockpit structures, emergency bay floor structures, electronic racks in Airbus A380	[22]
2195	plate	cryogenic tanks, fighter aircraft	[4, 34]
2196	extrusion	*structural parts in Airbus A380, thin sections for seat rails and fuselage stiffeners, thick sections for crossbeams, wing stringers and fuselage frames	[11, 31]
2196-T8511	extrusion	thick sections for floor beams in A380, thin sections for floor structures and fuselage stiffeners in A380	[32]
2197	plate	fighter aircraft bulkhead	[4]
2198	sheet	*damage tolerant components in commercial airframes, structural parts in Airbus A350, fuselage skin	[8, 11, 31]
2198-T8X	sheet	fuselage skin in Airbus A350	[35]
2199	sheet	fuselage skin in Airbus A380	[22]
2199-8E80	plate	*lower wing skin	[22]
2297	plate	space aircraft, fighter aircraft	[34]
8090	sheet	internal structures in AgustaWestland EH101 helicopter	[5]
	plate	seat tracks, internal structures, stringers, I-beams and channels in AgustaWestland EH101 helicopter, *upper/lower wing skins, *fuselage skins, *internal structures, *fairings, *nacelles, *fan casings, *access doors, *slats, *storage racks in aircraft	[3, 5]
	extrusion		
	forging	main cabin frame in AgustaWestland EH101 helicopter, lower wing skins, fuselage panels and doors	[3, 5, 25]
	tube	AgustaWestland EH101 helicopter	[3]
8090-AF	age-formed plate	*lower wing skins and internal structures in commercial aircraft	[3]
8090-T6	forging	*fuselage sections in Airbus A340 commercial aircraft	[3]
8090-T62	sheet	European Fighter Aircraft prototypes, AgustaWestland EH101 helicopter	[3]
8090-T8	plate	lower stringers, fuselage frames, longerons, access doors, fuselage skin, spars, ribs, flaps lower wings, cargo tracks	[1]
8090-T81	sheet	AgustaWestland EH101 helicopter, *fuselage sections in Airbus A340 commercial aircraft	[3]
	plate	medium strength for space applications, bulkheads	[1, 4]
8090-T8151	extrusion	*lower wing skins and internal structures in commercial aircraft	[3]
8090-T8171	plate	*lower wing skins and internal structures in commercial aircraft	[3]
8090-T82	extrusion	*fuselage sections in Airbus A340 commercial aircraft	[3]
8090-T83	sheet	D-nose skins of the leading edge in Airbus A330/A340 aircraft wing	[25]
8090-T851	sheet	*wing skin in A-15 fighter aircraft (demonstration only)	[26]
8090-T8511	extrusion	AgustaWestland EH101 helicopter, *fuselage sections in Airbus A340 commercial aircraft	[3]
8090-T8771	plate	medium strength for space applications	[4]
8091	—	high strength applications similar to 2090	[5]

8092	—	aerospace	[5]
8192	—	*general purpose use in aircraft	[3]
VAD23	plate	Soviet military aircraft	[4]
Weldalite049	plate	*US National Aerospace Plane, *Titan family of missiles, space applications	[1, 36]

Optimised materials' utilisation. The buy-to-fly ratio is an important factor that needs to be improved and represents the quantity of the material that is eventually used in an aircraft once it has gone through all the processing stages, compared to the quantity of the material that was produced initially [8]. Another solution is to reduce the number of parts used to assemble an airplane and use fewer, but integral parts to reduce weight and manufacturing time and effort [23].

Superior alloy performance. In the aerospace sector there is a constant demand for more damage tolerant alloys (combining fracture toughness, fatigue crack growth resistance and SCC resistance), such as the AA2198 and AA2050. The current alloy generation is intended to be improved through studying the hardening mechanisms, the Al-Cu-Li-Mg phase diagram, especially its Cu-rich side, and the effects of minor alloying additions [8]. Other fields of research include new dispersoid combinations to enhance the ability to control grain structures and optimise alloy chemistry and tempering [11].

Utilisation of new technologies. Innovative production and joining methods are required to decrease the final cost of the airplane, as well as its maintenance costs via weight savings. One method already in use is by machining the final component from a large plate so as to avoid joining the individual parts together. A typical example is the machining of the upper outer-wing, where normally the stringers would be joined to the skin with rivets [32]. Al-Li alloys have been designed to be compatible with this process [11]. Alternatively, novel joining techniques have to be employed, such as friction stir welding.

Implementation of new designs. A very straightforward way to reduce the aircraft weight is by using thinner sections, simply by taking advantage of the increased stiffness of the Al-Li alloys [3]. The most effective method to ensure the manufacture of the most efficient structure is by local tailoring of properties, separately for each component [11, 32]. Lequeu [11] states in his article that weight savings of 10-30% and anticipated cost reductions up to 40% are possible, through the combined application of novel joining techniques and local tailoring of properties.

1.6 Project aims and objectives

The main focus of this project was to find the optimum dispersoid content for the AA2198 alloy sheet. The present alloy has been patented with combined Zr and Mn additions for damage tolerant design applications of products over any thickness range [37]. However, this project will prove that this dispersoid combination yields the desired properties only in thick plate but not in thin sheet. The reason for this apparent incongruity was the subject of this research and was found to be due to interactions between the two dispersoid families present.

The original main goals of this project, as they were defined at its inception were:

- To find the optimum dispersoid content by assessing the properties of the AA2198 variants with different concentrations of Zr and Mn, in the five different areas below:
    - grain size control
    - recrystallisation
    - texture
    - fracture toughness
    - overageing

  This involved the detailed characterisation of the dispersoid distributions in the as-received T351 condition and after casting and homogenising.
- To identify any possible interactions between Zr- and Mn-dispersoids and analysis of the underlying mechanisms.
- To determine the effects of each dispersoid family present (Zr, Mn), either individually or in combination.

1.7 Thesis overview

The present thesis has been structured so that the chapters dealing with topics which are inter-related, yet of a different focus regarding the various microstructural features, can be put together in a logical order to produce a scientific text with a constituent flow. Three main areas of interest have been identified, relative to the effects of dispersoid additions; dispersoid formation and distribution, their role during thermal treatments and their effect on mechanical properties and ageing behaviour.

This thesis starts by highlighting the importance of the AA2198 alloy system and the reasons why it is examined, followed by a detailed review of all the current literature and principal theories employed in the interpretation of the results. The experimental section provides the reader with a description of the basic concepts of each technique used, as well as information on the key parameters for each one of them.

The presentation of results begins with an introductory chapter (Chapter 4) which gives a brief description of the main effects of the combined Zr and Mn additions on the properties of the AA2198 sheet. To understand the recrystallisation behaviour and mechanical properties, it is first crucial to analyse in detail the dispersoid distributions in all the alloys, which is the subject of Chapter 5. The dispersoid characteristics are studied at and during three different stages; formation during homogenisation, final product form (T351 condition), and prolonged heat treatments of the as-deformed materials (F temper) at elevated temperatures. The key measurements in all these three processing stages are those of composition, size and volume fraction, while observations such as the coherency state and morphology are also crucial to recrystallisation inhibition.

Following the chapter on dispersoid distributions, the thesis focuses on the resulting recrystallisation behaviour and grain structures in the F and T351 tempers (Chapter 6). Recrystallisation kinetics are measured and the underlying mechanisms revealed. The acting mechanisms are explained by also taking into consideration the distribution of each dispersoid type.

Chapter 7 focuses on mechanical properties and ageing, which are analysed as a function of the dispersoid content. These properties are the hardness after ageing at various temperatures (ambient, 155°C, 200°C) and the fracture toughness (measured from Kahn tear tests). Everything else, that is not directly relevant to the basic aims of this thesis, is presented in the Appendices.

CHAPTER 2: Literature Review

2.1 3^{rd} generation Al-Li alloys

The demand for lower density and higher strength Al alloys led to the original development of the Weldalite^{TM} alloy family by the Martin-Marietta laboratories in the United States [5], on which the most recent 3^{rd} generation Al-Li alloys are based. These alloys are really attractive for applications where the strength to weight ratio is a major concern, such as in aerospace. With a yield stress that can exceed 700 MPa, the Weldalite alloys provide strength levels higher than of virtually any other conventionally cast aluminium wrought products [5]. As reported by Pickens et al. [36], a Weldalite^{TM} 049 alloy forged at 400^{o}C exhibited a UTS of 802 MPa and a σ_y of 794 MPa, but with an unavoidable sacrifice in elongation, 0.3 %, in the T6 condition. This type of alloys can exhibit good cryogenic fracture toughness when appropriately processed [38-40]. Its disadvantages are low ductility, low toughness, strong texture and anisotropy of mechanical properties, which is caused by a low strength at 45^o off the RD for rolled plates [4, 22, 25]. In comparison, the 3^{rd} generation Al-Li alloys have evolved to give a better balance of properties and higher damage tolerance, but with a lower strength and Li level.

2.1.1 Precipitate phases and age hardening behaviour

The exceptionally high strength levels achieved in 3^{rd} generation Al-Li alloys combined with high damage tolerance derive mainly from the presence of the semi-coherent, plate-like T_1 phase (Al_2CuLi). An explanation for this intense precipitation hardening effect stems from the fact that this phase precipitates as thin plates on the principle glide plane in the Al matrix with four $\{111\}_{Al}$ habit plane variants, thus inhibiting the dislocation motion more effectively (Fig. 2.1). The nucleation process of T_1 still remains under question as various theories have been proposed.

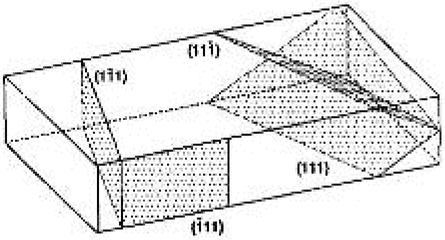

Fig. 2.1: Spatial correlation of the four crystallographic variants of the $\{111\}_{Al}$ habit planes of the T_1 phase [41].

Other metastable phases contributing to the strength increase in 3rd generation Al-Li alloys include GP zones, θ', δ', S' and Ω (a table with their main features is presented by Kumar et al. [42]). Several references on the stable and constituent phases (T_2, T_B, T, R, δ, θ, S, Al_7Cu_2Fe) of this system exist in the literature [43-54]. TEM images of some typical phases found in such systems are presented in Fig. 2.2.

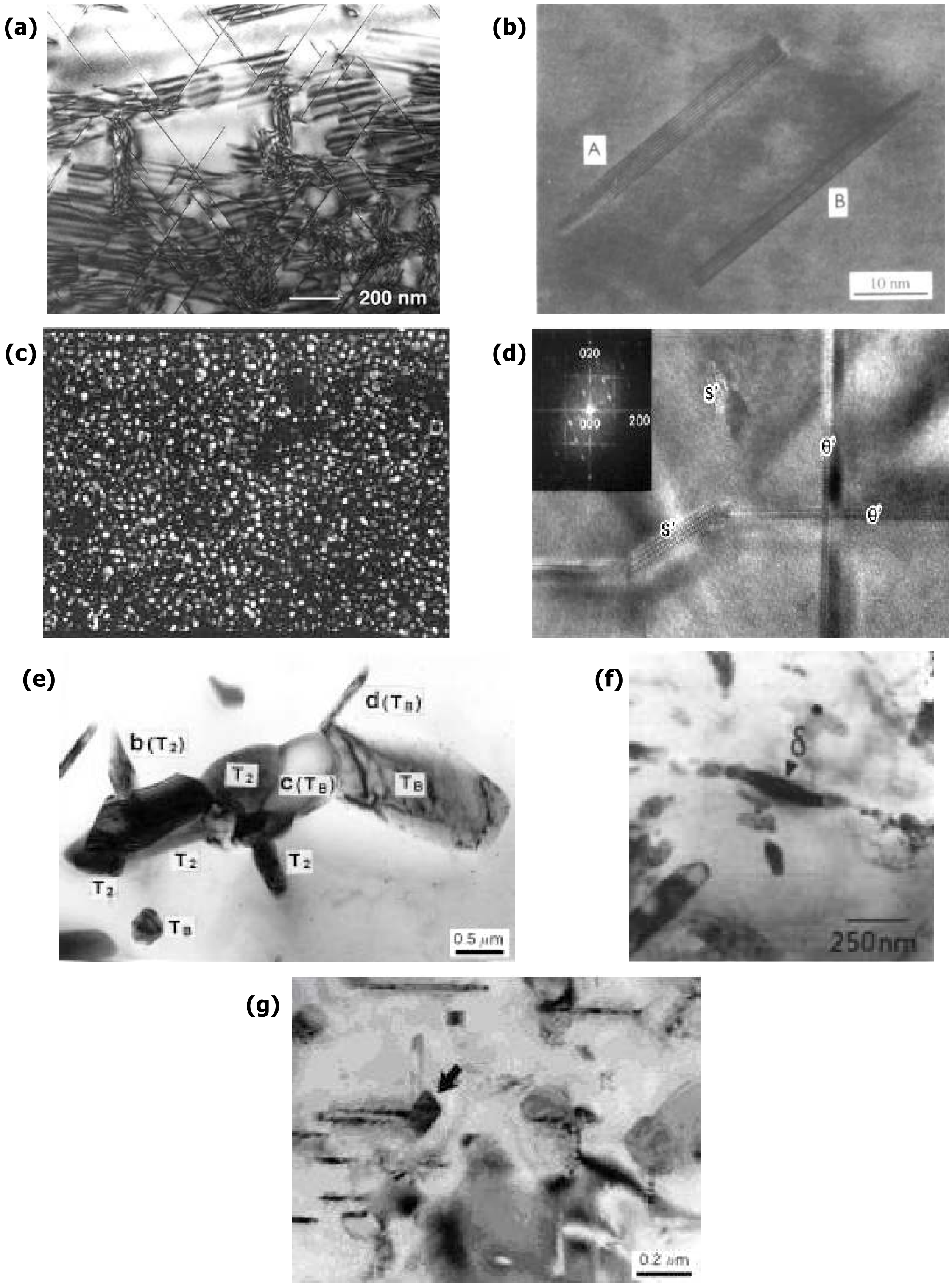

Fig. 2.2: Common ageing precipitates found in Al-Cu-Li alloys: **a)** T_1 phase near the $<110>_{Al}$ zone axis [55], **b)** Ω phase plates near the $<112>_{Al}$ zone axis (the picture is from an Al-Cu-Mg-Ag alloy) [56], **c)** DF-TEM image of δ' phase after 24h at 190°C [44], **d)** θ' and S' phases after 1h at 190°C [57], **e)** T_B and T_2 phases after overageing 9000h at 200°C [45], **f)** δ phase precipitated on a GB after 16h at 250°C [49], and **g)** R phase after overageing for 9000h at 200°C [45].

The T_1 phase has a thickness of only a few atomic planes and its habit plane with the Al matrix is $\{111\}_{Al}$ [58]. In previous years, various theories had been proposed regarding its crystal structure, but finally it has been defined as hexagonal with an orientation relationship with the aluminium matrix of $\{111\}_{Al} \parallel \{0001\}_{T1}$ and $<\bar{1}10>_{Al} \parallel <10\bar{1}0>_{T1}$ [59]. There is still a lot of debate concerning its space group. Some proposed crystal structures and values for the lattice parameters of the T_1 phase can be found in Table 2.1. In contrast to the commonly observed plate-like morphology, Park and Ardell [60] reported the occurrence of rod-shaped T_1 precipitates after ageing of an unstretched AA2090 alloy at 160°C. The new morphology had a different orientation relationship with the matrix of $\{3\bar{2}1\}_{Al} \parallel <10\bar{1}0>_{T1}$ and $<121>_{Al} \parallel <\bar{1}2\bar{1}0>_{T1}$. Although this resulted in a larger lattice mismatch than the plate-like phase, its presence was justified on the grounds of reduced dislocation density as the material was in a T6 condition.

Table 2.1 Lattice parameters and proposed crystal structures for the T_1 and Ω phases.

Phase	Proposed structure	Lattice parameters	Ref.
T_1	hexagonal	a=0.497 nm, c=0.935 nm	[44, 58]
	hexagonal	a=0.286 nm, c=0.935 nm	[58]
	trigonal	a=0.286 nm, c=0.935 nm	
Ω	monoclinic	a=b=0.496 nm, c=0.848 nm, γ=120°	
	orthorhombic	a=0.496 nm, b=0.859 nm, c=0.848 nm	[44, 58, 61]

The T_1 phase can be affected by other alloying elements in several ways. One phenomenon is the segregation of Mg and Ag at its interface, as was proven experimentally via atom probe analysis by Murayama and Hono [62] and verified recently by De Geuser et al. [63]. This observation is rather important as it may help towards identifying the exact nucleation mechanism of T_1. Another interesting phenomenon is the wetting of the interfaces of the main strengthening precipitates by the δ' Al_3Li phase, when the Li content is relatively low. This kind of interaction was also observed between Al_3Li and θ' [55, 63, 64] and GP zones [55, 65]. Although the previously mentioned atom probe work has not given any indication of Al_3Li wetting on the whole of the T_1 interface [62, 63, 66, 67], composite precipitates of these two phases have been observed in the past [65, 66]. An unusual phenomenon of structure evolution of the $\{111\}_{Al}$ habit plane precipitates, upon ageing of an Al-1.6Li-3.2Cu at 220°C, was observed by Yoshimura et al. [55], but did not appear for higher Li contents. In this work, the lattice parameters of the thin plates were found to vary locally within the precipitates, where they exhibited smaller c-axis values than T_1, which resembled those of the Ω phase.

Regarding the presence of the Ω phase in Al-Cu-Li alloys, its coexistence with T_1 is not yet clearly proven. These two phases have similar morphology and crystal structure and form on the same habit plane, so it is difficult to readily discriminate between them. Table 2.1 also presents some data on the crystal structure and lattice parameters of the Ω phase. This phase is said to be in abundance in alloys with a low Li content close to 0 wt% [55, 68] and with a Cu:Mg ratio above 5 [44], while T_1 prevails at higher Li contents. This gives an indication that there might be a composition regime where both phases coexist. The level of Li required for a transition from the Ω phase to the T_1, should depend on a number of factors which have not been fully defined so far; the ageing temperature and time being among them [61, 69]. One method for distinguishing between the two phases is by comparing lattice images of such plate-like precipitates in the $<110>_{Al}$ and $<112>_{Al}$ orientations [58]. Another method is to compare SAD patterns in the $<110>_{Al}$ and $<112>_{Al}$ zone axes [61]. The Ω phase reflections occupy different positions in the $<112>_{Al}$ zone axis and can be separated from those of the T_1 phase (Fig. 2.3) [70].

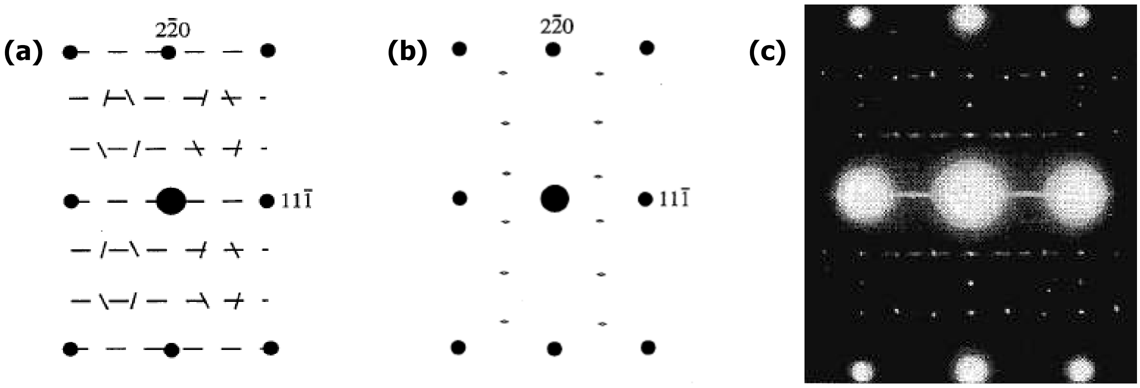

Fig. 2.3: SAD patterns from the $<112>_{Al}$ zone axis [70]: **a)** sketch of the T_1 phase reflections, **b)** sketch of the Ω phase reflections, and **c)** alloy AA2195 aged for 15h at 149°C.

Nucleation of the T_1 phase is a highly controversial subject and no specific mechanism has been proposed so far. Most certainly, one factor that significantly affects the nucleation of T_1 in Al-Cu-Li-based systems is the alloy composition. Starting from the undisputed nucleation sites, dislocations play a very important role in yielding a homogeneous distribution within the microstructure, due to preferential nucleation of T_1 within their strain field [57, 71-73]. An increased dislocation density prior to ageing leads to an improvement in ageing kinetics, as well as yield strength, UTS and elongation. In particular, T_1 nucleation is favoured by dislocation loops surrounding Zr-containing dispersoids [74]. Contradictory data also exists, claiming that loops cannot possibly be potential sites of heterogeneous nucleation [75]. Other nucleation sites for the T_1 phase that have been reported in the literature include:

- Stacking faults [75-77]. Combined addition of Mg and Ag, as well as low supersaturations, reduce the stacking fault energy and lead to formation of stacking faults on $\{111\}_{Al}$ planes.
- Low angle grain boundaries [47, 57, 72, 76, 78-81]. Even with the application of a pre-stretch, heterogeneous nucleation on subgrain boundaries cannot be avoided. Most often at the peak-aged condition, T_1 precipitation is quite intense on LAGBs where the phase

forms as short, thick plates. When the precipitate habit plane is parallel to the boundary's plane it can then grow longer. Methods of reducing the amount of precipitates on subgrains are by either increasing the Li content (from 0.5 to 1.6 wt% [78]), or applying a two-step ageing treatment with exposures at 132°C and 138°C [39, 40], or another multi-step ageing process [38, 82].

- High angle grain boundaries [47, 78]. Along with LAGB nucleation, heterogeneous precipitation on HAGBs, with associated PFZs, has also been observed in some cases where the T_1 forms as short, thick plates. In contrast to this statement, Tosten and colleagues [81] support that precipitation occurs only on LAGBs and not on HAGBs.
- Vacancies [72, 75, 80]. Their role is very important as they can change the location where T_1 precipitation occurs within the microstructure. A good example is that by Itoh et al. [74] where reduction of the vacancy concentration by direct ageing after solution treatment, eliminated precipitation on octahedral voids. The T_1 phase was reported to nucleate on them, thus resulting in a more uniform distribution in the matrix at low temperatures. They also attract each other, leading to the formation of loops which are potential nucleation sites. At high temperatures where vacancy diffusion is faster, they tend to migrate to large vacancy sinks, such as surfaces and grain boundaries, and leave a lower dislocation density in the matrix to support heterogeneous nucleation.
- Octahedral voids [74]. These voids are defined as vacancy clusters surrounded by $\{111\}_{Al}$ planes.
- Co-clusters [76-78]. Mg-Ag co-clusters form on $\{111\}_{Al}$ planes so as to minimize elastic energy and also act as heterogeneous nucleation sites. Their composition is reported to be Mg_3Ag. Mg-Ag co-clusters probably favour Cu-Li co-clustering, which would increase T_1 precipitation kinetics.
- GP zones [74, 77, 78]. At high supersaturations, T_1 precipitates form on GP zones on $\{111\}_{Al}$ planes. These co-clusters comprise of Mg, Ag and Cu.
- Dispersoids [83]. In recovered regions, T_1 precipitates form heterogeneously on Al_3Zr dispersoids.
- Matrix [57, 71-73]. As reported above, nucleation in the matrix yielding a homogeneous distribution can occur when there is not a large number density of dislocations which act as heterogeneous nucleation sites.

Combined atom probe and HRTEM analyses have been employed for the purpose of studying clusters and co-clusters of atoms that act as nuclei for the T_1 major strengthening phase. Reich et al. [67] support the theory that the T_1 nucleation mechanism is similar to that for Ω because Ag and Mg are observed in both cases to behave in the same manner and segregate to the precipitate interface. Murayama and Hono [62] and Honma and colleagues [84] reported the absence of Mg-Ag co-clusters; only Mg clusters were observed by the former researchers, while only Ag-vacancy pairs were detected by the latter ones. Finally, Ringer et al. [66] gave only speculative conclusions on their observation that Ag and Mg segregate to δ', claiming that T_1 is homogeneously distributed in the matrix because it nucleates on δ' precipitates, which have a homogeneous dispersion. This hypothesis has not been supported by any complementary work in subsequent years.

Deformation prior to ageing, both natural and artificial, results in some notable changes in the microstructures of Al-Cu-Li-Mg-Ag alloys and subsequently, their mechanical properties. Deformation can be applied by either stretching [85] or rolling [86]. The main goal of either processing method is to achieve a higher dislocation density for nucleation of the major strengthening phase. According to Lee et al. [87], only Li-containing alloys with Cu content over 2 wt% exhibit a pronounced hardness increase after stretching. Other 2xxx alloys without Li do not exhibit any strengthening phenomenon after pre-deformation. A typical example is the Al-Cu-Mg-Ag high strength system, the hardness of which is reduced with pre-deformation [88].

In Al-Cu-Li alloys, a large hardness increase has been reported on several occasions on ageing following stretching, but in some other instances the increase in strength was said to be minor. Lee et al. [87] claim that the change in strength of an Al-Cu-Li-Mg alloy depended on the ageing temperature and that the strengthening effect due to stretching was more pronounced at lower temperatures. In contrast, the data on Al-Cu-Li-Mg-Ag alloys from Ringer et al. [88] and Huang and Zheng [80] oppose this theory. Some of the undisputed effects of stretching are the acceleration of ageing kinetics, more homogenous distribution of T_1 precipitates, T_1 refinement and increase in its volume fraction, reduction in size and number density of δ', a hardness increase throughout the whole ageing curve and reduction in the reversion of hardness curves. Elongation is also believed by some to increase [87, 89], possibly because of the increased number density and more uniform distribution of the T_1 plates [87] that prevent shear localisation. However, a ductility decrease has also been reported after 6% rolling prior to ageing [80].

Regarding natural ageing, undeformed materials exhibit a higher response because stretching inhibits GP zone formation at room temperature [42, 73]. The δ' size and distribution are not influenced by stretching at room temperature [90].

So far in the literature, there has not been any work that focuses solely on the T_1 behavior upon overageing. However, the few existing relevant references are controversial. Temperature is considered to play an important role, since T_1 exhibits better thermal stability than Ω up to 200^oC [61], while for temperatures above 200^oC it becomes unstable and tends to be replaced initially by θ' and eventually by the θ phase. On the other hand, Gable et al. [91] still observed the T_1 phase at 300^oC even after ageing of Al-Li-Cu alloys for 500 h. Ageing of an Al-4.0Cu-0.5Li-0.3Mg-0.4Ag alloy for 9000h at 200^oC led to dissolution of T_1 and formation of T_B, T_2 and R phases [45]. Li content plays an important role in overageing, as a

1.0 wt% Li alloy had a higher volume fraction of T_1 and lower content of T_B and T_2 compared to an alloy with 0.8 wt% Li. Slight overageing of an AA2195 alloy at a lower temperature (40 h at 180°C) [76] yielded a slight change in the T_1 distribution with an associated decrease in the number density of θ' plates. At even lower temperatures, an Al-3.5Cu-0.8Li-0.4Mg-0.4Ag-0.13Zr alloy aged for 7016 h at 163°C illustrated the formation of two types of T_1 morphology [47]. The same treatment at 107°C did not have such a negative effect and yielded better mechanical properties.

2.1.2 Role of alloying elements

Each element present in the complex systems of Weldalite^{TM} type alloys plays a different role. The interactions among all these elements determine the ageing response and the resulting mechanical properties. Table 2.2 presents a summary of the effects of each element. The effects of Zr and Mn will be discussed later in §2.2, where the role of dispersoids is discussed. It should be noted here that most researchers agree on the effects of all the alloying elements, apart from Ag. Many controversial statements exist in the literature regarding Ag. There is thus a need for a fundamental study which would determine the exact role of Ag in the precipitation process. Limited references exist in which an effort has been made to explain the relevant mechanism by studying alloys with different silver contents, but their conclusions were unsatisfactory [44, 92].

Table 2.2: Effect of alloying elements on the microstructures of Weldalite^{TM} type alloys.

Element	Effects	Ref.
Cu	Reduces the solid solubility of Li. Cu atoms migrate to subgrain boundaries in unstretched aged alloys. When their segregation to GBs is reduced, the GB precipitates are also reduced. Their diffusivity increases due to the increased frequency of Cu atoms to join with vacancies through Mg-vacancy clusters. Cu yields high natural ageing response. Cu solute diffusion along dislocations controls the growth of T_1 plates. Lowering Cu content increases elongation, decreases the amount of constituent phases and improves fracture toughness. During quenching, independent Cu clusters are formed which are also associated with S' nucleation. Cu atoms are attracted to Mg-Ag co-clusters. Forms Mg-Cu-vacancy co-clusters promoting the nucleation of GP zones.	[42, 57, 76-78, 89, 93, 94]
Li	Li has a solid solution strengthening effect. Its solubility in the matrix increases due to Ag additions leading to lower growth of T_1 plates, but it is decreased in the presence of Cu. Li atoms migrate to LAGBs in unstretched aged alloys. Decreases the solid solubility of Mg. Enhances the age hardening response. Yields a high natural ageing response. Lowers the stacking fault energy and has high solid solubility. Few helices and dislocation loops exist for low Li contents, but disappear for higher amounts. Has a strong binding energy with vacancies forming Li-vacancy pairs and also prevents Ag from forming pairs with vacancies. These pairs form during quenching and are generally favoured by high Li content. They also provide effective nucleation sites for δ'. Li leads to plateau stages of hardness and resistivity changes by trapping most of the excess vacancies. Yields anisotropy to the material, which is fairly constant above	[42, 44, 45, 55, 61-64, 66, 68, 69, 76-78, 84, 88, 93-96]

	0.5 wt%. Dissolves into θ' plates transforming them into T_1. It is associated with the θ' and θ'' phases in that a shell of δ' is attached to them. Reduces number density of $\{111\}_{Al}$ precipitates, promotes a finer θ' dispersion and assists S' lath formation. Increases strength significantly up to 1.0-1.3 wt% Li. For contents above ~1.3 wt% Li, δ' forms at the expense of T_1. Li atoms replace Al atoms in the θ' phase to form the T_B phase. Increasing concentration above a certain level results in a transition of the major strengthening phase from Ω to T_1. With increasing Li more Cu is used up for T_1 nucleation and less is available to form θ'. Low Li content is responsible for the growth of the composite δ'/β' precipitates. Increasing Li reduces precipitation on the GBs and increases the vacancy concentration. More Cu-Li-vacancy clusters are also formed due to the presence of Mg and Ag, acting as nucleation sites for T_1 and leaving fewer clusters available for θ' precipitation. Impedes the formation of Ag-Mg co-clusters. Li in solid solution in the presence of Mg encourages GP zone formation.	
Mg	Strength increases monotonically with Mg up to 0.4 wt%. Its solid solubility is reduced under the presence of Li, precipitating as S' phase in the presence of Cu. Increases the concentration of vacancies due to the high binding energy with them. Traps excess vacancies providing low-energy nucleation sites for T_1 and hinders lattice diffusion which is responsible for precipitate growth. Mg-vacancy pairs also contribute to the plateau in resistivity change. Could be reducing natural ageing response by being trapped as solute atoms around dislocations introduced by stretching. Lowers the growth rate of T_1 and causes θ' phase formation, but reduces its growth rate. Segregates to the particle/matrix interface of T_1, Ω and θ phases and is incorporated in δ' particles. Eliminates serrated flow from stress-strain curves. Yields an abnormally high response to age hardening. Combined with Ag it promotes the T_1 and Ω precipitation, accelerates the kinetics of this reaction and the alloy's age-hardening response, thus eliminating the need for cold working prior to ageing, and yields more uniform T_1 distribution in the matrix. Increases natural ageing response. Mg clusters are formed at the initial ageing stage, which are associated with GP zones and S' nucleation. Accelerates formation of GP zones. Forms Mg-Cu-vacancy clusters promoting the nucleation of GP zones. Only Mg is essential for the formation of GP T_1 zones. Mg-Ag co-clusters form on $\{111\}_{Al}$ planes which act as nucleation sites for the T_1 phase (Mg and Ag are strongly attracted to each other owing to their fairly large electronegativity difference).	[42, 43, 57, 61-63, 66-68, 74, 76-78, 88, 89, 93-95]
Ag	Refines the T_1 precipitates. Cold working prior to ageing reduces the influence of Ag on T_1 precipitation. Increasing Ag content reduces the size of δ' due to increasing the Li solubility in Al, thus limiting the volume fraction of the precipitating phase. Ag also decreases growth rate of T_1 plates but in general does not have a large impact on microstructure. Tends to segregate to the T_1/α interface relieving coherency strains. Has strong affinity with vacancies but lower than that of Li so Ag-Mg co-clusters are not formed. Reduces stacking fault energy in Al. Segregates to the δ' precipitates. Combined with Mg, it eliminates the need for cold working prior to ageing. Increases peak hardness, shortens time to peak strength and yields a finer distribution and higher number density of T_1. Both Ag and Mg are essential for the formation of GP Ω zones. Enhances and accelerates T_1 precipitation by forming Mg-Ag co-clusters on $\{111\}_{Al}$ planes which act as nucleation sites, impedes θ' formation and causes lower growth rates for T_1 and θ'. Independent Ag clusters form during quenching. Reduces the extent of GP zone formation which also reduces the intensity of diffuse streaking in SAD patterns. Little Ag is dissolved in S particles modifying their composition. Favours precipitation of the T phase ($Al_6(Cu,Ag)Mg_4$).	[42, 44, 46, 48, 62, 63, 66, 73, 74, 76-78, 84, 88, 89, 92, 94, 95]
Zn	Reduces the coarsening rate of T_1 precipitates. Improves corrosion	[91,

	resistance.	97]
Be	Increases ageing kinetics and elongation with only a small strength reduction. Inhibits formation of GP phases during the early ageing stages to the benefit of T_1.	[92]
Ce	Slightly improves mechanical properties after extended low temperature ageing. Combined with Ag it increases T_1 stability.	[98]

2.1.3 Production route

The conventional processing route for high strength aluminium aerospace rolled products has been further developed recently to yield a more optimised microstructure with improved properties [4]. The older route appears in Fig. 2.4a and is simpler compared to the most recent route employed for the latest generation damage tolerant Al-Li alloys of Fig. 2.4b. The benefits of each stage are explained below [4, 99].

– *DC casting*. Initially, the alloy components are heated up at a high temperature above the melting point of Al (usually ~700°C) and then mixed to achieve homogeneity of the melt. Certain grain refiners are added to help obtain a fully equiaxed grain structure [100]. An ingot is produced by casting the molten metal into a mould.

– *Scalp*. A thick layer is removed from the surface of the cast ingot, so as to eliminate the extended porosity, surface cracks and oxidation, which occurred upon casting.

– *Homogenisation*. This stage aims to remove microsegregation and minimise macrosegregation from the ingot. Dispersoids are also formed at this point.

– *Breakdown rolling*. Subsequent passes of the ingot through the hot rolling mill reduce the plate’s thickness in steps to the final gauge. Rolling takes place at a high temperature which gradually decreases. Cooling to RT follows this stage.

– *Cross-rolling*. At the first breakdown stage, the slab is rolled so as to widen it to the correct size and weaken the deformation texture by decreasing the volume fraction of the Brass component throughout the whole thickness [101, 102]. Usually this takes place early on during the breakdown rolling.

– *Recrystallisation anneal*. Isothermal heating at a high temperature is applied in order to induce recrystallisation and consumption of the deformation texture components. Brass, in particular, is detrimental to anisotropy, so a lower volume fraction would be beneficial [101, 103, 104]. The applied heat treatment should be long enough to reduce the Brass content since grains of this orientation are consumed more slowly than S grains [105].

– *Finish hot-rolling*. A final hot-rolling stage is applied to achieve the final thickness of the plate/sheet product, at a gradually decreasing temperature. The grains tend to rotate towards β-fibre orientations, whose individual component volume fractions in the microstructure strongly depend on the exact amount of strain, as well as the solute content of the alloy [106]. Again the material is cooled down to RT following this stage.

- *Recovery anneal*. A short isothermal heat treatment at an intermediate temperature is employed immediately prior to the solution treatment, in order to remove most of the residual stresses from the rolling process. It also aids in reducing the driving force for recrystallisation at the next processing stage.
- *Solution heat treatment*. At the end of the recovery anneal, another short isothermal heating stage is applied at a higher temperature. A suitable temperature is chosen with the aid of thermodynamic modelling. Care should be taken so that this stage lasts long enough to dissolve all the phases that precipitated during the intermediate annealing treatments, but is also short enough to limit recrystallisation. Controlled quenching to RT follows the solution treatment to avoid re-precipitation of age-hardening phases.
- *Stretch*. The final plate/sheet is stretched to a small strain (2-5 %) so as to reduce residual stresses and remove distortion that occurs after solution treatment and also to introduce dislocations, which act as sites of heterogeneous nucleation for certain phases upon subsequent ageing (e.g. T_1 phase).
- *Artificial ageing*. A final heat treatment at a low temperature is employed so as to precipitate strengthening phases out of the supersaturated solid solution. Time and temperature are chosen depending on the targeted properties and application of the product. This usually occurs with controlled heating ramps and may involve more than one isothermal temperature steps.

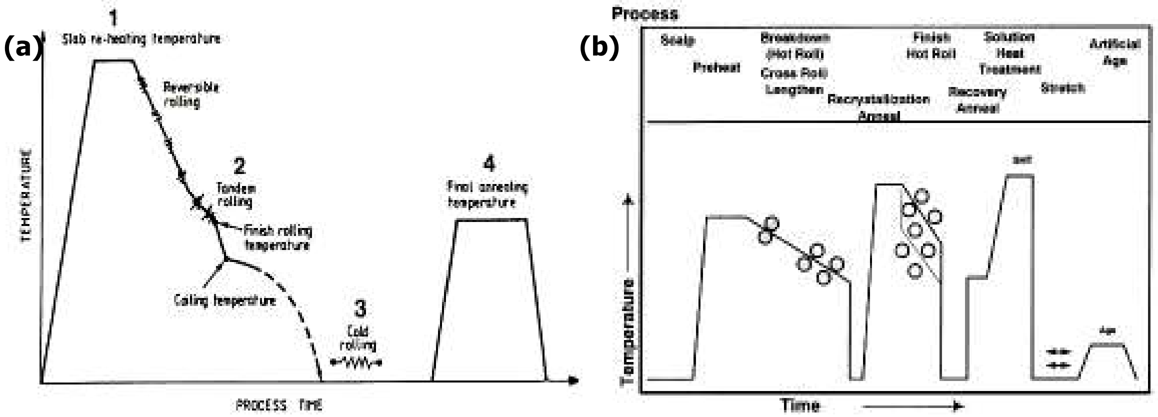

Fig. 2.4: Fabrication processes of Al rolled products: **a)** typical steps employed in previous years [99], and **b)** processing stages for 3rd generation damage tolerant Al-Li [4].

2.2 Dispersoid additions in Al aerospace alloys

The current section deals with the nature of dispersoid particles found in Al aerospace alloys. Initially, the theoretical background associated with the nucleation, growth and coarsening stages of the dispersoids is presented. The addition of Zr- and Mn-containing dispersoids is then discussed in more detail, regarding both their individual and combined presence. Parameters such as their coherency, morphology and size are also discussed. The behaviour of some other common combined binary and ternary dispersoid-forming additions is also mentioned.

2.2.1 Dispersoid precipitation

During homogenisation of a DC cast billet, dispersoids may precipitate either homogeneously or heterogeneously depending on the local solute supersaturation, temperature and dislocation density [107]. For homogeneous nucleation, the overall free energy change is equal to:

$$\Delta G_{hom} = \frac{4\pi r^3}{3}(\Delta G_v + \Delta G_s) + 4\pi r^2 \gamma \qquad (2\text{–}1)$$

where ΔG_v is the chemical driving force for nucleation due to the different composition of the dispersoid with the matrix, ΔG_s is the misfit strain energy per unit volume due to the different lattice parameters between the dispersoid and the matrix and γ is the interfacial energy [108]. For the nucleation of a dispersoid to occur, a certain energy barrier ΔG^* has to be exceeded:

$$\Delta G^* = \frac{16\pi r^2}{3(\Delta G_v + \Delta G_s)^2} \qquad (2\text{–}2)$$

The chemical driving force for nucleation and the misfit strain energy per unit volume can be given by the equations [109, 110]:

$$\Delta G_v = \frac{RT}{V_\beta}\left[c_{\alpha'}^{e} \ln\left(\frac{c_i}{c_\alpha^{e}}\right) + (1 - c_{\alpha'}^{e})\ln\left(\frac{1 - c_i}{1 - c_\alpha^{e}}\right)\right] \qquad (2\text{–}3)$$

$$\Delta G_s = 3\varepsilon^2\delta\left[1 - \left\{\frac{\delta}{\delta^*}\left(\frac{2K+1}{K+M-KM}\cdot\frac{1-v}{1+\nu}\right) - 1\right\}^{-1}\right] \qquad (2\text{–}4)$$

where V_β is the molar volume of the dispersoid phase, c_i is the instantaneous concentration in the matrix for the solute elements contained by the dispersoids, c_α^e is the equilibrium concentration in the matrix for the solute elements contained by the dispersoids and $c_{\alpha'}^e$ is the equilibrium concentration at the interface for the solute elements contained by the dispersoids [110], and also ε is the misfit strain, M and K are constants related to the particle shape and δ and δ^* are constants related to the shear modulus and Poisson's ratio of the dispersoids [109].

A form of the nucleation rate equation, including the time-dependence to achieve a steady state, is described by equation 2-5:

$$J = NZ\beta^* \exp\left(\frac{-\Delta G}{kT}\right)\exp\left(\frac{-\tau}{t}\right) \qquad (2\text{–}5)$$

where N is the number of nucleation sites per unit volume, Z is the Zeldovich factor equal to 0.05 [111], β^* is the rate of atom diffusion to an atomic embryo, t is the time and τ is the incubation period required for nucleation [107, 109].

In the case of heterogeneous nucleation of dispersoids at dislocations, the total free energy change is modified according to Eq. 2-6, taking into account the dislocation strain energy ΔG_{dis} when the nuclei are formed on them [108]. It should be mentioned that heterogeneous nucleation is favoured for low supersaturations or high temperatures and high dislocation densities [108].

$$\Delta G_{het} = \frac{4\pi r^3}{3}(\Delta G_v + \Delta G_s) + 4\pi r^2\gamma - \Delta G_{dis} \quad (2\text{–}6)$$

The particle growth rate depends on the concentration gradient at the particle/matrix interface which gives the driving force for the diffusion of solute [112], according to Eq. 2-7:

$$r = \lambda_i\,(Dt)^{1/2} \quad (2\text{–}7)$$

where D is the diffusion coefficient of the solute in the matrix and λ_i is a function of the supersaturation.

At the coarsening stage, the larger particles grow at the expense of the growth of the smaller ones, by consuming the excess solute that becomes diluted in the matrix. Eq. 2-8 describes particle coarsening for diffusion-controlled processes:

$$r(t)^3 - r_o(t)^3 = Kt \quad (2\text{–}8)$$

where $r_o(t)$ is the particle radius at t = 0, r(t) is the precipitate radius at any given time t and K is a constant [108].

Although classical nucleation and growth theory can effectively describe the Al_3Zr distributions [110, 113] they do not seem to apply to Mn-dispersoids. Lok et al. [111] came to this conclusion after comparing model predictions to experimental data regarding nucleation kinetics of dispersoids in an AA3103. In order to effectively predict the evolution of the particle distributions in Mn-containing alloys, particle break-up and re-alignment on rolling need to be taken into consideration, as well as the solute changes at the various heating stages (pre-heating, breakdown rolling, hot-rolling and back-annealing) which occur due to growth of constituent phases or dispersoids [114].

The two dispersoid families precipitate at different temperatures. The Al_3Zr phase is formed between approximately 385-535°C, as shown in Fig. 2.5a. The $Al_{20}Cu_2Mn_3$ phase is known to precipitate between 300-530°C [115], while other Mn-phases precipitate even at temperatures as high as 600°C, but at very slow rates as seen from Fig. 2.5b. This difference in the temperature regimes of the two dispersoid types entails an order of precipitation during ramp heating at the homogenisation stage, with the Mn-dispersoids forming first if there is sufficient Mn supersaturation.

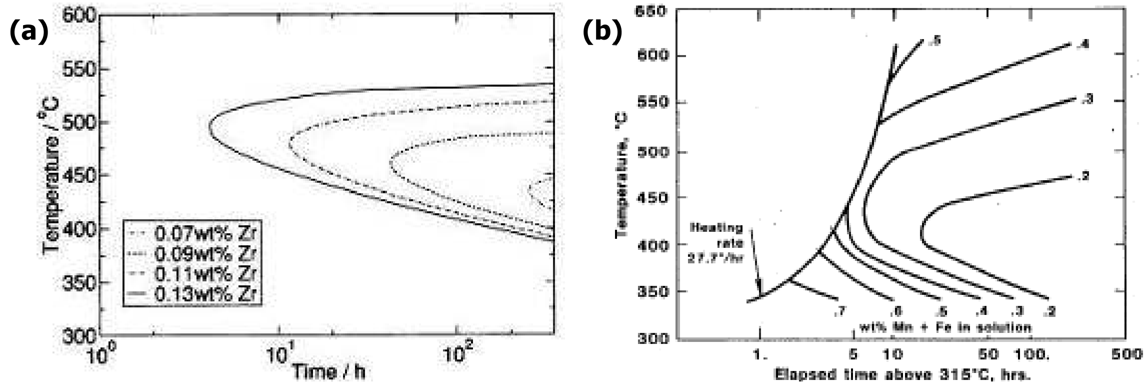

Fig. 2.5: Predicted temperature ranges of dispersoid precipitation: **a)** Al_3Zr dispersoids for various Zr contents in an AA7050 [116], and **b)** Mn and Fe content in solid solution in the matrix after pre-heating of an AA3003 ingot [117].

During casting, alloying elements are not distributed uniformly within the grains but they tend to segregate relative to the direction of the dendrite lateral growth. Further, because Mn and Zr have very low diffusion rates the microsegregation that occurs is only removed very slowly by homogenisation treatment (Fig. 2.6). More specifically, regarding the dispersoid-forming elements in this work, Zr segregates inversely towards the dendrite centres (Fig. 2.6a) while Mn tends to enrich the dendrite edges (Fig. 2.6b) [19]. The most important effect of this phenomenon is the potential formation of dispersoids throughout the dendrite, minimising the PFZs.

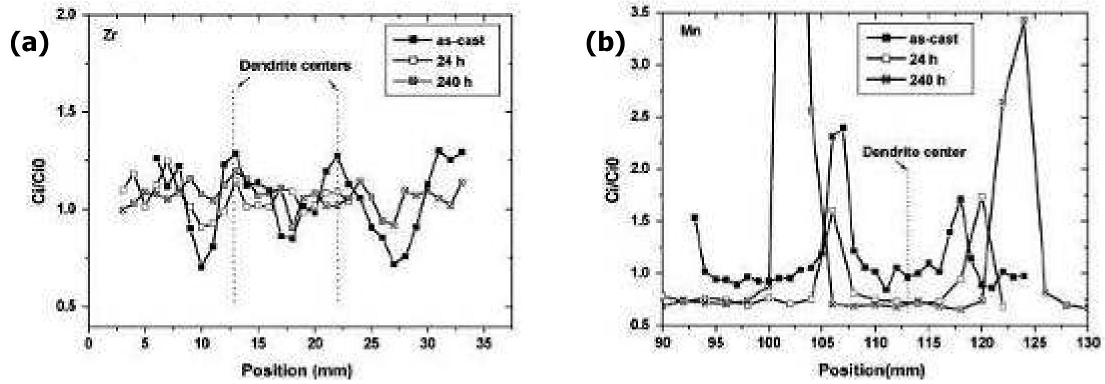

Fig. 2.6: Segregation of solute in an as-cast Al-1.01Mn-0.15Zr-0.21Fe-0.15Si alloy, before and after homogenisation [19]: **a)** Zr relative concentration, and **b)** Mn relative concentration.

It was mentioned earlier that particle nucleation strongly relies on solute supersaturation. In Zr-containing alloys Al_3Zr dispersoids form homogeneously in the dendrite centres, due to the higher Zr supersaturation as shown in region 3 of Fig. 2.7a. On the other hand, in areas of low Zr supersaturation, such as dendrite edges, they can exhibit heterogeneous precipitation and nucleate on dislocations and other precipitates (Figs. 2.7a-c) [113]. In Fig.2.7a it was suggested that the Al_3Zr dispersoids nucleated on η precipitates in the AA7050 studied by Robson and Prangnell [113]. In contrast, not many references exist on preferential nucleation of Mn-dispersoids. Zoeller and Sanders [118] have shown that $Al_{20}Cu_2Mn_3$ dispersoids can nucleate on the θ phase in an Al-4Cu-0.3Fe-0.4Mn-0.2Si alloy. Lodgaard and Ryum [119] reported the formation of α-Al(MnFe)Si dispersoids on the "u-phase" which had previously nucleated on β'-Mg_2Si precipitates (Fig. 2.7d). Upon dissolution of the "u-phase", the Mn-dispersoids were left aligned along the $<100>_{Al}$ and $<010>_{Al}$ orientations where this phase had formed (Fig. 2.7e). Finally, Li et al. [115] noticed the preferential nucleation of Mn-dispersoids on dislocations during homogenisation of 3xxx alloys.

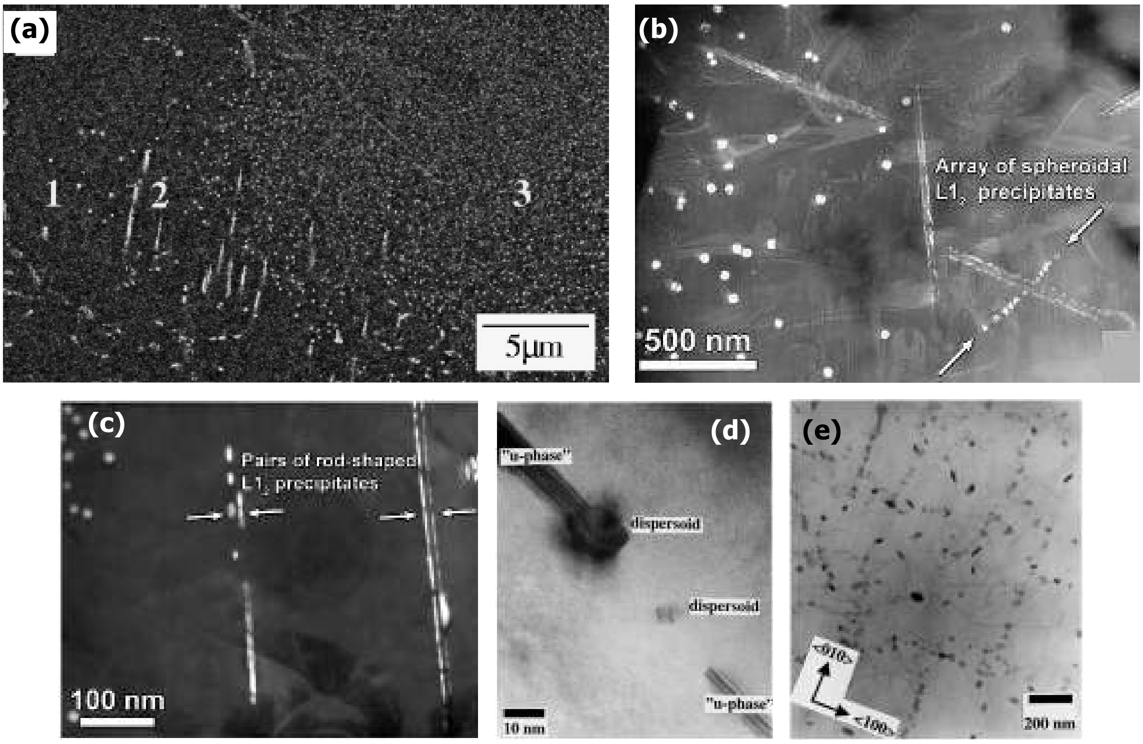

Fig. 2.7: Preferential nucleation of dispersoids on other precipitates in the matrix: **a)** Al_3Zr nucleated on η precipitates near a dendrite edge [113], **b)** aligned array of interdendritic spheroidal $L1_2$ Al_3Zr dispersoids in an Al-0.1Zr alloy [120], **c)** pairs of interdendritic rod-shaped $L1_2$ Al_3Zr or $Al_3(Zr_{1-x}Ti_x)$ dispersoids in an Al-0.1Zr-0.1Ti alloy [120], **d)** nucleation of an α-Al(MnFe)Si dispersoid on a u-phase particle in an Al-Mg-Si alloy [119], and **e)** alignment of α-Al(MnFe)Si dispersoids along $<010>_{Al}$ and $<100>_{Al}$ directions in an Al-Mg-Si alloy [119].

2.2.2 Zirconium and manganese dispersoid families

It is important to present here some features for both the Al_3Zr and $Al_{20}Cu_2Mn_3$ (or generally Mn-dispersoid) families. Starting with the former, the metastable β'-Al_3Zr phase forms at lower temperatures and has a cubic $L1_2$ structure with lattice parameter a=0.4066 nm [121] and a $\{001\}_{Al}$ habit plane [122]. At higher temperatures, this phase transforms to the equilibrium tetragonal DO_{23} phase with another tetragonal Al_3Zr phase forming at an intermediate stage, according to Guo and Ohtera [121]. The metastable Al_3Zr dispersoids mainly nucleate homogeneously and are very fine in size (a few tens of nanometres in diameter), generally having a spherical morphology and they are coherent with the matrix [120]. Other β' particle morphologies, such as faceted [123], rod-shaped [124] and cauliflower-shaped [120, 125], have also been observed (Fig. 2.8). The spherical dispersoids are generally favoured by low supersaturations, while the rod-shaped by high supersaturations [124]. The faceted dispersoids are believed to have resulted from interactions with the recrystallisation front, while the cauliflower-shaped dispersoids formed near dendrite edges where precipitation is more heterogeneous [120].

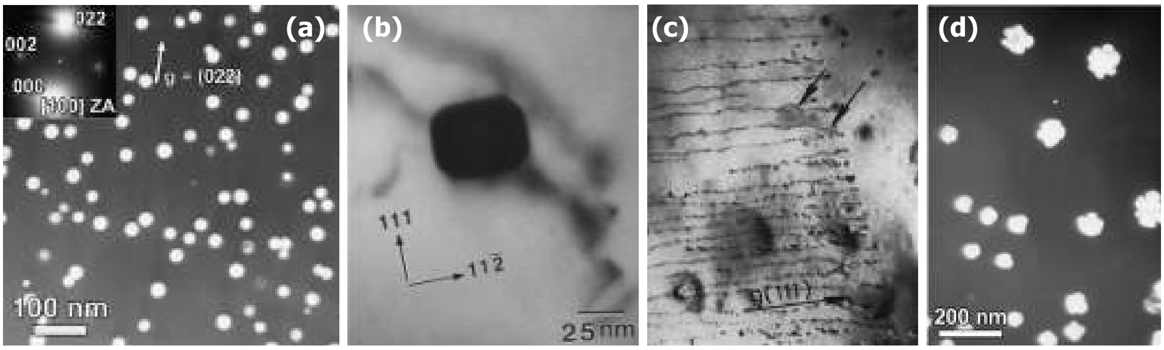

Fig. 2.8: Al_3Zr morphologies: **a)** spherical [120], **b)** faceted [123], **c)** rod-shaped [124], and **d)** cauliflower-shaped [120].

The $Al_{20}Cu_2Mn_3$ phase has an orthorhombic structure with lattice constants a=2.419 nm, b=1.251 nm and c=0.786 nm [126]. Elongated dispersoids of this type form with their longer axis parallel to the $[010]_{Al}$ direction [126], while other Mn-dispersoids with a rhomboidal morphology, such as the $Al_6(Mn,Fe)$, are randomly oriented in the matrix [127]. The orientation relationships between the $Al_6(Mn,Fe)$ phase and the matrix have been reported as $[100]_{Al} \parallel [\bar{2}10]_p$ and $(0\bar{1}1)_{Al} \parallel (001)_p$ [127]. Mn-dispersoids are incoherent with the matrix and are generally much larger than Al_3Zr, since they usually reach several hundreds of nanometres in length [128]. Their size, number density, distribution and morphology strongly depend on the homogenisation temperature, heating rate, holding time and microsegregation in the casting [118, 129].

In comparison, the effects of individual additions of the two dispersoid families on alloy properties, recrystallisation resistance and alloy strength, are higher for the equivalent atomic concentration of Zr compared to Mn [130-132].

Particle coherency is crucial, since it affects the growth mechanism and also can increase the pinning pressure on migrating GBs. GB pinning occurs when there is a low driving force for the boundary to bypass the particles and hence, they become semi-coherent upon contact with the GB [133]. This can occur discontinuously by GB diffusion. The pinning pressure is thought to be twice [134, 135] or four times [133] higher than for incoherent particles of the same size. Four different events have been identified regarding what may happen during the contact of coherent particles with a GB [133] and some of them are illustrated in Fig. 2.9.

- Particle bypassing by a HAGB leading to complete loss of coherency (Figs. 2.9a,b).
- Particle dissolution and re-precipitation as a coherent particle in the new grain, either heterogeneously on the GB or homogeneously within the grain. Re-precipitation is believed to occur during subsequent cooling and not during the heat treatment [136].

There have also been occasions where dispersoids dissolved completely probably because of their instability caused by their fine size (<10 nm) [137].

- Particle coarsening until unpinning of the GB is achieved and the particles are bypassed, leading to loss of coherency as the boundary passes (Fig. 2.9c).
- Particle cutting when the boundary passes through the dispersoid in such a manner that makes it rotate exactly as the matrix does and its coherency is maintained (Figs. 2.9d-f).

Regarding the bypassing mechanism, which is frequently observed, coherency with the new grain is lost because the particles maintain their initial orientations as the boundary passes beyond them [133]. In addition, several examples of phase transformations have been documented when particles are bypassed by a recrystallisation front; for example the metastable $L1_2$ Al_3Zr dispersoids transformed into equilibrium DO_{22} $(Al,Si)_3Zr$ in an Al-Mg-Si alloy [138], the metastable β'-Mg_2Si transformed into equilibrium β in the same type of alloy [139] and the θ'-Al_2Cu transformed into equilibrium θ in Al-Cu alloys [140].

During GB pinning, particle coarsening can be accelerated by the concomitant effect of faster solute diffusion along the GBs and the change in particle shape upon contact with the boundary [141]. Fig. 2.9c shows that particles become hemispherical when they pin a GB, rendering their radius larger than that of the coherent particles as a result of the shape distortion. This fact brings a higher driving force for solute diffusion from the matrix to the GB particle during cooperative coarsening [141]. Looking a little further, this phenomenon implies that when there is particle pinning, the rate of particle growth controls the rate of grain and subgrain growth as well. In fact, this has also been observed experimentally [139, 142].

Finally, the particle cutting mechanism (Figs. 2.9d-f) is quite rarely met. The reasons for this are related to a kinetics barrier rather than a thermodynamic one, which makes this process quite difficult to occur. This barrier would be the very low rate at which the GB cuts through the coherent particle, due to the reduced boundary mobility in ordered phases, aided by the difficulty of the atoms to be rearranged in such way so as to form the same atomic structure in the new orientation [133].

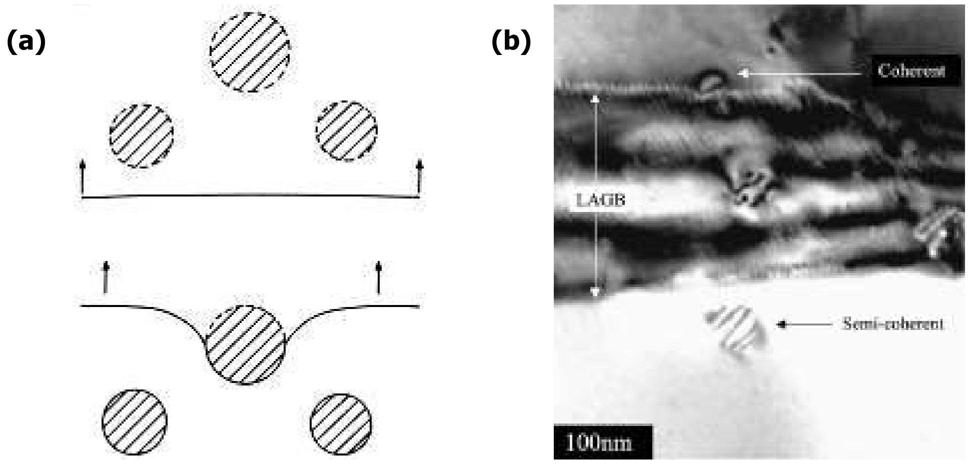

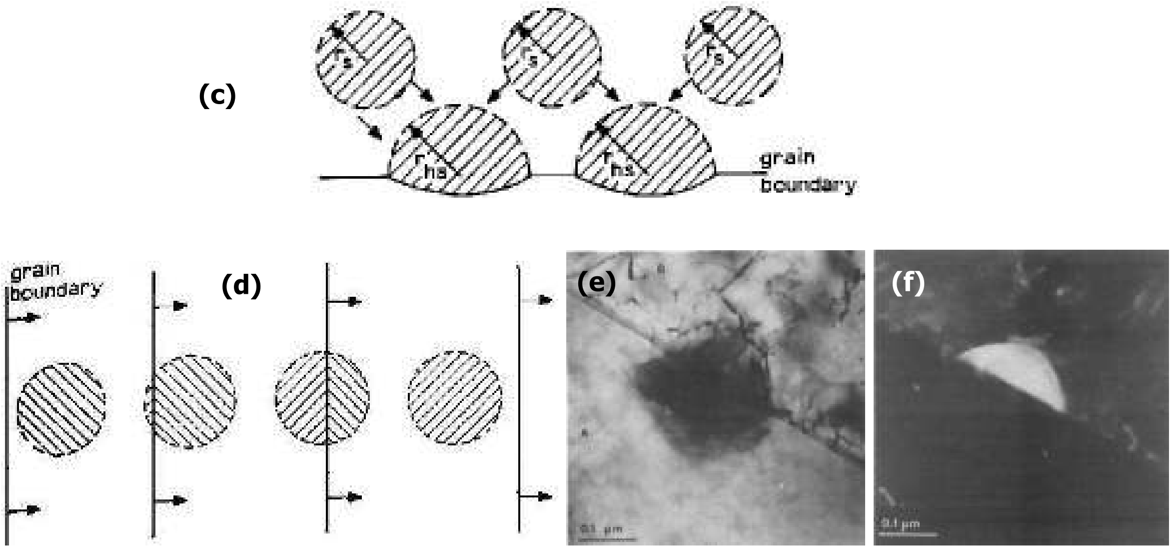

Fig. 2.9: Interaction of particles with GBs (dashed particle interfaces in the sketches denote coherency): **a)** bypassing of coherent particles by a HAGB, rendering them incoherent [133], **b)** coherency loss of an Al_3Sc dispersoid after being bypassed by a LAGB [143], **c)** change of particle shape when pinning a GB [133], **d)** particle-cutting mechanism [133], **e)** BF image of a γ' particle located on a GB in a Ni alloy [141], and **f)** DF image of the same particle exhibiting coherency with the new grain it was entered [141].

2.2.3 Common combined dispersoid additions in Al alloys

Attempts to design high performance aluminium products and improve their properties have led to the addition of two or more dispersoid-forming elements, so as to combine the benefits of the different types of particles generated. Trace levels of Zr have been proven to be the most desirable addition due to the ideal characteristics that the distribution of the β'-Al_3Zr phase can offer. However, it has been shown that when it is combined with other dispersoid-forming elements its action can be dramatically enhanced (e.g. Sc [144]). It should be noted that interactions between such elements, or even with the alloying elements of the base alloy, have been observed in the past. Numerous references exist in the literature to paired additions of dispersoid-formers, which usually lead to composite particles of the $Al_3(M,Zr)$ type (e.g. M: Sc [144], Li [145], V [146], Ti [147], Hf [148]). Another type of composite dispersoids reported is the $(Al,M)_3Zr$ in which the number of Zr atoms remains intact and it is the Al atoms that are being substituted (e.g. M: Si, Ge) according to first principle calculations [149].

There is increasing interest on triple or quadruple dispersoid additions in Al alloys and this has become the object of recent studies. Certain combinations of dispersoid-forming elements are already reported in the literature, such as ZrCrMn [150, 151], ZrScMn [152], ZrCrTi [153], ZrScHf [154], ZrMnTi [155] and ZrCrMnTi [156]. The overall aim is to merge all the benefits arising from each dispersoid family and obtain a desirable combination of recrystallisation resistance, mechanical properties and corrosion resistance.

2.2.4 Combined additions of Zr and Mn in Al alloys

Zirconium and manganese are commonly used together in commercial damage tolerant aluminium alloys for aerospace, however, their effect on the alloy properties remains vague. The rationale behind adding these two dispersoid-forming elements together is to improve recrystallisation resistance and thus mechanical properties. The benefit of the coexistence of Al_3Zr and Mn-dispersoids is the presence of particles in almost all areas of a grain, hence minimising the particle-depleted zones near the critical GB areas [18]. This phenomenon occurs due to the opposite microsegregation trends of the two elements of interest during solidification, where Zr segregates to the dendrite centres, while manganese segregates to the dendrite edges [19]. The claimed ultimate effect is the improvement of recrystallisation resistance (Fig. 2.10a), due to inhibition of the GB migration by the presence of dispersoids and the solute atoms across most parts of the grains [18]. However, in the case of individual additions of each of these two elements, regions of the grains with insufficient particle or solute content, consistent with the strong segregation patterns after casting, would constitute favourable sites for initiation of recrystallisation (Figs. 2.10b,c) [18, 132, 157]. Growth of recrystallisation nuclei would be more possible in such areas due to the lower pinning pressure on the GBs.

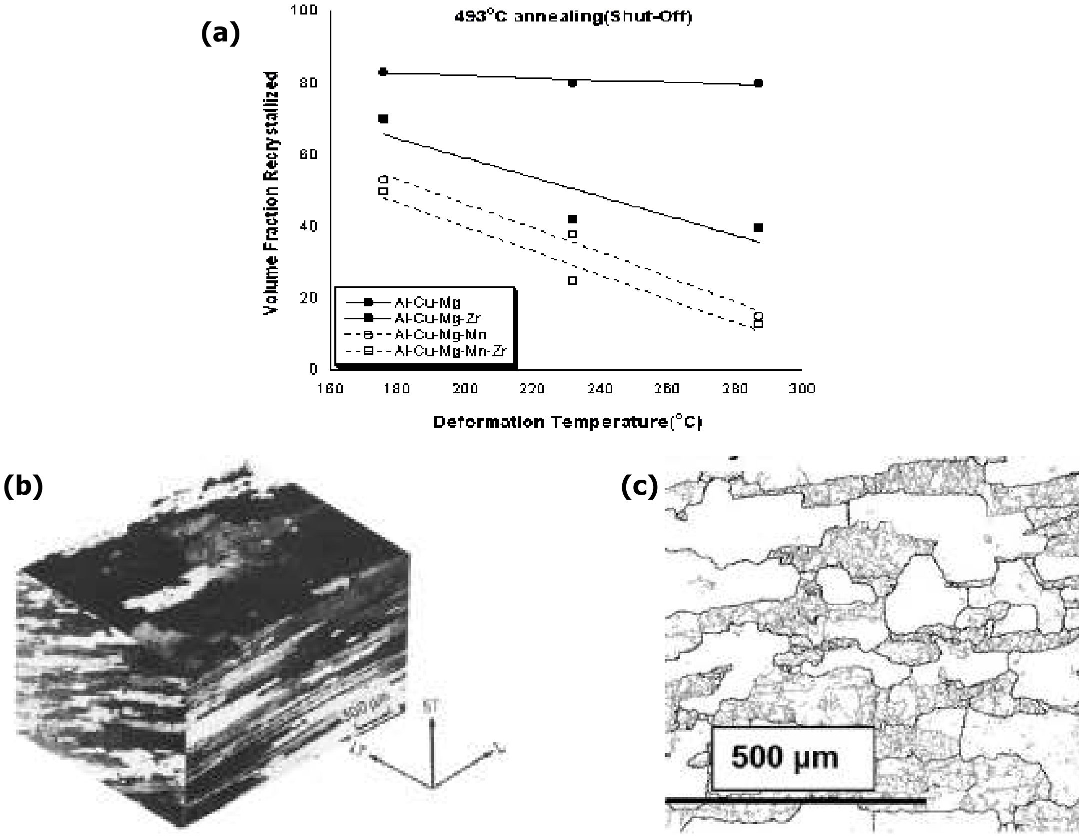

Fig. 2.10: Effects of combined Zr+Mn additions: **a)** improvement of recrystallisation resistance compared to the sole Zr or sole Mn addition [157], **b)** partially recrystallised microstructure of an Al-Cu-Li alloy sheet containing 0.51 wt% Mn [158], and **c)** partially recrystallised microstructure of an Al-Cu-Li alloy plate containing 0.11 wt% Zr [159].

At a microstructural level, any interaction between Zr and Mn is of key interest due to possible unforeseen consequences on the dispersoid distributions. To begin with, the effectiveness of these two elements is known to be strongly dependent on the alloy system they are added to. They are affected by the presence of other solutes in the microstructure, such as the typical impurities in Al alloys (e.g. Fe, Si) [18, 19, 117, 160-163], as well as other alloying elements (e.g. Zn, Cu, Mg, Si, Sc, Li) [18, 161, 164, 165]. More specifically, the effects of Zr and Mn are different in Al-Zn-Mg alloys than in Al-Mg-Si alloys, due to the relative amounts of these elements in dispersoids, or in solid solution, and the respective pinning efficiency in each case [161]. Coexistence of Zr and Mn in solid solution is believed to impede lattice diffusion, which results in lower velocity of dislocation climb [166]. Regarding effects on dispersoid distributions, contradictory data can be found in the literature. The solubility of Mn does not seem to be much affected by the presence of Zr, as only a marginal increase was reported, even when 1 wt% Zr was added to several binary Al-Mn alloys [167]. However, Mn in solid solution was reported to increase the volume fraction of the Al_3Zr and $Al_3(Zr,Sc)$ dispersoids [18, 19, 160] while, on the other end, the Mn-dispersoid distribution became coarser and with a lower number density in the presence of Zr [19, 167]. In contrast to this, Johansen et al. [168, 169] support that there is only very small interaction, if any, between Zr and Mn, since the distribution of Mn-dispersoids in their work was only marginally affected by the addition of Zr and vice versa.

The dissolution of transition elements within other dispersoid phases has also been observed in the past. Zr and Mn were found to dissolve within Al_3Cr dispersoids, but also Zr and Cr were detected in the Al_6Mn phase [151] in an alloy containing three dispersoid-forming elements. Other researchers suggested that Zr might be substituting for Mn atoms in the Al_6Mn phase [167] and that Fe and Si might be included in the Al_3Zr phase [162], but no definite conclusion was made in either case.

Previous results on recrystallisation resistance are controversial, since references about an increase as well as a decrease of resistance exist in the literature. The observed discrepancy for the Mn-dispersoids to be potent grain refiners and in parallel favour recrystallisation was reported by Lavernia et al. in their review [16], but unfortunately no explanation was provided, nor any references. The statement that they act as nucleation sites for recrystallisation due to their incoherency with the matrix is more of an assumption rather than scientific fact, since it suggests that PSN is occurring on them. No evidence has been found in the literature so far for Mn-dispersoids acting as PSN sites. Anyway, this would not be possible according to the PSN theory which concludes that nucleation of new grains takes place within the deformation zone in the matrix adjacent to large particles [14]. Mn-dispersoids are too small to impose significant lattice strain on the matrix and to generate a deformation zone with the required orientation gradient.

The main experimental conditions of reported studies of recrystallisation resistance are summarised in Table 2.3, in order to assess the importance of these parameters on recrystallisation behaviour. Only the cases where combined Zr+Mn additions were compared to the sole addition of Zr are presented. A first look at the data proves that the final plate/sheet thickness after processing, or the extent of deformation, does not seem to hold the primary role for this behaviour when a certain concentration of Zr and Mn is exceeded. The most important parameter is the exact dispersoid content, since a minimum Mn level as a function of the Zr level seems to be required for a sufficient pinning pressure to exist. This theory agrees with the experimental findings of Eschbach et al. [155] who supported that a Zr level of 0.15 wt% is required for an alloy containing 0.20-0.25 wt% Mn in order for sufficient recrystallisation resistance to be achieved. However, more details on the necessary dispersoid levels will be given in §6.5.3. It is interesting to note that Kim and colleagues [170] observed a complex behaviour where recrystallisation resistance was found to decrease at 430^{o}C, but increase on annealing between 460-500^{o}C, compared to the sole addition of Zr.

As regards processing and in-service performance, dual Zr+Mn additions compared to individual additions offer lower extrudability [152], better work hardenability [171], better high strain rate superplasticity [156], a significantly lower tendency for solidification cracking [172] and also a slight reduction of corrosion resistance [173]. Although an increase in UTS and σ_y have been observed by many researchers compared to when there is a sole Zr addition [174-176], the elongation behaviour has been found to either increase [171], decrease [176] or remain unchanged [174]. On the other hand, Cho and Bès [177] report that all mechanical properties of an AA2139 sheet, especially its fracture toughness, were diminished compared to the sole use of Mn addition. Hardness was also found to increase [171] and although Chang et al. [174] saw no effect on age hardening, Ohashi et al. [167] reported higher peak hardness for slightly shorter ageing times when 1 wt%Zr was added to an Al-7wt%Mn alloy.

Table 2.3: Reported effects of the combined addition of Zr and Mn for several alloy systems under various processing conditions. The effect was derived by comparing each alloy containing Zr+Mn to the same base alloy containing only Zr.

Alloy composition (wt%)	Addition / Effect	Thickness (mm)	Processing	Ref.
Al-4.70Mg-0.09Fe-0.05Si-0.18Cr-0.2Zr-1.57Mn	Mn to Zr / beneficial	12.7	hot-rolled	[132]
Al-3.9Cu-1.3Mg-0.11Zr-0.55Mn	Mn to Zr / beneficial	N.A.	69.3% hot compression	[157]
Al-0.15Si-0.21Fe-0.15Zr-1.01Mn	Mn to Zr / beneficial	1.1	90% cold-rolled	[18]
Al-4.93Mg-0.10Fe-0.04Si-0.20Zr-0.41Mn	Mn to Zr / beneficial in the presence of Cr as well	2	strain=4	[150]
Al-4.3Cu-0.17Li-1.46Mg-0.06Zr-0.43Mn	Mn to Zr / detrimental	20	hot-rolled	[159]
Al-0.8Cu-2.0Li-2.9Mg-0.14Zr-0.49Mn	Mn to Zr / beneficial above	1.5	30% cold-rolled after	[170]

	460°C, detrimental at 430°C		hot-rolling	
Al-3.3Cu-1.4Li-0.41Mg-0.31Ag-0.12Zr-0.32Mn Al-3.6Cu-0.97Li-0.40Mg-0.34Ag-0.12Zr-0.32Mn Al-3.6Cu-0.77Li-0.30Mg-0.31Ag-0.11Zr-0.32Mn Al-4.5Cu-0.34Li-0.44Mg-0.39Ag-0.09Zr-0.24Mn	Mn+Zr (no individual Zr addition)[*] / detrimental	2.3	hot-rolled after cold-rolling	[164]

[*] The combined Zr+Mn addition was not compared to the sole addition of Zr in this case but the results showed fully recrystallised microstructures.

2.3 Recovery and recrystallisation

The present section deals with the static annealing processes that follow deformation. Dynamic processes are not discussed here, since they were not the main subject of this thesis and their analysis is more complicated. Recovery may occur before, or alongside recrystallisation. The major difference between these two phenomena is their spatial homogeneity. Recovery evolves almost uniformly throughout the whole microstructure, with only small differences in size between the growing subgrains (Fig. 2.11a) [14]. In contrast, the nature of the primary recrystallisation process is discontinuous, since recrystallised grains selectively grow much larger than the rest of the microstructure (Fig. 2.11b). In the case where the recovered microstructure consists mainly of HAGBs, recovery is then termed “continuous recrystallisation”, since a new dislocation-free grain structure is produced [14]. This typically occurs at high strains and low initial grain sizes (Fig. 2.11c), which induce a high density of HAGBs, but the microstructural change is similar to Fig. 2.11a [178-180].

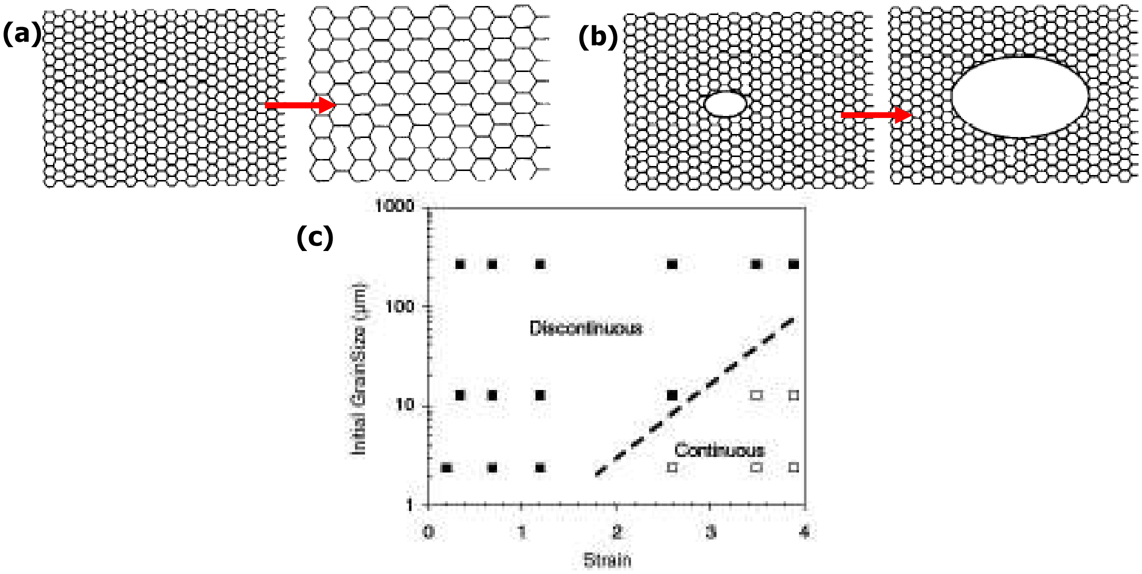

Fig. 2.11: Evolution of annealing processes: **a)** recovery (or continuous recrystallisation if the GBs are high-angle) [178], **b)** primary recrystallisation (or else discontinuous recrystallisation) [178], and **c)** transition between discontinuous and continuous recrystallisation as a function of strain and initial grain size in AA8006 [179].

2.3.1 General theory of recovery and recrystallisation

Recrystallisation describes the annealing process in which a deformed material undergoes a transition towards its starting strain-free grain structure prior to deformation, in order to regain its initial microstructure and properties. Its effect on mechanical properties is of critical importance, not so much because of the extent of these changes, but because of the subsequent influence of the microstructural modifications on the material's behaviour. Other properties such as electrical resistivity and density are also modified. Recovery involves the re-organisation of statistically stored dislocations into lower energy configurations and coarsening of the subgrain structure without any significant HAGB migration. This involves non-conservative dislocation motion such as climb.

The mechanism behind subgrain formation is that of dislocation annihilation and rearrangement into more stable structures of lower energy [14]. The typical steps involved in the recovery process of a deformed microstructure containing dislocation tangles, involving dislocation rearrangement, are: a) cell formation, b) annihilation of dislocations within the cell interior by incorporating them in the cell walls, c) subgrain formation, and d) subgrain growth. The sequential or simultaneous appearance of these stages depends on the material and processing parameters during deformation and annealing. Subgrain formation is generally favoured by high stacking fault energy and a low solute content that minimises drag on dislocation motion. A large deformation strain increases the stored energy and driving force for recovery, and also, a high deformation temperature promotes dynamic recovery.

The determination of the rate of recovery is quite complex and only empirical relationships exist to describe the kinetics of this process [14]. Subgrain growth, on the other hand, can be described by an equation involving the annealing time and initial subgrain size before annealing:

$$D^n - D_o^n = ct \qquad (2\text{–}9)$$

where D_o is the initial subgrain size, t is the time and n and c are constants. The driving force for subgrain growth is provided by the stored energy, while the growth rate is strongly affected by the presence of pinning particles. It should be highlighted that the growth rate of subgrains also strongly depends on their orientation. The typical rolling texture components (Brass, S, Copper, Cube, Goss) exhibit the lowest coarsening rates, while other texture components coarsen much faster [181]. This is explained in terms of the surrounding local texture which inhibits boundary mobility. Since the rolling texture components prevail in a rolled microstructure, there is a higher possibility that their surrounding subgrains are of similar orientation. Thus, the misorientation is low and boundary mobility is also low, which reduces subgrain growth (Fig. 2.12). The surrounding environment can also affect the subgrain misorientation during annealing. When orientation gradients are present in the microstructure, the higher mobility boundaries will migrate and the microstructure will eventually be governed by subgrains of higher average misorientation [14]. On the other hand, the average misorientation would be smaller if no orientation gradients existed, but this case is not very common. This happens due to appropriate LAGB movement, so as to reduce the length of high energy boundaries, leading to a more stable microstructure of lower energy.

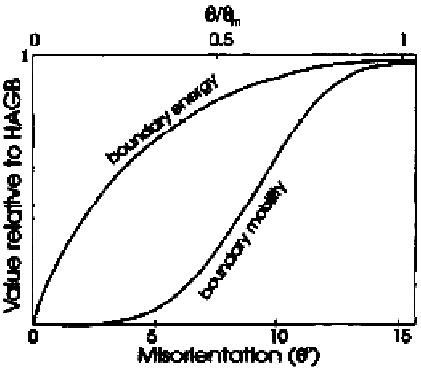

Fig. 2.12: Dependence of boundary energy and boundary mobility on misorientation [178].

Recrystallisation is defined as the development of a new dislocation-free grain structure in a deformed material by the creation and migration of HAGBs, whose motion is induced by the stored energy of plastic deformation [182]. Recrystallisation occurs in competition with recovery, since the driving force for both of them stems from the same source; the energy stored in the material in the form of dislocations or LAGBs. The prevalence of either process depends on several material and experimental parameters. Normally, low annealing temperatures favour recovery to the expense of recrystallisation. The general equation describing the recrystallisation process as a function of time is given by the well-known Johnson-Mehl-Avrami-Kolmogorov equation:

$$X_v = 1 - \exp(-kt^n) \qquad (2\text{–}10)$$

where X_v is the volume fraction of the recrystallised material, t is the time and k and n are constants [183]. However, Eq. 2-10 does not apply globally and is generally fitted to empirical data and the recrystallised volume fraction will be affected in the presence of pinning particles.

2.3.2 Nucleation of recrystallisation

There are some inherent difficulties in studying the subject of nucleation of recrystallisation due to the fine scale and discontinuous nature of the process. The most effective method would be to combine an in-situ examination with 3-D mapping during annealing, with a spatial resolution down to the dislocation size [184]. The most important nucleation mechanisms and nucleation sites are described below. Regarding some fundamental principles of the nucleation of recrystallisation, it is now accepted that the orientations of the new grains are already present in the microstructure after deformation and do not appear during annealing [14, 182, 184]. In general, a necessary condition for a nucleus to grow and become a recrystallised grain is the presence of an orientation gradient in the microstructure, so as to produce a HAGB and a critical subgrain size that has to be exceeded after overcoming the pinning pressure of fine particles. In addition, the presence of a special orientation relationship of the nucleus with the surrounding matrix can favour migration of the recrystallisation front by increasing its mobility.

The "preformed nucleus" model is one of the basic recrystallisation mechanisms. Some of the prerequisites for this mechanism are the presence of an orientation gradient, the growth of subgrains leading to nucleus formation via LAGB migration and, finally, discontinuous or abnormal subgrain growth of the nucleus [14, 184]. In certain cases the orientations of the recrystallised grains are very different compared to the surrounding matrix. It is now known that they were present after deformation but were too small to be identified. This typically occurs in the vicinity of GBs or at triple points where some grains appear to be rotated at large angles relative to the matrix. An example of the latter case is shown in Fig. 2.13, where fine bands of highly misoriented HAGBs were formed next to a GB triple point.

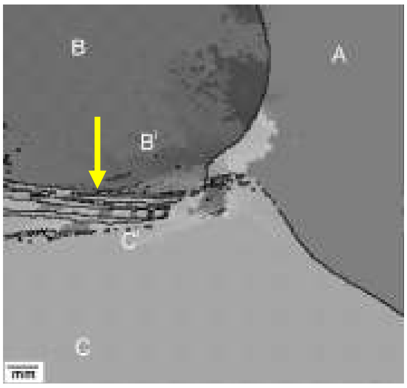

Fig. 2.13: Bands of misorientations higher than 40° from the adjacent grains, at a triple GB junction in an Al-0.3%Mn alloy after 50% cold-rolling [184].

Typical nucleation sites where a preformed nucleus can appear are GBs, transition bands, shear bands and large second phase particles (particle stimulated nucleation, PSN) [14]. The first of these has many similarities to the SIBM mechanism which is discussed later. Transition bands are regions of large misorientation gradients that develop due to slip processes (Fig. 2.14). The presence of large misorientations within short distances facilitates the appearance of a HAGB after some extent of recovery has taken place. Similarly, a distinctive feature of shear bands is also the large misorientation gradients. These bands appear as lines at 35° to the RD during rolling (Fig. 2.15). They are the outcome of strain localisation and their presence strongly depends on the processing conditions and microstructural characteristics. Subject to the type of shear bands (Copper-type for high stacking fault energy metals [185] and Brass-type for low stacking fault energy metals [186]), the orientations of the recrystallised grains will vary slightly, or significantly, relative to the surrounding substructure.

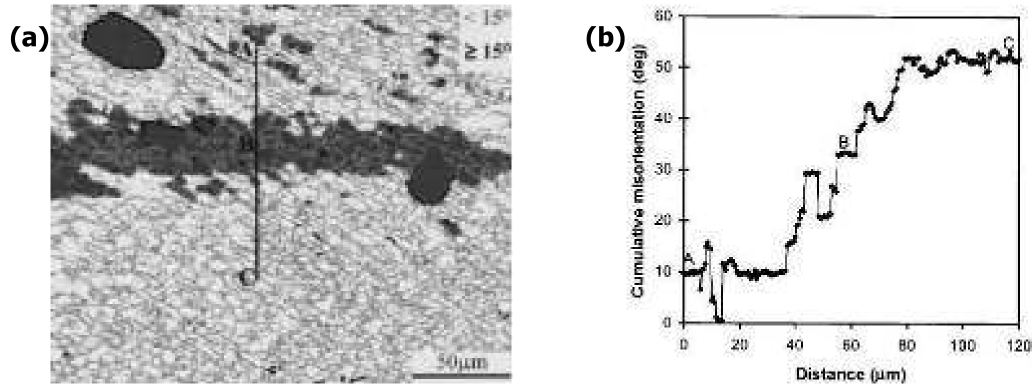

Fig. 2.14: Nucleation of new grains at a transition band [187]: **a)** EBSD map (Cube grains appear dark), and **b)**misorientation line scan of the same area.

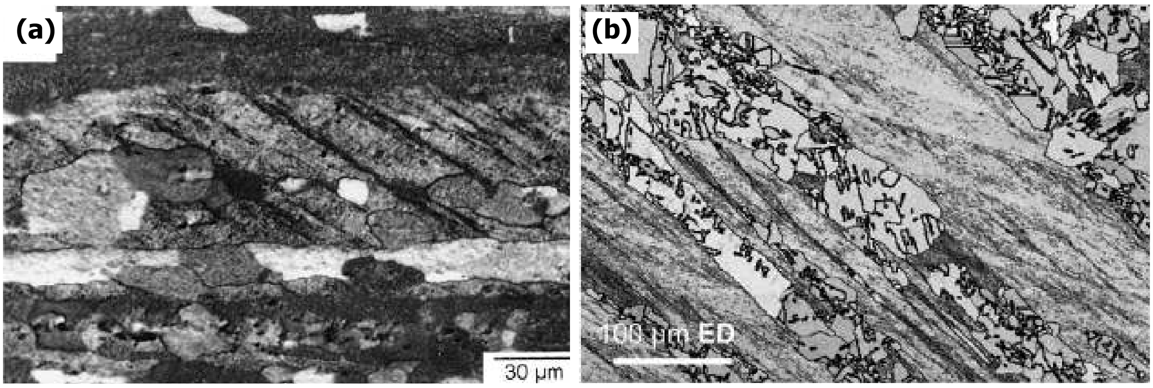

Fig. 2.15: Nucleation of recrystallised grains at shear bands: **a)** Copper-type shear bands in an Al-1wt%Mg alloy [185], and **b)** Brass-type shear bands in a Cu-2wt%Al alloy [186].

The PSN mechanism occurs as a consequence of the plastic incompatibility of large, hard particles with the matrix. This results in high local orientation gradients with the matrix surrounding a non-deforming particle after deformation. The critical particle size to allow recrystallised grains to nucleate on a particle is above 1µm, but PSN can also occur on slightly smaller particles if they are clustered and at high strain rates [14]. A deformation zone characterised by a large misorientation gradient is formed in the vicinity of the particle and extends to a short distance from its interface, equal to one particle diameter (Figs. 2.16a,b). If the critical particle size is not exceeded, the recrystallised grain will not grow beyond the deformation zone. Usually only one grain nucleates in the deformation zone, although it is possible to have more nuclei if the particle is very large.

Nucleation of the new grains within the deformation zone does not occur necessarily at the particle interface, but close to it since the misorientation gradient is highest in this area (Fig. 2.16b) [14]. This gradient is also responsible for the resemblance of PSN to nucleation at transition bands. The mechanism involves the fast migration of subgrain boundaries within the deformation zone leading to the formation of a HAGB due to the steep orientation gradient, which then consumes the rest of the zone.

Apart from the deformation zone, deformation bands can also exist close to particles and extend to distances even larger than 10 particle diameters from the interface (Fig. 2.16c) [182]. Such bands are developed by the interaction of the particle with the surrounding matrix, which causes the latter to rotate towards stable orientations during deformation.

Regarding the orientations of the PSN grains, it has to be stressed that they are not random and they have some relationship with that of the matrix [14, 184]. These orientations are present in the deformation zone before recrystallisation occurs. Studies on single crystal specimens have shown that a sharp texture is present after PSN, due to the more confined range of orientations that resulted after deforming a matrix of specific orientation. In the case of polycrystals, the subgrains or grains initially surrounding a particle would inevitably give a wider range of orientations after deformation and they would, in turn, yield a larger variation in the PSN orientations. Fig. 2.16d shows the orientation distribution in the deformation zone around a large particle, as predicted by Finite Element calculations.

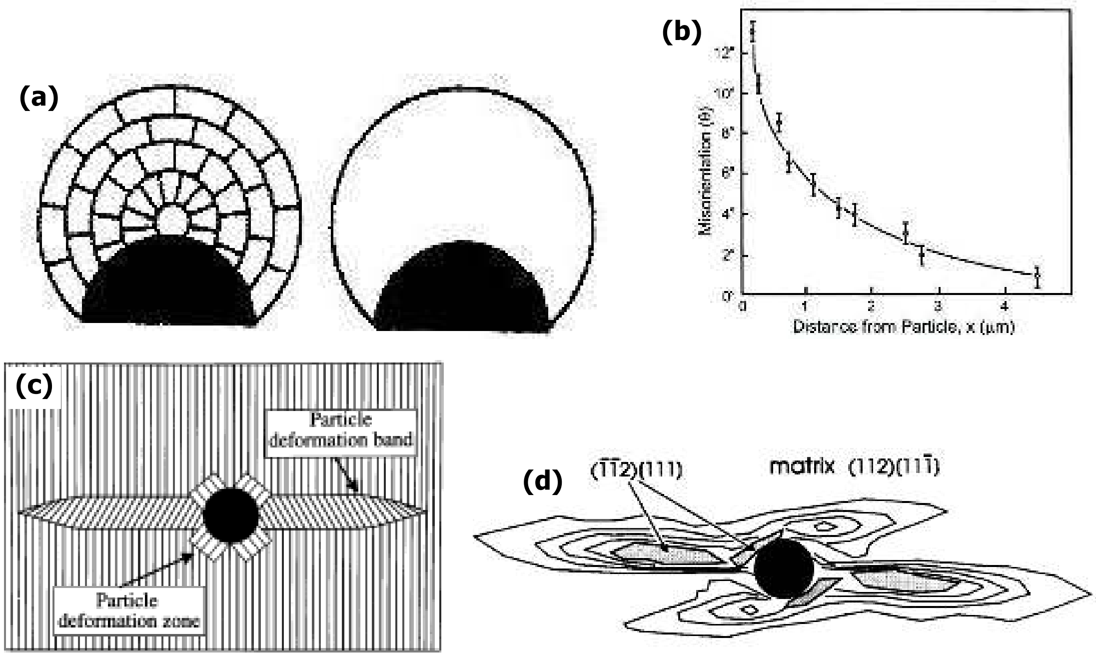

Fig. 2.16: Deformation zones around large particles: **a)** recrystallisation in a deformation zone around a large particle [188], **b)** misorientation gradient within the deformation zone [14], **c)** deformation band extending to a larger distance from the particle than the deformation zone [182], and **d)** finite element modelling calculations for the orientations in the deformation zone around a large particle [182].

Two essential conditions for PSN to occur are that deformation takes place below a certain temperature and that the strain rate exceeds a minimum value [14]. These two parameters ensure that relaxation of the plastic misfit between the particle and the matrix can not occur by diffusion, thus minimising recovery of the substructure, and that a high dislocation density is produced by the particles during deformation, so that the driving force for recrystallisation remains high. Additionally, the annealing temperature, total strain and presence of second phases are also of vital importance. High annealing temperatures, high strains and the presence of a volume fraction of large particles up to a certain limit, favour PSN (Figs.

2.17a,b). A high volume fraction of large particle thus gives a low recrystallised grain size. Their distribution can also affect PSN, since it was shown that nucleation is favoured between two particles or in particle clusters (Fig. 2.17c).

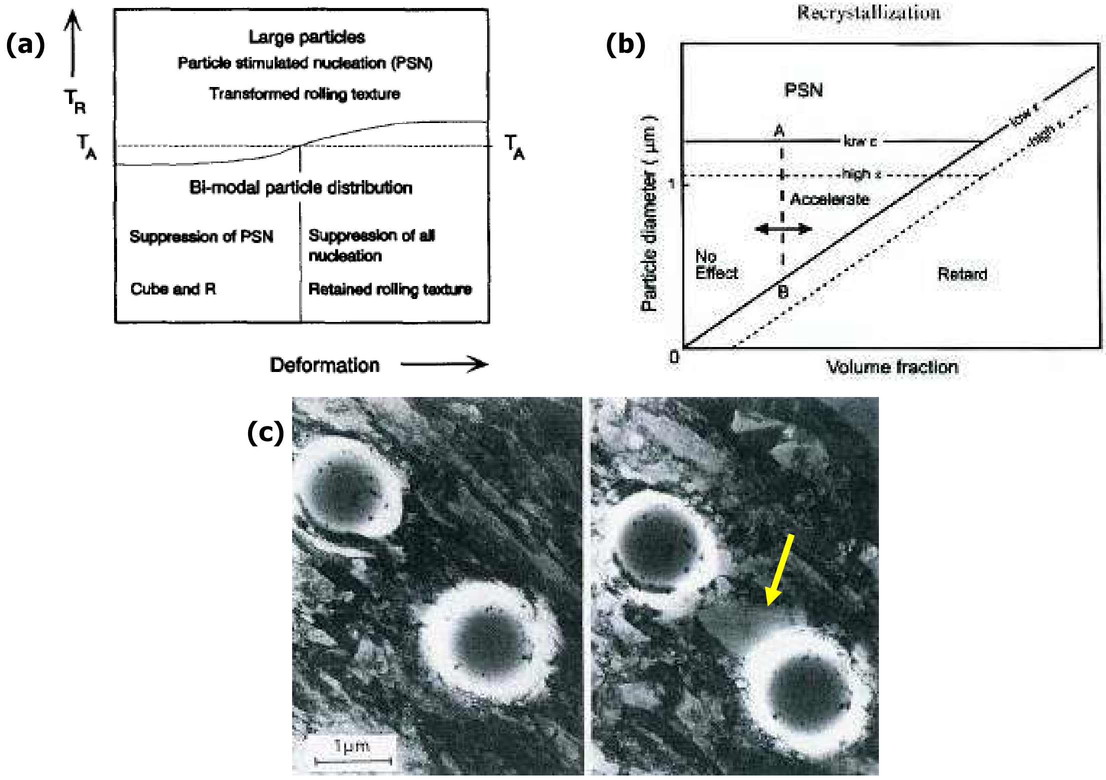

Fig. 2.17: Some factors influencing the PSN mechanism: **a)** annealing temperature and strain [189], **b)** features of the particle distribution and strain [14], and **c)** two closely-spaced, large particles nucleate a new grain in the region between them [190].

It is of great interest to comment on the occurrence of PSN in the presence of bimodal particle distributions, as this is relevant to the Zr+Mn-containing alloys of the present study. The presence of fine pinning particles can significantly alter the critical particle size for nucleation and the final recrystallised grain size by providing a pinning effect within the deformation zone surrounding coarse particles [14]. Under such conditions, a PSN nucleus may not be able to grow beyond the deformation zone. The critical particle size for bimodal distributions is given by the equation:

$$d_g = \frac{4\gamma_b}{P_D - P_Z} \qquad (2\text{–}11)$$

where P_D is the stored energy after deformation and P_Z is the Zener pinning pressure of the finer particles.

A model was proposed by Lloyd [191] to describe the recrystallisation behaviour of Al-Mn alloys with bimodal particle distributions. He observed that the large constituent particles, which lay on GBs in the cast material were aligned after cold-rolling and a lower number density of finer dispersoids was present in the same region (Fig. 2.18a). Hence, recovery occurred preferentially in such regions which were free of pinning particles, with the grains growing mainly along RD and little in ND (Fig. 2.18b). The surrounding subgrains coarsened only slightly due to pinning by the Mn-dispersoids. Eventually, recrystallisation was completed by the ND migration of grains that initiated in those areas, following HAGB formation in the regions of Mn-constituents and significant coarsening of the Mn-dispersoids that were pinning the subgrains (Figs. 2.18c,d).

Although the exact details of the suggested recrystallisation mechanism were not convincing, two of its features should be kept in mind; the initiation of recrystallisation in regions of constituent Mn-particles and the fact that coarsening of the pinning dispersoids resulted in a reduction in the recrystallisation resistance of the Al-Mn alloys.

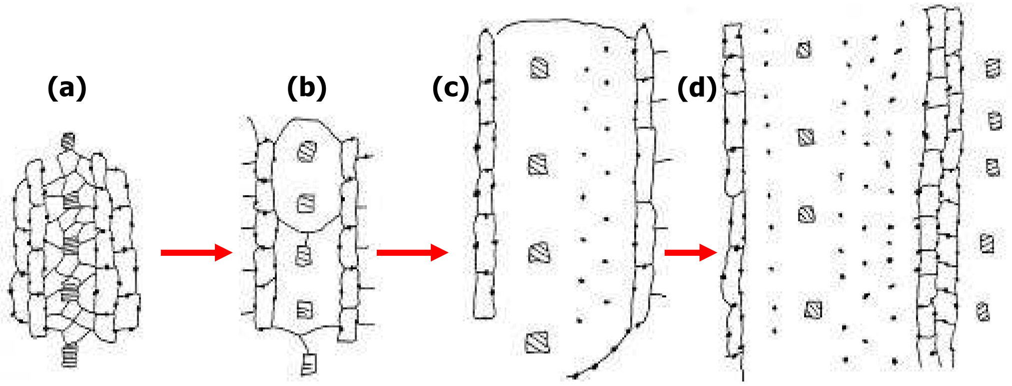

Fig. 2.18: Recrystallisation model proposed for Al-Mn alloys with a bimodal particle size distribution (large particles: Mn-constituent phases; small particles: Mn-dispersoids) [191].

Recrystallisation nuclei may also form on prior GBs via the strain induced boundary migration (SIBM) mechanism. The driving force for boundary bulging comes from a difference in the dislocation content (or stored energy that involves the subgrain size and misorientation) between the two sides of the HAGB (Fig. 2.19a) [14]. When a curved boundary is formed by SIBM, the region behind it is characterised by a lower dislocation content. This mechanism operates mainly at low strains and high temperatures. Other parameters that affect it are the structure of piled-up dislocations at GBs [192], the orientation relationship between the two adjacent grains, since this affects the LAGB mobility mainly [193] and the deformation strain, although this last parameter mostly affects LAGBs and little the HAGBs [194]. A distinguishing element of SIBM is that the recrystallised grains have orientations similar to those of the grains from which they have grown [193].

The SIBM mechanism appears in two forms; single subgrain and multiple subgrain or broad front SIMB. In the former case, the bulge is generated by a single subgrain (Fig. 2.19a). This happens especially in well recovered microstructures, where the stored energy difference between the neighbouring grains becomes less important than the achievement of a critical subgrain size [14]. On the other hand, multiple subgrain SIBM occurs with several subgrains (or a large number of dislocations) attached to the lower side of the advancing HAGB (Fig. 2.19b). The effect of this feature is the imposition of a restraining force on the boundary movement, though this is reduced with the increase of the bulge length [195]. Regarding which of the two forms of SIBM will prevail, the subgrain misorientation and size on each side of the HAGB is crucial. Single subgrain SIBM takes place for subgrain misorientations higher than 1° and for grains of similar stored energy, while multiple subgrain SIBM takes place for subgrain misorientations lower than 1°, or when the substructure is in the form of dislocation cells instead of subgrains. The pinning effect of dispersoids promotes multiple subgrain SIBM, which is then feasible at higher misorientations due to the pinning pressure reducing the net driving force for boundary migration [14].

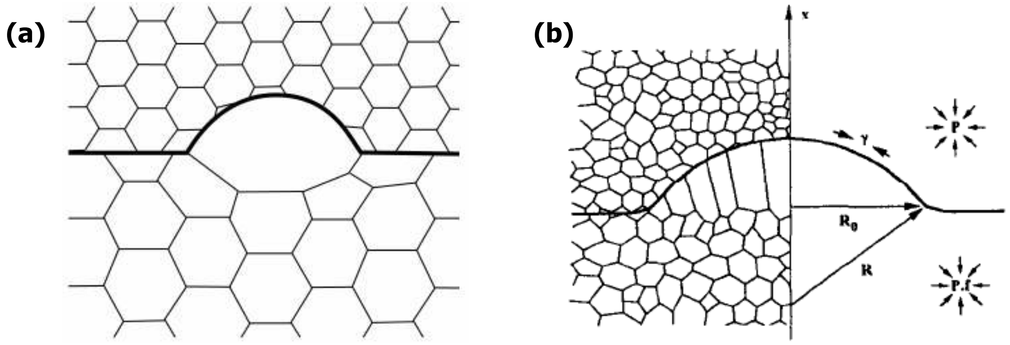

Fig. 2.19: SIBM mechanism: **a)** single-subgrain SIBM [184], and **b)** multiple-subgrain SIBM [195].

For annealing conditions where precipitation on HAGBs and recrystallisation occur simultaneously, or highly heterogeneous dispersoid densities exist, broad front SIBM is favoured [196]. This mechanism is illustrated in Fig. 2.20. In regions of the HAGB where little precipitation has occurred it is more possible for a bulge to bow out. These nuclei grow laterally along the RD until their boundaries meet. Eventually, they appear to be separated by LAGBs and such recrystallised grains can reach several hundred microns in length.

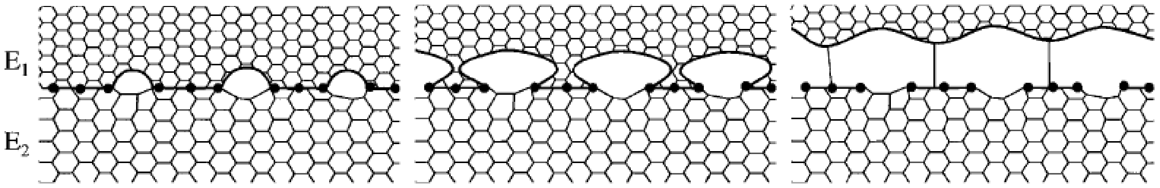

Fig. 2.20: Broad front SIBM mechanism in Al-Mn alloys: nucleation of recrystallised grains on a HAGB, which then grow laterally until they meet each other and are separated by a LAGB [196].

Generally, regardless of the nucleation mechanism, there are two basic principles that define which orientations will prevail in the recrystallised microstructure. These are named "oriented nucleation" and "oriented growth". The first term describes the situation where a higher percentage of recrystallised grains of a particular orientation nucleate in the matrix, as compared to grains of other orientations. The second term describes the situation where recrystallised grains of certain orientations obtain a size much larger than the average grain size [182]. Another reason for the extensive growth of certain recrystallised grains is the orientation pinning effect. According to this theory, recrystallised grains having orientations largely different than the majority of the deformed matrix, will be able to grow to a much larger size than the average since they are not inhibited by a reduced boundary mobility between grains of similar orientation [182]. However, the oriented growth and orientation pinning effects are not sufficient on their own to justify the larger size of selected grains and the micro-growth selection criterion is required to complete this mechanism [197]. Thus boundaries that have a special orientation relationship with the matrix, which increases their mobility, such as the Σ7 boundaries with a 40^o<111> relationship with the matrix, will migrate faster and help certain grains coarsen much faster than others. Hence, this can modify the recrystallisation texture during annealing.

2.3.3 Interactions between dispersoids and grain boundaries – Zener pinning

The presence of second phases in the microstructure is crucial because their interaction with the GBs results into restriction of grain growth and recrystallisation. Several parameters determine this interaction, such as particle size, strength, shape, coherency and distribution. The Zener pinning pressure represents the magnitude of the force exerted in a direction opposite to the boundary movement. Initially, the case of a spherical particle is examined for the sake of simplicity. The maximum Zener pinning pressure when the particle is in contact with a boundary in three dimensions is given by the equation:

$$P_z = \pi r \gamma \qquad (2\text{–}12)$$

where r is the particle radius and γ the surface tension of the boundary [134, 198].

The next step is to calculate how many particles interact with a GB, per unit area of the boundary for a random particle distribution. This value is equal to the ratio of the total volume of particles per unit volume over the average volume of one particle:

$$n_s = \frac{3V_f}{4\pi r^2} \qquad (2\text{–}13)$$

where V_f is the volume fraction of the particles [198] and the Zener pinning pressure becomes:

$$P_z = n_s P_z = \frac{3V_f\gamma}{2r} \qquad (2\text{–}14)$$

However, the particle shape is crucial since it affects the pinning pressure locally when in contact with the boundary [134, 135, 198-200]. For elongated particles meeting the GB with their long axis perpendicular to the boundary plane, the pinning force can increase up to a large extent when the particle aspect ratio is very high (case 1 in Fig. 2.21a). In the case where the particle meets the boundary with its wide side face-on (case 2 in Fig. 2.21a), the pinning force again increases with increasing aspect ratio, but to a lower extent than in case 1. Similarly, plate-shaped and needle-shaped particles exhibit the highest pinning pressure on a GB when they interact with it with their wide side facing the boundary plane (Fig. 2.21b). At other angles, the pinning forces are much lower.

However, the interaction of the particles with the boundaries is quite complicated and depends strongly on the boundary shape [199]. Figs. 2.21c-e illustrate the effect of the contact angle on the boundary shape during the interaction with an elliptical particle. When the particle has its long axis perpendicular or parallel to the boundary plane, the boundary exhibits curvature on one side only (Figs. 2.21c,d). When the contact angle is intermediate, the boundary might exhibit curvature on opposite sides, which alters the surface tensions and hence the pinning force of the particle (Fig. 2.21e) [199].

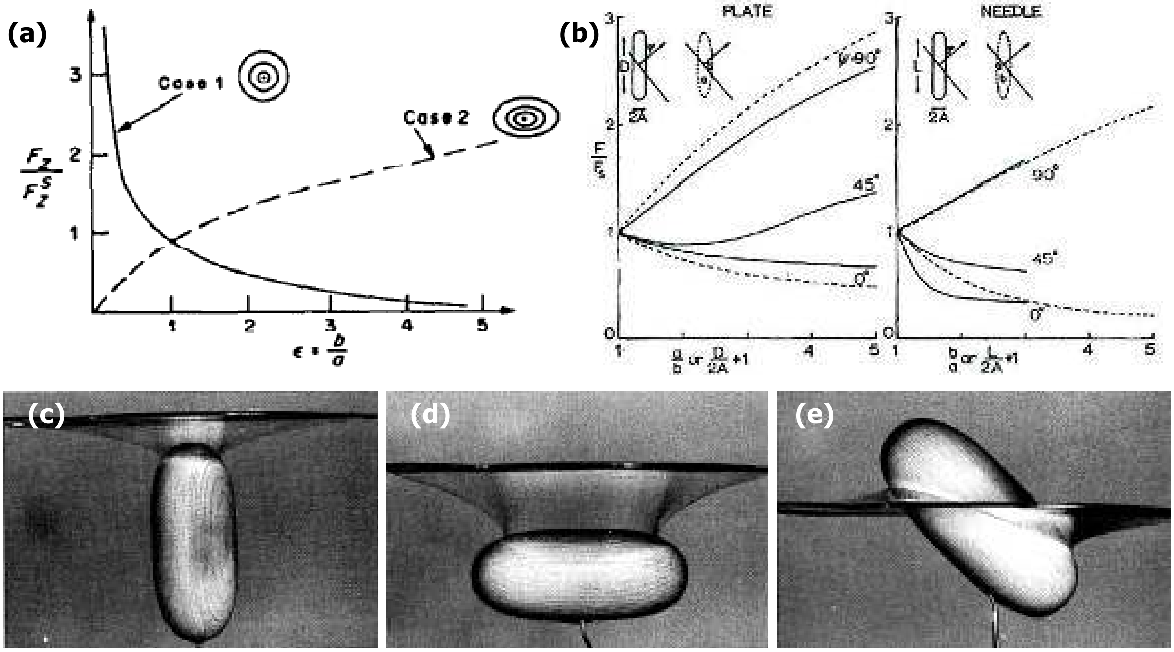

Fig. 2.21: Effect of particle aspect ratio on pinning pressure (normalised relative to the pressure from a spherical particle): **a)** elongated particles with their long axis perpendicular and parallel to the boundary plane [134], and **b)** plate- and needle-shaped particles facing the boundary at various angles [135]. Liquid film simulations of an elliptical particle meeting a boundary at various angles: **c)** long axis perpendicular to the boundary plane [199], **d)** long axis parallel to the boundary plane [199], and **e)** long axis tilted between 0-90° to the boundary plane [199].

The coherency of the particles is also important, but not as much as the shape factor. The effect of the particle volume fraction, on the other hand, is a lot more complicated and results may vary significantly. Several values have been allocated to the exponent of the volume fraction in Eq. 2-15, depending on the exact details of the approach in each work summarised by Manohar et al. [198]. The Zener limit gives the critical maximum grain radius where grain growth would be entirely suppressed:

$$R_c = \frac{4r}{3V_f} \qquad (2\text{–}15)$$

In rolled sheet, Zr- and Mn-dispersoids tend to appear distributed in a non-random manner, since they form bands after large thickness reductions. Such bands interact in a specific way with the migrating GBs, as Fig. 2.22a suggests, where the boundary is allowed to move between the dispersoid bands when the driving force exceeds a certain value [134]. Additionally, the shape of the recrystallised grains becomes more flattened (Fig. 2.22b) due to the influence of particles (higher aspect ratio RD/ND), when the ratio of pinning pressure over the driving force exceeds a critical value [134].

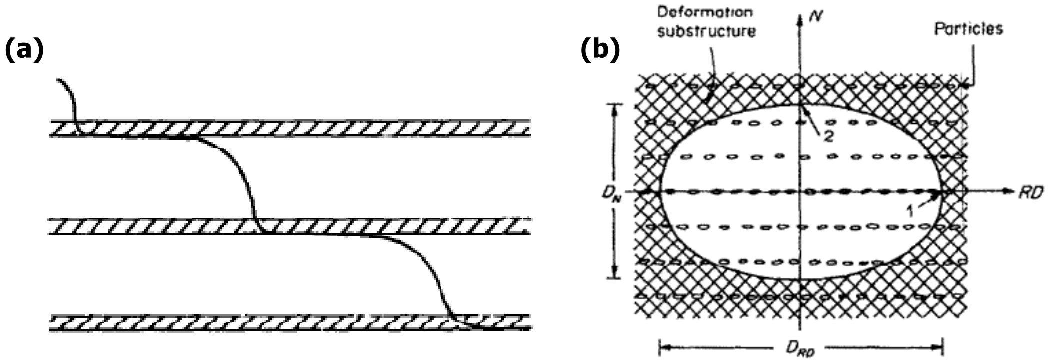

Fig. 2.22: Interaction of arrays of particles with migrating GBs [134]: **a)** GB movement between bands of particles, and **b)** a recrystallised grain containing several particle bands.

2.4 Texture

Texture is defined as the total sum of the crystallographic orientations of grains in a polycrystalline material relative to a sample reference frame. Its intensity indicates if the microstructure is randomly oriented, or if large aggregates of grains have specific lattice orientations. Knowledge of such information can help towards the design of alloys with particular properties, since many physical and mechanical properties are highly dependent on the texture [14]. Grain orientations change throughout the whole fabrication process of a metal sheet (§2.1.3). Grain structures in as-cast slabs are randomly oriented in the presence of grain refiners, but in subsequent stages the directional nature of the rolling deformation is passed on from the macrostructure to the microstructure [99]. Deformation processes such as rolling and stretching strengthen the texture, while others such as annealing tend to weaken it as a consequence of recrystallisation [201].

Texture is responsible for the presence of anisotropy in rolled sheet. This statement implies that anisotropy would thus also depend on all those factors that influence texture. Isotropic products would be preferred from manufacturers, since it is far less complicated to use components whose mechanical properties are uniform in all directions. Anisotropy is a major issue in wrought Al alloys and its presence is partly caused by texture, but is also caused by GB alignment along the RD and by the presence of directional banding and alignment of particles [202]. This unwanted feature has to be dealt with by appropriate design strategies for the manufacturing process, with respect to the final material properties. Four types of anisotropy exist according to Jata et al. [202] and are outlined below in order of importance.

- *In-plane anisotropy*, where the σ_y is lower at 45^o from the RD than in the RD or TD directions.

- *Through-thickness anisotropy*, where the σ_y along the RD is lower near the surface and increases towards mid-thickness. It is also possible that there is an in-plane anisotropy through the thickness of a plate [101].
- *Axisymmetric flow anisotropy*, in extruded products of low aspect ratios where the σ_y is quite high and marginally smaller than the UTS.
- *Elastic anisotropy*, that gives rise to anisotropy in elastic properties.

Texture is divided in two main categories depending on the nature of the microstructure. These are termed deformation and recrystallisation textures and are used to describe grain orientations in deformed and recrystallised volumes respectively. Texture is a very sensitive property that strongly relies on alloy composition and the processing variables. However, it should be born in mind that all these parameters are not independent from each other.

2.4.1 Deformation textures in Al alloys

The crystal orientation upon deformation depends on the number of activated slip systems and the amount of slip that takes place on each of them. A number of models have been developed which predict the behaviour of grains during deformation. Classic models include the Sachs, Taylor-full constraints (FC) and Taylor-relaxed constraints (RC) models [14], while the most up-to-date are the LAMEL [203] and ALAMEL (i.e. advanced LAMEL) models [204, 205]. Each model describes the extent of interaction between neighbouring grains and how freely they are allowed to move under an applied load. Some examples are shown in Fig. 2.23. Unfortunately, none of them can completely simulate polycrystal plasticity in order to yield accurate quantified texture results.

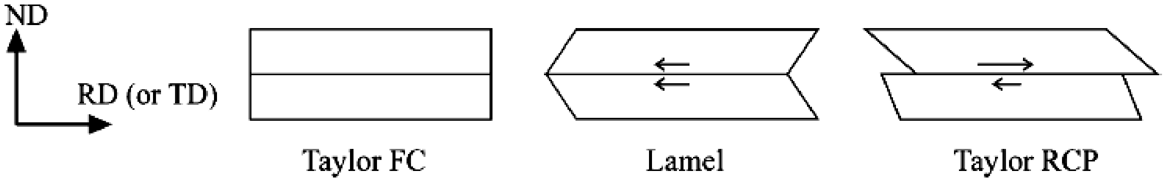

Fig. 2.23: Representation of the main principles regarding grain interactions upon which the fundamental texture prediction models are based (arrows indicate the direction of shear) [203].

In texture notation, the grain orientation is usually described by a crystallographic plane and an associated direction. The typically used notation {hkl}<uvw>, indicates that the {hkl} plane is parallel to the sample's surface, while the <uvw> orientation, lying within this plane, is parallel to a certain direction, such as the rolling direction [99]. The most common methods for representing textures are the orientation distribution function (ODF) and pole figures. This second type was employed for this thesis, because extensive information on textures was not required. ODFs are generally more descriptive, since they provide three-dimensional information from the Euler angle space, compared to the two-dimensional information obtained by pole figures [14, 206]. The most important fibres and deformation texture components in FCC alloys are shown in Fig. 2.24.

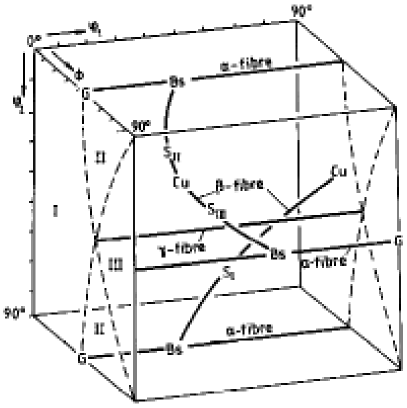

Fig. 2.24: Main fibres and deformation texture components for FCC alloys within the Euler angle space (G: Goss, Bs: Brass, Cu: Copper) [207].

The effect of solute is one of the most important parameters that influence the grain rotations during the deformation process. The introduction of solute elements in Al with a high stacking fault energy changes the texture from one having Copper as the main component, to a Brass-dominated texture [14]. In the case of Li-containing alloys, the deformation texture is strongly altered in binary Al-Li alloys when the Li concentration exceeds 2 wt% and rotates towards the Brass component [208]. This is linked to the precipitation of δ' particles which leads to shear localisation. For Li contents below 2 wt%, deformation texture development is more complicated in Al-Cu-Li alloys. The dominant texture component depends on the Li/Cu ratio and a value of approximately 6.5 appears to yield the highest Brass content, due to the prevalence of the T_1 precipitates [103]. These particles are cut by dislocations, thus leading to slip inhomogeneities.

Trace elements and impurities also play a crucial role in the development of deformation textures. A typical example is the presence of Fe solute, which even at concentration levels such as ppm can dramatically change the deformation texture due to an effect on dislocation mobility [209]. A marginal decrease in the amount of Fe in solid solution is adequate to randomise texture at the mid-thickness of a rolled sheet and favour the typical hot-rolling components at its surface.

The presence of particles also affects the deformation texture to an extent determined by their size and volume fraction. Large, non-deformable particles randomise texture due to the deformation zone they create around them [210]. Fine, shearable particles introduce a strong Brass component, due to the promotion of slip heterogeneity and them being cut by dislocations during deformation. These particles are the $L1_2$ ordered δ' phase in binary Al-Li alloys which favours co-planar slip by superdislocation pairs [208] and the T_1 phase in ternary Al-Cu-Li alloys [103]. The relative amounts of the β-fibre components are also influenced by the habit plane of such precipitates [103]. Fine, non-shearable particles homogenise slip and prevent shear band formation, so the deformation texture is rotated towards Copper [210].

2.4.2 Recrystallisation textures in Al alloys

The orientations of the grains that nucleated during annealing are not random and have their origin in the initial deformation texture of the matrix prior to annealing [184]. However, the recrystallisation texture of a two-phase Al alloy is influenced by the presence of large particles or by precipitation of fine particles during annealing, which inhibits the boundary migration and grain growth [14].

Regarding the main parameters that affect recrystallisation textures in Al alloys, the presence of solute has a very important influence. The new recrystallised grains are related to the previously existing deformation texture that had formed under the strong influence of the solute content. Concerning binary Al-Li alloys, a higher amount of Li in SS decreases the percentage of the main orientations of the recrystallised grains, Goss and Cube [208]. In the case of ternary Al-Cu-Li alloys, low Li/Cu ratios were found to marginally promote the formation of R-Cube and Cube, although their volume fractions were quite low [103].

Second phases also strongly affect the recrystallisation texture. Large, non-deformable particles provide nucleation sites for PSN in their surrounding deformation zone and tend to randomise the texture [14, 189, 201, 211], while retained deformation texture components are also present in the microstructure [212]. Fine, shearable particles promote the Cube and R components for low strains and P, Q and Goss for higher strains [211]. Bimodal particle distributions are a more complicated situation and their effect is determined by the annealing time, temperature and strain [189].

During recrystallisation, some orientations might be consumed faster than others leading to dominance of specific recrystallisation textures, or to retention of certain deformation texture components. Preferential consumption of the β-fibre components by recrystallised grains is more extensive for Copper and S for two main reasons; their higher stored energy compared to other components [213] and their 40^{o}<111> orientation relationship with Cube grains which develop upon recrystallisation [99, 214]. Copper especially reduces much faster than all other orientations, while Brass, S and Goss decrease slightly for low recrystallised volume fractions, then stabilise and eventually are consumed at high rates for large volume fractions of recrystallisation [105]. As evidenced by Guiglionda et al. [213], preferential consumption of specific orientations also depends on strain; an increase from 1 to 1.4 led to a change of the preferentially consumed deformation component from Copper to S. However, in severely deformed microstructures, such as those formed by ECAP, a reduction in Brass is evident but it is much more difficult to be explained [215].

On certain occasions the volume fraction of the main β-fibre components may remain in the microstructure at significant levels after annealing. Specifically, Brass is well-known to be more resistant to recrystallisation [201, 216], due to its lower stored energy compared to Copper or S [14, 213]. When it is consumed though, Goss-oriented grains are favoured due to the 40°<111> orientation relationship between them [99]. There are also other ways for the retention of this orientation in the microstructure, even in recrystallised grains. Higginson and Bate [217] reported that large Brass-oriented recrystallised grains can develop via broad front SIBM during annealing. Brass occurs during deformation as a stable orientation and it is a preferred SIBM nucleus during recrystallisation due to its low stored energy, enhanced by high Zener pinning.

Another case where there is a remnant deformation texture is that of extended recovery, or continuous recrystallisation, which takes place at large strains [14, 180] and rolling texture orientations are retained in the microstructure within recrystallised grains. The R texture component (close to S) usually forms via this mechanism [218], but the same has been reported for Brass as well [105]. According to Liu et al. [219], similar orientations in deformed and recrystallised areas have been considered in the past as signs of continuous recrystallisation.

2.4.3 Textures in Li-containing Al alloys

Older generations of Al-Li alloys have been shown to exhibit stronger textures than conventional high strength Al alloys and particularly higher concentrations of Brass orientation (e.g. [99, 202, 220, 221]). This fact is directly linked to their high anisotropy of mechanical properties, as will be explained later. Most 2nd generation Al-Li alloys (such as AA2090 and AA8090) exhibit stronger Brass and lower S than other Al alloys after hot-rolling. In certain cases where this effect is not so pronounced, such as in the results of Rohmanji et al. [222] for an AA8090 where Brass and S are present almost at equal amounts, severe cold-rolling is probably the explanation for this discrepancy since it favours the formation of S. In that work in the 0.8 mm sheet the grains probably rotated towards the high stored energy S component, along with a significant percentage of Copper.

The 3rd generation Al-Li alloys have been processed in a different way in the last few years, so that the elevated Brass content is reduced compared to the first variants of the same generation (§2.1.3). The earlier variants of this alloy type, such as AA2095 [33] and AA2195 [223, 224], were characterised by large differences between the volume fractions of Brass and S. In the latest variants of the 3rd generation Al-Li alloys, although the Li content is identical to the earlier variants (~1 wt%), their texture is much different and exhibits a lower percentage of Brass. This claim is supported by recent results of Cho et al. [101] on an AA2195 alloy where they found more S than Brass in a 39 mm thick hot-rolled plate. Most possibly this plate has been processed via a suitable route to reduce the Brass content (similar to that illustrated in Fig. 2.4b). Another recent variant of 3rd generation Al-Li alloys, that has been reported to exhibit a higher content of S than Brass, is the AA2050 studied by Contrepois et al. [97]. On the other hand, a 6 mm thick sheet of the AA2198 alloy studied by Decreus et al. [12], showed a much higher amount of Brass (60%) compared to all other components. The explanation for the observed discrepancy in this last case is related to the presence of Mn that increased the level of recrystallisation and will be explained in §2.4.5.

2.4.4 Brass texture and anisotropy in Al-Li alloys

The yield stress anisotropy of Al-Li alloys is mainly affected by texture and especially by the Brass content. In particular, a higher volume fraction of Brass causes in-plane anisotropy by increasing the strength in the TD of a plate [101, 103], in addition to greater through-thickness anisotropy by increasing the strength at mid-thickness [104]. Fig. 2.25 gives an illustration of the relationship between the Brass content and the resulting yield stress anisotropy. It is clear that in most of the Al-Li alloys on the graph, a reduction in the concentration of the Brass component results in a concomitant decrease in anisotropy. In contrast, anisotropy in 7xxx series alloys does not depend so strongly on the Brass content, so it is obvious that other parameters also affect anisotropy.

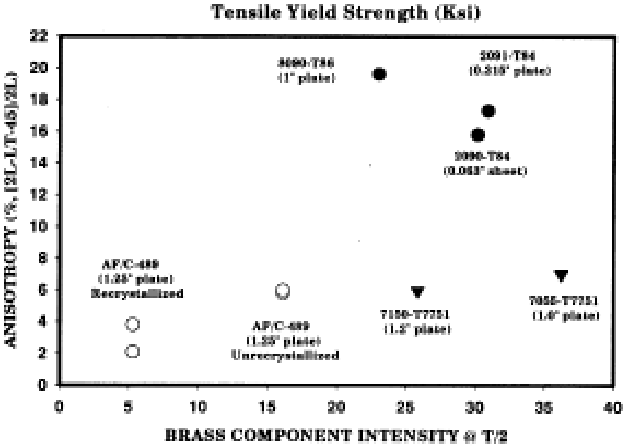

Fig. 2.25: Effect of the Brass texture component on the in-plane anisotropy of some high strength Al alloys [4]. Alloy AF/C-489 is also a 2nd generation Al-Li-Cu alloy [202].

Since the ideal orientation of Brass has such a major significance for the mechanical properties of Al-Li alloys, a detailed assessment of its formation is given below. Of the main parameters that affect the Brass component, the most important is the presence of solute elements, which makes the texture deviate from the typical Copper-type texture in FCC alloys [14]. Generally, it is favoured during high temperature deformation in contrast to Copper and S which are cold-rolling products [225]. The dislocation densities and stored energies of all three components have been reported to vary accordingly, with the values for S and Copper being higher than of Brass [213]. The lower stored energy agrees with the experimentally measured lower misorientations of Brass subgrains compared to Copper, S and Goss deformation components [14]. Additionally, Bate et al. [226] reported that Brass dominated at high strains above 3.7 during high temperature deformation, while it had a similar intensity with the rest of the β-fibre orientations at strains below 2 (Fig. 2.26). Brass is favoured for low strain rate values [227], while high values of the strain rate sensitivity of flow stress have an equal effect [228]. Finally, Bate and Oscarsson [229] mentioned an observation made by Nes, that a larger initial grain size prior to rolling leads to a higher amount of Brass.

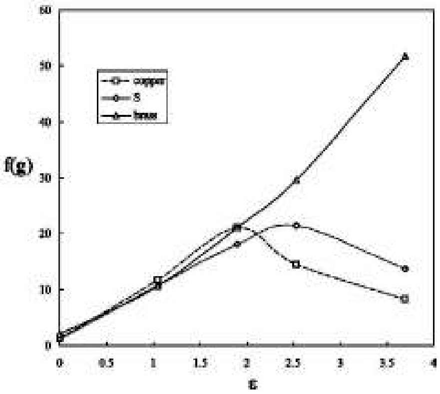

Fig. 2.26: Intensity of the main β-fibre components as a function of strain during compression of an Al-Cu-Zr alloy at 375°C [226].

Many theories have been developed over the years, involving a lot of debate, in order to understand the origin of the Brass component during deformation. The most up-to-date review is given by Leffers and Ray [230] but unfortunately it is focused on copper and brass alloys, which have medium and low stacking fault energies respectively, contrary to aluminium alloys that have a high energy. The majority of the suggested mechanisms are based on crystal plasticity theories that deal with the interaction of neighbouring grains during deformation and their freedom of movement in three dimensions. The only theories whose essence deviates from this typical approach, are those of Bate and Oscarsson [229], Maurice and Driver [227, 231] and Bate et al. [226]. Table 2.4 summarises some of the most important findings on this subject.

Table 2.4: Evolution of theories during the years, on the origin of Brass formation in Al during deformation.

Proposed mechanism of Brass formation	Author(s)	Year	Ref.
Slip localisation due to cutting of fine particles yields a change from FC to RC or NC deformation mode, where only the best oriented slip systems are active. Brass is favoured since it only needs two systems.	Engler et al.	1989	[210]
The Goss component is favoured from shear band formation due to slip localisation and it rotates towards Brass with further deformation.	Engler et al.	1989	[210]
	Hirsch	1990	[206]
Retained volume with a Brass orientation from previous hot-rolling before cold-rolling.	Bowen	1990	[99]
Deformation banding under the concurrent presence of extensive solute pinning of the dislocation motion. These bands usually form at angles higher than 45° to the RD and possibly are $\{112\}_{Al}$ planes.	Bate et al.	1990	[229]
A mixed octahedral and non-octahedral slip on the systems {111}<110> and {112}<110> is responsible for a higher Brass due to better accommodation of the	Maurice et al.	1997	[227, 231]

exerted shears. Combination of the octahedral slip with the systems {110}<110> and {100}<110> also has the same effect on the shear forces. A supplementary effect comes from grain shape anisotropy.			
Dynamic grain growth during hot deformation favours Brass grains preferentially due to the low stored energy of its subgrains. Additional contribution to this mechanism comes from a high Zener pinning and possibly dynamic recovery when the HAGBs obtain a minimum saturation value during hot deformation.	Bate et al.	2004	[226]

2.4.5 Role of dispersoids in texture formation

The effects of all types of particles on texture were described briefly earlier and for more detail, the reader is referred to the relevant literature [14, 103, 189, 201, 210-212]. Due to their importance to this thesis, this section discusses further the effect of dispersoids which are added to control the grain structure, recrystallisation resistance and fracture toughness of Al alloys.

The effect of dispersoids on texture strongly depends on their size, volume fraction and the tendency to be cut or by-passed by dislocations [14]. However, the direct effect of dispersoids on the deformation texture is difficult to separate from their influence on the recrystallisation behaviour during hot-rolling. It is also of major relevance to this study that during hot-rolling, recrystallisation occurs in between rolling passes [202] and the starting texture of the plate is changed from one pass to the next, due to the new orientations arising from the recrystallised grains. As a result of this, different grain rotations take place and, consequently, the final texture will be different. Hence it would be more appropriate to say that dispersoids have a strong indirect effect on texture during hot-rolling, which is related to the recrystallisation resistance.

Most of the studies in the literature are focused on recrystallisation texture development in the presence of dispersoids, rather than deformation texture. Regarding Zr- and Mn-dispersoids in general, the former type helps to maintain an unrecrystallised microstructure while the latter type cannot effectively suppress recrystallisation [132]. Hence, texture is known to be weakened and altered by recrystallisation [201]. Regarding deformation textures, there are several contradicting references in the literature. Some report that dispersoids show no significant effect [232], while others show a clear dependence on the number and size of the particles [212]. In the author's opinion, this second evidence is more accurate. In this work it was stated that the small number density of fine and shearable particles will favour higher amounts of Copper and S, but also increase the intensity of Brass and Goss components, while the small number density of the larger Mn-dispersoids will give a sharper texture with a higher volume fraction of Copper.

On the other hand, recrystallisation textures are much more strongly dependent on dispersoids in Al alloys. A major factor is the presence of simultaneous precipitation of dispersoids during recrystallisation, which can dramatically alter the recrystallised texture [233] and also lead to "island grain" formation [234]. Here, the fine Al_3Zr particles will favour Goss, Q and P, as well as orientations satisfying the 40°<111> growth criterion at high annealing temperatures [212]. The larger Mn-dispersoids are expected to favour retained deformation textures [212]. The development of certain orientations will not occur unless a specific volume fraction of particles is exceeded [235]. Additionally, these particles can inhibit more effectively the growth of orientations arising via PSN, than others nucleating on transition bands [236].

The deformation textures in the latest variants of the 3rd generation Al-Li alloys can be interpreted by assessing their dispersoid content, in terms of the recrystallisation resistance they offer and this appears to have caused much confusion in the literature. It appears that the alloys showing a higher tendency to recrystallise during the hot-rolling passes, exhibit lower Brass than expected in the final form. This is possibly due to preferential consumption of Brass by the recrystallised grains. This observation agrees with the findings of Jata et al. [202], who unfortunately could not explain why this was happening. The Al_3Zr dispersoids in thick plate are known to be insufficient recrystallisation inhibitors, as reported by Warner [8]. This implies that the AA2195 thick plate recrystallises to a certain extent during the hot-rolling process. Further, the AA2050 alloy contains a combination of Zr- and Mn-dispersoids which yields an arguably higher recrystallisation resistance during hot-rolling as shown by the large discrepancies of the existing data in the literature (§2.2.4). However, preliminary results from the present thesis support the view that the combined addition of these dispersoids deteriorates recrystallisation resistance [237]. Conversely, the AA2198 alloy contained only Zr and it was completely unrecrystallised in the final rolled sheet [12]. Hence, it is possible that the AA2195 plate and AA2050 sheet with a lower recrystallisation resistance contained a lower amount of Brass than S, compared to the highly recrystallisation resistant AA2198 that had a much higher Brass content. To sum up, the recrystallisation resistance of these three alloys correlated perfectly with the amount of the Brass component in the final microstructure.

2.5 Fracture behaviour of Al-Li alloys

Metallic materials are in most cases ductile. Although their fracture resistance depends on several parameters, the possible fracture paths and fracture modes are specific and they are outlined in Table 2.5. In contrast, mixed fracture modes are commonly seen in high strength Al alloys and the relative amounts of each one depend on the alloy condition. However, quantification is quite difficult and although some attempts have been reported [238], the results are not entirely reliable. The reason for this is that because fracture surfaces are 3-dimensional, they cannot be effectively processed by 2-dimensional image analysis. The parameters that affect fracture will be discussed in §2.5.2. The Kahn tear test employed in the present study is characterised by a tensile tearing deformation mode. This mode results in a fracture surface where the elongated dimples are oriented towards the point where the crack starts from [239].

Table 2.5: Summary of all the possible fracture paths and fracture modes in metallic alloys [239].

Fracture path	intergranular	transgranular
Fracture mode	dimple rupture	
	cleavage	
	fatigue	
	decohesive rupture	

It has been reported that the main fracture mode in Al-Li alloys is grain boundary ductile fracture, which may occur in several ways [240]. Hence, GB precipitates are expected to hold a vital role in the deformation behaviour of this type of alloys. Fracture resistance relies on the combination of several different factors [16], such as:

- coarse constituent phases resulting from the as-cast microstructure,
- GB impurities,
- large number of GB precipitates,
- strain localisation due to slip band formation,
- PFZs adjacent to GBs, promoting stress concentration on them,
- low energy interface between the equilibrium Al-Li phase δ and the matrix.

Regarding strain localisation, its effect comes from the accumulation of high stresses at the edge of the slip lines, which extend to the GBs and they can eventually open up the boundary. The last factor above, namely the low energy δ/matrix interface, concerns only older generation Al-Li alloys with a much higher Li content than the 3rd generation alloys studied here. Thus, this factor is not expected to affect the AA2198 alloy.

Various fracture mechanisms have been suggested so far for Al-Li alloys [16]. These are namely:

- cracks initiating at Fe- and Si-constituent phases with microvoids growing on them,
- microvoids develop on dispersoids and then coalesce, connecting later to the voids on the cracked constituents,
- shear band formation, which results in strain localisation that lowers the alloy strength,
- intergranular fracture because of coarse GB precipitates,
- intergranular fracture because of PFZs,
- the extent of deformation in the area ahead of the crack tip affects the critical strain to fracture.

2.5.1 Fracture toughness in thin sheet

The stresses that are acting in the area ahead of a crack tip are related to the energy required for the crack to propagate. Fig. 2.27 illustrates these stresses at any point at a distance r and angle θ from the edge of the crack. The extent of crack propagation depends on the strain energy difference of the stress fields before and after crack extension. The equations giving these stresses are:

$$\sigma_x = \frac{K}{\sqrt{2\pi r}} \cos\frac{\theta}{2}\left(1 - \sin\frac{\theta}{2}\sin\frac{3\theta}{2}\right) \qquad (2\text{–}16)$$

$$\sigma_y = \frac{K}{\sqrt{2\pi r}} \cos\frac{\theta}{2}\left(1 + \sin\frac{\theta}{2}\sin\frac{3\theta}{2}\right) \qquad (2\text{–}17)$$

$$\tau_{xy} = \frac{K}{\sqrt{2\pi r}} \sin\frac{\theta}{2}\cos\frac{\theta}{2}\cos\frac{3\theta}{2} \qquad (2\text{–}18)$$

where K is a parameter that depends on the stress acting in the y direction away from the crack, the crack length (2α) and the sheet dimensions [241].

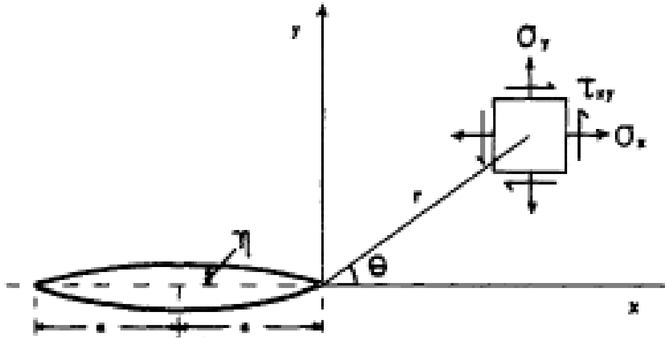

Fig. 2.27: Stresses acting in the region ahead of a crack tip [241].

A plastic zone is formed adjacent to the crack tip due to the stresses in that region being higher than the yield stress of the material [241]. Fig. 2.28a shows the location of the plastic zone relative to the crack. The size of the plastic zone will define if plane stress or plane strain conditions will prevail during deformation. If it is small compared to the crack length, the influence on the total strain energy of the material will be small and a plane stress state of the stresses will be approximated. In the opposite case, the condition will be closer to plane strain. The following analysis proves why this is happening.

The plastic zone increases the effective length of the crack, which becomes equal to $\alpha + r_Y$. The distance r_Y denotes the point in front of the crack tip where the stresses would be maximum, exceeding the yield stress of the material. The stress distribution can be seen in the top graph of Fig. 2.28a. The correction term r_Y represents the plastic zone in two dimensions as a circle and is expressed in a simple form by:

$$r_Y = \frac{K_C^{\,2}}{2\pi\sigma_Y^{\,2}} \qquad (2\text{–}19)$$

where σ_Y is the yield stress of the material and K_C its fracture toughness. Eq. 2-19 is valid for a plane stress state only [241].

The stresses in the plastic zone will also be in a plane stress state when the sheet thickness is small compared to the size of the plastic zone. This happens because the plastic zone will be closer to the free surface of the specimen. On the other hand, when the sheet thickness is much larger than the size of the plastic zone, the stresses near the specimen surface will be lower than the yield stress of the material and plane strain condition will prevail.

Regarding the effect of specimen thickness on fracture toughness, K_C, Fig. 2.28b illustrates their relationship. The plastic zone induces shear fracture at the free surfaces of the specimen when the sheet thickness is small. However, for a larger sheet thickness there is a higher volume of material in the elastic state which imposes higher impedance on the crack propagation. In fact, the larger the sheet thickness, the higher this restriction will be and the fracture toughness moves towards a minimum value (K_{IC}) which is characteristic of the material properties only and is unaffected by the testing parameters [241].

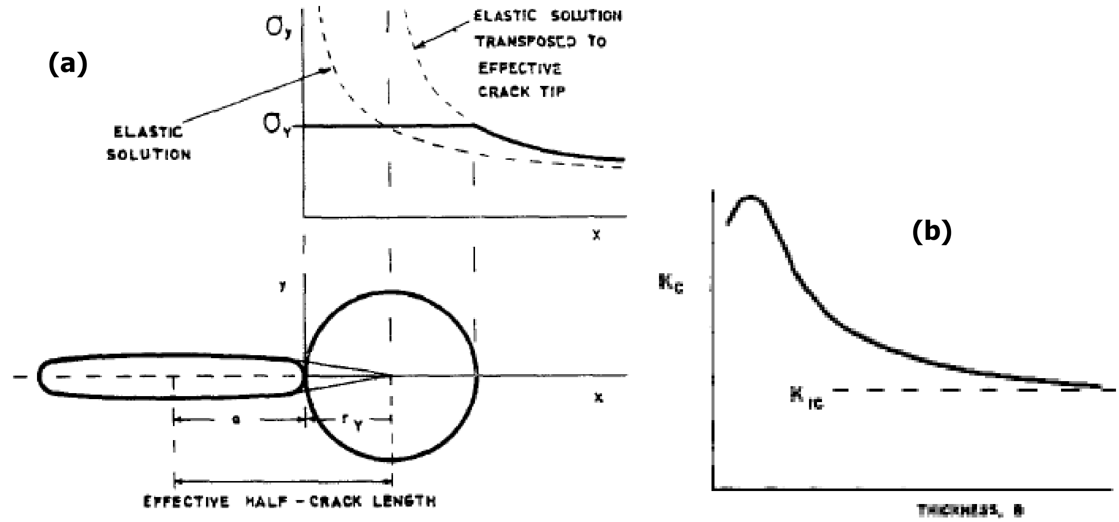

Fig. 2.28: Assessment of the stress state [241]: **a)** circular plastic zone adjacent to a crack tip and stress distribution in that area, and **b)** influence of plate thickness on K_C.

2.5.2 Influence of microstructural features on toughness

The mechanical properties of Al alloys and of 3rd generation Al-Cu-Li alloys in particular, strongly depend on several microstructural parameters, which are discussed below including; second phases, ageing, PFZs, grain size, recrystallisation and texture. The most important effect on fracture toughness comes from the presence of large particles, such as constituent phases and dispersoids. Zr additions have a lower impact since they do not trigger the formation of large constituent phases, except for fine coherent Al_3Zr dispersoids. The remaining Zr atoms simply stay in solid solution. The effect of the Mn addition is more ambiguous, due to the higher volume fraction of large constituent particles, which is enhanced by the GB segregation of this element and its interaction with Fe and Si. For this reason, only the effects of the large Mn-particles will be analysed here.

Regarding the large constituent phases, their shape and spacing are the most crucial factors that will determine the fracture mode. Equiaxed Mn-particles lead to fracture via decohesion with the matrix at their interface, while non-equiaxed ones tend to crack [242]. A large interparticle spacing yields higher fracture toughness, due to the slower coalescence of voids which nucleated on the particles [239, 243]. The result is to absorb more deformation energy before fracture and the fracture surface consists of large dimples (Fig. 2.29a). In contrast, a small interparticle spacing leads to lower fracture toughness and finer dimples.

A mechanism suggested for the nucleation of voids on large elongated particles is illustrated in Fig. 2.29b. Five stages were identified [244], in the sequence indicated by the arrows in the image:

- at low strains, dislocation pile-ups are formed at GBs and large particles as a result of coarse slip,
- the accumulated stress at the particle/matrix interface exceeds the fracture strength of the particle and a crack is initiated,
- voids grow mainly laterally and less in the deformation direction due to the hydrostatic stress,
- at higher strains, decohesion of the particle/matrix interface occurs at the ends of the cracked elongated particles,
- voids coalesce within groups of GB particles and initiate cracks that traverse the GBs or the adjacent PFZs.

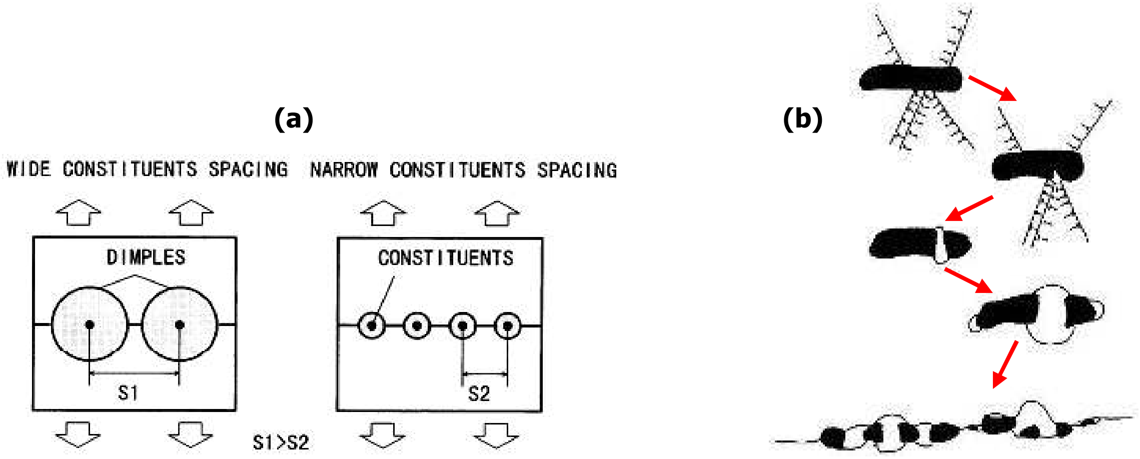

Fig. 2.29: Effect of constituent phases on fracture toughness: **a)** effect of interparticle spacing for large particles [243], and **b)** mechanism of void nucleation on large elongated particles [244].

The presence of Mn-dispersoids is more complicated and involves contradicting effects. Their beneficial action is that they change the fracture mode from intergranular to transgranular [171, 245], with small dimples associated with them [246]. Additionally, they reduce the crack propagation rate much more effectively than the fine Al_3Zr dispersoids [243]. An increase in the volume fraction of Mn-dispersoids leads to competition between the effects of a slower microvoid coalescence due to slip homogenisation, which improves ductile fracture toughness, and of an acceleration in microvoid coalescence due to the shorter interparticle spacing (Fig. 2.30a) [242]. Which of these two effects will prevail depends on the exact Mn content. Additions lower than 0.5 wt% are usually not beneficial to fracture toughness [16, 171, 245, 247]. Except for the work of Walsh et al. [242] where an AA2134 alloy with 0.3 wt% Mn exhibited the highest fracture toughness of the alloys tested, it appears that the optimum Mn content should be between 0.6-1.2 wt% [171, 245]. However, the gain from a relatively large Mn concentration is counteracted by an inevitably large volume fraction of constituent phases, which decreases fracture toughness [247].

The ageing treatment can also affect fracture toughness quite significantly, especially in the absence of dispersoids which homogenise slip. Localised slip is prevalent in underaged conditions, while upon overageing, slip becomes more dispersed [242, 248]. In a grain with fine shearable precipitates, slip bands are formed due to the shearing of precipitates by the moving dislocations (Fig. 2.30b). Ductile fracture then occurs in PFZs where the slip bands extend to and the high local stresses there can crack the boundary open [240]. Usually PFZs in Al-Cu-Li alloys are formed due to the dissolution of δ' precipitates and the Li segregation to the GB to form the equilibrium δ phase (e.g. Fig. 2.30c) [249]. The shearable precipitates in the grain interior of high-Li Al alloys are typically the δ' phase. However, in 3rd generation Al-Cu-Li alloys where the δ' phase does not form, such as the AA2198 alloy, planar slip in an underaged condition is attributed to shearing of GP zones [248].

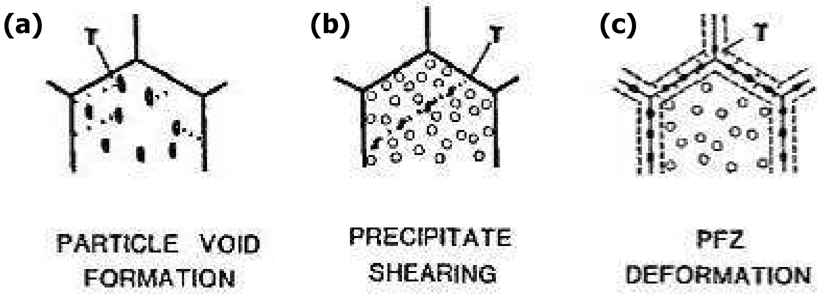

Fig. 2.30: Possible crack propagation mechanisms [250]: **a)** microvoid coalescence starting from the large incoherent Mn-dispersoids, **b)** coarse slip band within a grain, introduced by shearing of the ageing precipitates, and **c)** cracking along PFZs due to stress concentration at GBs.

Grain size and grain shape influence both the fracture mode and fracture resistance. In addition, this parameter is strongly related to the dispersoid content and degree of recrystallisation. It has been proven that a fine grain size is generally linked to a higher fracture toughness [251] and, in particular, it increases both the crack initiation and propagation energy [248]. The reason for the higher toughness is the better redistribution of stresses within the plastic zone [252]. Further, the fracture mode associated with a fine grain size is a combination of transgranular and intersubgranular along the LAGBs (Fig. 2.31) [16]. On the other hand, coarse grains promote brittle intergranular fracture [155]. It should be noted though that when the presence of PFZs is quite intense, such as in Al-Li alloys strengthened by the δ' phase, the finer grain size may have a negative effect on fracture toughness. This happens because the PFZs are connected and form long continuous networks where cracks can propagate more easily, leading to severe intergranular fracture [253].

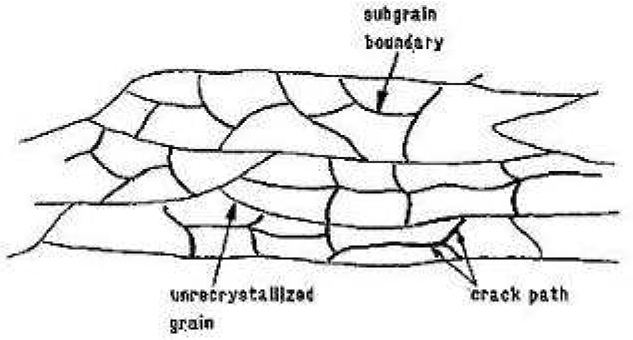

Fig. 2.31: Intersubgranular rupture in an unrecrystallised microstructure [16].

The effects of recrystallisation and texture need to be treated together since they are entirely interdependent; i.e. a higher degree of recrystallisation induces a weaker texture. It is unquestionable from a huge number of reports in the literature that unrecrystallised microstructures give better fracture toughness than recrystallised ones [16, 155, 248, 251, 254]. The reason is that in recrystallised microstructures, void nucleation on GBs and constituent phases is much easier than initiating slip in a neighbouring grain that might not be suitably oriented due to the high misorientation after recrystallisation [254]. Also, the fracture mode in unrecrystallised microstructures is almost entirely transgranular, while it changes to brittle intergranular in recrystallised ones [248, 254]. Equally, a stronger texture is more beneficial because of the lower misorientation between the subgrains that facilitates slip dissociation from one subgrain to another [16, 254].

Finally, the effect of the yield stress anisotropy should not be neglected. This phenomenon arises from the preferential orientation of grains and particles along the deformation direction, but also from strong texture. Al-Li alloys exhibit strong in-plane anisotropy, as their strength at 45^{o} off the RD is much lower than that for RD and TD [202]. Additionally, strength in TD is lower than in RD [101, 202] and also strength and fracture toughness were found to be superior in ND than in TD [255].

CHAPTER 3: Materials and Methods

3.1 Materials

All the materials used in this work were supplied by Alcan CRV. The main alloy investigated was based on AA2198, and was received in the form of hot-rolled 6 mm thick sheet, in two different conditions; the as-fabricated state right after hot-rolling (F temper) and after further processing which consisted of solution-treatment, a 2% stretch and natural ageing (T351 temper). Five different variants of the AA2198 base alloy were studied. Four of them had various levels of Zr and Mn and a standard homogenisation treatment (10 h ramp from RT to 505°C – 12 h holding at 505°C) while the alloy containing only Zr, was also available with a more complex homogenisation treatment (10 h ramp from RT to 500°C – 8 h holding at 500°C – 36 h holding at 532°C) which will be termed here as duplex homogenisation and, from here onwards, this alloy will be designated as 0.1Zr-D.

An as-cast slice of a very similar AA2050 alloy was also supplied to examine the effects of segregation and different homogenisation treatments on dispersoid distributions as well as the interaction of the two dispersoid families during homogenisation. The composition of the AA2050 is very similar to that of AA2198 and it was used in this study simply because there was no as-cast material of the latter alloy available. The nominal compositions and designations of all the materials are given in Table 3.1.

Table 3.1: Designations and nominal compositions of the alloys used; measured in wt% (Al is balance).

Alloy	Cu	Li	Mg	Ag	Zn	Zr	Mn
2198_0.1Zr-D	2.90-3.50	0.80-1.10	0.25-0.80	0.10-0.50	0.02	0.108	0.01
2198_0.1Zr	2.90-3.50	0.80-1.10	0.25-0.80	0.10-0.50	0.02	0.108	0.01
2198_0.1Zr-0.3Mn	2.90-3.50	0.80-1.10	0.25-0.80	0.10-0.50	0.02	0.111	0.31
2198_0.05Zr-0.3Mn	2.90-3.50	0.80-1.10	0.25-0.80	0.10-0.50	0.02	0.053	0.31
2198_0.4Mn	2.90-3.50	0.80-1.10	0.25-0.80	0.10-0.50	0.02	0.010	0.40
2050	3.20-3.90	0.70-1.30	0.20-0.60	0.20-0.70	<0.25	0.10	0.30

Impurities for AA2198 and AA2050: <0.10 wt% for each of Fe, Si, Ti.

3.2 Heat treatments

All heat treatments were carried out in an air-circulating furnace, since the surface oxidation of the samples was not of concern and the important results of this study are taken from the region near the mid-thickness of the sheet.

Ageing. An ageing temperature of 155°C was recommended by Alcan CRV and the times for which the samples were heated, were up to 100 h. This heat treatment consisted of an initial ramp stage to the desired temperature, at a heating rate of 75 K/h. In order to study the effects of overageing, a higher temperature was chosen so as to accelerate the kinetics of the phase transformations involved. Samples were heat treated at 200°C, again with a 75 K/h ramp stage initially, for times up to 250 h and then quenched in water.

Annealing. High temperature heat treatments were carried out to investigate all the phenomena related to recrystallisation behaviour and dispersoid distributions. Isothermal heating, followed by quenching in water, was carried out at 490°C, 505°C and 535°C. Extreme care is required during high temperature heat treatments. Due to the high diffusion rate of Li in Al [256], those regions near the free surfaces are depleted of Li to form surface oxides [257] thus, inevitably, the solute pinning effect on GBs is reduced in those regions due to the lower amount of solute atoms in solid solution. Thus samples cut from the centre of a larger specimen needed to be examined at the surface that was facing towards the interior and not at the one exposed directly to air in the furnace. This phenomenon becomes more intense with increasing time due to the extended diffusion that takes place. If this strategy is not followed, the recrystallised volume fraction will be much higher than the real value.

Homogenisation. Two different homogenisation treatments were employed in this study; the first comprised of a 10 h heating ramp from RT to 505°C, followed by holding for 12 h and the second with a 10 h heating ramp from RT to 535°C, followed by isothermal heating for 32 h. All samples were water-quenched when removed from the furnace.

3.3 Mechanical properties

3.3.1 Hardness tests

Background. Hardness on the macroscale can be measured via the indentation of a pyramid-shaped diamond tip into the material's surface under a constant applied load. For the Vickers hardness scale, the equation giving the hardness value is:

$$\mathrm{VHN} = 1.8544 \cdot \frac{P}{d^2} \qquad (3\text{–}1)$$

where P is the applied force (kgf) and d the average length of the indentation's diagonals (mm) [258].

Experimental. The Vickers method was employed to measure the hardness of as-received and aged materials with a load of 10 kg. The samples were slightly ground before the tests in order to remove the thin surface oxide layer which had been formed during manufacturing. Identification of the Vickers pyramid's edges on the metal surface becomes much easier in this way, thus increasing the accuracy in the determination of the final hardness. The final result for each condition was averaged from five measurements on the RD-TD plane. All measurements were carried out according to the ASTM standard E 92-82(2003)$^{\varepsilon 2}$ [258].

3.3.2 Microhardness tests

Background. Microhardness tests are useful for determining the hardness values of small areas for which macrohardness is not suitable. Due to the fact that it refers to a smaller scale of the microstructure compared to macrohardness, microhardness is consequently more sensitive to scatter since it requires a higher degree of homogeneity in the material. Vickers microhardness values can be calculated again by Eq. 3-1 [259].

Experimental. The tests were carried out as described in the ASTM standard E384-99$^{\varepsilon 1}$ [259]. Samples were cold-mounted in epoxy resin with their RD-ND plane on the surface, mechanically ground and slightly etched in Kellers reagent to reveal the GBs. All measurements were taken using a load of 0.2 kg, with five points averaged to obtain the final value for each condition.

3.3.3 Kahn-type tear tests

Background. The Kahn tear test can be employed to measure a material's notch toughness and crack propagation resistance in sheet with a thickness between 1 mm and 6.35 mm. The samples must have exact dimensions and can be cut in several orientations relative to the RD (Fig. 3.1a) [260].

A typical curve obtained from these measurements is shown in Fig. 3.1b. Only the first half of the curve is used for calculating toughness, as the second occurs after the crack has opened up completely and it actually corresponds to a tensile test of the almost fractured specimen. The information that can be extracted from such a graph is the unit initiation energy (UIE), the unit propagation energy (UPE), the unit total energy (UTE) which is the sum of UIE and UPE, and finally, the tear strength. These properties are calculated by Eqs. 3-2 to 3-5 [261].

$$\mathrm{UIE} = \frac{\mathrm{initiation\_area}}{\mathrm{b} \cdot \mathrm{t}} \qquad (3\text{–}2)$$

$$\mathrm{UPE} = \frac{\mathrm{propagation\_area}}{\mathrm{b} \cdot \mathrm{t}} \qquad (3\text{–}3)$$

$$\mathrm{UTE} = \mathrm{UIE} + \mathrm{UPE} \qquad (3\text{–}4)$$

$$\text{Tear strength} = \frac{4 \cdot F_{max}}{b \cdot t} \qquad (3\text{–}5)$$

where the "initiation area" corresponds to the area of the first half of the curve in Fig. 3.1b, before the vertical straight line, while the "propagation area" is the area after that line. b denotes the length from the notch tip to the flat edge of the specimen and t the sample thickness.

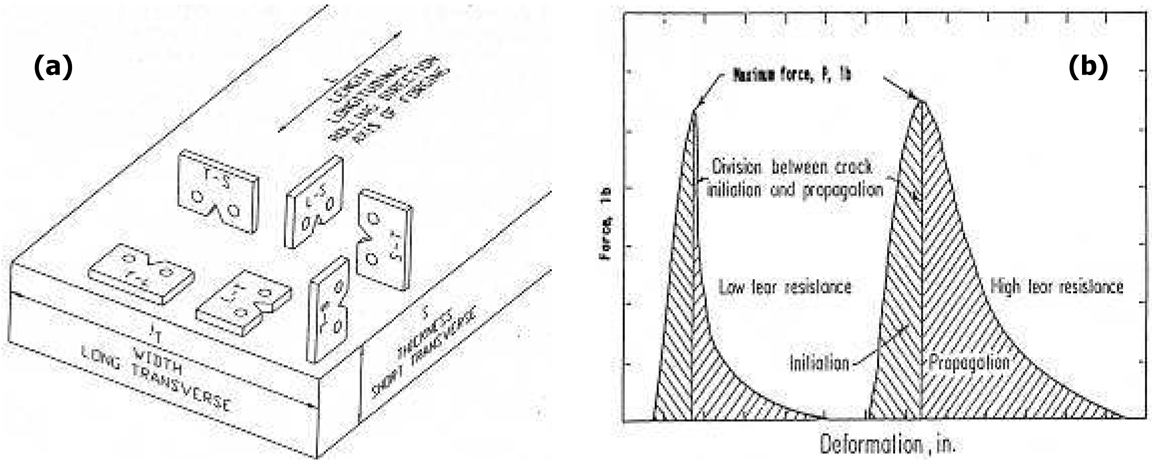

Fig. 3.1: a) Kahn tear test sample orientations relative to the rolling direction of a sheet. **b)** Typical load-displacement curve obtained from this type of test [260].

It is well-known that the fracture mode depends on specimen thickness and changes from plane strain to plane stress when moving from thick plates to thin sheet [262]. However, there is a limiting thickness value below which fracture toughness stops increasing and starts decreasing due to the smaller volume of the material that can withstand the plastic deformation. The plane stress mode in the present tests is related to specimen geometry as well, apart from the metallurgical parameters. Thus the measured energy values need to be converted into unit values so that they can represent a material's properties irrespective of its shape and size.

Experimental. Samples were prepared so that they were centred on the mid-thickness of the sheet, by reducing both of its surfaces down to the final thickness. The dimensions of the samples used in the present tests, were 57.15 mm x 36.51 mm x 2.95 mm, with a notch depth of 25.40 mm and a notch angle of 60^o. Specimens were cut from all five AA2198 alloys, each of them in three different conditions (T351, 14h@155^{o}C, 100h@155^{o}C) and in two different orientations relevant to the RD of the sheet, namely L-T and T-L (shown in Fig. 3.1a). Especially for the 0.1Zr and 0.1Zr-0.3Mn alloys, samples were prepared from a third orientation as well, which was 45^o from the RD. In the L-T orientation, the long axis of the specimen was parallel to the RD with the notch along the TD, while in T-L the sample lay perpendicular to RD with the notch along the RD. Before the tests, all samples were examined under the optical microscope to check if their notch tip had a smooth finish and optimum circularity (0.025 mm), in order to obtain consistent results [261]. A pre-load between 200-

400 N was applied and the extensometer was calibrated with a gauge tool. The strain rate was set to 1.3 mm/min.

3.4 Microstructural characterisation techniques

3.4.1 Transmission electron microscopy (TEM)

Background. The advantage of TEM is that it can give a wide variety of information about a sample, simply by changing either the operating mode, or the type of detector of different types of radiation (Fig. 3.2a).

During bright field imaging, which is the standard operating mode, a set of condenser lenses focuses the electrons emitted from the electron gun, so that they form a beam that will go through the specimen. The objective lens uses the electrons exiting the specimen at small angles relevant to the direct beam, to produce a diffraction pattern at the back focal plane and by using an objective aperture, a bright field image at the image plane (Fig. 3.2b) [263, 264].

The diffraction mode can provide information about the crystal structure of the material. By inserting the selected area diffraction aperture, information can be obtained by a smaller area on the specimen (Fig. 3.2b) which is why thin samples mainly reveal elastic diffraction contrast [264].

In dark field imaging, a diffracted beam is used to create the image instead of the transmitted beam. All the areas/features of the sample which are responsible for the presence of that particular beam can thus be viewed (Fig. 3.2c) [264].

Experimental. For TEM, discs 3 mm in diameter were spark-cut from the RD-ND plane (the same as that examined by SEM and EBSD). In certain cases where a comparison between surface and mid-thickness areas had to be carried out, specimens were cut from the RD-TD plane. The spark-cut discs were ground down to a thickness in the range 70-100 μm and polished until perforation with a Struers Tenupol-5 in a solution of 70% methanol - 30% nitric acid at 12 V. The solution’s temperature was maintained at -30^{o}C. The microscope used was a high resolution FEI Tecnai F30 FEG-TEM operating at 300 kV.

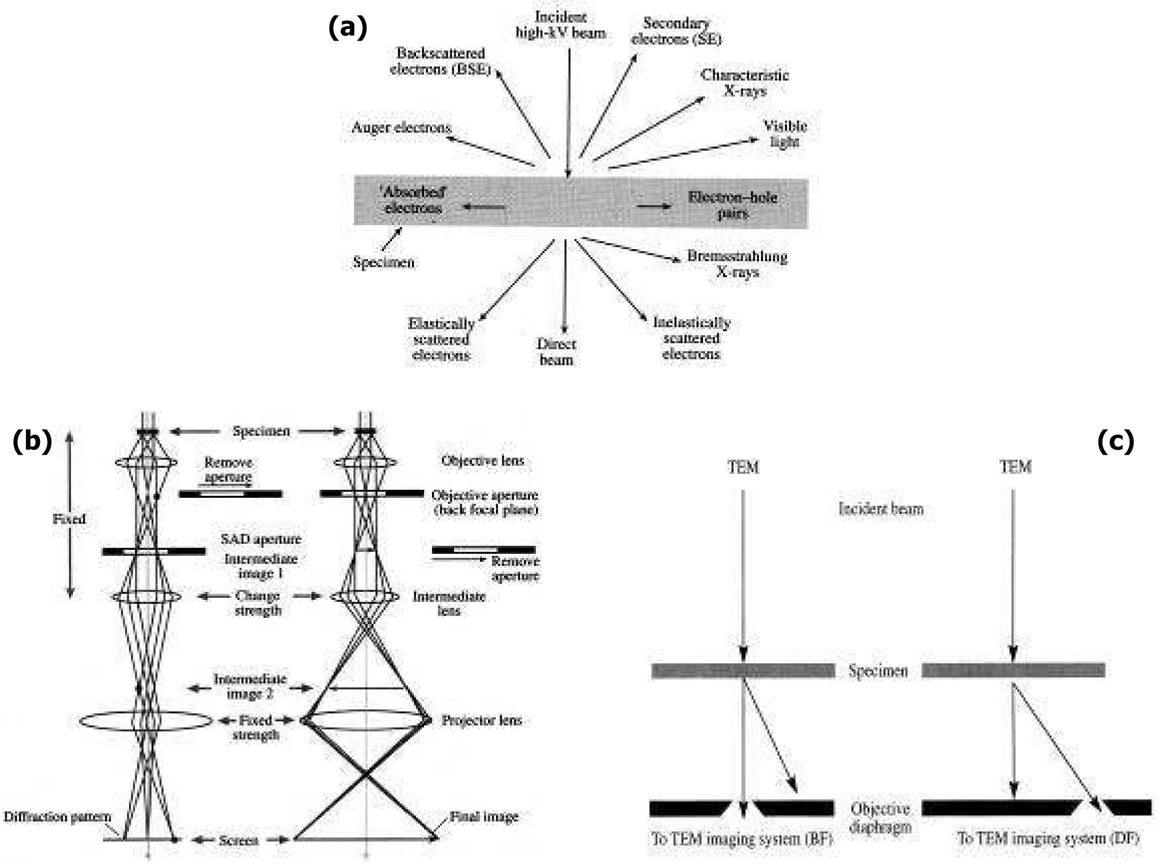

Fig. 3.2: Schematic diagrams showing: **a)** types of radiation emitted from a TEM sample, **b)** differences between diffraction and bright field mode, and **c)** differences between bright field and dark field imaging modes [263].

3.4.2 Scanning transmission electron microscopy (STEM)

Background. When this imaging mode is operating in the microscope, two pairs of scan coils, located between the second condenser lens and the upper objective pole piece, become activated and shift the beam across the specimen while scanning a certain area (Fig. 3.3a) [263].

An annular dark field detector is located around the bright field detector and can be used to collect only the electrons scattered further than a certain angle off the optical axis (Fig. 3.3b). A high angle annular dark field detector (HAADF) collects electrons incoherently scattered at angles above 50 mrad (~3^o), hence rendering possible the formation of images with atomic number contrast (Fig. 3.3b) [263].

Experimental. The FEI Tecnai FEG-TEM was also used in STEM mode. Pictures with atomic number contrast were taken using the high angle annular dark field detector. Pictures of dispersoid distributions and for size measurements were taken in this mode, since it is easier to distinguish the edges of the particles while, at the same time, avoiding various scattering effects from the matrix. Also, EDX analysis was carried out in this mode.

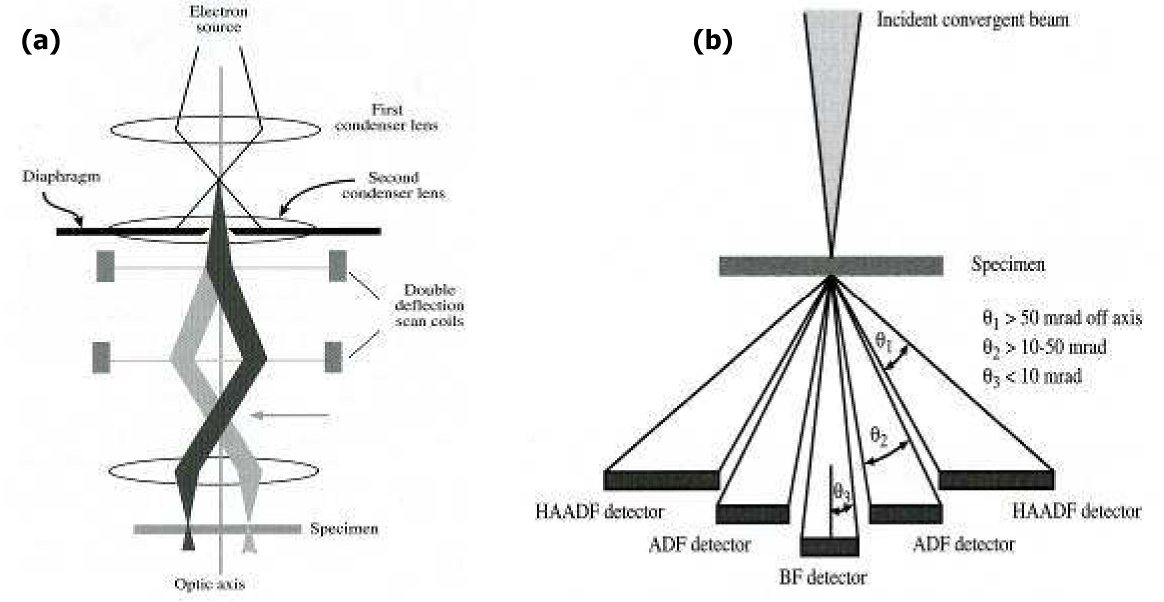

Fig. 3.3: a) Detailed diagram of the operation of STEM mode. **b)** Collection angles for bright field, annular dark field and high angle annular dark field detectors [263].

3.4.3 Energy dispersive x-ray spectroscopy (TEM/EDX)

Background. EDX systems are based on Si(Li) semiconductor detectors. The x-rays resulting from the interaction of the electron beam with the specimen are collected by the detector where they cause electron-hole pair formation. The energy generated by these pairs, depicts the energy of the particular x-ray which was responsible for its formation. The intensity of each of these interactions is recorded by a multi-channel analyzer (MCA), which allocates them into channels of the corresponding energies, and so the final spectrum is created.

Experimental. EDX line scans and spot analyses were both used in this work. Spot size is a key parameter for both processes and should be adjusted so that the dead time of detection is kept below 50%. In general, spot sizes in STEM mode between 8 and 11 have been used depending on sample thickness. Specifically for line profiles, a sufficient number of points need to be analysed (30-50) with an appropriate dwell time to adjust the counts (around 4000 msec). For maximum detection of x-rays, specimens have to be tilted to a 20^o angle. The data were processed via the ES Vision software of Emispec Systems Inc. For the quantification of the spectra, an empirical model was fitted to the background to exclude it from the composition calculations, since this type of background removal gave the optimum fit with the spectrum compared to the other available options.

3.4.4 Electron energy loss spectroscopy (EELS)

Background. The EELS technique is used to obtain information on the electrons from the transmitted primary beam which are inelastically and, inevitably, elastically scattered by the specimen. A spectrum of the number of electrons is measured as a function of the energy loss and shows how strongly the electrons have been scattered by the atoms in the material [263, 265].

The spectrometer is placed right under the viewing screen of the TEM so that the transmitted electrons can be classified using a magnetic prism, on the grounds of their energy loss within the sample (Fig. 3.4a) [263, 265].

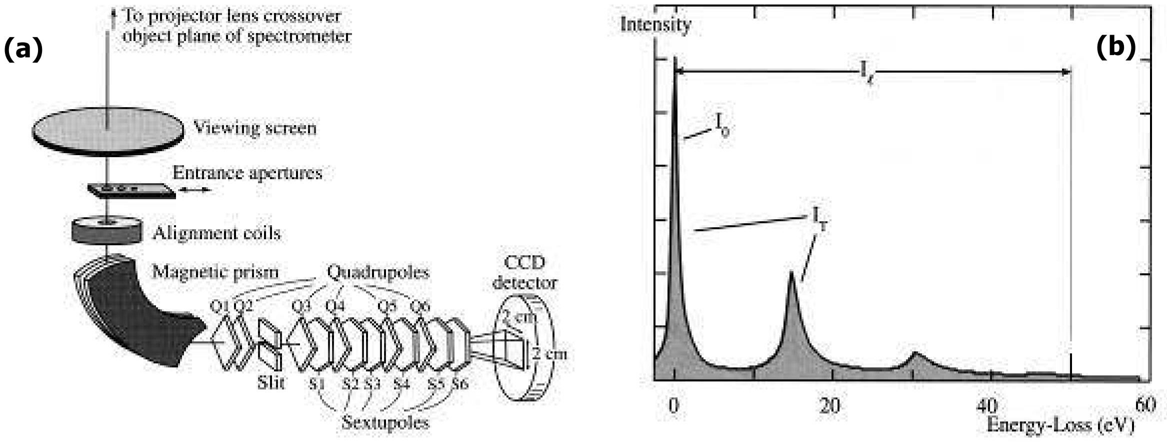

Fig. 3.4: a) Components of an EELS detector. **b)** Main features of a typical EELS spectrum [263].

The sample thickness can be calculated by the EELS spectrum through an experimentally straightforward method. However, several calculations are required that might incorporate errors in the final results. The equation for the sample thickness is [263]:

$$t = \lambda \cdot \ln\left(\frac{I_T}{I_o}\right) \qquad (3\text{–}7)$$

where λ is the mean free path of the material for the specific experimental conditions used, I_T is the total intensity of the spectrum (usually considered equal to I_l in Fig. 3.4b, which is the total intensity up to approximately 50 eV) and I_o is the intensity of the zero-loss peak, which corresponds to the elastically scattered electrons. The rest of the equations necessary for the calculation of the specimen's thickness are:

$$\lambda = \frac{106 \cdot F \cdot E_o}{E_m \cdot \ln\left(\frac{2 \cdot \beta \cdot E_o}{E_m}\right)} \qquad (3\text{–}8)$$

$$E_m = 7.6 \cdot Z^{0.36} \qquad (3\text{–}9)$$

$$F = \frac{1 + \frac{E_o}{1022}}{1 + \left(\frac{E_o}{511}\right)^2} \qquad (3\text{–}10)$$

where E_o is the microscope's operating voltage (keV), β the collection semiangle (mrad), E_m the average energy loss (eV), Z the atomic number of the material and F a relativistic correction factor (keV^{-1}) [263]. According to Williams and Carter [263], this is currently the simplest and most accurate method for TEM foil thickness measurement.

Experimental. This technique was used to measure sample thickness and subsequently calculate dispersoid volume fractions. An entrance aperture of 0.6 mm was chosen for the EELS detector and the energy resolution of the spectrum was set to 0.3 eV/pix. It has to be noted that only a condenser aperture with the maximum possible size was used (150μm), without an objective aperture. In this case the collection semi-angle can be taken equal to 100 mrad [263]. The thickness of 10 different areas, together with the corresponding number of particles in each, was averaged to obtain more statistically reliable results.

Table 3.2: Experimental values of the parameters used in the calculations for the mean free path and final value of the Al mean free path for the present conditions.

Z	E_o (keV)	E_m (eV)	F (kev^{-1})	β (mrad)	λ (nm)
13	300	19.135	1.058	100	199

3.4.5 Electron tomography

Background. Electron tomography has been developed to bridge the scale gap between the two commonly used techniques of atom probe field ion microscopy and x-ray tomography [266].

In electron tomography, a series of images is acquired by tilting the TEM sample by a small angle between the two tilt maxima. All the images need to be aligned very accurately along the same tilt axis so that the final 3-D image is not distorted. For the reconstruction stage, the "weighted backprojection" method is employed. This method is based on compiling all the acquired 2-D images into a 3-D reconstructed volume. The term "weighted" refers to a filter used in this process to distribute the data more evenly. As seen in Fig. 3.5, the straight lines represent the planes of each image taken, so when they are compiled there are too many data points near the centre and far fewer near the edge of the reconstructed volume. The applied filter reduces the number of central data points used in the reconstruction process in order to increase the precision of the final 3-D image [267, 268].

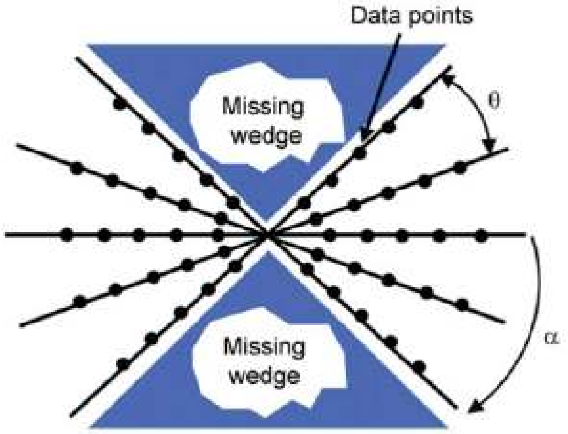

Fig. 3.5: Illustration of electron tomography data collection in Fourier space. α is the maximum tilt angle of the specimen and θ the angular spacing. The "missing wedge" shows the gap in the data due to the restrictions in specimen tilt within the TEM column.

Experimental. Electron tomography was carried out at the Electron Microscopy Group in the Department of Materials at the University of Cambridge, with the assistance of Professor Paul Midgley and Dr Juan-Carlos Hernandez-Garrido. For this type of experiment, sample preparation is quite crucial as the hole on the specimen needs to be located as close to the centre as possible. This will prevent any shadowing effects on the area of interest. A specialised TEM rod was used, that can tilt the specimen to very high angles which are impossible to reach with conventional holders. The specimen was tilted between -74° and +76° and a STEM picture was taken every 2°. The operating voltage of the microscope for these experiments was 200 kV, applying an extraction voltage of 4300 V and a spot size 7 in STEM mode. All the STEM pictures were combined to form a tilt series which was then aligned using the FEI software Inspect3D before volume reconstruction took place. Following reconstruction, the final stage is processing the data with the Amira software to obtain the 3D images.

3.4.6 Scanning electron microscopy (SEM)

Background. SEMs resemble TEMs in several aspects, but their main difference is that the former are suitable for studying surfaces of bulk specimens, while the latter are employed to obtain information from the interior of thin foils. Regarding its operation, the electron beam is moved across the sample surface by a set of coils and scans that particular area. Rays of inelastically scattered electrons can be collected by appropriate detectors, depending on the information sought. Secondary electrons are mainly produced by the incident electron beam, which also generates a lower level of backscattered electrons. Each type of electrons is collected by separate detectors [269].

Experimental. Samples were cut from the RD-ND plane of the sheet and electropolished in a solution of 70% methanol - 30% nitric acid at 12 V and a temperature of -30°C. The immersion time varied with each sample's condition and processing history; annealed samples were kept in the solution for approximately 30 sec while as-fabricated samples, in as-cast or as-hot-rolled form, were treated only for 10-15 sec. The microscope used was an FEI Sirion FEG-SEM.

The majority of pictures used for microstructural observations were taken in BSE mode at a voltage of 8 kV. SE mode was mainly employed to look at fracture surfaces. The applied voltage was 15 kV and the spot size used in this case was higher than in BSE mode.

3.4.7 Energy dispersive x-ray spectroscopy (SEM/EDX)

Background. Although the set-up for the EDX system in a SEM is different than in a TEM, the details of operation are exactly the same as described in §3.4.3.

Experimental. Large constituent phases inside dimples on the fracture surfaces of tear test samples were analysed by mapping their elemental composition. The microscope used for EDX measurements was a Philips XL30 FEG-SEM operating at a voltage of 20 kV.

3.4.8 Electron backscatter diffraction (EBSD)

Background. The experimental set-up required for EBSD measurements is illustrated in Fig. 3.6. The specimen is tilted to 70^o from the horizontal so that a higher number of electrons are backscattered. A back diffraction Kikuchi pattern, corresponding to each point of measurement, is formed by these electrons and it is captured by a low-light video camera while the background is simultaneously subtracted. The Kikuchi pattern is then processed by the EBSD software; indexing takes place to find the best solution that fits the pattern and finally a file with the data of the measurement is saved [270, 271].

Experimental. EBSD data were analysed to extract information on grain size and shape as well as textures. For the former, two maps were acquired for each condition with a varying step size and magnification depending on the condition. A 2 μm step at a magnification of x100 was used for the as-received T351 materials, a 1 μm step at x200 for the as-received F temper materials, while for all the annealed samples a 3 μm step at x100 was used. For texture measurements in annealed samples, a 10 μm step size was used at a magnification of x50, but solely for a narrow band corresponding exactly to the mid-thickness of the sheet, so as to exclude the through-thickness texture gradient.

All samples were examined in the RD-ND plane after being electropolished. A working distance of 10 mm was chosen so as to enhance the detection of diffracted electrons, since short working distances tend to place the direction of maximum scattering close to the centre of the camera's lens [270]. The microscope used, was again the FEI Sirion FEG-SEM operating at 20 kV.

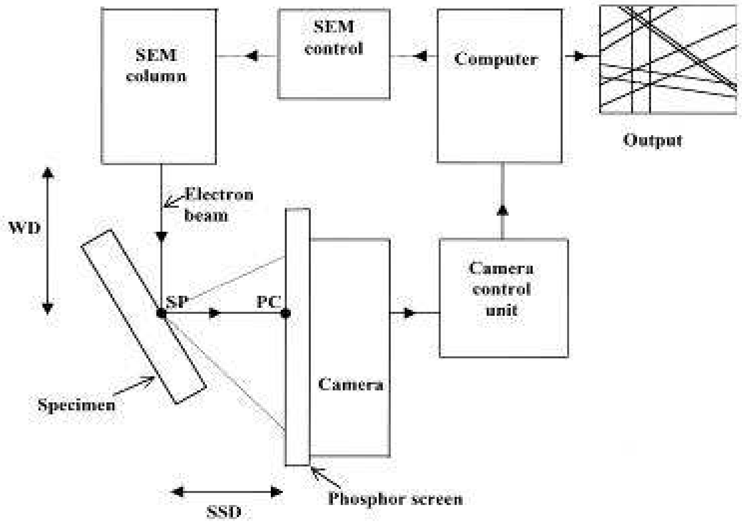

Fig. 3.6: Experimental set-up for EBSD measurements [270].

3.4.9 Electron probe microanalysis (EPMA)

Background. The main component for the operation of the electron microprobe is the wavelength dispersive spectrometer (WDS). Scan coils are used to move the beam across the sample's surface and only emitted x-rays of the desired element are allowed to go through the entrance slit which is located at point S in Fig. 3.7. This slit narrows the amplitude of the x-rays so that they hit the analysing crystal at specific angles. Subsequently, those x-rays that are diffracted according to Bragg's law will reach the detector, passing through the exit slit at point D in Fig. 3.7, and their intensity will be recorded as a function of wavelength/energy/Bragg angle. The detector, crystal and specimen have to be located on specific points of the periphery of the Rowland circle for the principle of operation to come in effect. The advantage of this technique is the ability to define with high accuracy the intensity and energy of the emitted x-rays from a sample, thus yielding a quite reliable measurement of composition. For the quantification of the results, the ratio of the intensity of a chosen element in the specimen over that of the same pure element, is considered to be a function of the mass concentration of the analysed element [269, 272].

Experimental. This technique was used to measure elemental segregation along the ND of the sheet. The four main AA2198 alloys in T351 condition with the standard homogenisation processing were measured. Line scans were set up starting at 30 μm from the sheet surface down to the mid-thickness with a 100 μm step. The step size used was the maximum possible at a voltage of 15 kV. All samples were mounted in araldite epoxy resin to protect the vacuum inside the microscope's chamber. To ensure higher accuracy of the results, each line scan was set far from any large constituent phases. The instrument used was a Cameca SX100 electron probe microanalyser.

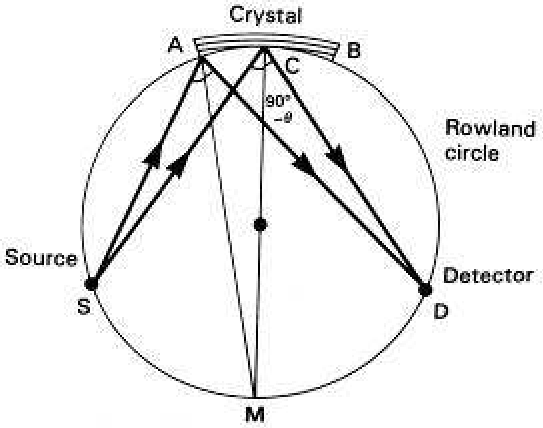

Fig. 3.7: Schematic illustration of the geometrical arrangement of a spectrometer's components on a 'Rowland circle' [272].

CHAPTER 4: Overall Influence of Joint Zr-Mn Additions on the AA2198 Sheet Grain Structures

4.1 Introduction

The present chapter gives an overview of the general microstructural modifications that occur in the final commercial product form (T351 condition), stemming from the coexistence of the two dispersoid families. In this condition, the sheet has been solution heat treated for 20 min at 505^{o}C, stretched to a strain of 2% and naturally aged. As mentioned previously in §2.2.4, the combined addition of Zr and Mn was expected to lead to an improvement in the recrystallisation resistance of plate products. Based on this logic, these two elements were added together in the present AA2198 alloy sheet, but the results were not exactly as anticipated; inhibition of grain growth was achieved, but recrystallisation resistance deteriorated compared to the alloy containing only Zr. An unexpected, hitherto unidentified interaction between the two dispersoid-forming elements was responsible for this phenomenon, which significantly altered the final microstructure. An overview of these effects is presented in the following section.

4.2 Grain structures in the final sheet form (T351)

The most interesting observation in the as-received T351 materials was the change in volume fraction of recrystallisation as a function of the dispersoid content. This provided the initial evidence of a possible interaction between Zr and Mn when these two elements are added together. There was a rather strange phenomenon regarding the GB pinning behaviour, since the combined Zr-Mn addition was effective for reducing grain size, but not for inhibiting recrystallisation. Fig. 4.1 clearly shows that the recrystallised volume fraction in the 0.1Zr-0.3Mn alloy at mid-thickness was fairly high (13%), while in the 0.1Zr alloy it was minor (1.5%). The value for the 0.1Zr-D alloy shows that even a coarser Al_3Zr distribution could pose a more successful barrier to recrystallisation (V_f=5%). A Zr content of 0.05 wt% was not sufficient to prevent recrystallisation and a large volume of the material ended up with a recrystallised microstructure. At the other extreme of adding only Mn, the microstructure became completely recrystallised in the presence of 0.4 wt% Mn. In general, recrystallisation was more pronounced near the sheet surface.

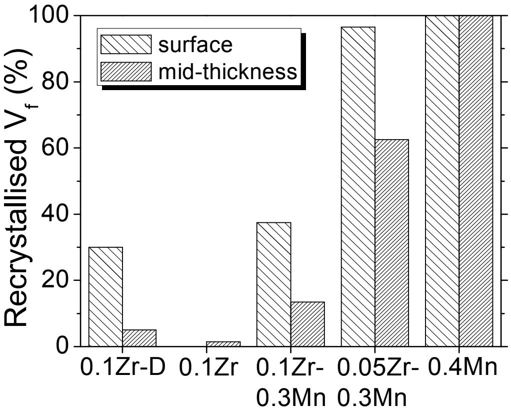

Fig. 4.1: Recrystallised volume fraction at the surface and mid-thickness plane of the sheet for all alloys in the T351 condition.

The microstructures in this condition depend strongly on the presence of dispersoids which provide the means to control grain growth during annealing treatments, as well as the extent of recrystallisation [14]. The pinning ability of dispersoids is determined by their size, volume fraction, distribution and coherency [14]. Hence, it was expected that the finer and coherent Al_3Zr phase would be a more potent recrystallisation inhibitor compared to the much larger and incoherent $Al_{20}Cu_2Mn_3$ phase [16]. Indeed, from Fig. 4.2 it is clear that the addition of 0.1 wt% Zr, with or without the presence of Mn, ensured that the fibrous grain structure resulting from hot rolling was maintained even after solution treatment, with insignificant levels of recrystallisation. Even a coarser Al_3Zr distribution in the 0.1Zr-D alloy, produced by a more extended homogenisation treatment with a second stage at a higher temperature (§3.1), had the same effect. Lowering the Zr content to 0.05 wt% led to a significant decrease in the GB pinning ability in the 0.05Zr-0.3Mn alloy, which was 62.5% recrystallised. In the case when no Zr was added at all, the sole presence of Mn was not sufficient to restrict GB motion during solution treatment so the outcome was a coarse and fully recrystallised grain structure, as shown in Figs. 4.2i,j for the 0.4Mn alloy. In all cases the grains remained highly elongated along RD due to the high strain imposed during rolling. For the slightly recrystallised alloys, the effects of the various dispersoid contents on the microstructures and the extent of recrystallisation are much clearer in the EBSD maps near the surface of the sheet than at mid-thickness.

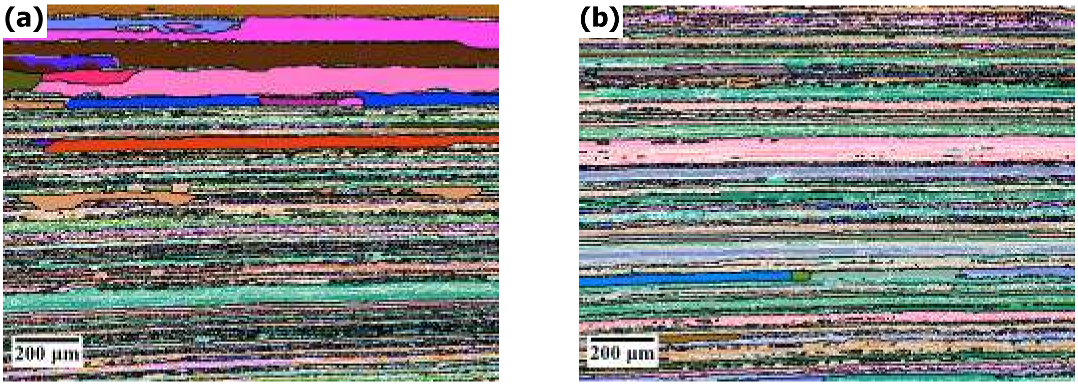

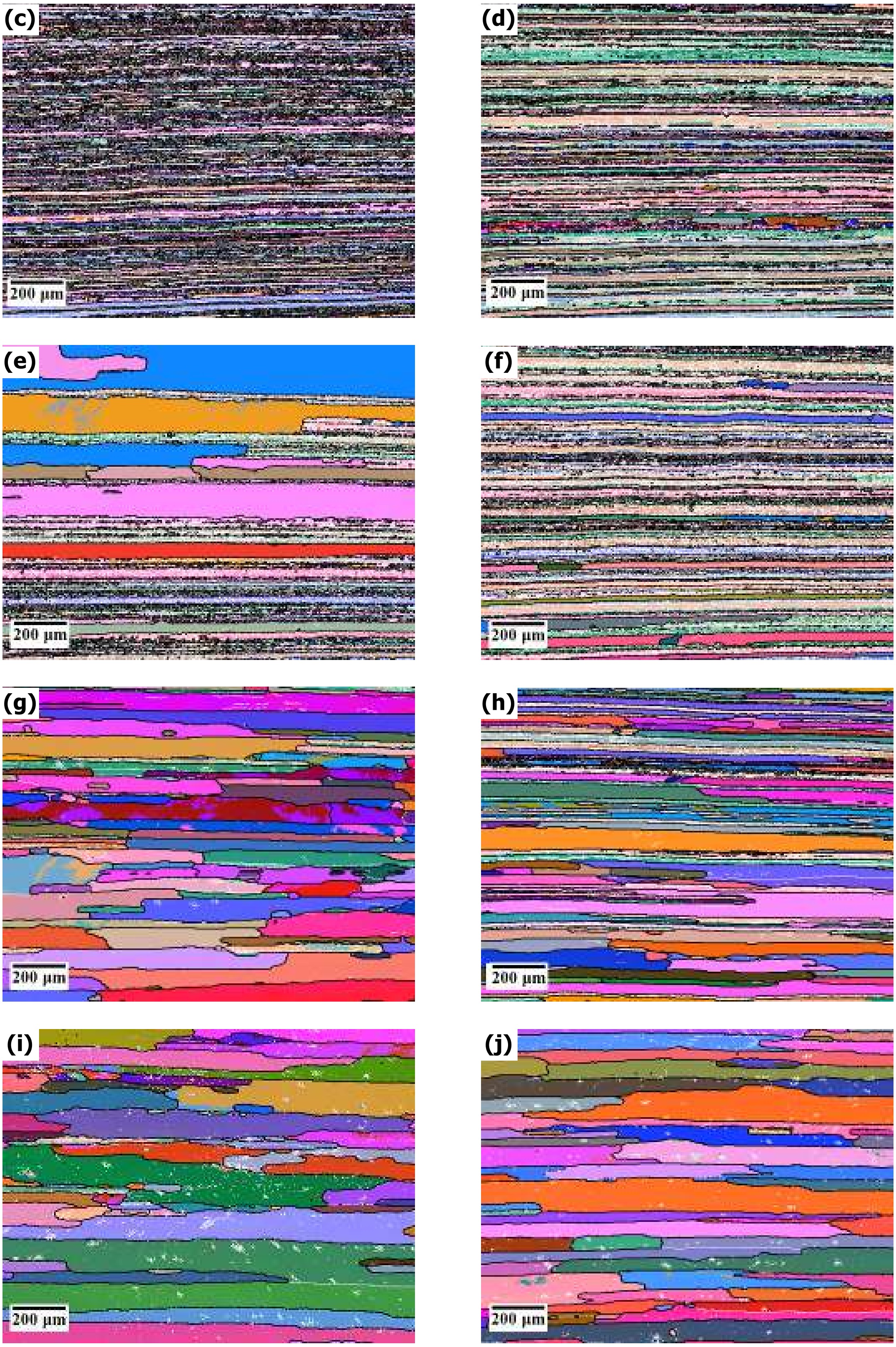

Fig. 4.2: EBSD maps showing the grain structure morphology at the surface (left) and mid-thickness (right) planes of all alloys in the T351 condition (orientations are represented by Euler colours): **a,b)** 0.1Zr-D, **c,d)** 0.1Zr, **e,f)** 0.1Zr-0.3Mn, **g,h)** 0.05Zr-0.3Mn, and **i,j)** 0.4Mn.

Regarding the substructure present in the unrecrystallised regions, the 0.1Zr and 0.1Zr-0.3Mn alloys exhibited typical hot-rolled microstructures that consisted of well-defined subgrains (Fig. 4.3a,b) with a low remnant density of free dislocations in their interiors (Fig.

4.3c). Most of the dislocations had formed subgrain boundaries. Subgrains in the 0.1Zr alloy were longer and more elongated along the RD, compared to the 0.1Zr-0.3Mn alloy. The subgrain aspect ratio values at the mid-thickness plane of the sheet were measured to be 5.1 and 2.4 respectively for the two alloys. This difference was caused by a difference in the pinning pressures depending on the dispersoid family present and their respective distribution, which defines how they interact with the recovered substructure. More details will be given on this topic in Chapter 5 and once the dispersoid volume fractions are discussed in §4.4.

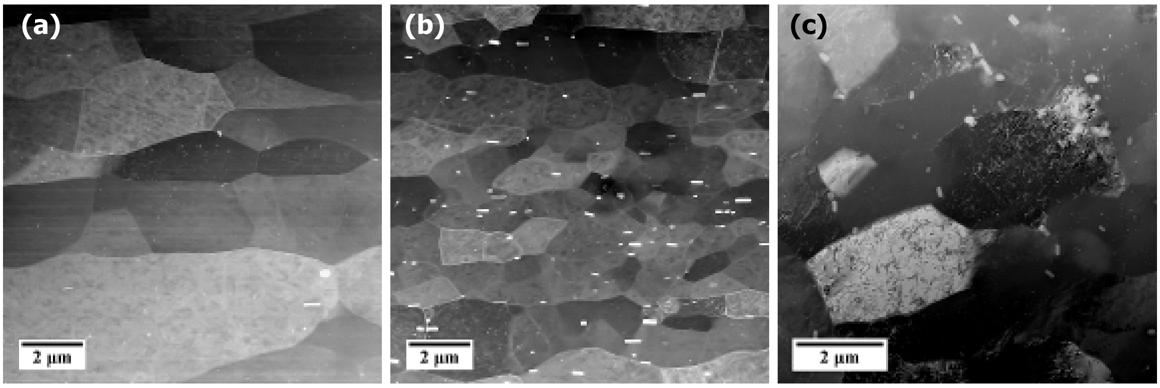

Fig. 4.3: STEM-HAADF images showing subgrain structures: **a)** well-defined subgrains in the 0.1Zr alloy, highly elongated along RD, **b)** well-defined subgrains in the 0.1Zr-0.3Mn alloy with smaller aspect ratio, and **c)** two subgrains in a two-beam condition in the 0.1Zr-0.3Mn alloy, exhibiting strong diffraction contrast from free dislocations in their interior.

Quantified data from EBSD measurements aided in the comparison of all grain structures in the T351 temper. Only maps taken at the sheet's mid-thickness were considered for these results. The HAGB spacings in all alloys clearly illustrated the previously observed trends. The average HAGB spacing and LAGB spacing along ND appeared to change in a similar fashion as a function of the dispersoid content (Fig. 4.3a). The 0.1Zr-0.3Mn alloy had the finest grain spacing of all, equal to 5.8 μm, followed by the 0.1Zr alloy with an average HAGB spacing of 7.4 μm. This difference becomes more notable if one considers that the recrystallised volume fraction in the former alloy was higher than in the latter (Fig. 4.4). Thus, even with a significant number of coarse recrystallised grains being included in the calculations, the final HAGB spacing value was still smaller. The coarser Al_3Zr distribution in the 0.1Zr-D alloy was not as effective as the previous two alloys, so the resulting HAGB spacing was slightly larger (8.2 μm). A much higher increase was observed when the amount of Zr was lowered to 0.05 wt% (18.4 μm) and when no Zr was added, the HAGB spacing increased even further, as was the case for the 0.4Mn alloy (50.6 μm). It has to be noted here that the LAGB spacing for the 0.4Mn alloy does not appear in the graph in Fig. 4.3a because there was no defined substructure present in this alloy.

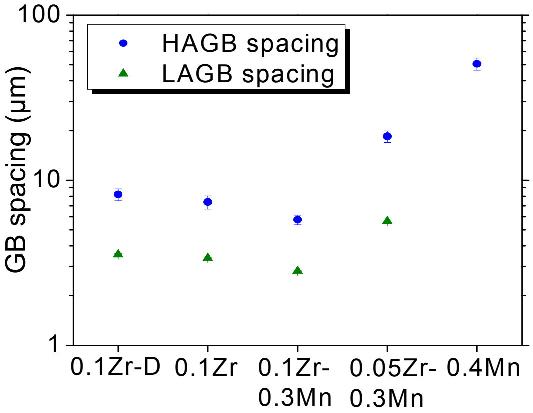

Fig. 4.4: HAGB and LAGB spacing along ND measured from EBSD maps in the T351 condition for all five alloys.

The apparent contradiction that the Mn-dispersoids are able to restrict grain growth, but also less effective in limiting recrystallisation has been reported before, as mentioned in §2.2.4 [16], but no explanations were given. At this stage, no safe explanation can be given for this observation. Details will be given later in this thesis after the dispersoid distributions have been thoroughly examined.

4.3 Textures in the T351 temper

By preventing recrystallisation, the dispersoid content plays a very important role in the textures of the AA2198 alloys. Since each of the Zr- and Mn-dispersoids offer different boundary pinning effects, the textures of the final products will strongly depend on the extent of recovery and recrystallisation that took place during the processing stages. In general, unrecrystallised materials have stronger textures as compared to recrystallised ones [201].

Texture maps of the present alloys were obtained using EBSD and are presented in Fig. 4.5. Since 0.1 wt% Zr was a sufficient amount to inhibit grain growth and recrystallisation up to a certain level, the microstructures of the respective alloys consisted mainly of β-fibre components (Brass and S, depicted in red and light blue respectively).

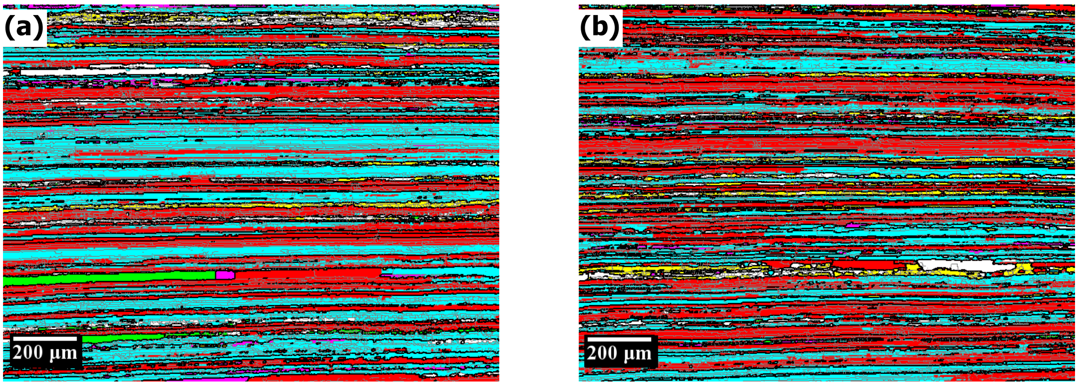

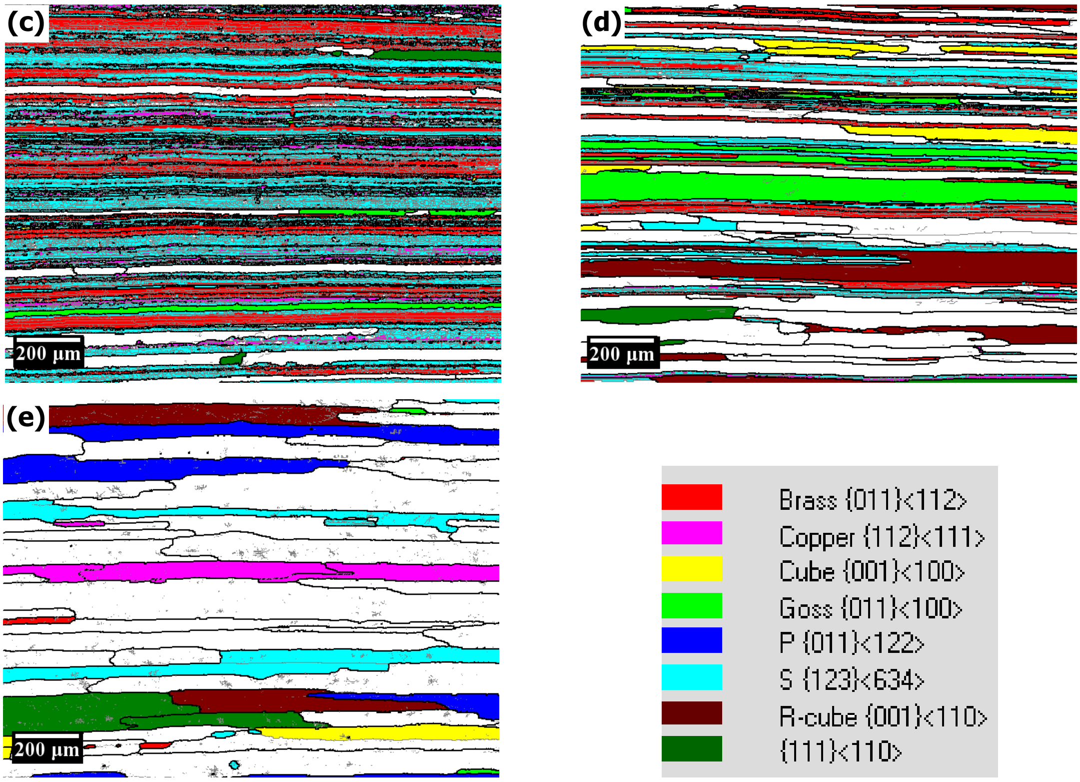

Fig. 4.5: EBSD texture maps of all alloys in the T351 temper: **a)** 0.1Zr-D alloy, **b)** 0.1Zr alloy, **c)** 0.1Zr-0.3Mn alloy, **d)** 0.05Zr-0.3Mn alloy, and **e)** 0.4Mn alloy. The legend explains which colour corresponds to each of the orientations measured. Grains appearing in white represent orientations other than those mentioned in the legend.

The strength of texture of the T351 alloys demonstrated a direct dependence on the recrystallised volume in the microstructure. The 0.1Zr alloy with the lowest volume fraction of recrystallisation, illustrated the strongest texture of all, as can be seen from the {111} pole figure in Fig. 4.6b. This pole figure exhibited the least orientation spread and the maximum intensity was 19.05 times the random distribution. The pole figure of the 0.1Zr-D alloy (Fig. 4.6a), the second most resistant alloy to recrystallisation, again showed a strong orientation density in the β-fibre positions, but this time there were also some randomly distributed orientations representing recrystallised grains. Additionally, there was a slightly higher orientation spread at the positions of the main texture components. A further increase in the recrystallised volume fraction led to a weaker texture in the 0.1Zr-0.3Mn alloy (max: 14.54). Several orientations outside the locations of the main β-fibre components were present (Fig. 4.6c) and corresponded to the recrystallised grains, which mainly had random orientations. Finally, the two alloys with the highest recrystallised volume fractions were characterised by a mostly random texture (Figs. 4.6d,e). The residual deformed microstructure in the 0.05Zr-0.3Mn alloy gave orientations in the β-fibre regions on the pole figure. However, their intensity was low due to the small number of these grains. On the other hand, the 0.4Mn alloy shows the dominant orientations at random positions as a consequence of the fully recrystallised microstructure. The maximum intensity is 5.40, far lower than of the mainly unrecrystallised Zr-containing alloys.

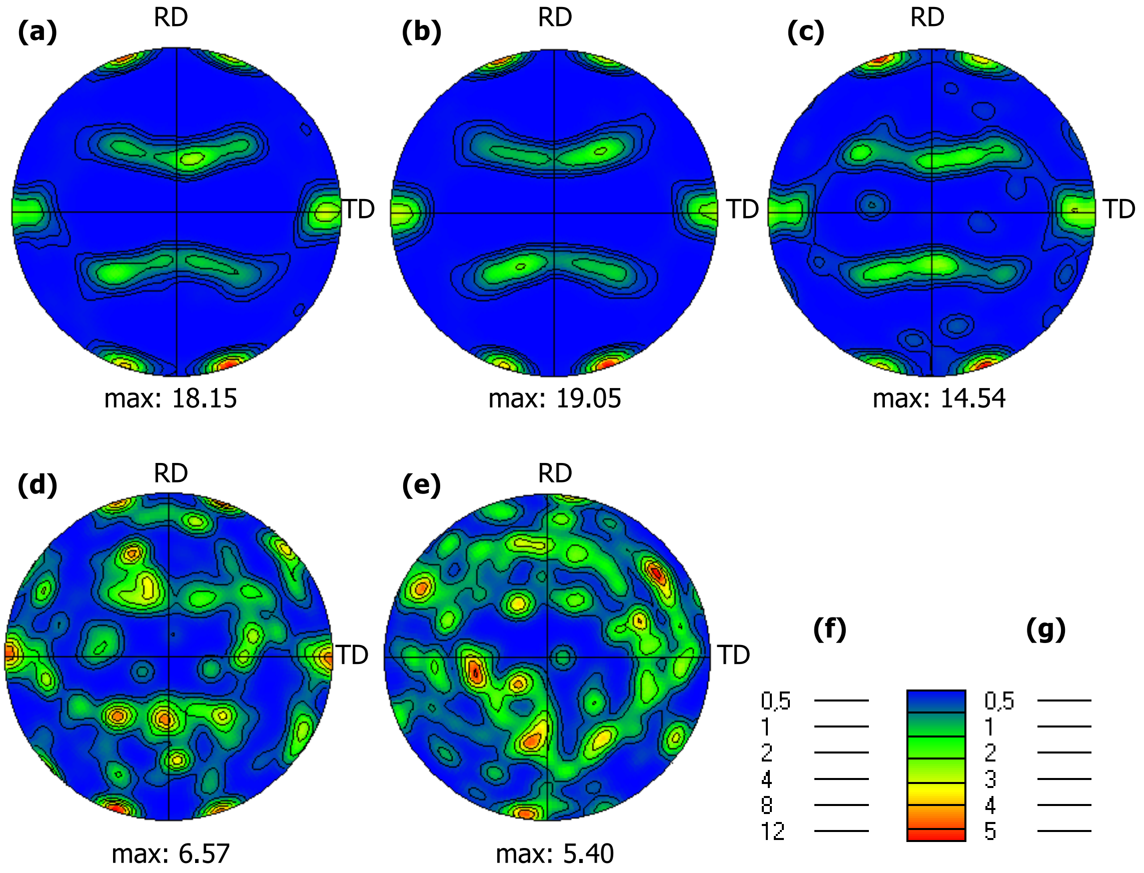

Fig. 4.6: {111} pole figures of all alloys in the T351 temper: **a)** 0.1Zr-D alloy, **b)** 0.1Zr alloy, **c)** 0.1Zr-0.3Mn alloy, **d)** 0.05Zr-0.3Mn alloy, **e)** 0.4Mn alloy, **f)** contour levels for the images a,b,c, and **g)** contour levels for the images d,e.

Quantification of the texture maps of Fig. 4.5 yielded the graphs in Fig. 4.7, where the volume fraction of each texture component was plotted for all five alloys. As already discussed, the deformation texture mainly consisted of β-fibre components, so the alloys with a lower amount of recrystallisation were expected to have higher volume fractions of Brass, S and Copper. Indeed, the three alloys containing 0.1 wt% Zr exhibited very high amounts of Brass and S, but very few grains had other orientations. From the minor components, Copper and Cube were the ones most often seen (Fig. 4.7a). The 0.05Zr-0.3Mn alloy had quite low volume fractions of deformation texture components due to its largely recrystallised microstructure. Although some differences seemed to exist in the relative amounts of Brass and S depending on each alloy, it would be dangerous to draw conclusions at this stage regarding the influence of dispersoid content on these texture components. It is likely that the recrystallised grains selectively consumed certain orientations, but this will be discussed together with the recrystallisation mechanisms in §6.4.

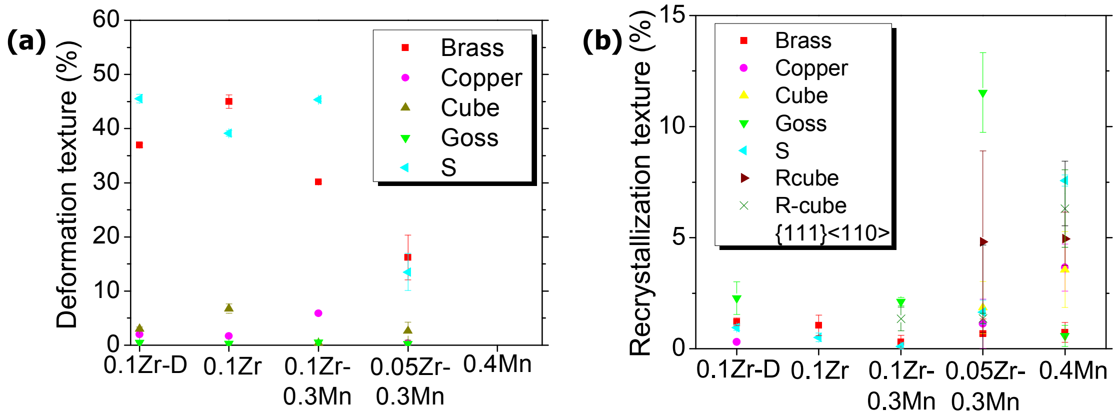

Fig. 4.7: Volume fractions of texture components, quantified from EBSD maps for each alloy in the T351 condition: **a)** deformation texture, and **b)** recrystallisation texture.

The deformation textures in the present AA2198 sheet are characteristic of Al-Li alloys. Typical Al-Li textures consist of S, Brass and Copper components, the specific amount of each depending on the thermomechanical processing conditions. In general, S is a high energy component that forms during cold-rolling [103] and Brass is favoured by hot-rolling [103, 225-227].

The results of Hales and Hafley [224] for an AA2195 plate 7.5 mm thick were similar for the 0.1Zr alloy of this work, since there was more Brass than S and only trace of Copper present. Both these alloys had a lamellar grain structure and highly elongated grains. Other results similar to the 0.1Zr-D and 0.1Zr-0.3Mn alloy here, were those of Cho et al. [101] for a AA2195-T8 plate and of Contrepois et al. [97] for an AA2050 alloy. In both cases, more S than Brass was reported. The sole discrepancy from the current work was the paper of Decreus et al. [12] on an AA2198 sheet (same as the 0.1Zr alloy here) where a Brass texture prevailed with a secondary component {124}<112>, also termed R. These findings are rather unexpected since the R component is a recrystallisation texture component [218] and also, there is an inexplicably huge difference from the results of the present thesis, where the same material was studied.

On the other hand, the recrystallisation textures did not show any particular pattern of preferential formation since there was a weak recrystallisation texture and the number of the analysed recrystallised grains was very low. Hence the recrystallised grains in the T351 alloys appeared to be of random orientations. This is clear from the really low volume fractions in every case (Fig. 4.7b). The recrystallisation component with the highest volume fraction was Goss in the 0.05Zr-0.3Mn alloy but, because of the low number of new grains, this might not be representative of the whole sample volume. More details on textures will be presented in §6.5.

4.4 Effect of manganese on the Al_3Zr distribution

The increased recrystallised volume fraction with the coexistence of Zr and Mn was ascribed to a change in the Al_3Zr distribution. The alteration of the Al_3Zr distribution was observed with the aid of TEM. STEM-HAADF images were taken so that the particles could be distinguished from the matrix and EELS was used to calculate the sample thickness (§3.4.4). Fig. 4.8 clearly shows the reduction in the number of Al_3Zr dispersoids in the 0.1Zr-0.3Mn alloy compared to the 0.1Zr alloy despite the same Zr concentration. Due to the heterogeneous distribution of this phase, both areas were chosen to contain a dispersoid band that typically has a higher volume fraction than the surrounding regions. Although the TEM specimen in the area of Fig. 4.8a for the 0.1Zr alloy was slightly thinner than that of Fig. 4.8b for the 0.1Zr-0.3Mn, the number of particles in it was much higher than for the latter. The measured number densities in both areas in Figs. 4.8a,b were 390 and 131 respectively. The reason for this reduction in number density due to an interaction between zirconium and manganese is very important and will be further discussed in the whole of Chapter 5 along with more detailed measurements on dispersoid distributions.

Thus the addition of 0.3 wt% Mn together with 0.1 wt% Zr in the AA2198 alloy, led to a large decrease in the number density of the Al_3Zr dispersoids compared to the 0.1Zr alloy. Since the Al_3Zr dispersoids can pin GBs more efficiently compared to $Al_{20}Cu_2Mn_3$ ones, the distribution of this phase will therefore greatly influence the recrystallisation behaviour. Consequently, a lower resistance to recrystallisation is expected from a lower number density of the more efficient Al_3Zr pinning particles.

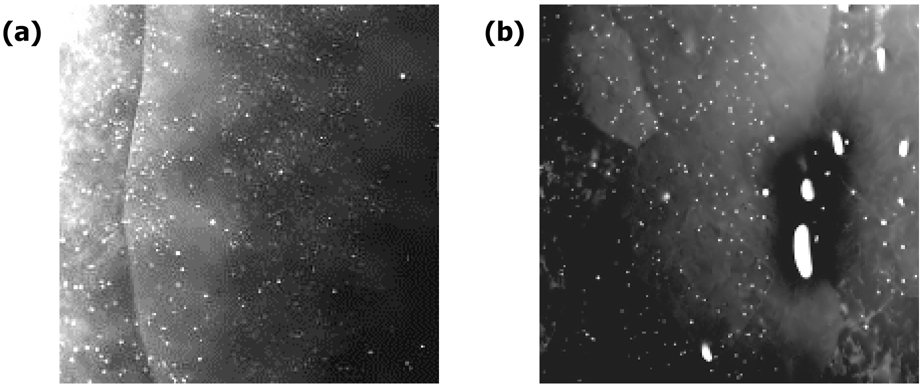

Fig. 4.8: Comparison of Al_3Zr number densities in areas of similar thickness (STEM-HAADF images at the same magnification): **a)** 0.1Zr alloy (thickness: 246 nm), and **b)** 0.1Zr-0.3Mn alloy (thickness: 303 nm).

4.5 Summary of the general effects of joint Zr-Mn additions

Examination of the AA2198 alloy in the T351 temper verified the superiority of Zr over Mn, both as grain growth and recrystallisation inhibitor. The appropriate level of Zr required for this role was 0.1 wt%, since a reduction to 0.05 wt% led to undesired recrystallisation. In contrast, the levels of Mn tested in this work (0.3 and 0.4 wt%) were not sufficient to restrict either grain coarsening or recrystallisation.

A novel phenomenon was observed for the 0.1Zr-0.3Mn alloy which exhibited the lowest grain growth of all alloys, but had a relatively high recrystallised volume fraction (13%). In comparison, the 0.1Zr alloy containing the same amount of Zr, showed a slightly coarser substructure but recrystallised only marginally (1.5%). A coarse Al_3Zr distribution still produced a lower extent of recrystallisation at mid-thickness and near the surface compared to the 0.1Zr-0.3Mn alloy.

The innovative finding in this study was the identification of an interaction between Zr and Mn when these two dispersoid-forming elements were added together. The presence of Mn decreased the volume fraction of the Al_3Zr phase, which appears to be the dispersoid family controlling recrystallisation more effectively [132]. This led to the increased recrystallised volume fraction, since new grains nucleated in those areas. However, the ability to inhibit grain growth remained unaffected from this interaction. This phenomenon will be explained in the following chapters.

In addition, the combined presence of Zr and Mn resulted in a weaker texture due to the higher extent of recrystallisation. Prevalence of either S or Brass deformation components showed a possible dependence on the dispersoid type present. Recrystallised grains were mainly of random orientations.

CHAPTER 5: Dependence of Dispersoid Distributions on Zr and Mn Content

5.1 Introduction

It is essential, before discussing recrystallisation resistance and related issues, to start with a detailed analysis of the dispersoid distributions in all the experimental alloys. In Chapter 4 it was shown that the combined addition of Zr+Mn caused an unexpected interaction of these two elements, resulting in a reduction in the number density of the Al_3Zr dispersoids in the 0.1Zr-0.3Mn alloy, and a lower recrystallisation resistance compared to the alloy containing only Zr. Here, will be examined how exactly both the Zr- and Mn-dispersoid families are affected by the coexistence of Zr and Mn in the same alloy, during the material's processing stages.

The analysis of the dispersoid distributions in the present chapter starts by analysing their chemical composition to reveal the identity of the phases. Since it is known that the addition of Zr yields only the Al_3Zr phase and additional Mn may result in several Mn-containing phases, depending on the alloy composition, this analysis was mainly focused on the Mn-containing particles. Further results on the dispersoids are presented, regarding their size, volume fraction, interparticle distance and coarsening behaviour. A qualitative approach was also employed to assess the morphology and coherency of the particles, since these parameters can affect their pinning capacity. In addition, in order to explain the reduction in the number density of Al_3Zr dispersoids in the 0.1Zr-0.3Mn alloy their distribution within Mn-dispersoid bands was analysed and, also, samples were examined to see if Zr dissolves within the Mn-dispersoids, or Mn-rich GB phases, or if some other effect is present.

In all alloys, dispersoids are typically heterogeneously distributed and this behaviour originates from microsegregation effects in the as-cast material. For this reason, this study initiated from the as-cast material and continued to the final T351 condition. An AA2050 DC casting was used for this purpose due to the unavailability of the AA2198 in this form. The AA2050 had a similar composition to the AA2198 and contained a similar amount of Zr and Mn (§3.1). Samples homogenised at higher temperatures were also examined. The most important finding in this section was the modification of the distribution of the Al_3Zr dispersoids when they developed in the presence of Mn. STEM-EDX measurements helped to draw vital conclusions on this matter.

5.2 Chemical analysis of the principle dispersoid types and GB phases

5.2.1 Dispersoid analysis

Initially, it was high priority of this chapter to identify the composition of the main dispersoid types present in the microstructure after homogenisation, before analysing them further at different processing stages and seeking signs of a Zr-Mn interaction. Although minor Zr additions in aluminium are expected to form the metastable β'-Al_3Zr phase, according to the Al-Zr phase diagram [273], the addition of Mn in Al can lead to several different phases depending on the composition of the alloy. In short, the $Al_{20}Cu_2Mn_3$ phase is known to precipitate in the presence of Cu, while the Al_6Mn phase forms when Cu is absent [158]. At this stage the presence of Zr in the Mn-containing phases was not characterised, as the aim was to identify the main dispersoid types. This important topic will be returned to in §5.7.3.

Starting with the Zr-containing phase, particles were analysed in the T351 temper. The exact condition is not important since the dispersoid composition should remain relatively unchanged after homogenisation. It is obvious from the EDX spectrum in Fig. 5.1 that the analysed particles contained only Al and Zr. The Cu peak is coming from the matrix, due to the amount of this element in solid solution. Hence, this phase was concluded to be the Al_3Zr. The dispersoids also gave the normal superlattice reflections in selected area diffraction.

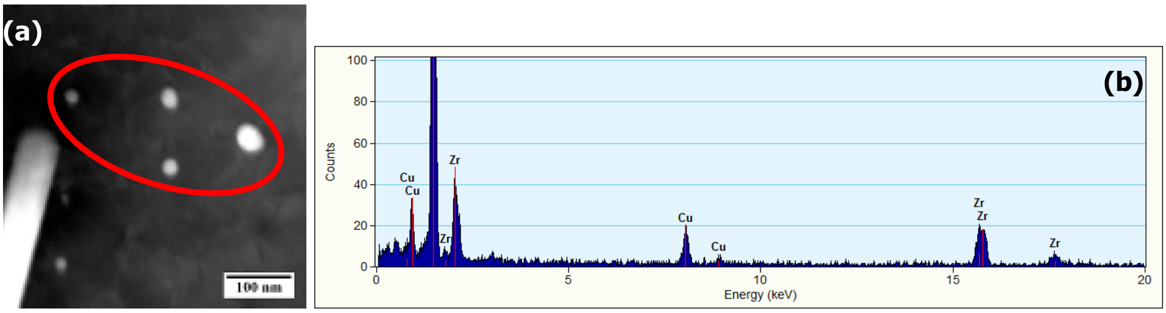

Fig. 5.1: Composition of the small spherical Al_3Zr dispersoids in the 0.1Zr-0.3Mn alloy (T351 temper): **a)** STEM-HAADF image of the analysed particles, and **b)** EDX spectrum.

The composition of the different types of Mn-dispersoids was also analysed by STEM-EDX in the fully homogenised AA2050 alloy, at the end of HT-1 (i.e. 10 h ramp heating to 505°C and a plateau of 12 h at 505°C). The analysis was carried out in this condition to see if the particle composition changed depending on their position within a grain, taking into account the Mn microsegregation that occurs on casting (this will be discussed further in §5.3.1). The measurements were carried out on a large number of particles on each of the three main morphologies present within the grain interior; elongated, elliptical and faceted.

The results from EDX spot analyses of the Mn-dispersoids are presented in Fig. 5.2. The Cu and Mn contents of the Mn-dispersoids were plotted as a function of the respective Al content. In all three cases in Figs. 5.2a-c, the points lie very close to the superimposed lines which represent the Cu and Mn contents in the $Al_{20}Cu_2Mn_3$ phase. The slight deviation observed in each case, is due to effects from the sample thickness and the contribution from the other solute elements [264]. The Li content in particular, which is quite high in this alloy (~3.8 at%) and cannot be detected by x-rays, possibly also affected the final values of the other elements. The measured values are also affected by the Cu content in the matrix. From Fig. 5.2d, where all points from images a-c are included, it is obvious that there is only one Mn-containing dispersoid phase present. Thus, the different morphologies of the Mn-dispersoids were not caused by the existence of several different phases, but are due to nucleation and growth factors that will be explained later. The final conclusion from this analysis was that the Mn-containing dispersoids were all identified as the $Al_{20}Cu_2Mn_3$ phase.

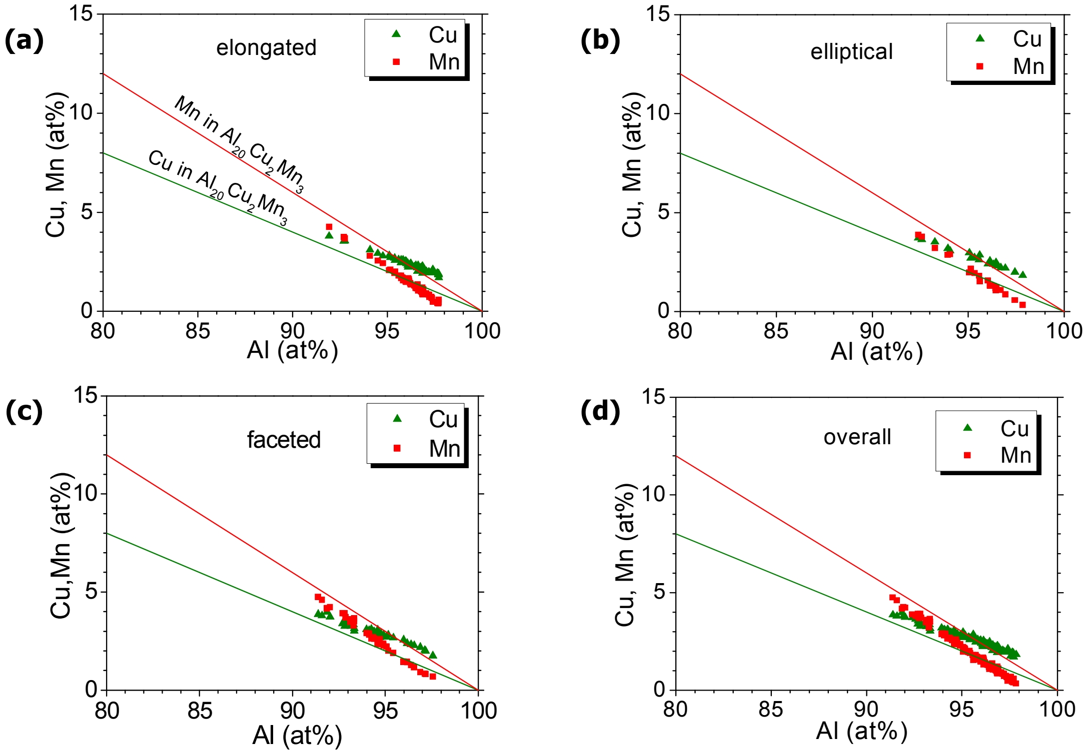

Fig. 5.2: Composition plots of Cu and Mn content vs. Al content, constructed from STEM-EDX measurements from the three main dispersoid morphologies observed: **a)** elongated dispersoids, **b)** elliptical dispersoids, **c)** faceted dispersoids, and **d)** all data points from the previous graphs combined.

5.2.2 Grain boundary phase analysis

Particles on grain boundaries in the alloys were also analysed by EDX to determine their composition. These particles tended to be larger than those in the matrix, since they could exceed 1 μm in size. Several different phases seemed to exist, but two of them were dominant; the AlCuMn and AlCuMnFe. Both phases had Cu and Mn contents far from the previously identified $Al_{20}Cu_2Mn_3$ phase, as shown by the superimposed lines in Figs. 5.3a,b. The straight lines fitted to the experimental data, indicate a large deviation from the dispersoid composition. The most important feature was that the Cu content was much higher than the Mn content in these GB phases.

In any case, it was difficult to accurately determine the exact stoichiometry in the phases. Comparison to literature data did not show any match of the AlCuMn phase with other known phases. The reported decagonal phase $Al_{66.08}Cu_{21.35}Mn_{12.57}$ [274] has a much higher Mn content than the present one. Due to the very low Mn content of this phase, it seems quite possible that Mn atoms substituted for Al atoms in the crystal lattice of the equilibrium θ-Al_2Cu. In fact, the 33.33 at% Cu content corresponds to 65.76 at% Al according to the fitted line in Fig. 5.3a. This percentage deviates marginally from the 66.67 at% Al, which would be expected for the Al_2Cu phase. Since the Mn content is relatively stable throughout the whole composition range, it can be concluded that there is a maximum limit of this element that can be dissolved in the Al_2Cu phase. This amount can be calculated by solving the equation describing the Cu data (Eq. 5-1) and it was found equal to ~2.20 at%.

$$[Cu] = 99.76 - 1.02 \cdot [Al] \tag{5–1}$$

On the other hand, the Cu content of the AlCuMnFe phase (Fig. 5.3b) was lower compared to the AlCuMn phase. This means that Fe atoms substituted for Cu atoms, since the decrease in Cu content between the AlCuMn and AlCuMnFe phases was approximately equal to the Fe content and the Mn content remained almost the same. However, the $Al_{73.91}Cu_{15.13}Mn_{7.13}Fe_{3.83}$ [275] and the F-icosahedral $Al_{66.08}Cu_{21.35}Mn_{8.29}Fe_{4.28}$ [274] phases reported in the literature, are different from the present one as they contain more Mn than Fe.

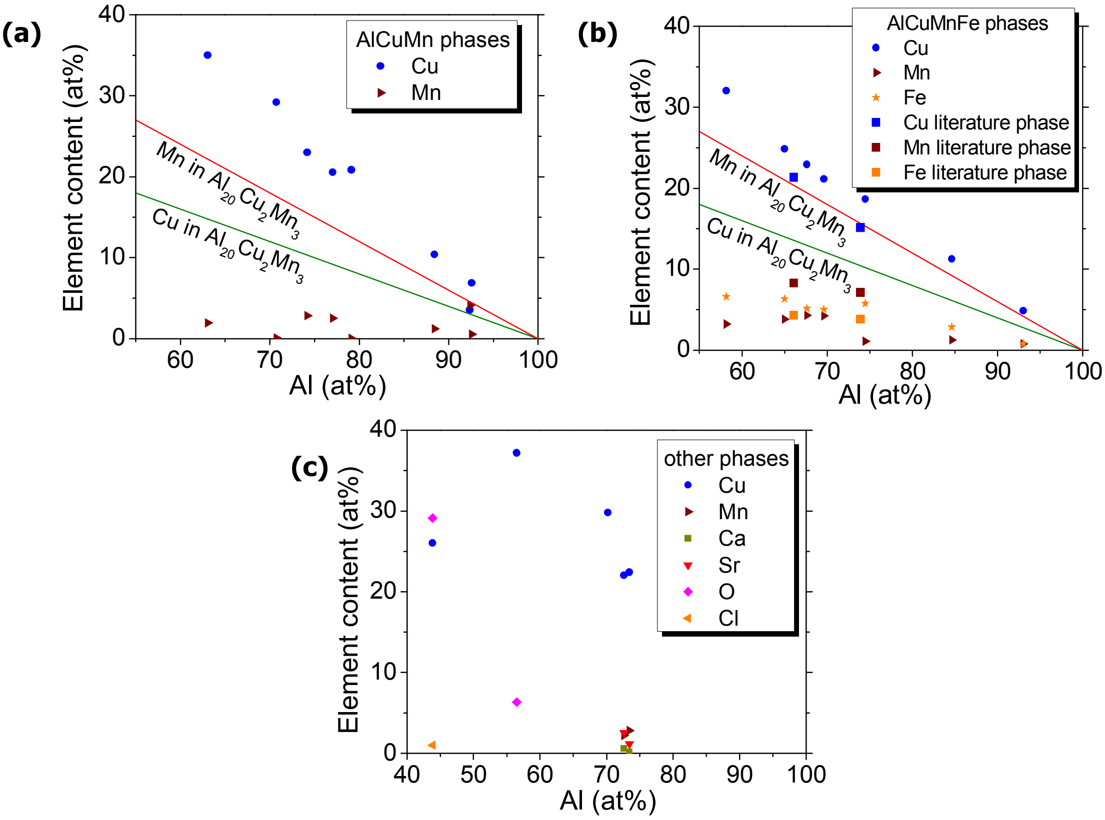

Fig. 5.3: Composition plots from STEM-EDX measurements of Mn-containing GB phases at the end of HT-1 from the AA2050 cast and homogenised alloy: **a)** phases containing Al, Cu, Mn, **b)** phases containing Al, Cu, Mn, Fe (compositions of literature phases: $Al_{73.91}Cu_{15.13}Mn_{7.13}Fe_{3.83}$ and $Al_{66.08}Cu_{21.35}Mn_{8.29}Fe_{4.28}$), and **c)** phases containing other combinations of elements.

A number of other GB phases, containing different combinations of alloying elements, were also present (Fig. 5.3c). However, no Al_2CuMg phase was found, which is usually present in the similar AA2024 alloy and this phase must be in solution [275]. A general conclusion from the GB phase analysis is that the $Al_{20}Cu_2Mn_3$ phase does not form on GBs.

5.3 Dispersoid formation during homogenisation

The stage of homogenisation is of vital importance in the production of wrought Al products, since it has a dual effect of dissolving the coarse GB phases and to form dispersoids. Before looking into the details of dispersoid formation in §5.3.1 and §5.3.2, the homogenisation process itself will be analysed. This will help to understand the effect of the homogenisation treatment on recrystallisation resistance which is studied later in this work.

Two different homogenisation treatments were applied to the as-cast alloy, which were recommended by Alcan CRV. Both processes involved an initial 10 h ramp heating stage to the final temperature before the isothermal hold. HT-1 involved homogenising for 12 h at 505°C and HT-2 for 32 h at 535°C. The homogenisation routes are shown in Fig. 5.4 relative to the TTT curve for initiation of the Al_3Zr phase precipitation in an AA7050 alloy, containing the same amount of Zr as the AA2198 and AA2050 alloys, predicted by Robson in previous work [116]. The TTT curve is only shown here as a rough guide, since such curves are entirely dependent on the exact alloy composition and moreover, they refer to isothermal conditions. Since the dissolution of second phases is a diffusion-controlled process, this would be most effective when carried out at the highest possible temperature. However, a very high temperature would not yield an optimum dispersoid distribution, as the particles tend to nucleate with a lower density and coarsen significantly [113].

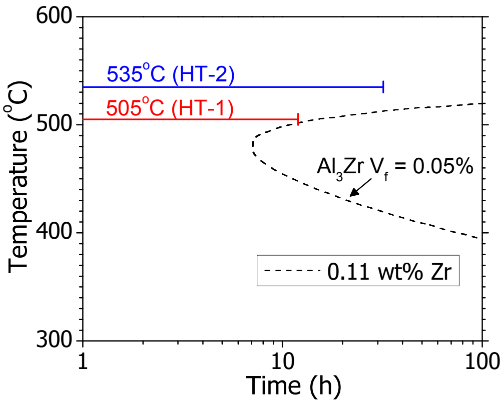

Fig. 5.4: The homogenisation treatments of this work are superimposed on the TTT curve for 0.05% precipitation of Al_3Zr, as-predicted by Robson for an AA7050 alloy containing 0.11 wt% Zr [116].

The as-cast microstructure consisted of a mixture of GB phases and undissolved particles within the grains. Fig. 5.5a shows that the GBs were almost completely covered by eutectic phases. In the grain interior, metastable phases of various compositions and morphologies had precipitated upon slow cooling after casting (Fig. 5.5b). Most of these phases contain Cu and they can be easily dissolved during the homogenisation stage as will be seen later, due to their higher diffusion rate in Al relative to other elements such as Mn, Zr, Fe etc. [276].

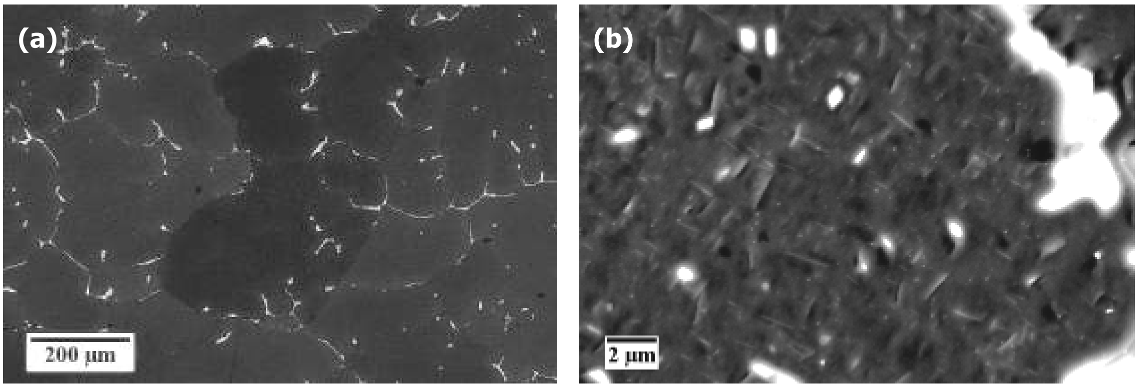

Fig. 5.5: The as-cast microstructure of the AA2050 alloy: **a)** distribution of GB inter-dendritic phases, and **b)** the morphology of phases formed next to the GBs.

The effect of both heat treatments on the dissolution of second phases in the microstructure is seen in Fig. 5.6. The ramp heating stage did not dissolve a significant amount of GB phases below a relatively high temperature, which accelerates the dissolution kinetics for HT-1. Looking at images (a), (c), (e) and (g), the increasing extent of GB phase dissolution is clear between the 6 h ramp sample and the 12 h plateau at 505^{o}C. Comparison between images (g) and (i) proves the fact that the HT-2 heat treatment is more beneficial to the microstructure in terms of eutectic phase dissolution than the HT-1.

The higher number of pits on the sample surface at the end of the HT-2 treatment indicated that spheroidisation of the retained GB phases occurred (example shown in image (k)). The shape of these phases changes from thick strips on the GBs into large spherical particles. These large particles fall out more easily than the thick films decorating the GBs during the SEM sample preparation. Thus they leave behind characteristic pits which lie directly on, or adjacent to, the GBs (images (g),(i)). The larger number of pits for HT-2 in image (i) compared to HT-1 in image (g) was observed because spheroidisation was at a more advanced stage after the higher homogenisation temperature.

A closer view of the microstructure can reveal the changes at a particle level. The images on the right-hand side of Fig. 5.6 show the particle distribution close to GBs. After 6 h of ramp heating in the HT-1, there was no significant difference from the as-cast particle distribution (image (b)). Diffusion was not fast enough up to this point of the ramp (311^{o}C) due to the low temperature and could not help dissolve a high volume fraction of second phases, so the microstructure consisted of coarse plate-like Cu-containing particles next to the GBs. At the end of the ramp stage at 505^{o}C (image (d)), most of those plate-shaped particles dissolved and there were signs that very small dispersoids had started forming. These were mainly Mn-dispersoids, as was shown in §5.2.1. However, the Al_3Zr dispersoids were difficult to observe at this magnification. Upon further isothermal heating for 6 h at 505^{o}C, growth of some of these dispersoids occurred (image (f)). At the end of the HT-1 a higher volume fraction of dispersoids was present and also their shape changed, in that a significant number of the particles became more elongated (image (h)). A comparison between the final stages of both heat treatments (images (h),(j)) showed that fewer and larger dispersoids formed with HT-2.

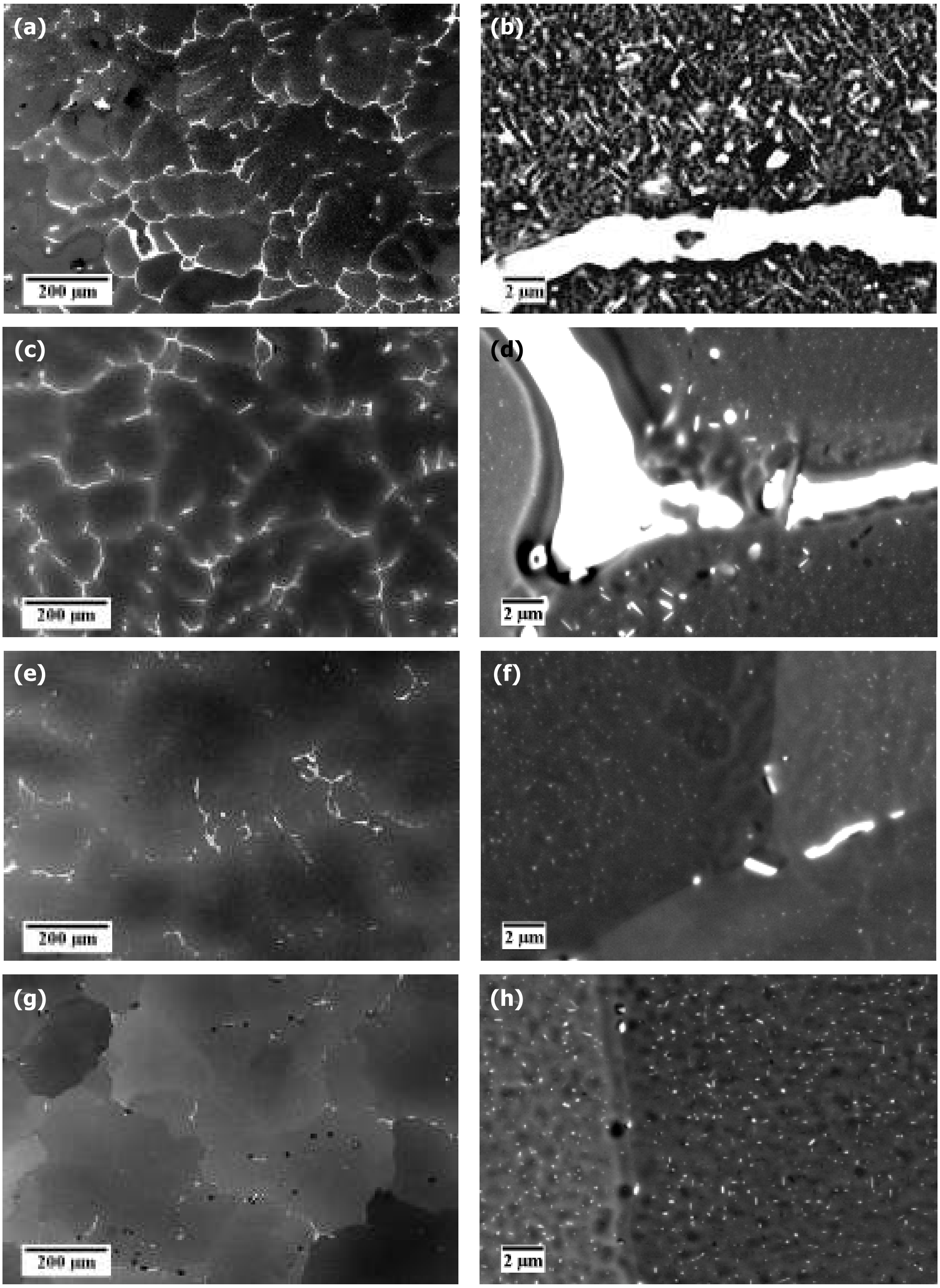

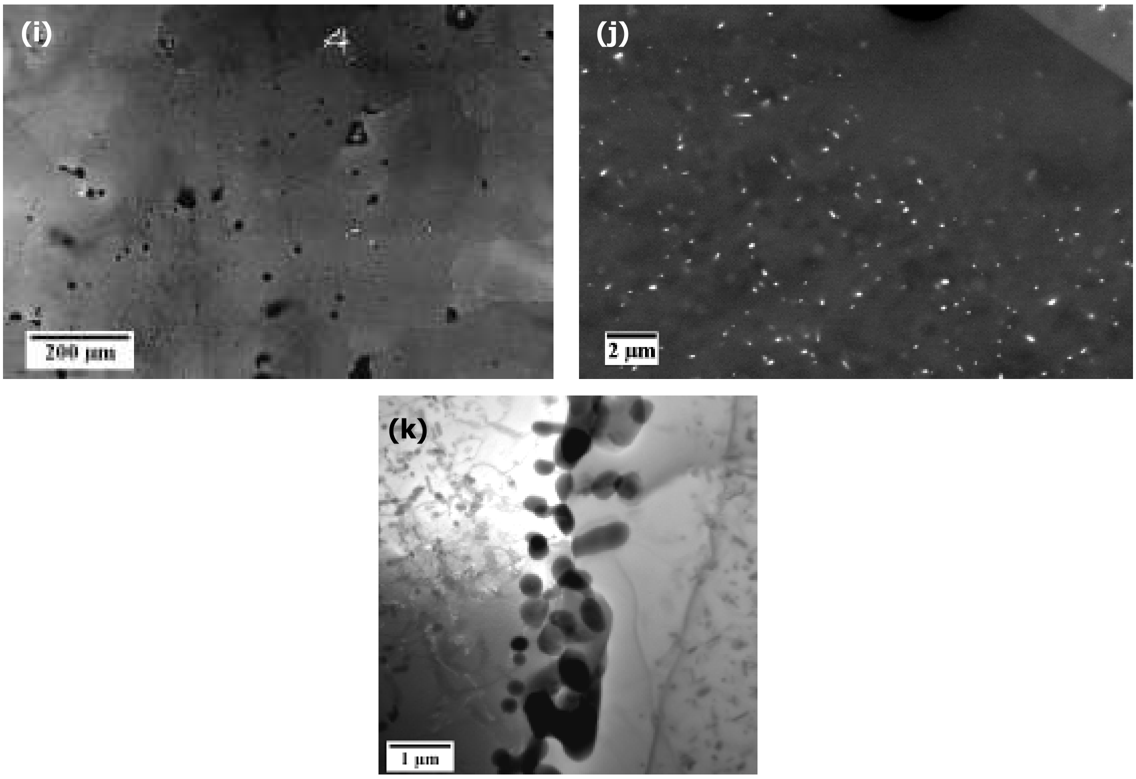

Fig. 5.6: Left: General microstructure at various stages during homogenisation. Right: Higher magnification next to GBs. **a,b)** HT-1, 6 h ramp (311°C), **c,d)** HT-1, 10 h end of ramp (505°C), **e,f)** HT-1, full ramp and 6 h plateau (505°C), **g,h)** HT-1, full ramp and 12 h plateau (505°C), **i,j)** HT-2, full ramp and 32 h plateau (535°C), and **k)** spheroidisation of GB phases.

In summary, although the homogenisation treatment HT-2 in Fig. 5.4 managed to dissolve a larger amount of GB phases due to the higher temperature compared to HT-1, it seemed to take quite a long time for the desired dispersoids to precipitate. Dispersoid formation was studied in this work mainly for the standard homogenisation treatment HT-1. It is obvious that HT-1 is much closer to the nose of the TTT curve compared to HT-2; hence, a higher Al_3Zr volume fraction was expected for this route and a much coarser Al_3Zr distribution with a lower volume fraction would be anticipated for HT-2. The conclusion from this section is that HT-1 can yield a better dispersoid distribution than HT-2, at the expense of a slightly higher content of undissolved GB phases, and this is why the rest of the analysis will focus on this particular heat treatment only.

5.3.1 Microsegregation within grains

It is well-known that zirconium and manganese atoms segregate in an opposite manner during casting and this pattern remains to a certain extent even after homogenisation [19]. Fig. 5.7 presents a set of STEM pictures at two different magnifications, suitable for each dispersoid type, taken along half a grain width in the fully homogenised AA2050 alloy in order to assess the differences in the spatial distribution of each dispersoid family. The higher magnification images near the GB in Fig. 5.7 showed very few Al_3Zr dispersoids amongst the

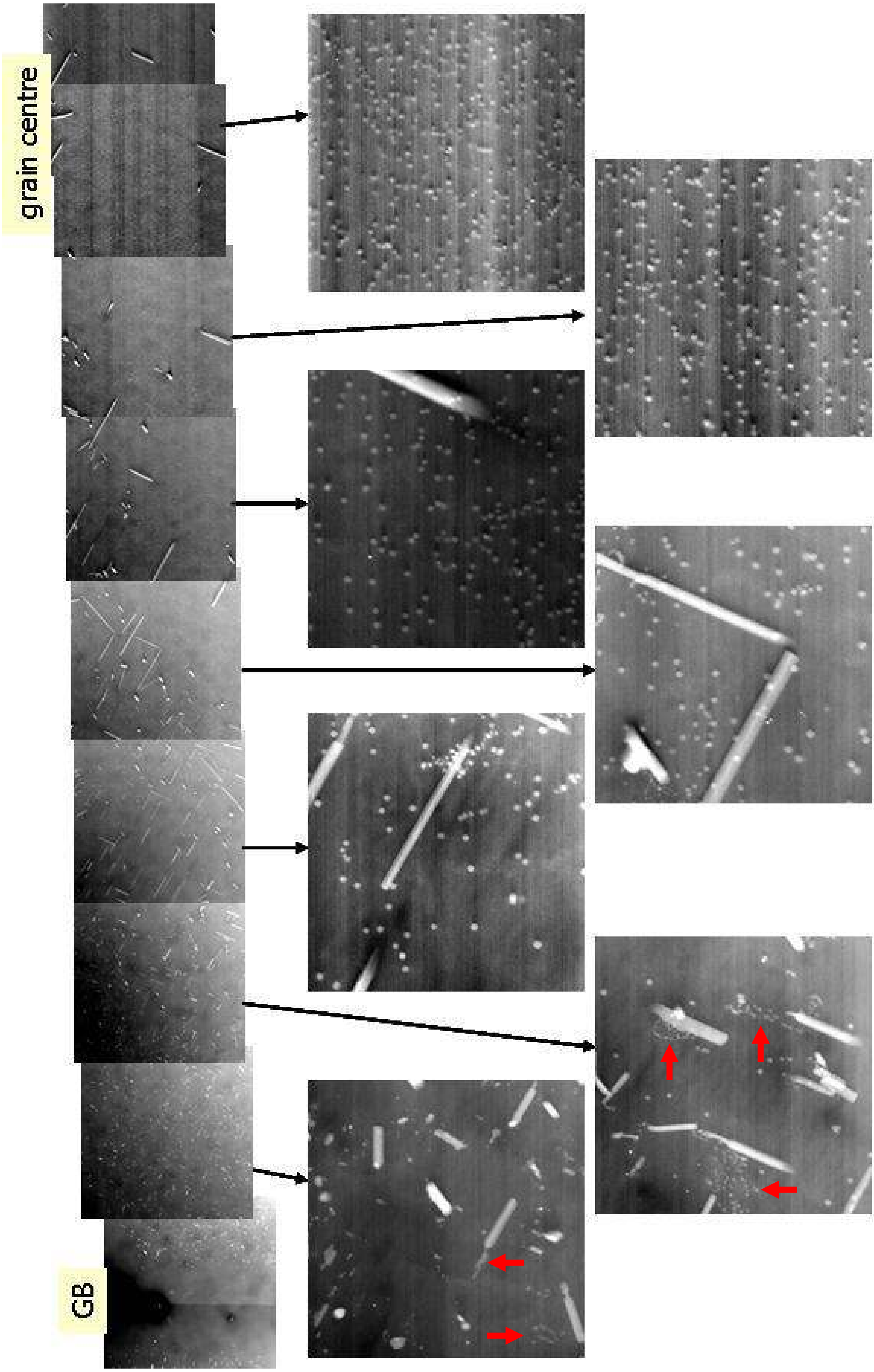

Fig. 5.7: Cross-grain profile from the GB to the grain centre, showing the distribution of Mn-dispersoids (lower magnification pictures - left) and Zr-dispersoids (higher magnification pictures - right) at the end of HT-1. Red arrows indicate heterogeneous nucleation of Al_3Zr dispersoids.

numerous $Al_{20}Cu_2Mn_3$ particles, but these appeared in clusters. Moving towards the grain centre, the number density of the Al_3Zr dispersoids increased dramatically and their distribution became more homogeneous. In contrast, the density of the $Al_{20}Cu_2Mn_3$ phase decreased close to zero at the grain centre. This behaviour was a direct result of the opposite microsegregation patterns of Zr and Mn. However, a narrow PFZ was observed adjacent to the GB, where the volume fractions of both Zr- and Mn-dispersoids in that region approached zero due to the local loss of Mn to the GB phases.

Fig. 5.8a presents the predicted dispersoid distributions for the AA2198 alloy after full homogenisation via HT-1. These curves were produced by C. Sigli of Alcan CRV, using the Alcan Thermodynamic Package Prophase [277]. The model combines thermodynamic data with an analysis of solute partitioning and back diffusion. The Mn-dispersoids were expected to precipitate with a much higher volume fraction near the GBs due to their higher supersaturation compared to the grain centre, while for Zr-particles the exactly opposite behaviour was anticipated. This occurs because Mn is a eutectic addition with a partition coefficient equal to 0.90 [278], while Zr is a peritectic addition with a partition coefficient higher than 1 (no specific value was found in the literature) [279]. Cu is also a eutectic addition in Al, similar to Mn. TEM-EDX measurements revealed a decrease in the Cu concentration from approximately 1.7 at% to 1.25 at%, from the GB to the grain centre (Fig. 5.8b). However, dispersoid formation is not so affected by its variation due to its high overall content in the matrix.

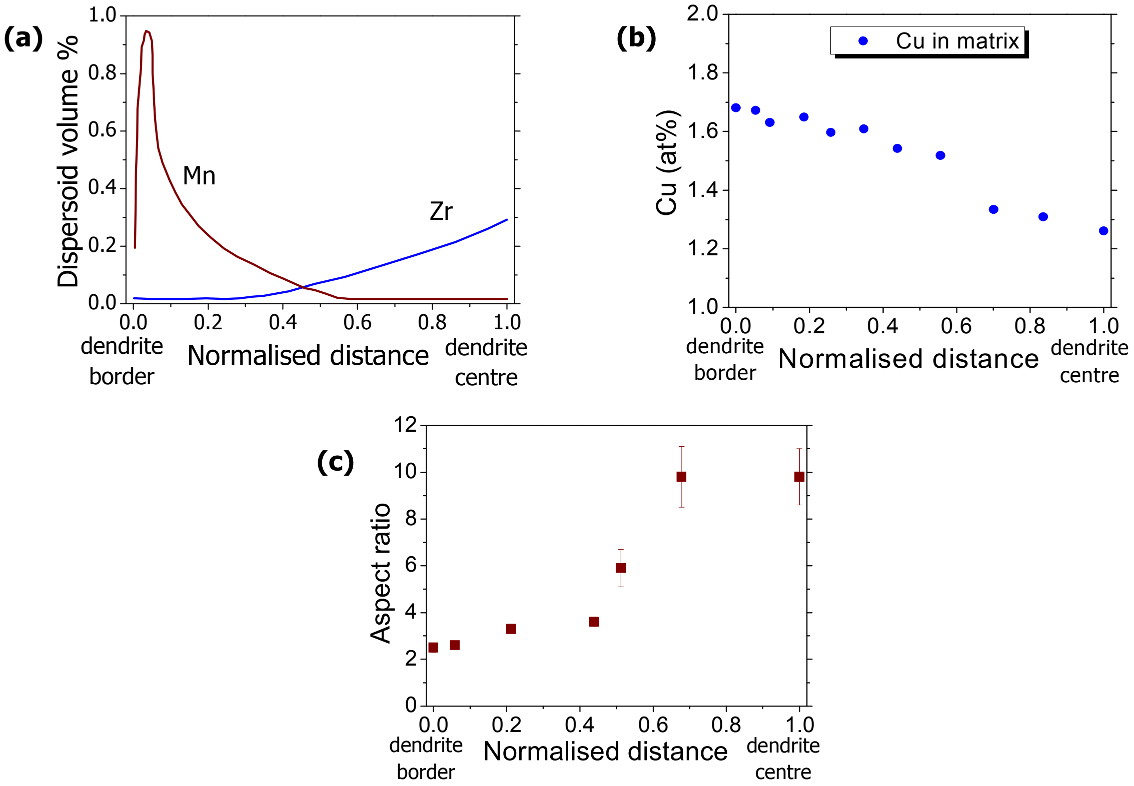

Fig. 5.8: Microsegregation across a dendrite arm after full homogenisation of the cast AA2050 slice via HT-1: **a)** Zr- and Mn-dispersoid volume fractions, predicted for this work using the Alcan Thermodynamic Package Prophase [277], **b)** microsegregation of Cu measured in the matrix, and **c)** Mn-dispersoid aspect ratio.

Particle size measurements showed that a direct outcome of the reduction in Mn supersaturation towards the grain centre, is the large increase in the aspect ratio of the Mn-dispersoids by nearly 5 times compared to particles near the GBs (Fig. 5.8c). In contrast, Al_3Zr particles appeared to be larger close to the GB, where they also formed heterogeneously in clusters, due to their opposite microsegregation pattern.

5.3.2 Dispersoid interactions during precipitation

Because of the decrease of the Al_3Zr number density in the presence of Mn, as shown in §4.4, it is of vital importance to know the sequence in which the Al_3Zr and $Al_{20}Cu_2Mn_3$ dispersoid families precipitate upon homogenisation, in order to understand if there is any interaction during their nucleation. The aim of the current section is to resolve if there is evidence of preferential nucleation of the Al_3Zr or $Al_{20}Cu_2Mn_3$ dispersoid families on each other during homogenisation, thus modifying the Al_3Zr distribution in the 0.1Zr-0.3Mn alloy as compared to in the 0.1Zr alloy in T351.

Both types of particles were expected to start precipitating at some point during the ramp heating stage, which lasted 10 h. The $Al_{20}Cu_2Mn_3$ phase is known to precipitate between 300 and 530°C [115], hence it started nucleating before the Al_3Zr. Looking at the 9 h ramp to 505°C condition, it was clear that the $Al_{20}Cu_2Mn_3$ dispersoids precipitated first mainly near the GBs and had already achieved a significant volume fraction and a large size (Fig. 5.9a). In contrast, the Al_3Zr phase had only just started nucleating at this stage (Figs. 5.9b,c). The Al_3Zr phase has to reach a relatively high temperature in order to precipitate at a significant volume fraction within such a short time interval, as indicated by the TTT diagram in Fig. 5.4. As seen from the same diagram, precipitation of Al_3Zr at 450°C initiates after approximately 10 h. This explains why after the 9 h ramp heating to 505°C (456°C) there were mainly $Al_{20}Cu_2Mn_3$ dispersoids and only a limited number of Al_3Zr dispersoids present. This observation is valid throughout the grain, from the grain edge (Fig. 5.9b) to the grain centre (Fig. 5.9c).

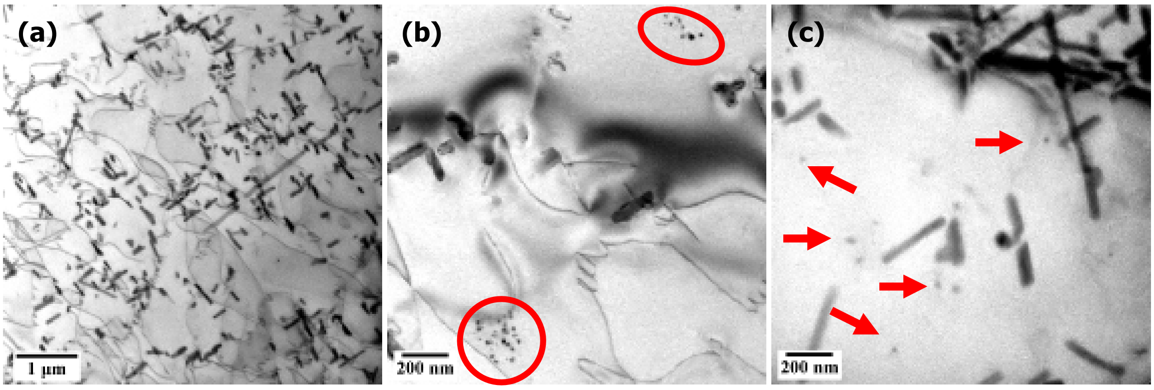

Fig. 5.9: Dispersoid nucleation during homogenisation (9 h ramp heating to 505°C via HT-1 (456°C)): **a)** well-developed distribution of $Al_{20}Cu_2Mn_3$ dispersoids near the grain centre, **b)** Al_3Zr precipitated heterogeneously forming clusters near GBs, and **c)** a small number of Al_3Zr dispersoids precipitated homogeneously at the grain centre.

Hence, if any kind of interaction exists between the two phases, it would have to be ascribed to some heterogeneous precipitation phenomenon of the Al_3Zr phase on the $Al_{20}Cu_2Mn_3$ dispersoids which form first.

The elongated $Al_{20}Cu_2Mn_3$ particles precipitate with their long axis parallel to the [001] direction [127, 280]. The smaller aspect ratio $Al_{20}Cu_2Mn_3$ dispersoids seemed to be more randomly oriented, in agreement with the findings of Ratchev et al. [127] for Al_6(Mn,Fe) particles in the AA5182. On the other hand, the Al_3Zr phase behaved quite differently and precipitated in a mixed manner; both homogeneous and heterogeneous nucleation was observed. In regions of low Zr supersaturation, such as near the GBs, the preferred nucleation sites were either dislocations or soluble Cu-particles that dissolved after solution treatment. Dislocations enhance solute diffusion, as well as acting to reduce coherency strains of the nucleus [108]. Clear evidence of heterogeneous nucleation is provided in Fig. 5.7, where red arrows indicate clusters of Al_3Zr dispersoids, and also in Figs. 5.10a,b. Judging by the shape of the clusters in these images, Zr was either contained within Al_2Cu plates in the casting, which dissolved later and led to the formation of Al_3Zr dispersoids upon the release of Zr atoms, or the Al3Zr dispersoids precipitated heterogeneously on the Cu-particles. No precise conclusion can be drawn at this stage. The shape of the soluble Cu-containing phases in the as-cast microstructure can be seen in Fig. 5.10c and it matches that of the Al_3Zr arrays. On the other hand, homogeneous nucleation occurred predominantly towards the grain centre where the Zr supersaturation was high.

On certain occasions, Al_3Zr particles were observed to be attached to the interface of an $Al_{20}Cu_2Mn_3$ dispersoid (Fig. 5.10d). It has to be made clear that this fact does not imply that the two particles co-nucleated. Electron tomography experiments on the rolled sheet proved that such events are due to thickness effects and the particles are overlapping (§5.7.2). Additionally, the dislocations protruding into the particle interface may possibly attract Al_3Zr dispersoids to nucleate heterogeneously on them. A typical dislocation distribution in a homogenised material is shown in Fig. 5.10e.

Consequently, the interaction between zirconium and manganese during homogenisation did not seem to occur in the context of nucleation of one dispersoid phase on the other. The $Al_{20}Cu_2Mn_3$ dispersoids precipitated first and the subsequently nucleated Al_3Zr ones did not appear to precipitate on the pre-existing Mn-dispersoids. In any case, the Al_3Zr nucleation was dictated by the microsegregation of Zr within the dendrite and by the distribution of dislocations and soluble particles in areas of low Zr supersaturation.

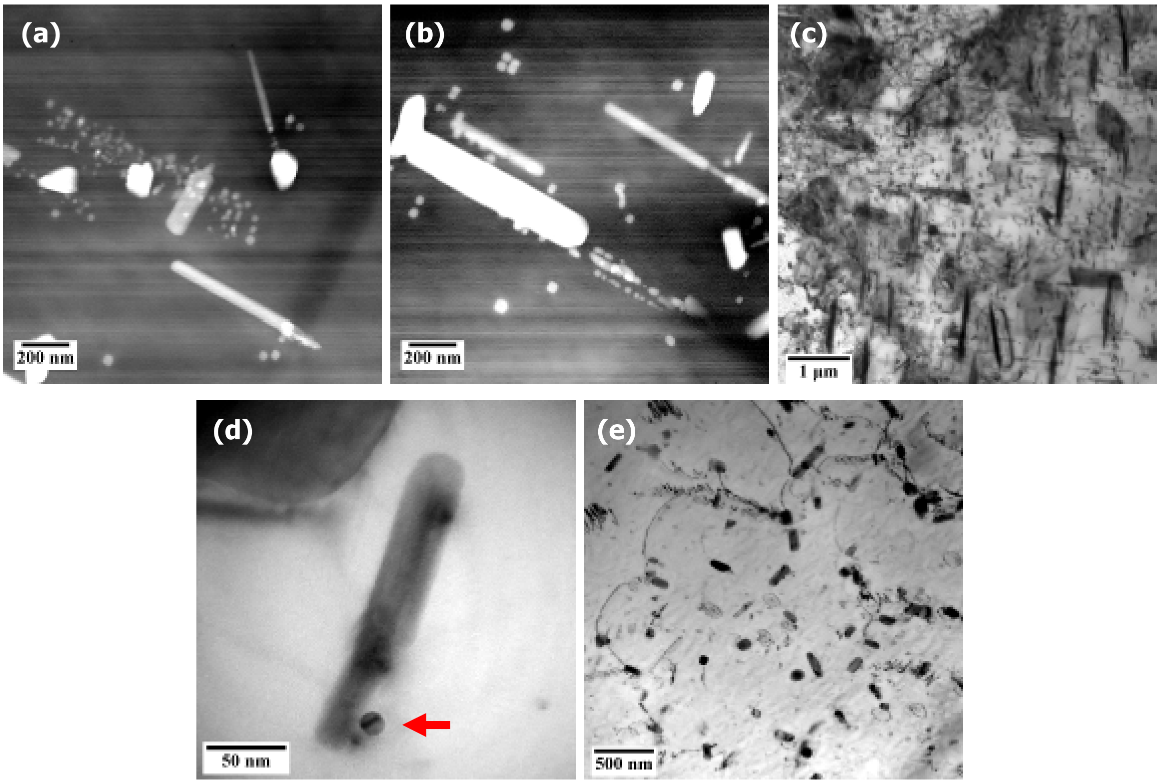

Fig. 5.10: Heterogeneous nucleation of Al_3Zr dispersoids during homogenisation: **a)** a wide band of heterogeneously nucleated Al_3Zr dispersoids from a tilted Al_2Cu plate, **b)** Al_3Zr dispersoids nucleated on straight lines extending from $Al_{20}Cu_2Mn_3$ particles, **c)** morphology of soluble Cu-phases in the as-cast microstructure before homogenisation, **d)** a spherical Al_3Zr dispersoid appears as if it nucleated on an $Al_{20}Cu_2Mn_3$ dispersoid due to overlapping through the TEM sample thickness, and **e)** dislocations associated with $Al_{20}Cu_2Mn_3$ dispersoid interfaces.

5.4 Distribution and morphology of dispersoids after rolling

The spatial distribution of the dispersoids within a rolled product is crucial in terms of its recrystallisation resistance, due to the impact it has on restraining GB motion. Besides recrystallisation, the grain structure and grain shape are also affected by the particle distribution, whether it is random or non-random [134], and by their morphology. In the present work, the distributions of the Al_3Zr and $Al_{20}Cu_2Mn_3$ dispersoids were also studied in depth and quantified, where possible, in the final rolled sheet. The representative microstructures of all the T351 alloys, in terms of dispersoids, are shown in Fig. 5.11 from the RD-ND plane for comparison. Qualitative differences in size and number density are readily visible. The Al_3Zr dispersoids are larger in size in the 0.1Zr-D alloy, the 0.1Zr-0.3Mn and 0.1Zr alloys follow containing finer dispersoids. On the other hand, it is more difficult to make accurate observations for the $Al_{20}Cu_2Mn_3$ dispersoids without obtaining quantified data first. No conclusions on the number density can be drawn from these pictures, since they were taken at regions with different thickness. Banding, coherency and morphology of the dispersoids are all important factors that influence the pinning pressure applied on GBs and they are discussed in the following subsections.

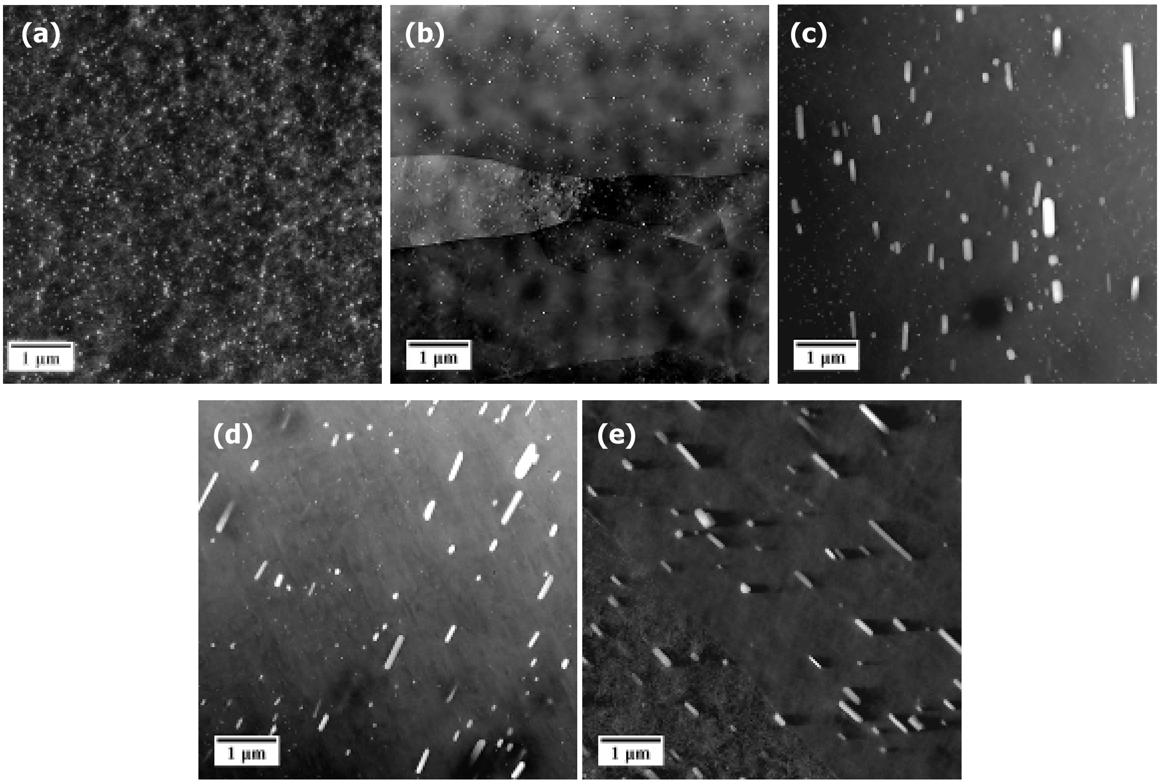

Fig. 5.11: Representative dispersoid distributions in all five alloys in T351 (RD-ND plane): **a)** 0.1Zr-D, **b)** 0.1Zr, **c)** 0.1Zr-0.3Mn, **d)** 0.05Zr-0.3Mn, and **e)** 0.4Mn.

5.4.1 Dispersoid banding in the rolled sheet

One of the major consequences of rolling is the alignment of dispersoids along the RD. In addition, dispersoids form distinct bands due to their heterogeneous precipitation pattern arising from the microsegregation pattern within grains during casting, as was mentioned in §5.3.1. Both types of dispersoids in the present alloys formed bands in the rolled sheet. Unfortunately, it was very difficult to quantify the distance between the bands because there was a very wide variation in the band width along the ND and the dispersoids can only be observed from very thin areas of TEM specimens. Also, the boundaries of these zones were not always clearly defined, making the measurements very subjective.

A banded distribution of dispersoids yields a different pinning pressure than a random distribution, the effect of which has been estimated by Nes et al. [134]. All the alloys in the T351 condition contained banded distributions of particles due to the high strain imposed during rolling (i.e. 4.2). Fig. 5.12 shows some examples of dispersoid banding. The Al_3Zr dispersoids exhibited more defined and narrow bands than the $Al_{20}Cu_2Mn_3$ particles. As a consequence, the Zener pressure for a layered distribution of particles could not be easily calculated experimentally.

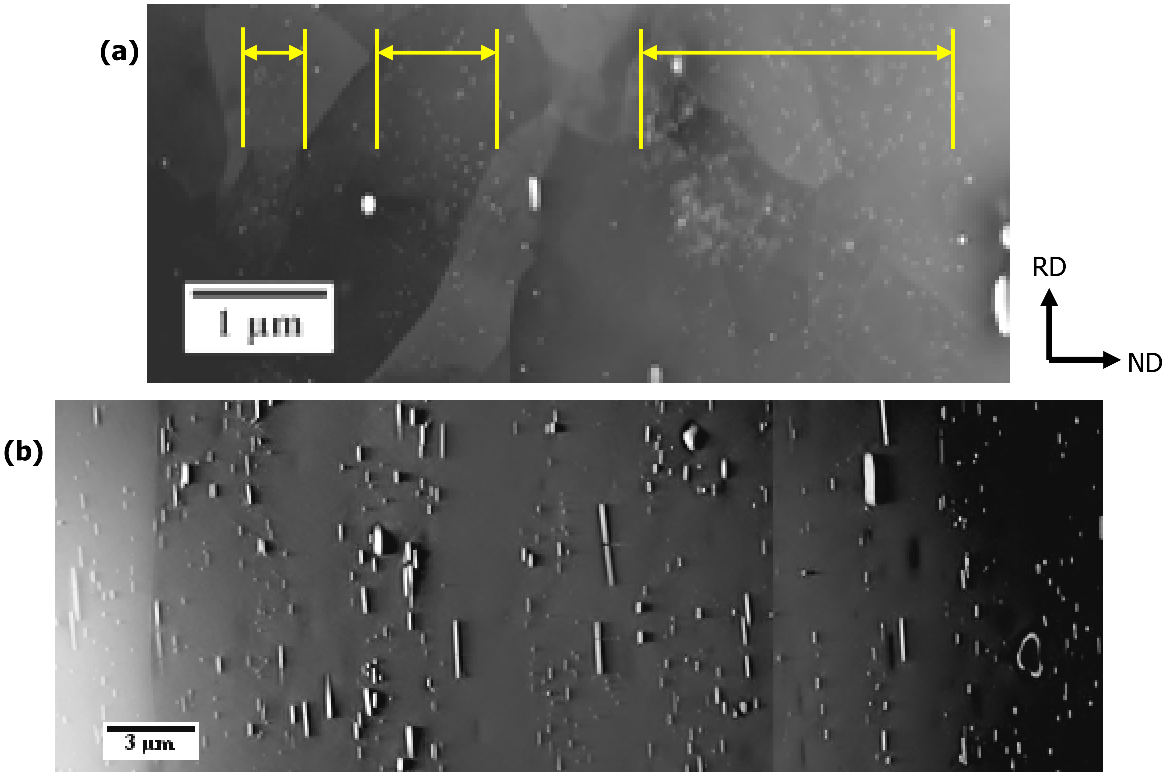

Fig. 5.12: Illustration of dispersoid banding in the rolled 6 mm thick sheet (T351): **a)** Al_3Zr bands in the 0.1Zr-0.3Mn alloy, and **b)** $Al_{20}Cu_2Mn_3$ bands in the 0.4Mn alloy.

5.4.2 Particle coherency

Coherent dispersoids offer higher pinning pressure than incoherent particles of the same size [133-135]. However, this factor is acknowledged to have a small impact on the numerical values of the Zener pinning pressure. This section aims to investigate the interaction of Al_3Zr dispersoids with LAGBs, or HAGBs, and to see if they retain coherency with the matrix when they are bypassed by a migrating boundary. The $Al_{20}Cu_2Mn_3$ dispersoids are known to be incoherent [158], so they will not be discussed in this section.

Jones and Humphreys [143] reported that coherent Al_3Sc dispersoids, that are analogous to the Al_3Zr phase, grew and became semi-coherent when they were bypassed by LAGBs. This was probably owing to particle coarsening via a pipe diffusion mechanism and subsequent unpinning of the GB when the dispersoids exceeded a certain size. Additionally, the Al_3Sc phase loses coherency at a relatively small size [281]. However, this conclusion does not necessarily apply for the Al_3Zr dispersoids of the present study. Al_3Zr coarsening is slower than of Al_3Sc, due to the slower diffusion of Zr in the Al matrix [281, 282]. Coherency can also be maintained up to a large diameter [282]. This is explained in more detail later in the current section. Semi-coherent dispersoids were only seen here after extended annealing at 535°C. Large size differences in the dispersoids in deformed areas in the T351 temper, most probably pre-existed due to microsegregation effects in the as-cast microstructure.

Regarding the passage of HAGBs past the Al_3Zr dispersoids, the acting mechanism depends on the temperature and driving force for boundary migration [133]. Particle dissolution was not observed here, since it is only reported to occur when recrystallisation takes place at temperatures near the solvus of the pinning particles. When the driving force for boundary migration was low so that the Al_3Zr particle was in contact with the boundary plane for a long time, it was noted that it was semi-coherent on the side which was in contact with the GB [133], such as in the example of Fig. 5.13 and the particle shape thus became distorted and deviated significantly from that of a sphere. This arises due to surface tension form the boundary and partial loss of coherency on one face.

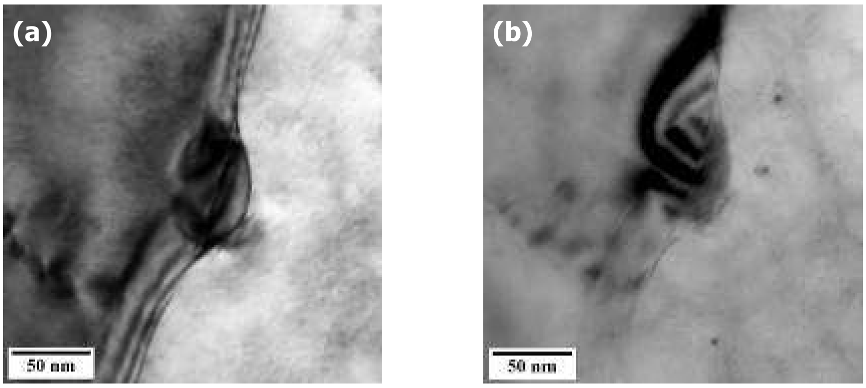

Fig. 5.13: Al_3Zr coherency during impingement by a GB: **a)** distortion of the dispersoid shape, and **b)** two-beam condition of the same dispersoid showing semi-coherency with the matrix.

Particle cutting might also occur when in contact with a grain boundary. Jones and Humphreys [143] in the same work that was mentioned earlier, found that dispersoids re-orientated in the new grain when they were bypassed by a recrystallisation front. This argument is supported from the literature [133, 141] and examples of this were observed in this study as well. Fig. 5.14a shows Al_3Zr dispersoids being cut by a GB as it migrated. The side of the particle lying into the new grain was re-orientated, accordingly to match the orientation of that grain and maintain coherency. Dark field TEM images prove the cutting mechanism. Superlattice reflections corresponding to the Al_3Zr phase were used to obtain Figs. 5.14b,c. In image (c) only the part that came through the boundary diffracted strongly in the new grain. This proves that the dispersoid will be fully coherent eventually, once it is bypassed by the boundary.

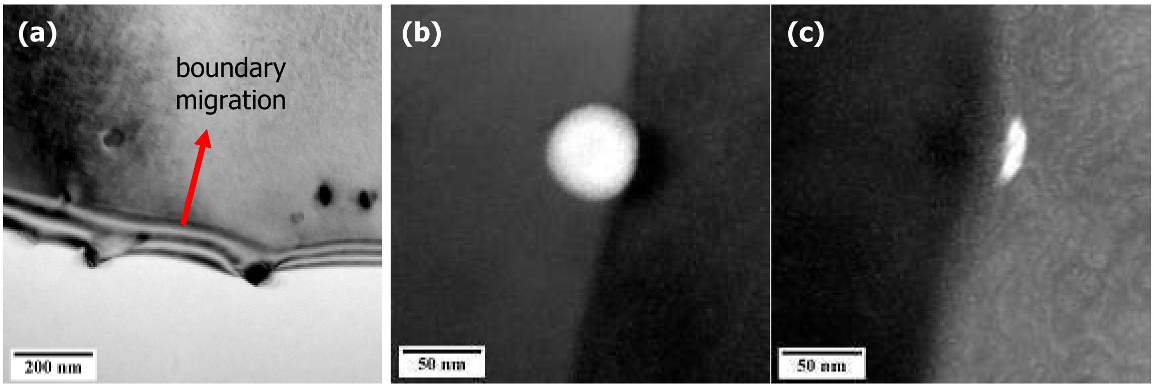

Fig. 5.14: Cutting of Al_3Zr dispersoids by a GB: **a)** dispersoids are cut by the GB and re-orientate in the new grain to maintain coherency, **b)** DF-TEM image of an Al_3Zr dispersoid on a GB, fully coherent with the grain on the left, and **c)** superlattice DF-TEM image showing coherency of part of a dispersoid with the new grain on the right.

The boundary curvature also defines the magnitude of the force exerted on the particle by the GB before it passes through [283]. Fig. 5.15 illustrates two examples of extreme (a) and lower (b) curvature. The Al_3Zr dispersoid in the former picture was completely embedded in the boundary even at a distance almost twice its diameter. The GB has extended, exhibiting extreme curvature and is at the point of separating from the particle. On the other hand, the latter image shows a GB that has started cutting through a dispersoid after a short distance only. The part that has already passed the boundary diffracts strongly in the new grain, indicating that it is coherent with the new matrix.

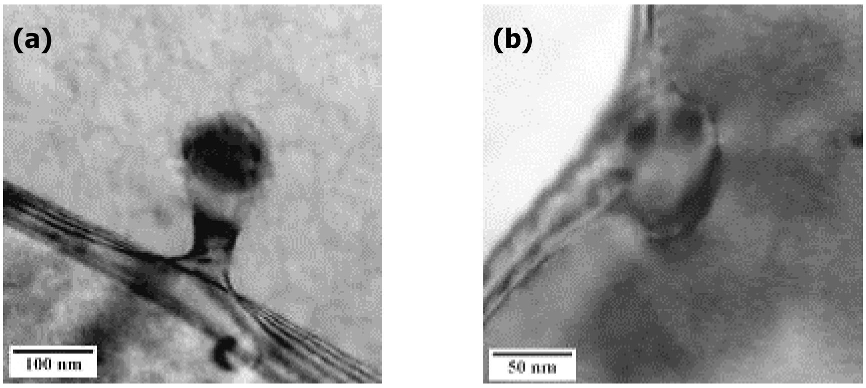

Fig. 5.15: Effect of GB curvature on Al_3Zr coherency: **a)** an extremely distorted GB pocket containing a dispersoid that retains some coherency with the old grain, and **b)** GB penetrated by a dispersoid that becomes coherent with the new grain.

Dispersoid size is another important factor for coherency loss. With increasing its diameter, the Al_3Zr phase becomes semi-coherent and eventually incoherent with the matrix. Although both Al_3Sc and Al_3Zr dispersoids have identical $L1_2$ crystal structures, the critical size for coherency loss is much smaller in the former phase than in the latter, due to the higher lattice misfit for Al_3Sc [122, 281, 284]. The critical size for coherency loss and introduction of a dislocation at the particle/matrix interface according to Røyset and Ryum [281], can be calculated by the equation:

$$d_{crit} = \frac{b}{\delta} \qquad (5–2)$$

where b is the Burgers vector for Al given equal to $2.86 \cdot 10^{-10}$ m [285] and δ is the lattice misfit of the precipitate with the matrix, which is given in a simple form by the equation:

$$\delta = \frac{\alpha_p - \alpha_m}{\frac{1}{2}(\alpha_p + \alpha_m)} \qquad (5–3)$$

where α_p and α_m are the lattice constants for the precipitate and matrix respectively [286].

Employing Eqs. 5-2 and 5-3 and substituting the lattice constants for both phases and the Al matrix (Al: 0.4049 nm [281], Al_3Zr: 0.4066 nm [121], Al_3Sc: 0.4103 nm [281]), the critical diameters calculated were 68.1 nm for Al_3Zr and 21.5 nm for Al_3Sc. Hence, it is clear that the former phase can coarsen three times more than the latter and still manage to retain its coherency. It should be noted that these values are only approximate since the lattice misfit depends on other parameters as well, such as temperature [281].

Measurements of the critical size of Al_3Sc dispersoids support that the calculated value above lies within the size range observed from experimental evidence [287, 288]. Data for the present case is shown in Fig. 5.16. An area containing coherent Al_3Zr dispersoids with the characteristic Ashby-Brown contrast [287, 289, 290] in an annealed sample is shown in (a). A wide range of sizes was measured for that region and the results are presented in Table 5.1.

Table 5.1: Diameter measurements for the Al_3Zr dispersoids in Figs. 5.16d,e.

Particle	A	B	C	D	E	F	G
Diameter (nm)	78.6	47.7	54.9	49.0	46.9	56.2	96.0

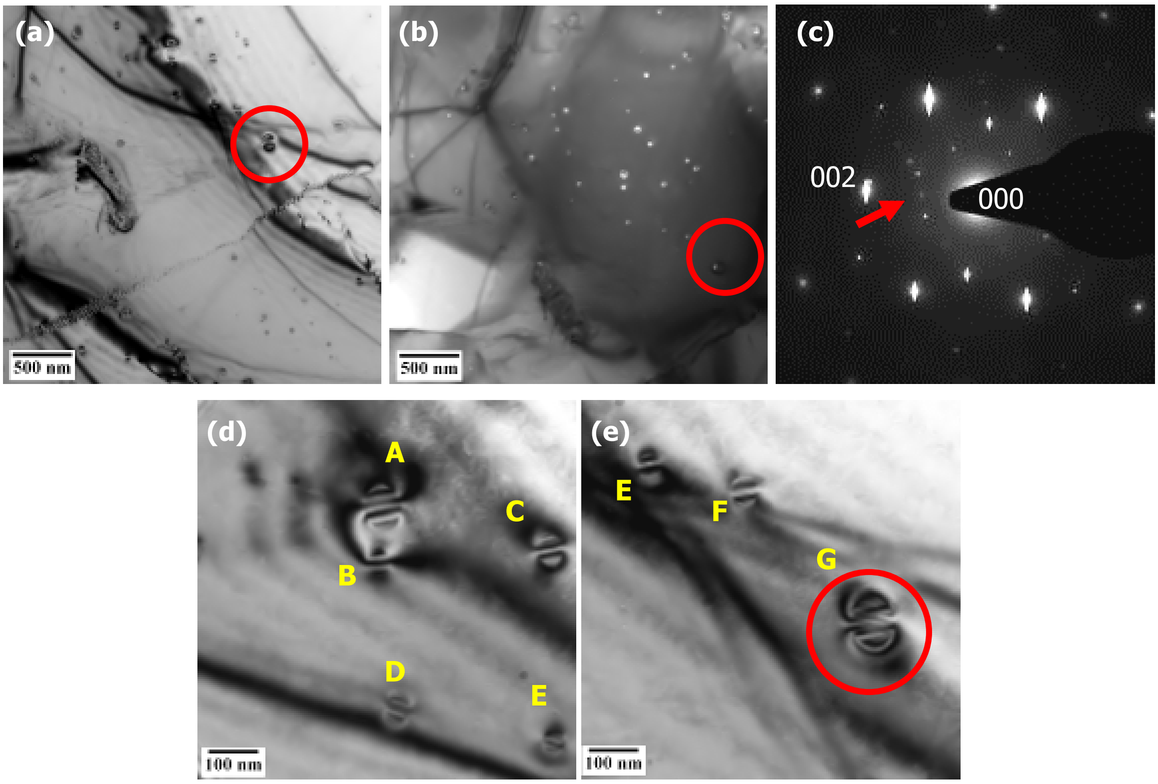

Fig. 5.16: Effect of size on Al_3Zr coherency (0.1Zr-D alloy, annealed for 72 h at 535°C, the red circle around the same dispersoid in a,b,e, acts as an orientation guide): **a)** BF image of coherent dispersoids exhibiting the typical Ashby-Brown contrast, **b)** DF image of the same area as in (a), **c)** DP corresponding to the same area, showing the $<110>_{Al}$ zone axis (arrow pointing at 001 superlattice reflection), **d)** higher magnification from (a), and **e)** a second, neighbouring area from (a) at higher magnification.

The superlattice reflections in the diffraction pattern in Fig. 5.16c clearly prove the existence of semi-coherent or incoherent Al_3Zr dispersoids in this particular area. In the $<110>_{Al}$ zone axis, coherent Al_3Zr dispersoids would yield 001 reflections, between the 000 reflection of the transmitted beam and the 002 reflection of the matrix. However, there seemed to be more reflections in neighbouring positions which indicate that there were incoherent dispersoids present as well. In complete agreement with the earlier critical diameter calculations, particles A and G were found to have lost coherency. Indeed, images (d) and (e) show that the strain field around them was distorted and this was more intense for the larger particle G. Additional proof is provided by the dark field image in (b), where dispersoid G did not seem to diffract strongly and appeared mainly dark. A small bright spot was visible on it, suggesting that just a minor part of it was still coherent. On the other hand, particle A diffracted more strongly suggesting that it was still at the initial stage of coherency loss. Iwamura and Miura [287] have presented images with typical patterns of coherency loss for $L1_2$ particles.

In summary, the different scenarios regarding the coherency of the Al_3Zr dispersoids with the Al matrix, and how they interact with a GB, are met at different frequencies. These cases can be classified according to their importance, starting from the most frequently observed to the least, as follows:

- GB pinning with partial coherency loss due to shape distortion,
- particle cutting and re-orientation with the new grain to retain full coherency,
- particles exceeding the critical size for coherency loss (particles smaller than ~80 nm were still coherent if not affected by the passage of a GB),
- particle bypassing and complete coherency loss, but only when the critical particle size is exceeded.

It should be noted that no dissolution in the migrating GB and re-precipitation was observed for the Al_3Zr phase in this work.

5.4.3 Morphology

Dispersoid morphology is a very important parameter regarding their interaction with GBs, since different shapes yield different pinning pressures [134, 135, 198-200]. A complete assessment was carried out here for both dispersoid families, including during the homogenisation stage, after rolling in the T351 temper and for annealed conditions at 535°C.

At the initial stages of their formation during the homogenisation treatment, TEM-EDX analysis showed that there may be two types of Zr-containing phases with different morphologies; the typical spherical and coherent β'-Al_3Zr phase and a very small number of rod-like particles which did not dissolve upon homogenisation of the cast material. The latter are shown in Fig. 5.17a. Both particles in the image were found within a cluster of spherical Al_3Zr dispersoids, being aligned in the direction of that aggregate. The rod-shaped particles dissolved or broke up to form spherical dispersoids during the following processing stages, since they were not observed in the rolled T351 condition. Rystad and Ryum [125] have also observed several shapes of the Al_3Zr phase during annealing of cast samples, deviating from the typical sphere and all having the $L1_2$ crystal structure. Furthermore, Ryum [291] reported the existence of such rod-like particles in Al-Zr alloys, similar in appearance to dendritic-type particles in an Al-Hf alloy. In comparison, the Al_3Zr dispersoids that formed in the centre of the dendrites, where there was higher Zr supersaturation, were predominantly spherical and coherent (Fig. 5.7).

The $Al_{20}Cu_2Mn_3$ dispersoids on the other hand, exhibited a more complicated morphology depending on their location within the grain. Particles close to the GBs had shorter aspect ratios (as discussed in §5.3.1) with their length generally not exceeding 500 nm (Fig. 5.17b). In the grain centre, particles reached several microns in length and were quite thin, due to a reduction in Mn-supersaturation (Fig. 5.17c).

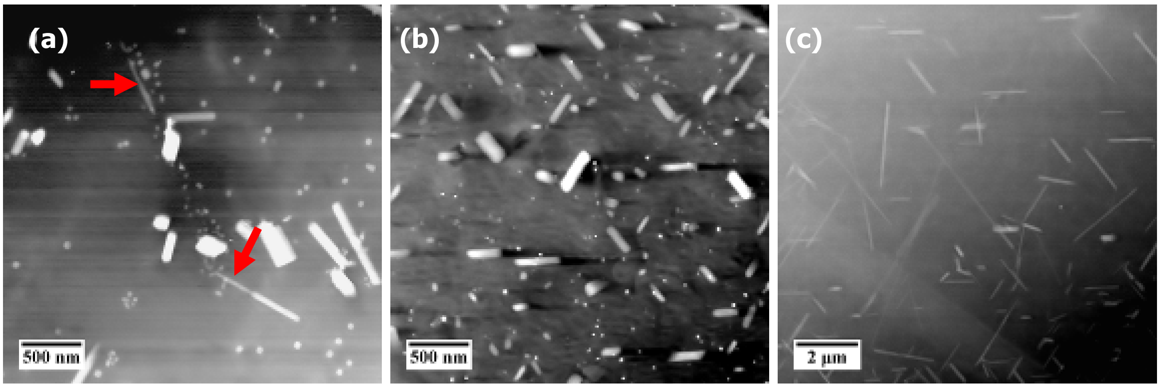

Fig. 5.17: Dispersoid morphology after homogenisation: **a)** spherical, clustered Al_3Zr dispersoids and rod-like Zr-precipitates indicated by arrows, **b)** short, thick $Al_{20}Cu_2Mn_3$ dispersoids near the GB, and **c)** long, thin $Al_{20}Cu_2Mn_3$ dispersoids at the grain centre.

In the T351 condition, all the dispersoids were significantly coarser compared to after the homogenisation stage, especially the $Al_{20}Cu_2Mn_3$ ones. The Al_3Zr dispersoids were around 20 nm in the 0.1Zr and 0.1Zr-0.3Mn alloys, thus they remained spherical and coherent. Some of them are shown in Fig. 5.18a exhibiting the characteristic strain contrast. Coarser Al_3Zr particles, usually located at the edge of a dispersoid band, exhibited different morphologies. Fig. 5.18b shows some of the faceted Al_3Zr particles highlighted. Satya Prasad et al. [123] studied in depth such faceted Al_3Zr morphologies and presented a detailed analysis of their orientation relationship with the Al matrix.

The Mn-dispersoids had several different shapes as seen in Fig. 5.18c. At this stage, all these dispersoids were coarse and incoherent with the matrix. It has to be noted that after rolling no preferred crystallographic orientation was observed and they were all aligned along the RD. The wide range of morphologies in a small area resulted from the high strain imposed during rolling, which caused the formation of bands containing particles from all parts of the homogenised grain, plus the break-up of the higher aspect ratio plates. The smaller dispersoids appeared to be either spherical or elliptical and possibly they were the ones located near the GBs after homogenisation. However, some of them might be parts of longer particles that broke during rolling, or were affected by a migrating GB during the solution treatment. The elongated dispersoids were formed near the centre of the homogenised grain and after being partly broken up, they have coarsened further during the subsequent hot-rolling and solution treatment. Faceted, low aspect ratio dispersoids were also present, but it was more difficult to predict where they originated from. These particles were quite coarse and might even be prior GB phases. The most important conclusion for the T351 condition is that the vast majority of the $Al_{20}Cu_2Mn_3$ dispersoids were of the elongated type and aligned in the rolling plane along the RD.

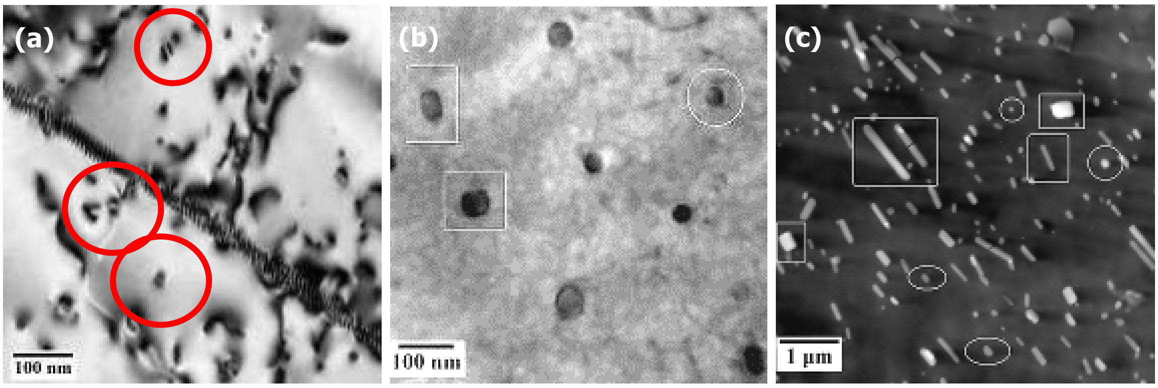

Fig. 5.18: Dispersoid morphologies in the T351 condition: **a)** fine, spherical, coherent Al_3Zr dispersoids, **b)** coarse Al_3Zr dispersoids, and **c)** various morphologies of $Al_{20}Cu_2Mn_3$ dispersoids in the 0.4Mn alloy.

It is interesting to note that the morphology observed from the RD-ND plane was not always representative of the actual shape of the particle in 3 dimensions. Electron tomography experiments (§3.4.5) proved that some dispersoids did not have a uniform shape in three dimensions. Particle A in Fig. 5.19a, seemed to be elliptical from the top view of the RD-ND plane. However, when the TEM specimen was tilted by 74^{o} (Fig. 5.19b), the particle exhibited facets and appeared much larger in size from that angle. This variation is also seen in the reconstructed volume in images (c) and (d). Equally, particle B seemed to have 4 or maybe 5 facets from the top view, but from the tilted view it appeared to be almost hexagonal. The shape variation in the three dimensions will clearly affect the pinning pressure of the particles on the GBs.

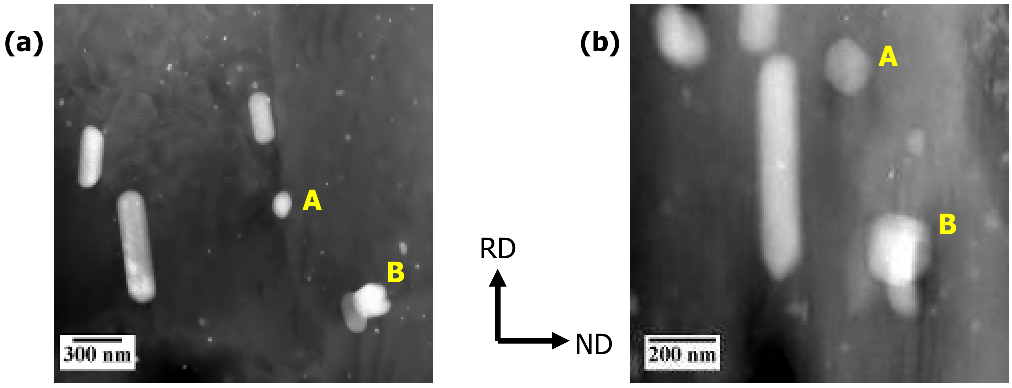

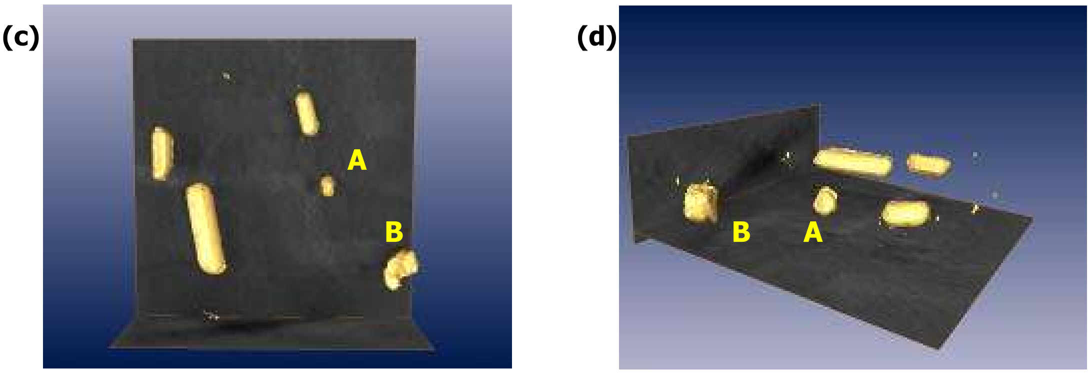

Fig. 5.19: Analysis of $Al_{20}Cu_2Mn_3$ dispersoid morphology via electron tomography: **a)** mapped area at 0° tilt, **b)** same area at 74° tilt, **c)** top view of the reconstructed particles, and **d)** side view of the reconstructed particles.

The dispersoid morphologies changed significantly during extended annealing treatments. Both Zr- and Mn-particles started developing facets upon extended coarsening. Fig. 5.20a shows faceted Al_3Zr dispersoids similar to those in the T351 condition (Fig. 5.18b), except that in this case they were even coarser after 144 h at 535°C. The $Al_{20}Cu_2Mn_3$ dispersoids had well-developed facets on all sides irrespective of their size (Fig. 5.20a). In the T351 temper, the elongated dispersoids had curved edges, but after annealing for 144 h at 535°C these edges became flat and the particles appeared rectangular from the RD-ND section. The same was observed for the smaller dispersoids that appeared elliptical in the T351 condition.

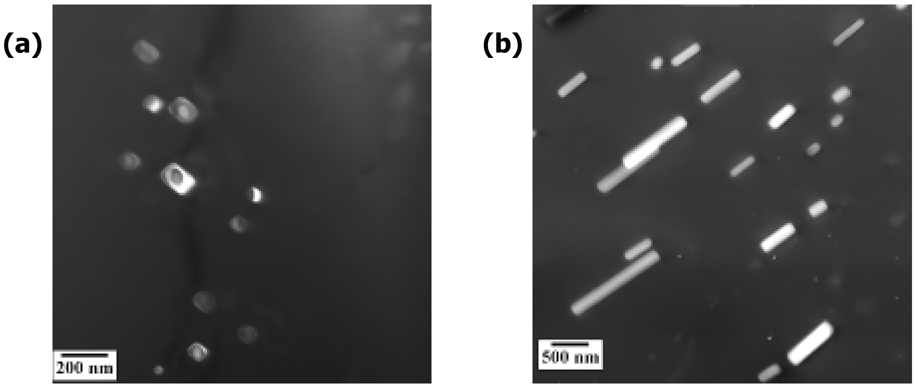

Fig. 5.20: Change in dispersoid morphology during annealing at 535°C: **a)** DF-TEM image of faceted Al_3Zr dispersoids (0.1Zr-0.3Mn alloy, 144 h), and **b)** STEM-HAADF image of elongated $Al_{20}Cu_2Mn_3$ dispersoids with distinctly developed facets on all sides (0.4Mn alloy, 144 h).

5.5 Dispersoid statistics in the T351 condition

Both dispersoid families were analysed systematically in the T351 rolled sheet condition in terms of their size, size distribution and volume fraction. Statistical measurements were obtained below the surface and from the mid-thickness by examining samples prepared from the RD-TD plane, so as to assess the degree of the through-thickness gradients caused by the macroscopic compositional and thermal variations. Samples from the RD-ND plane were also examined in order to evaluate the influence of recrystallised and unrecrystallised grains on the particle size and morphology. This sample orientation is more representative of the microstructure, since it helps to understand the interaction of the dispersoids with GBs and to make direct comparisons with EBSD maps.

The most important observation was that the Al_3Zr dispersoids exhibited an obvious dependence on the alloy composition. The addition of Mn generally increased their average diameter, equally to the reduction of the Zr content.

The dispersoid size was also found to differ throughout the sheet thickness. The Al_3Zr dispersoids were larger near the surface compared to the mid-thickness sheet plane, in all the Zr-containing alloys in the T351 condition (Fig. 5.21a). This difference seemed to depend mainly on the alloy composition, being larger in the Mn-containing alloys.

The 0.1Zr alloy, with an almost unrecrystallised microstructure throughout the sheet thickness, had the smallest difference in the Al_3Zr diameter. In the 0.1Zr-0.3Mn alloy, there was a large difference in the dispersoid size, which could be associated with the Zr macrosegregation towards the sheet mid-thickness. The coarser Al_3Zr distribution near the surface was, thus, unable to restrict recrystallisation and this led to a large difference with the recrystallised volume fraction at mid-thickness (§4.2), where the dispersoid size was much smaller. This might be another consequence of the combined Zr-Mn addition. However, this was difficult to determine experimentally.

In the 0.1Zr-D alloy which underwent a prolonged homogenisation treatment, with a second isothermal stage at a higher temperature, there was barely any difference in the Al_3Zr dispersoid size between the surface and mid-thickness. This alloy also showed a larger recrystallised volume fraction at the sheet surface. This occurred because the generally coarse size of Al_3Zr dispersoids could then not sufficiently pin the GB motion driven by a higher stored energy in the surface region after rolling.

Fig. 5.21b shows the change in dispersoid length and width in each Mn-containing alloy. The length of the $Al_{20}Cu_2Mn_3$ dispersoids exhibited no consistent variation throughout the sheet thickness. The most reliable data seems to be that of the dispersoid width, which exhibited a clear trend and decreased from the 0.1Zr-0.3Mn alloy to the 0.05Zr-0.3Mn and finally to the 0.4Mn. It appears from the graph that by increasing the Mn/Zr ratio, the width of the Mn-particles decreases. Although this reduction was marginal, it was later confirmed to be real by the coarsening kinetics data given in §5.6.2, where the same trend was observed for the three Mn-containing alloys and it became more pronounced after a prolonged annealing treatment. Thus it is possible that the $Al_{20}Cu_2Mn_3$ phase was affected by the presence of the Zr solute. On the other hand, the dispersoid length can be affected by several factors such as particle break up during rolling and cutting due to GB migration. This may explain the absence of a constant trend in the data of Fig. 5.21b.

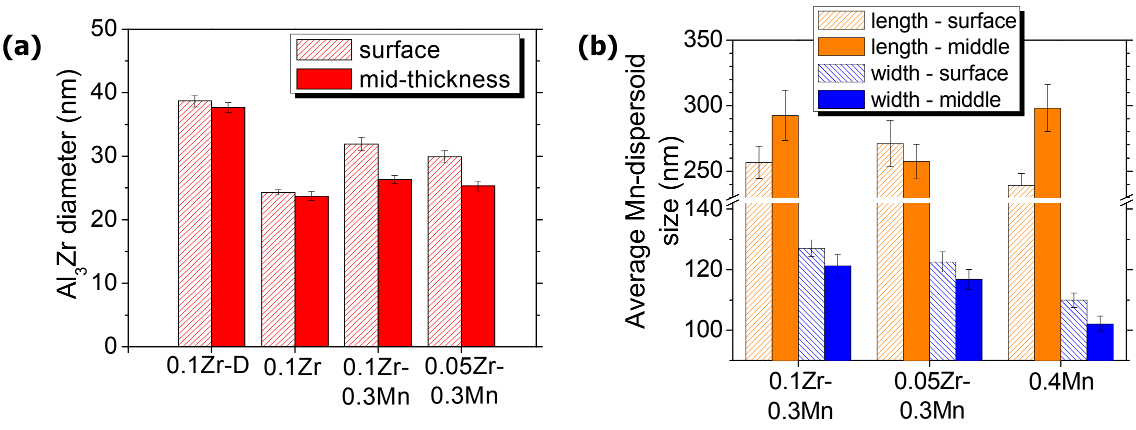

Fig. 5.21: Influence of through-thickness position and recrystallisation on the Al_3Zr size: **a)** Al_3Zr diameter at the sheet surface and mid-thickness, and **b)** plot of the average length and width of the $Al_{20}Cu_2Mn_3$ dispersoids in the T351 sheet at the surface and mid-thickness.

Samples were also prepared from the RD-ND plane. Fig. 5.22 presents the change in the average size of both dispersoid types in all alloys in the T351 condition. Again, the largest Al_3Zr particles were found in the 0.1Zr-D alloy and the smallest ones in the 0.1Zr alloy. The Al_3Zr dispersoids were again found to be coarser in the 0.1Zr-0.3Mn alloy compared to the 0.1Zr with the same homogenisation treatment. The difference in the RD-ND section was that the 0.05Zr-0.3Mn alloy appeared to have coarser Al_3Zr dispersoids than the 0.1Zr-0.3Mn alloy. This result is more reasonable compared to the RD-TD section, since the lower Zr supersaturation in this alloy was expected to yield larger particles. Regarding the $Al_{20}Cu_2Mn_3$ dispersoids, the trend in size for the various compositions is clearer compared to the previous measurements from the RD-TD plane. The length increases and the width decreases in the order: 0.1Zr-0.3Mn, 0.05Zr-0.3Mn, 0.4Mn.

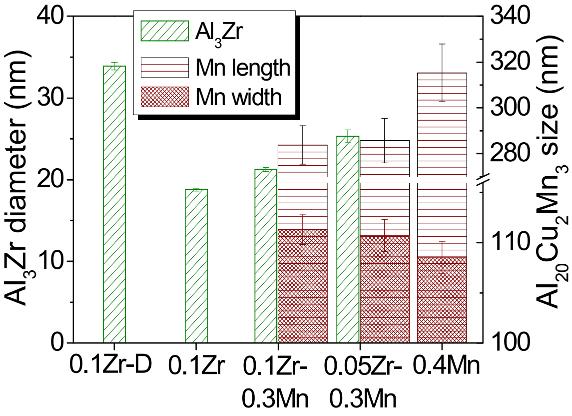

Fig. 5.22: Average size of the spherical Al_3Zr and elongated $Al_{20}Cu_2Mn_3$ dispersoids, measured from the RD-ND plane in the T351 temper for all alloys.

Particle volume fractions were measured in the as-received T351 temper in the TEM with the method explained in Appendix I. These measurements were carried out so as to try to explain the phenomenon mentioned in §4.4, where the Al_3Zr number density was seen to dramatically decrease in the presence of Mn. Knowledge of the dispersoid volume fraction helps to assess the pinning pressure exerted on the GBs by each dispersoid type, when it is combined with the average particle size (V_f/r ratio). However, the number density and interparticle spacing in three dimensions are also of great importance. It should be pointed out that all the values in the graphs of Fig. 5.23 correspond to dispersoid bands only and are not average values in the whole volume as presented in a previous publication [237]. The average interparticle spacing, Δ_3, in three dimensions was calculated by Eq. 5-5, after calculating the average particle number density N_v [14]:

$$N_v = \frac{3V_f}{4\pi r^3} \qquad (5\text{–}4)$$

$$\Delta_3 = 0.554 \cdot N_v^{-1/3} \qquad (5\text{–}5)$$

The fine and coherent Al_3Zr dispersoids were expected to offer a higher GB pinning compared to the larger and incoherent $Al_{20}Cu_2Mn_3$ particles [132]. Although theoretically the V_f/r ratio is directly proportional to the pinning efficiency of the dispersoid content, a detailed study of the graphs in Fig. 5.23 indicates that the pinning capability of the Al_3Zr particles does not solely depend on the V_f/r ratio. This was concluded from the fact that the 0.1Zr-D alloy had a larger V_f and V_f/r ratio than the standard 0.1Zr alloy (Figs. 5.23a,b), but lower recrystallisation resistance. This difference is probably caused by the much lower number density and the larger interparticle spacing of the Al_3Zr dispersoids (Figs. 5.23c,d) after the duplex homogenisation treatment, which are a consequence of their much coarser size. When Mn was added together with Zr, the V_f and V_f/r ratio values of the two alloys did not exhibit significant differences, but were still slightly higher for the 0.1Zr alloy. In contrast, the number density was lower and the interparticle spacing higher for the 0.1Zr-0.3Mn alloy.

Regarding the $Al_{20}Cu_2Mn_3$ dispersoids, their volume fractions were an order of magnitude higher than of the Al_3Zr particles, despite their lower number densities (Fig. 5.23c). The V_f, V_f/r and number density clearly increased when lowering the Zr content and increasing Mn (Fig. 5.23a), with the 0.4Mn alloy exhibiting the highest values. The opposite trend was observed for the interparticle spacing as well. It thus appears that zirconium reduces the density of $Al_{20}Cu_2Mn_3$ dispersoids in the same way that manganese inhibits the formation of Al_3Zr dispersoids. Hence, mutual impedance exists when these two elements are added together. Another important conclusion from these graphs is that the Al_3Zr phase is the most important in controlling recrystallisation.

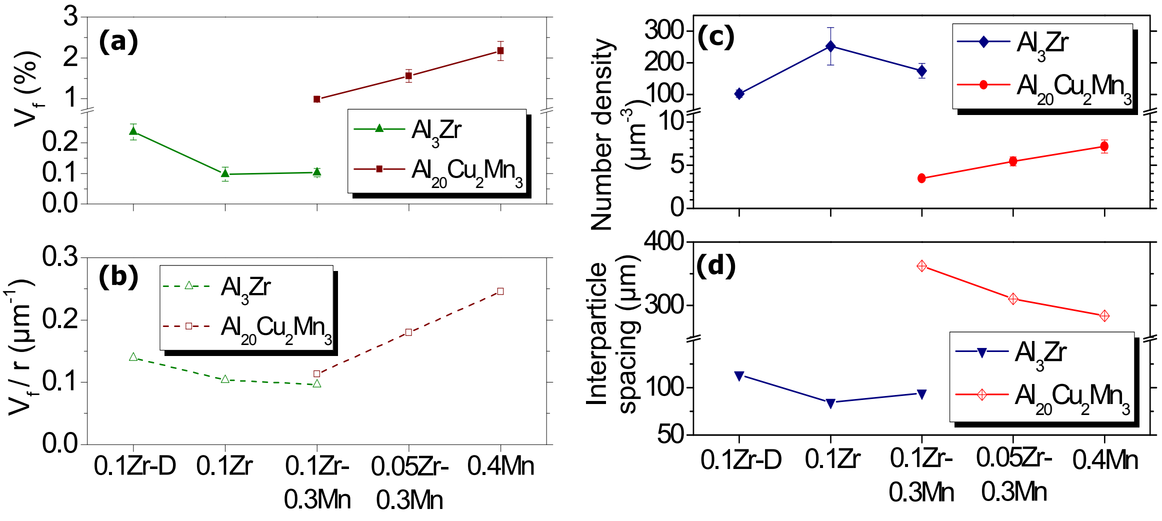

Fig. 5.23: Measured volume fractions and related parameters for the Al_3Zr and $Al_{20}Cu_2Mn_3$ dispersoids in the T351 temper (RD-ND plane): **a)** volume fraction, **b)** V_f/r ratio, **c)** dispersoid number density, and **d)** interparticle spacing in three dimensions.

In short, the V_f/r ratio is not the sole critical parameter that defines recrystallisation resistance, as the number density and interparticle spacing in three dimensions appear to relate better to the susceptibility to recrystallisation. The 0.1Zr alloy had the highest Al_3Zr number density of all the Zr-containing alloys and also the smallest particle size, a fairly high V_f/r ratio and the lowest interparticle spacing. The $Al_{20}Cu_2Mn_3$ dispersoids had a much higher volume fraction and higher V_f/r ratio than the Al_3Zr particles, but their lower number density and larger interparticle spacing deteriorated their pinning capability to a great extent. The best Mn-particle distribution was exhibited by the 0.4Mn alloy, but obviously alone was not sufficient to prevent recrystallisation. The interaction between the Al_3Zr and $Al_{20}Cu_2Mn_3$ dispersoids in the 0.1Zr-0.3Mn alloy seemed to be bilateral, with each dispersoid family forming at a lower volume fraction and number density in the presence of the other.

5.6 Dispersoid coarsening behaviour

A study of the dispersoid coarsening kinetics can help understand how they develop during the processing stages. Measurements were carried out for both Zr- and Mn-dispersoids. Annealing took place at 535°C from two different tempers; the as-deformed F temper and the solution treated, stretched and naturally aged T351 temper. A comparison between these two tempers, as well as between recovered and recrystallised areas, was used to show the effect of contact with boundaries, as well as dislocations, on Al_3Zr coarsening.

5.6.1 Al_3Zr dispersoid coarsening

An anticipated size difference between Al_3Zr dispersoids from recrystallised and recovered areas is illustrated in Fig. 5.24a for the 0.1Zr-0.3Mn alloy, starting from the F temper. The largest difference between Al_3Zr particles in these two regions was observed for the initial T351 condition (Figs. 5.24b,c). This difference was most probably caused by microsegregation effects remaining from the as-cast microstructure. In areas of grains where coarser Al_3Zr dispersoids formed due to a low initial solute supersaturation in the casting, recrystallisation could not be sufficiently suppressed during the following processing stages and these particles were consequently found within recrystallised grains in the T351 condition. An example of this phenomenon is shown in Fig. 5.24d. This hypothesis is also supported by the data in §5.7.1.

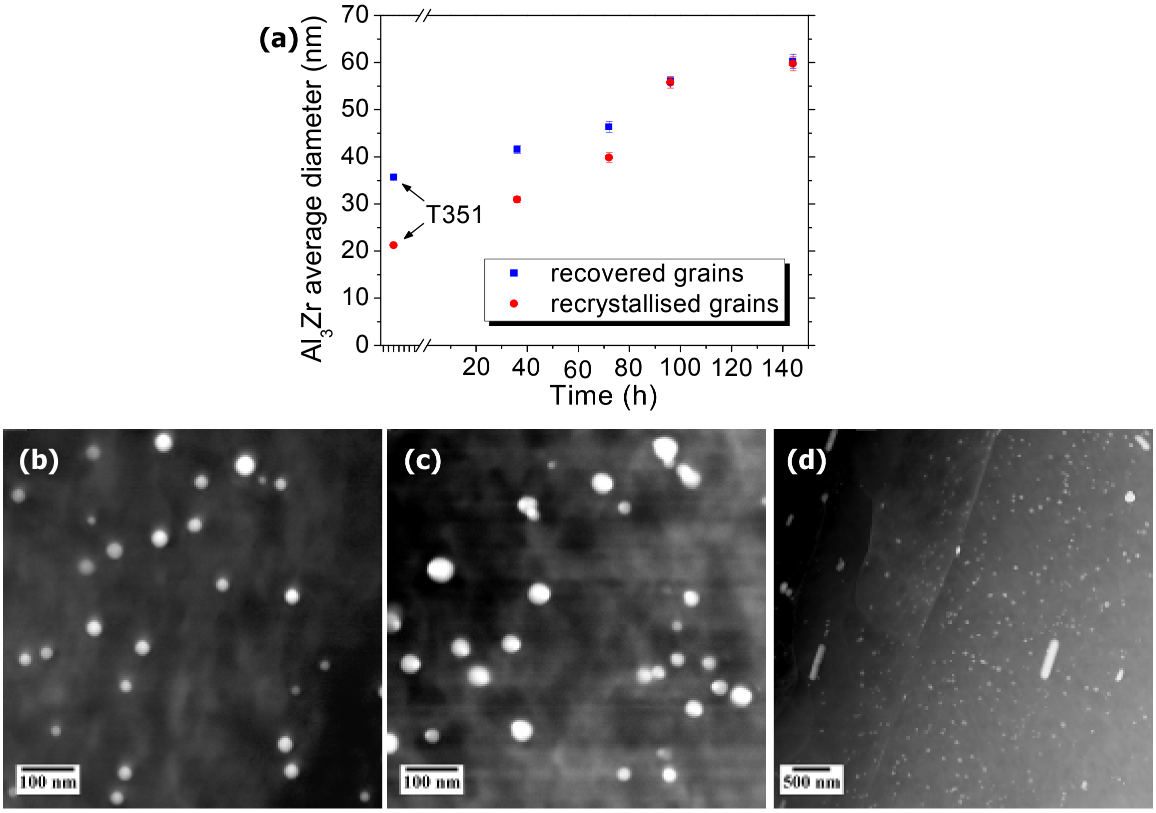

Fig. 5.24: Al_3Zr coarsening in the 0.1Zr-0.3Mn alloy: **a)** Al_3Zr coarsening kinetics in recrystallised and recovered areas of the 0.1Zr-0.3Mn alloy after annealing at 535°C from the F temper, **b)** Al_3Zr distribution in a recovered area in T351, **c)** Al_3Zr distribution in a recrystallised grain in T351, and **d)** Al_3Zr distribution near the recrystallisation front (T351).

Reports exist in the literature where a large difference in particle size has been found in recrystallised grains compared to recovered grains [139, 140]. The particles investigated contained elements that could diffuse fast in the Al matrix and such a change in size was thus possible during the annealing treatment due to the phase transformation that took place on the migrating front (e.g. the β'-Mg_2Si phase transformed to β [139] and the θ′ phase to θ [140]). However, Zr does not diffuse as quickly and such a phase transformation has not been observed here for the Al_3Zr phase. The results of Himuro et al. [138] contradict this claim, but they did not take into account the fact that the $(Al,Si)_3Zr$ dispersoids found within recrystallised grains might have been there from the as-cast state. They proposed that in this case a migrating front was responsible for the transformation of fine, coherent Al_3Zr precipitates into Si-containing ones, which were incoherent and much coarser than in the unrecrystallised grains. However, in the work of Himuro et al., the material was not homogenised and segregation probably existed in the microstructure, facilitating heterogeneous precipitation phenomena similar to the one they observed.

5.6.2 $Al_{20}Cu_2Mn_3$ dispersoid coarsening

The coarsening rate of the $Al_{20}Cu_2Mn_3$ dispersoids was quantified at three stages during annealing at 535°C, within recrystallised grains in each alloy examined. The choice of recrystallised grains was necessary for the sake of consistency in all three alloys analysed for this purpose, since the 0.4Mn alloy was fully recrystallised, even in the T351 condition. Between 200 and 400 particles were measured for each alloy at every condition, in order to obtain statistically reliable results. The results are given in Fig. 5.25.

During annealing, the length and width of the $Al_{20}Cu_2Mn_3$ dispersoids showed a prominent increase in most cases (Fig. 5.25). In the 0.4Mn alloy only, there seemed to be stagnation in length over 72 h at 535°C. The largest increase in length was exhibited by the 0.05Zr-0.3Mn alloy, while the largest increase in width was seen for the 0.1Zr-0.3Mn alloy. It was observed that the dispersoid coarsening behaviour varied relative to the alloy's precise Zr and Mn contents. The massive rise in width upon annealing of the 0.1Zr-0.3Mn alloy indicates that coarsening was more rapid along the short axis of the elongated particles compared to their long axis, whereas the width increased less quickly in the 0.05Zr-0.3Mn alloy and faster along the long axis, with their aspect ratio decreasing. Finally, coarsening in the 0.4Mn alloy occurred almost equally in both axes since the aspect ratio remained constant.

As a general trend, a higher Zr content favoured the thickening of the $Al_{20}Cu_2Mn_3$ dispersoids in the 0.1Zr-0.3Mn alloy, as illustrated by the decrease in the particle aspect ratio for 72 and 144 h in Fig. 5.25. For a lower Zr content, particle growth was more extensive along the long axis. This was revealed by the increase of the aspect ratio for 72 and 144 h in the 0.05Zr-0.3Mn alloy. An illustration of this effect is shown in Fig. 5.26, where the change in aspect ratio during annealing at 535°C can be seen. Nevertheless, the exact mechanism cannot be explained only from the present results. For the 0.4Mn alloy, the saturation in the increase of length and width at 144 h was indicative of the higher Mn supersaturation in the matrix which led to faster coarsening.

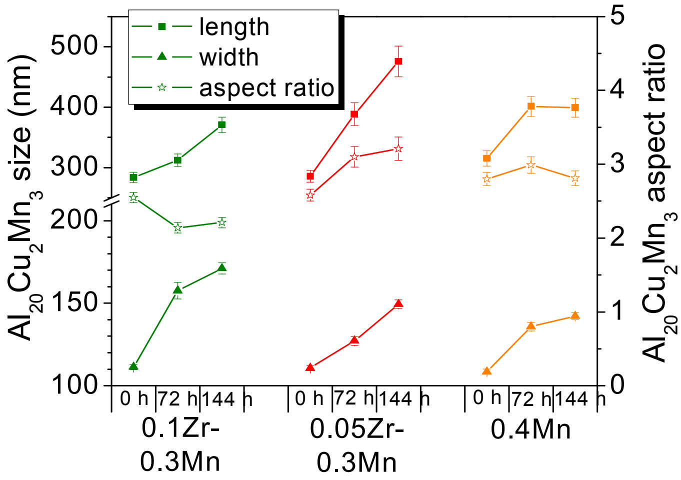

Fig. 5.25: Coarsening data of the $Al_{20}Cu_2Mn_3$ dispersoids as a function of alloy content upon annealing at 535°C from the F temper. The length, width and aspect ratio refer to the RD-ND plane.

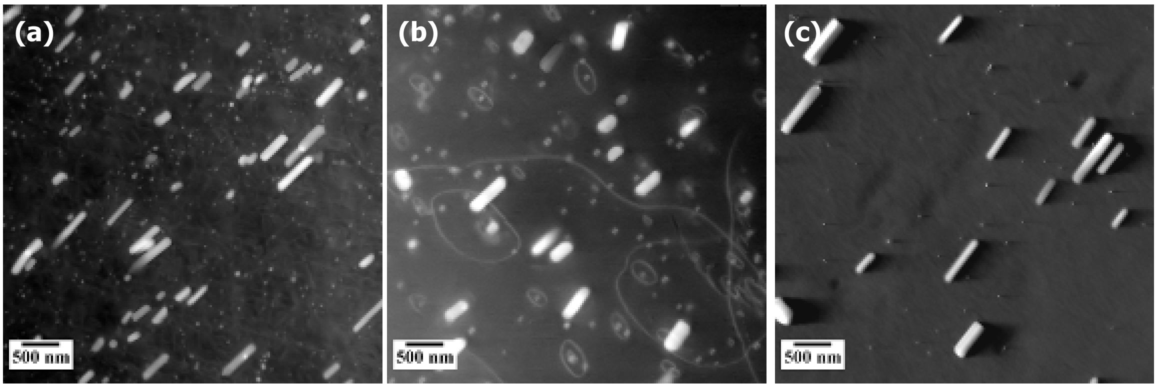

Fig. 5.26: Morphologies of $Al_{20}Cu_2Mn_3$ dispersoids, showing the change in aspect ratio at various stages during annealing at 535°C: **a)** 0.1Zr-0.3Mn alloy in the T351 temper, **b)** 0.1Zr-0.3Mn alloy after 144 h at 535°C, and **c)** 0.05Zr-0.3Mn alloy after 144 h at 535°C.

5.7 Modification of the Al_3Zr distribution in the presence of manganese

Up to this point in the present thesis, it has been shown several times that there is an interaction between Zr and Mn when they are added together as dispersoid-formers in an alloy and it encourages recrystallisation, but the exact mechanisms responsible for this have not been extensively analysed. This last section of Chapter 5 aims to do exactly this. A detailed assessment of all the identified reasons for the reduction of the Al_3Zr pinning pressure is also presented.

5.7.1 Al_3Zr distribution within bands in the rolled sheet

The majority of the recrystallised grains in the 0.1Zr-0.3Mn alloy in the T351 condition were associated with Mn-dispersoid bands. An example is shown in Fig. 5.27a. In this image,

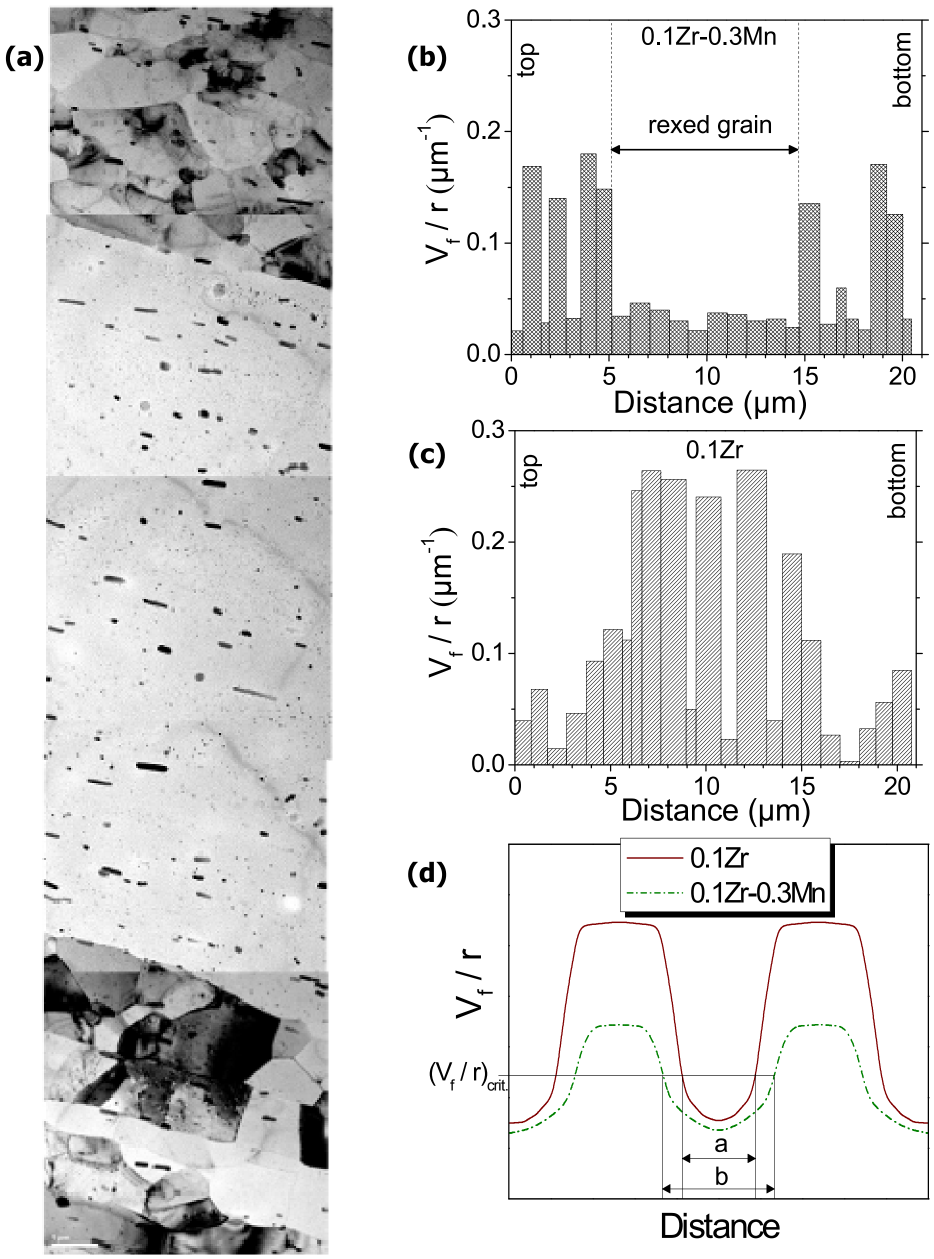

Fig. 5.27: Effect of Al_3Zr dispersoid bands in the rolled sheet on recrystallisation: **a)** showing a band of Mn-dispersoids within a recrystallised grain in the RD-ND plane (annealed 5 min at 535°C), **b)** the V_f/r ratio of Al_3Zr along ND in the 0.1Zr-0.3Mn T351 alloy including a recrystallised grain between two Al_3Zr bands, **c)** the V_f/r ratio of Al_3Zr along ND in the 0.1Zr T351 alloy including an Al_3Zr band, and **d)** schematic diagram of V_f/r ratios across Al_3Zr bands for the 0.1Zr and 0.1Zr-0.3Mn alloys.

a recrystallised grain occupied the region where the number density of the $Al_{20}Cu_2Mn_3$ dispersoids was the highest. The number density of these particles was much lower in the surrounding subgrains. At this stage, it cannot be concluded if the new grain nucleated on these incoherent dispersoids or on larger intermetallics or some other microstructural feature. However, the effect of each dispersoid family on limiting recrystallisation can be determined by quantifying their pinning pressure distribution in such areas, since both were present.

In order to assess the roles of each dispersoid family in the observed recrystallisation phenomenon discussed here, the typical V_f/r ratio of the Al_3Zr particles was measured along a short ND segment for the 0.1Zr and 0.1Zr-0.3Mn alloys in the T351 condition. This parameter provides some indication of the GB pinning pressure. Fig. 5.27b clearly shows that in the 0.1Zr-0.3Mn alloy the Al_3Zr particles are severely banded and have a low density where recrystallisation takes place. The growth of the recrystallised grain also stopped at the points where the V_f/r value was high enough to restrict further migration of the HAGB. The V_f/r values were extremely low within the recrystallised grain, thus, little significant pinning was offered. This effect on the Al_3Zr dispersoid distribution is a leftover from the microsegregation of Zr and Mn in the as-cast microstructure, but is also probably a sign of a strong interaction between the two dispersoid families. The result is that in the rolled sheet in T351, recrystallisation can initiate more easily within the $Al_{20}Cu_2Mn_3$ dispersoid bands due to the low pinning pressure from Al_3Zr particles in these areas.

In the case of the 0.1Zr alloy, the Al_3Zr distribution was distinctly different along a ND segment of similar length as before (Fig. 5.27c). The dispersoid bands were much wider and with a much higher V_f/r value than for the 0.1Zr-0.3Mn alloy. Even outside the band, V_f/r was not as low and was also higher than in the recrystallised grain in Fig. 5.27b. In this case the bands with lower dispersoid pinning pressures were obviously not wide enough to permit possible growth of recrystallised grains.

In rolled thin sheet the $Al_{20}Cu_2Mn_3$ dispersoids cannot apply adequate pinning pressure on their own, as concluded from the 0.4Mn alloy which contained solely Mn-dispersoids and was fully recrystallised in T351. Hence, a very important parameter regarding recrystallisation is the ND spacing between Al_3Zr bands that can offer sufficient pinning pressure, since if this is too small there would not be enough space for a new grain to reach a critical size for growth.

A schematic diagram of the suggested model can be seen in Fig. 5.27d, which describes the variation in the Al_3Zr pinning pressure along ND. Since a critical V_f/r value is required for GB pinning to be effective, a microstructure with narrower Al_3Zr bands would incur a larger distance between them where the pinning pressure would be inadequate to inhibit recrystallisation. A direct consequence of this would be an increase in the possibility of nucleation events for new grains in these areas. This spatial consideration is demonstrated in the same graph by the widths 'a' and 'b' which show the distance between points of equivalent V_f/r ratio for both the 0.1Zr and 0.1Zr-0.3Mn respectively.

5.7.2 Spatial correlation of Al_3Zr and $Al_{20}Cu_2Mn_3$ dispersoids

The Al_3Zr distribution within bands of $Al_{20}Cu_2Mn_3$ dispersoids was observed in three dimensions with the aid of electron tomography in the TEM in an attempt to determine if any spatial correlation existed between them. From these experiments it was verified that the number density of the Al_3Zr particles was quite low in such regions. A sequence of TEM images at subsequent tilt angles is presented in Fig. 5.28. It was proven that the two dispersoid types are not connected in any way and there was no preferential nucleation on

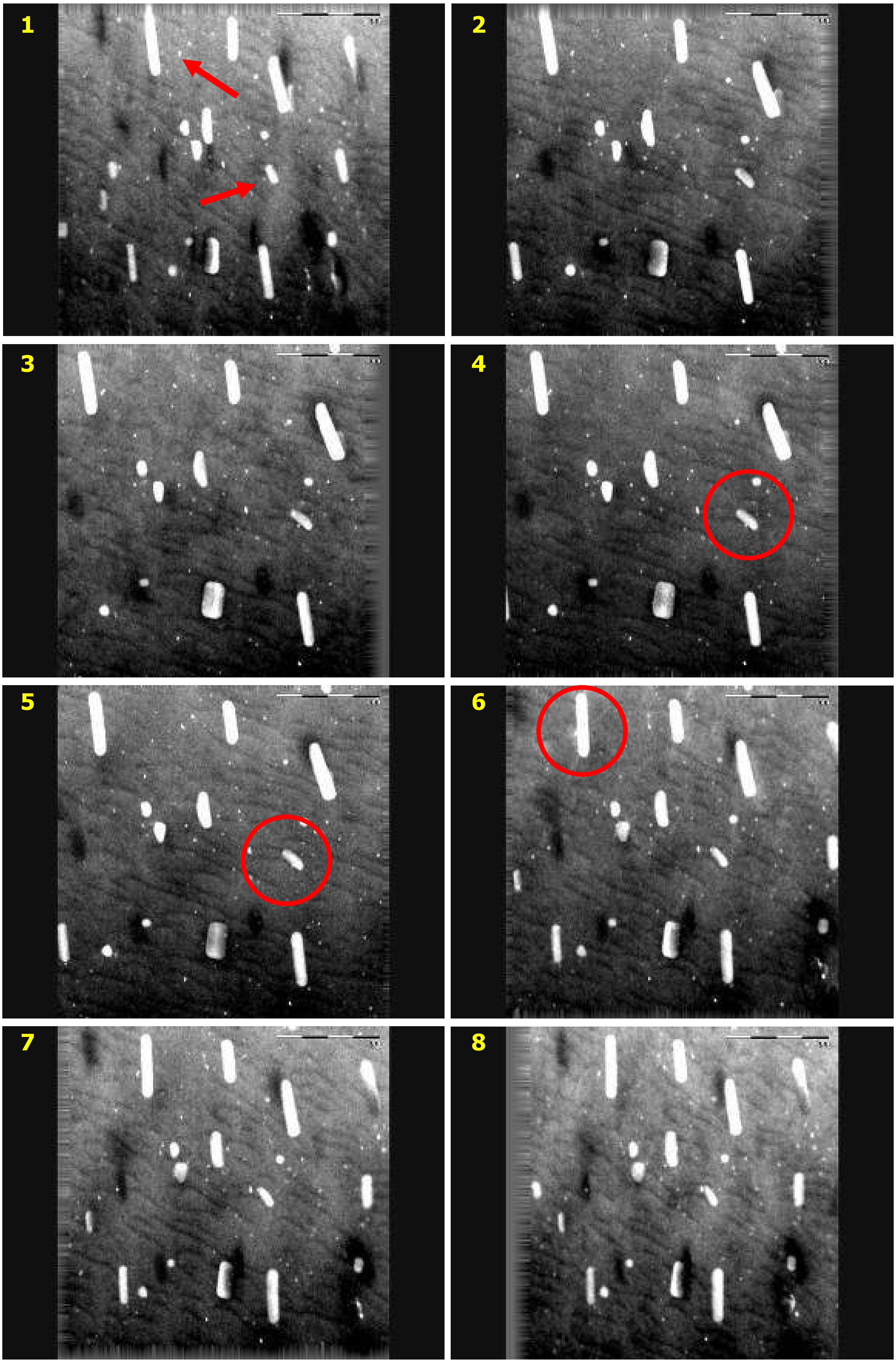

Fig. 5.28: Sequence of images (1-8) taken at different tilt angles of the TEM sample during an electron tomography experiment. The Al_3Zr dispersoids are shown not to be spatially related to the $Al_{20}Cu_2Mn_3$.

each other, as already discussed in §5.3.2. If one follows the small particles indicated by red arrows through the sequence of images, it is obvious that at some tilt angles they appear to be attached to the interface of a Mn-dispersoid. However, this is merely due to overlapping within the thickness of the TEM foil. When looking at a normal TEM sample in plan view, this overlap is not directly evident and could be mistaken as co-nucleation.

5.7.3 Influence of manganese on zirconium inclusion within particles other than Al_3Zr

Since the Al_3Zr volume fraction was found to decrease in the 0.1Zr-0.3Mn alloy as mentioned earlier, detailed EDX analysis was carried out in order to determine if there was any Zr inclusion into other types of particles. Samples were investigated from the homogenised, T351 and annealed conditions, to see if dissolution occurred into different phases at each stage. The results verified that Zr is incorporated into phases other than Al_3Zr at all the stages analysed.

Particles analysed by means of TEM-EDX in the fully homogenised AA2050 ingot slice are presented initially. Fig. 5.29 illustrates some examples of Mn-particles that were found to include Zr. All three cases involved particles that contained Al, Cu, and Mn. Image (a) shows a small particle attached to a larger substrate particle right on the GB. The underlying particle contained only Al, Cu, Mn and trace of Fe at some points with no Zr. Image (b) presents another $Al_xCu_yMn_z$ particle on a GB which contained a trace of Zr. From these two images it is concluded that traces of Zr could be detected in some dispersoids or GB phases after homogenising the cast billet, although this could have happened during solidification. But particles in the interior of the grain also contained Zr. Image (c) shows a relatively small $Al_xCu_yMn_z$ particle in the grain interior that again contained some Zr (located at 0.17 normalised distance from the GB - see Fig. 5.30).

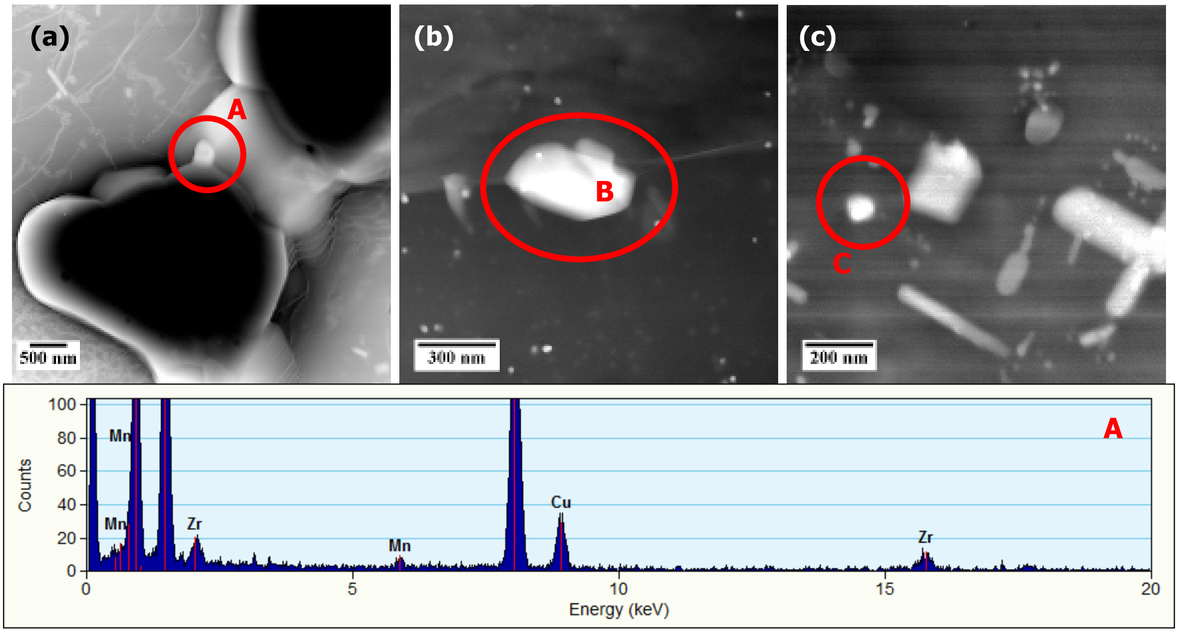

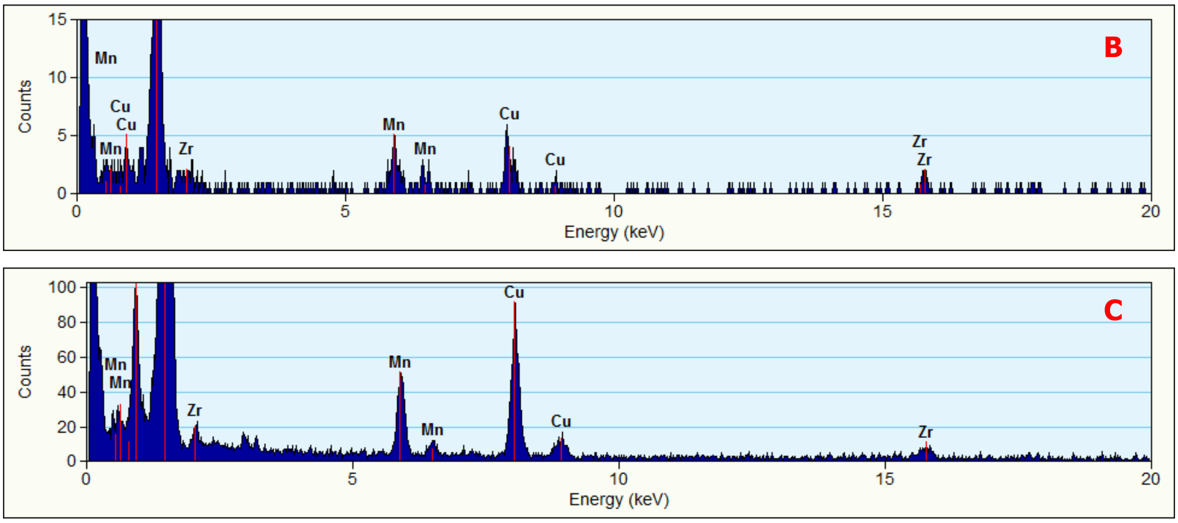

Fig. 5.29: $Al_xCu_yMn_z$ particles containing Zr after homogenisation for 12 h at 505°C: **a)** particle lying on a larger GB phase, **b)** individual particle on a GB, and **c)** particle in the matrix. The EDX diagrams for the particles A, B and C in the STEM-HAADF images are also presented.

In the fully homogenised condition, particles were analysed across a grain in the fully homogenised AA2050 to identify the locations where Zr would be incorporated within particles other than the Al_3Zr. Such particles were found in the whole area analysed, from the GB to the grain centre, but mainly closer to the GB (Fig. 5.30). The exact positions of the particles within the grain have been marked with a cross in the graph below. In particular, most of the particles containing Zr were found closer to the GB and this is owing to two reasons. First, the total number density of Mn-containing particles is much lower near the grain centre and proportionally fewer particles are expected to interact with Zr. The second argument is that near the GB the Zr supersaturation is extremely low, as Fig. 5.8a showed earlier. Hence, heterogeneous precipitation phenomena are expected in that area, which can explain how Zr atoms ended up contained in Mn-dispersoids.

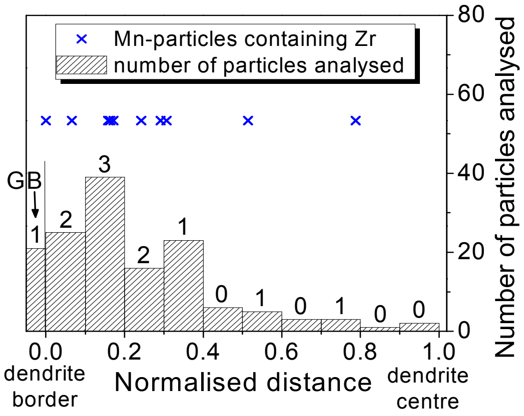

Fig. 5.30: Positions across half a dendrite length for Mn-particles that were found to contain Zr. The number of particles that contained Zr in that region of the grain is written above the columns.

Despite the solid evidence for this interaction between Zr and Mn, the frequency of this phenomenon was such that it indicated that it may not be the entire reason for the reduction in the Al_3Zr volume fraction. Zirconium was present only in a very small percentage of Mn-containing and other particles and at a minimal concentration. The data from the EDX analysis of one grain only was quantified and the frequencies for all types of particles are listed in Table 5.2. It is clear that faceted and elliptical particles in the matrix are most frequently detected to contain Zr, but also GB phases contain Zr quite often. On the contrary, no Zr was found in the highly elongated dispersoids, although a very large number of them was analysed.

Table 5.2: EDX results showing the frequency of Zr incorporation within $Al_xCu_yMn_z$ particles in the grain analysed in the fully homogenised AA2050.

	GB phases	**Elongated**	**Elliptical**	**Faceted**	**Total**
Number of particles analysed	21	65	21	37	144
Particles containing Zr	1	0	3	6	10
Percentage (%)	4.76	0	14.29	16.20	6.94

In the T351 condition, it was more difficult to assess the spatial correlation of the particles with the microsegregation patterns in homogenised grains, since the microstructure was highly distorted after rolling. However, some Mn-particles were observed to have Zr in their interior and at their interface. For example, the $Al_{20}Cu_2Mn_3$ dispersoid in Fig. 5.31a showed a low Zr concentration at its centre when scanned across its short axis (Fig. 5.31b). The EDX peaks did not exhibit a high intensity, but the differences sought at such low addition levels were expected to be minor. The particle had an almost elliptical shape and dimensions approximately 80 x 150 nm. An example of the high aspect ratio $Al_{20}Cu_2Mn_3$ dispersoids without any detectable Zr is given in Figs. 5.31c,d.

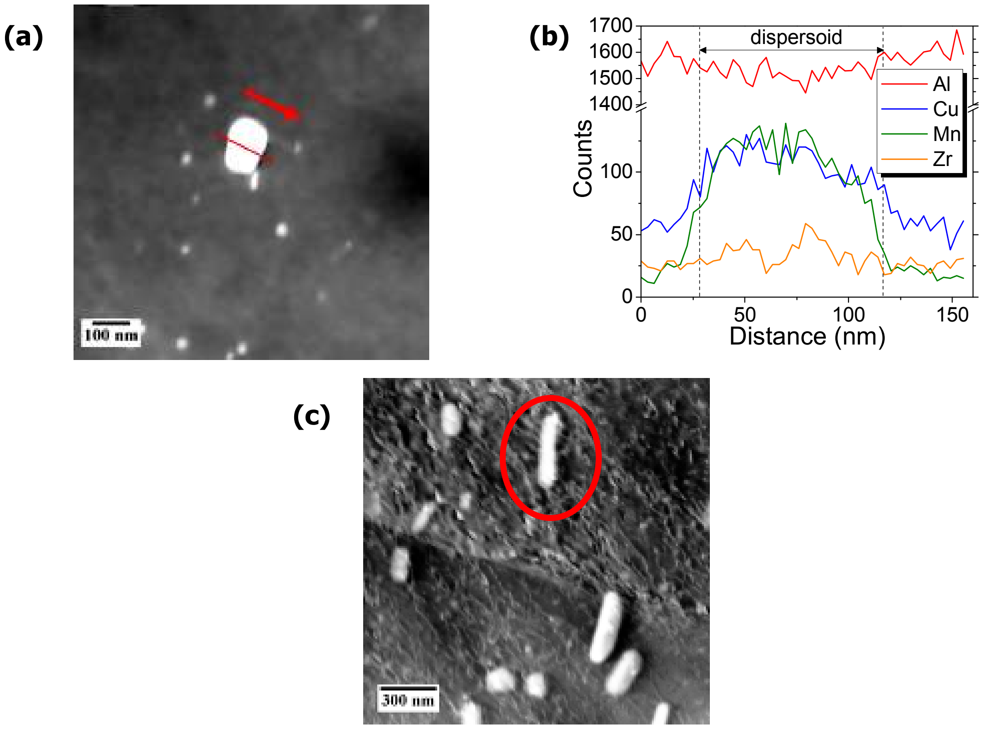

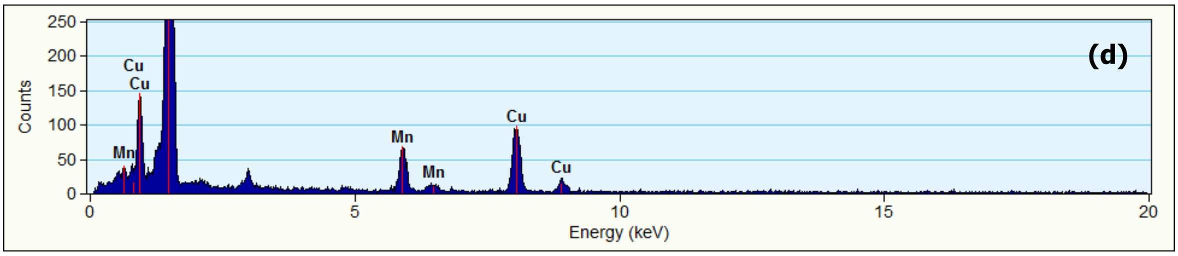

Fig. 5.31: $Al_{20}Cu_2Mn_3$ dispersoids analysed by TEM-EDX in the rolled T351 temper: **a)** an elliptical dispersoid containing Zr, **b)** EDX profiles of the main elements across the elliptical dispersoid, **c)** an elongated dispersoid not containing any detectable Zr, and **d)** EDX spectrum of the elongated dispersoid.

Another $Al_{20}Cu_2Mn_3$ dispersoid presented in Fig. 5.32 exemplifies a more complicated case in STEM-HAADF imaging, where atomic number contrast is visible and higher atomic numbers appear brighter. A bright layer located mainly at its interface, but also in its interior, was indicative of the presence of Zr. EDX line scans were performed across the short and long axes of the dispersoid (Figs. 5.32b,d). Along the short axis, Zr was found segregated at the two interfaces. In the long axis Zr was detected close to the interface, not right on it on one side of the particle, but exactly at the interface on the other side. This segregation pattern cannot be explained in much detail with the present EDX results. However, during growth the slowest diffusing elements usually form a shell around a particle containing other core elements which diffuse faster. This has been clearly observed for $Al_3(Zr,Sc)$ dispersoids where the more slowly diffusing Zr forms a shell around a Sc-rich core [292]. In the present case, Zr diffuses more slowly in the Al matrix compared to Cu and Mn [276], thus it would be expected to segregate at the particle interface. This result is the first detailed study of Zr dissolution within Mn-dispersoids, after the initial assumptions by Ohashi et al. [167] and the more recent EDX results of Kaibyshev et al. [151].

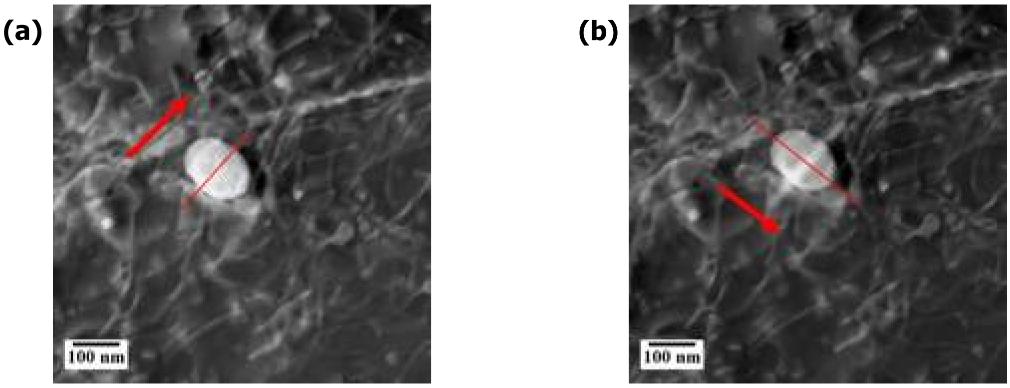

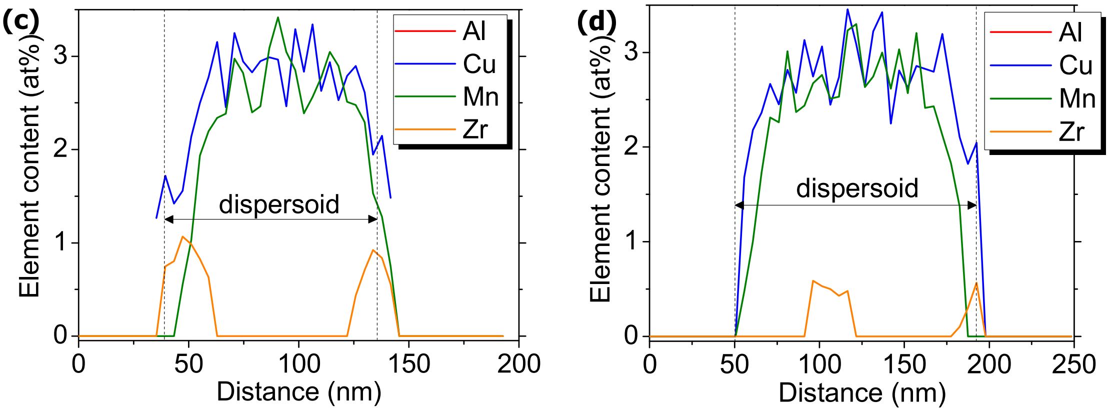

Fig. 5.32: $Al_{20}Cu_2Mn_3$ dispersoid containing bands of Zr at its interface and interior (STEM-HAADF images): **a)** EDX line scan across the short axis of the dispersoid, **b)** EDX line scan across the long axis of the same dispersoid, **c)** Zr profile for scan in (a), and **d)** respective Zr profile for scan in (b).

During annealing of the 0.1Zr-0.3Mn alloy from the F temper, a new phase was found that had not been observed in the two previous conditions. EDX analysis proved that this phase had a composition $Al_xCu_yZr_z$. These particles were found within recrystallised grains and also on the recrystallisation front after annealing for 4 min at 535°C. Examples can be seen in Figs. 5.33a-c highlighted by red circles. A composition plot was constructed in order to define the composition of the phase (Fig. 5.33d). Most data points seem to fall on straight lines that approach the chemical composition of the Al_2Cu phase. Straight lines were carefully fitted to the data points of Cu and Zr individually so as to derive an equation that best described the observed trend. To achieve this, a small number of data points had to be masked. The equations of the fitted lines were:

$$[Cu] = -0.914 \cdot [Al] + 91.718 \qquad (5\text{-}4)$$

$$[Zr] = -0.085 \cdot [Al] + 8.258 \qquad (5\text{-}5)$$

In the Al_2Cu phase, the concentration of Al is 66.667 at% and of Cu 33.333 at%. By substituting into equations 5-4 and 5-5 the value for [Al] equal to 66.667, the compositions of Cu and Zr became 30.804 and 2.591 at% respectively. The sum of these two contents gave a total of 33.395 at%. So the phase was identified as $Al_2(Cu,Zr)$, with the Zr atoms substituting for the Cu atoms at a ratio of: $\frac{33.333}{2.591} = \frac{12.865}{1}$

This means that approximately one every 13 atoms of Cu is substituted by a Zr atom in the crystal lattice of this phase. Other phases reported to include Zr together with Cu and Al, are the $Al_7Cu_3Zr_2$ and Al_3CuZr_2 [293], but these compositions do not match the experimental data of the present study.

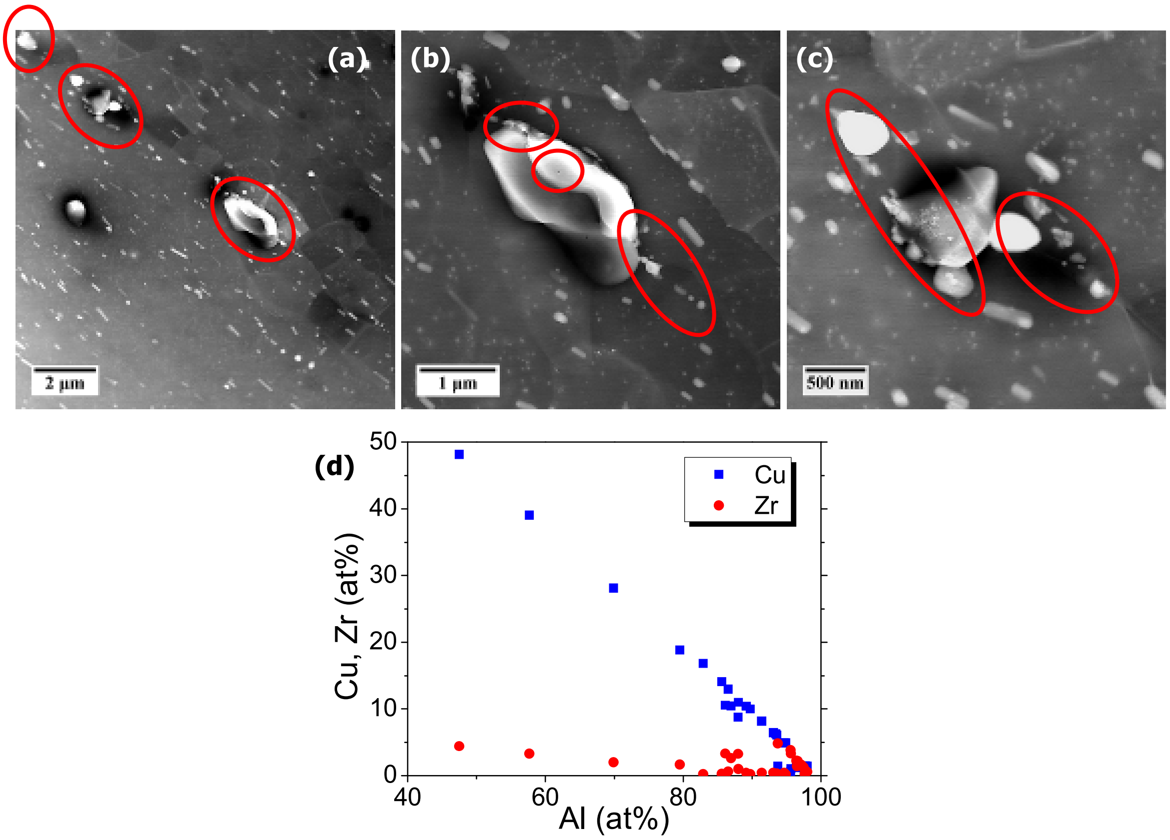

Fig. 5.33: An $Al_xCu_yZr_z$ phase after annealing 4 min at 535°C (in red circles): **a)** large Zr-containing particles lying on a GB, **b)** higher magnification from (a) showing smaller Zr-containing particles in that area, **c)** higher magnification from (b), and **d)** composition plot of Cu and Zr content vs. Al content for the particles seen in recrystallised grains.

On further annealing, a rather rare condition was found, where two large spherical Al_3Zr dispersoids were touching the recrystallisation front and were also in contact with two needle-like particles on the GB (Fig. 5.34a). Only one of these two particles, on the left hand side, contained Zr as shown by EDX line scans (Fig. 5.34b). The one on the right contained only Al and Cu. A fairly strange distribution of Cu seemed to exist since its concentration increased abruptly inside the recrystallised grain on the right side of image (a). This phenomenon probably appeared from Cu atoms that were originally in the GB and dispersed into the matrix when the recrystallisation front migrated, creating a Cu-rich solid solution in that region. On the other hand, Zr atoms were distributed only inside the GB particle. This fact shows that there is no dissolution of Al_3Zr dispersoids in the GB and subsequent re-precipitation from the excess Zr solute in the recrystallised grain.

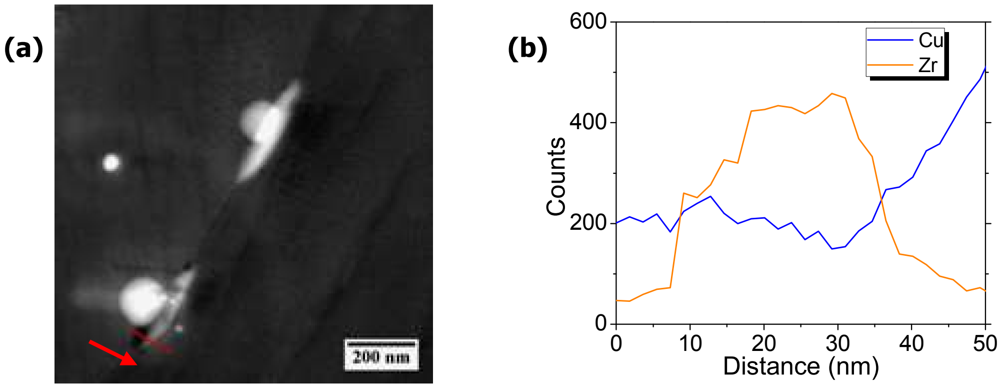

Fig. 5.34: 0.1Zr-0.3Mn alloy after 72h at 535°C: **a)** STEM-HAADF image of two Al_3Zr dispersoids in contact with two elongated particles on a recrystallisation front, and **b)** EDX line profiles of Cu and Zr (in the direction of the red arrow in (a)).

Finally, zirconium was also detected within an $Al_xAg_yZr_z$ phase in the rolled 0.1Zr-0.3Mn alloy in T351 (Fig. 5.35). Fine Ag-containing particles, below 10 nm in diameter, were present in the AA2198 alloy at all processing stages from the F temper to T351 (see Appendix II). They were also seen in the homogenised AA2050. Similar to the previous findings on Zr inclusion, the $Al_xAg_yZr_z$ phase may have appeared in regions of low Zr supersaturation where heterogeneous nucleation is expected.

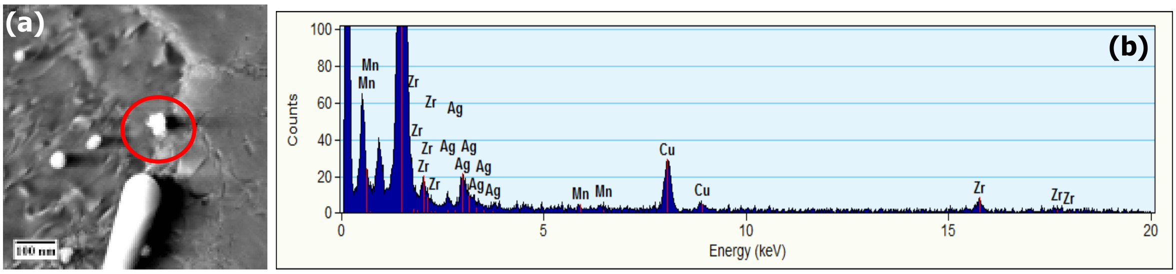

Fig. 5.35: $Al_xAg_yZr_z$ phase in the 0.1Zr-0.3Mn alloy in T351: **a)** STEM-HAADF image showing its morphology, and **b)** EDX spectrum.

5.7.4 Calculation of the amount of Zr dissolved within Mn-containing dispersoids

It is known from the literature that a lower supersaturation of an element leads to a lower nucleation rate of particles containing that element [108]. Model predictions by Robson and Prangnell [113] support that a lower Zr supersaturation led to a lower Al_3Zr volume fraction. Consequently, the particle size is expected to be larger in such cases [294]. This was confirmed by the presence of Al_3Zr dispersoids with larger diameter, lower number density and lower volume fraction in the 0.1Zr-0.3Mn alloy in T351 compared to the 0.1Zr alloy. The current section aims to clarify if this effect emerged from the reduction of Zr in solid solution due to their segregation to Mn-dispersoids.

In order to assess the importance of the effect of the Zr inclusion within Mn-dispersoids, a simple calculation needs to be carried out which will give the maximum amount of Zr that was removed from the matrix. The input data in this calculation are the volume fraction of the Mn-dispersoids (~1%), the fraction of the Mn-particles that contain Zr (~7%, taken from Table 5.2) and the average Zr content present in the Mn-particles (1 at%, taken from Fig. 5.32). It has to be pointed out that the calculated number will constitute the upper limit of the real value, since some of the input parameters are overestimated. I.e. the fraction of Mn-particles containing Zr is in fact smaller than 7% because Table 5.2 presents only particles that were chosen to be analysed with EDX and does not constitute a representative number density for the whole microstructure. A higher number of elliptical and faceted particles were selected during the analysis, since it was known that Zr was more probable to be included in them rather than in elongated dispersoids. Also, the average Zr content within Mn-particles is not known precisely and some more issues arise here. It is not known if the amount of Zr is constant for all particles, due to the heterogeneous segregation pattern as seen from Figs. 5.31 and 5.32. The dispersoids analysed in these two images were found to be rich in Zr either in their core or at their edges. The maximum value measured (~1 at% for the dispersoid in Fig. 5.32) was used for the present calculations. The actual amount of segregated Zr can be seen in Fig. 5.36 for the fully homogenised AA2050. Hence the amount of Zr lost from the matrix would be:

$$0.01 \times 0.07 \times 1 = 7 \cdot 10^{-4} \text{ at\%}$$

and the reduction relative to the initial amount of Zr in the matrix is:

$$\frac{7 \cdot 10^{-4}}{0.1} = 0.007 \text{ or } 0.7\%$$

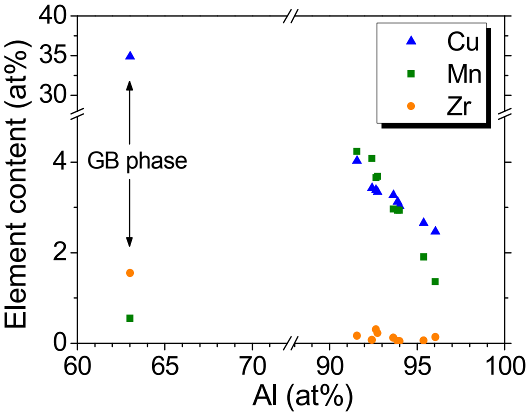

Fig. 5.36: Concentration plot for the Mn-particles of Table 5.2 that were found to contain Zr.

Thus it is reasonable to conclude that the inclusion of Zr within Mn-particles is not a sufficient factor on its own to account for the observed modification of the Al_3Zr distribution. Another explanation for the observed phenomena in this work could be an increase in the solid solubility of Zr in the Al matrix due to the Mn addition, although this is opposing to the existing theories and the anticipated effect would be the opposite. A second possible explanation is the hindering of the precipitation kinetics of the Al_3Zr dispersoids by the Mn addition (the opposite is also valid since Zr appeared to decrease the number density of Mn-dispersoids). However, both of the suggested effects are simply possible causes of the observations and a definite conclusion as to the operating mechanism cannot be drawn from the present results. Indeed, if either of the proposed mechanisms is correct, it is likely to be as a result of local clustering on an atomic scale that would require atom probe work to explore, and this was beyond the scope of the current work.

5.8 Summary of the Zr- and Mn-dispersoid distributions

The present chapter reviewed the distribution of the Zr- and Mn-dispersoids in all the alloys in several conditions, in order to explain the nature of the observed interaction between the two dispersoids families when they are present together, which reduced the number density of Al_3Zr dispersoids. The dispersoid types observed were the Al_3Zr and $Al_{20}Cu_2Mn_3$ phases, as concluded from EDX measurements.

The $Al_{20}Cu_2Mn_3$ phase formed first during homogenisation and then the Al_3Zr phase followed at slightly higher temperatures and longer time. This difference was due to the higher diffusion rate of Mn in the matrix as compared to Zr. These two elements tend to segregate in an opposite manner within the grains, with a high density of Mn-particles forming close to the GBs and a high density of Zr-dispersoids forming in the grain centre. This effect had a direct impact on the particle morphology and resulted in banding that remained even in the rolled T351 condition.

A study of the dispersoid coarsening behaviour provided information regarding the growth of the dispersoids and the factors affecting them. The Al_3Zr dispersoids grew faster in recovered areas compared to recrystallised ones. On the other hand, the $Al_{20}Cu_2Mn_3$ phase was strongly influenced by the presence of Zr, which favoured growth in the short axis of the particles and reduced their aspect ratio.

The dispersoid size was found to be clearly affected by the through-thickness position, extent of recrystallisation, homogenisation treatment and the presence of other alloying elements. The smallest Al_3Zr size was observed in the 0.1Zr alloy, while the $Al_{20}Cu_2Mn_3$ particles were longest in the 0.4Mn alloy.

The interaction between Zr and Mn is complex and gives rise to several effects, with the main parameters affected being the dispersoid size, volume fraction and number density. There seemed to be mutual impedance in the formation of both dispersoid families, since the volume fractions of both phases were significantly decreased when Zr and Mn were added together. The Al_3Zr volume fraction was especially low within bands of Mn-dispersoids. Overall, the lower Al_3Zr number density in the 0.1Zr-0.3Mn alloy increased the width of bands of equivalently low pinning pressure relative to the 0.1Zr alloy. This would have the effect of encouraging recrystallisation, particularly if this band width becomes greater than the critical nucleus size for recrystallisation.

The interaction between Zr and Mn was not possible to be completely clarified in this work. The Zr segregation within Mn-containing particles only contributed to a small extent and thus could not account for all the observed changes in the dispersoid distributions of the two families. Two other reasons might be responsible; an increase in Zr solid solubility or the hindering of dispersoid precipitation kinetics. However, neither of these two arguments could be verified in this work. In addition, the solid solubility of Zr would be expected to behave in an opposite manner and decrease with the Mn addition, according to the current knowledge.

CHAPTER 6: Recrystallisation Resistance as a Function of the Dispersoid Type Present

6.1 Introduction

After analysing the dispersoid distributions and the interaction between Zr and Mn, the next step was to study the mechanisms by which recrystallisation takes place. The mechanisms are expected to rely strongly on the dispersoid content and distribution, and usually more than one is operating in high strength Al alloys. The parameters that affect the nucleation of new grains in the AA2198 materials studied and their further evolution are discussed in this chapter. For this purpose, this chapter starts by presenting the effect of dispersoids on subgrain size, which is directly linked to the stored energy and extent of recovery in each alloy. The recrystallisation kinetics curves are then plotted and discussed for all the alloys. The acting recrystallisation mechanisms are then examined separately for each alloy. In order to study the recrystallisation behaviour, all the alloys had to be heat treated from the as-rolled F temper. However, it should be reminded that the 0.1Zr alloy was only available with the duplex homogenisation treatment in this condition. Thus, when the sole Zr addition is discussed, reference will only be made to this material.

6.2 Effect of heterogeneous Zener pinning on the subgrain size and stored energy

As mentioned in Chapter 5, the inverse microsegregation patterns of Zr and Mn within a dendrite during casting lead to a heterogeneous distribution of dispersoids which remains even in the rolled sheet. Since the Zr addition is more effective in GB pinning than the Mn addition, it is of great interest to determine if their coexistence in the 0.1Zr-0.3Mn alloy would cause a heterogeneous subgrain size distribution locally, depending on the dispersoid type present in that region of the microstructure. A possible heterogeneous subgrain size distribution within the microstructure of the 0.1Zr-0.3Mn alloy would give qualitative information on the stored energy distribution.

The reason for the greater ability of the 0.1Zr-0.3Mn alloy to have a lower average subgrain size compared to the rest of the alloys (§4.2), can be better understood from Fig. 6.1

in combination with Table 6.1. Fig. 6.1a illustrates the benefit of the dual Zr+Mn addition over the sole Zr addition. In area A in the 0.1Zr alloy, the Al_3Zr dispersoid band had a thickness of 1 μm and since the subgrain boundaries lay outside it, subgrain A was allowed to coarsen to a width of 2.40 μm. It should be noted that the boundary moved freely until it reached the neighbouring Al_3Zr dispersoid band at the edge of subgrain B where it came to a halt, hence it appeared completely straight and parallel to the band. On the left side of subgrain A, the boundary still migrated in the dispersoid-free area to the left to reach another Al_3Zr band and this is why it appears to be slightly slanted. It is reasonable to assume that subgrain A expanded due to its larger size compared to the surrounding subgrains, which gave a higher driving force for this movement. In contrast, when the Al_3Zr band width was wider than the subgrain spacing, boundaries were pinned and coarsening was successfully suppressed such as for subgrains B-E in Fig. 6.1a. The Al_3Zr band had a width of 3.50 μm and restrained all the subgrains in that area to an ND spacing smaller than 1.50 μm (Table 6.1). Subgrain F was located at the edge of the Al_3Zr band where only a few coarse dispersoids were present, so the pinning pressure was not high enough to inhibit subgrain growth. In fact, along the line of measurement of the values in Table 6.1, the minimum ND spacing of subgrain F was still larger than the maximum ND spacing of subgrains B to E.

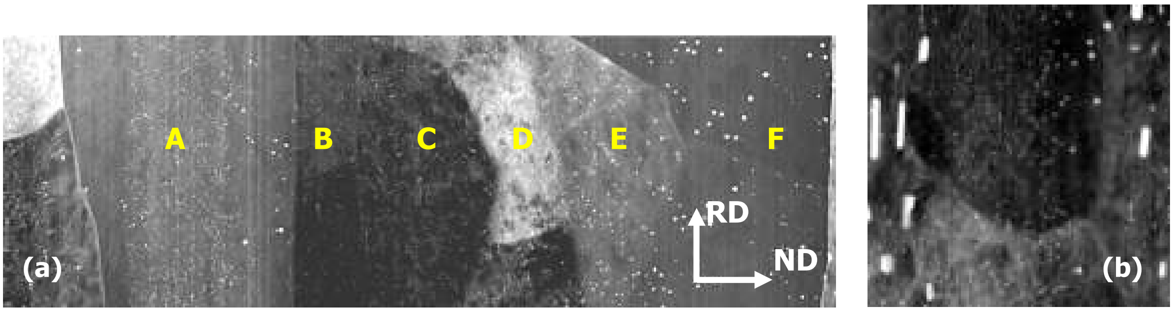

Fig. 6.1: STEM-HAADF pictures illustrating the pinning effect of the two types of dispersoids when present in bands: **a)** correlation of subgrain width to Al_3Zr dispersoid band width in the 0.1Zr alloy, and **b)** $Al_{20}Cu_2Mn_3$ dispersoids pinning subgrain boundaries that have bypassed a narrow band of Al_3Zr dispersoids in the 0.1Zr-0.3Mn alloy.

Table 6.1: Measurements from Fig. 6.1a of the Al_3Zr band spacing and maximum subgrain spacing along ND in the 0.1Zr alloy (T351 temper).

Area	A	B	C	D	E	F
Subgrain spacing (μm)	2.40	0.65	1.50	0.75	1.45	1.55
Al_3Zr band spacing (μm)	1.00	3.50				—

In comparison to the above, Fig. 6.1b depicts the pinning behaviour in the 0.1Zr-0.3Mn alloy. An Al_3Zr band smaller than the subgrain size, was not able to restrict the boundary movement and the subgrain coarsened along the ND. However, the Mn-dispersoids, which were located at the edge of the Al_3Zr band, have pinned the boundary and confined its further migration. In the same region, the 0.1Zr alloy was free of particles and hence the boundaries were free to migrate without meeting any obstacles. Therefore, the as-cast microstructure in combination with the homogenisation process and the rolling schedule, were crucial to the recrystallisation resistance of the alloy. All these processing stages affect the width of the Al_3Zr-free bands and the subgrain spacing, so the relative values of these two parameters can have a significant effect on the subgrain size after recovery.

All the above discussion can be verified by Fig. 6.2. The subgrain structure of the 0.1Zr-0.3Mn alloy was quite different. The Al_3Zr bands produced larger and more elongated subgrains (Fig. 6.2a) in contrast to the effects of the $Al_{20}Cu_2Mn_3$ bands and of the Mn solute that produced subgrains of lower size and aspect ratio (Fig. 6.2b). This fact is in agreement with the aspect ratios measured through the sheet thickness, which are presented later on in Fig. 6.22c.

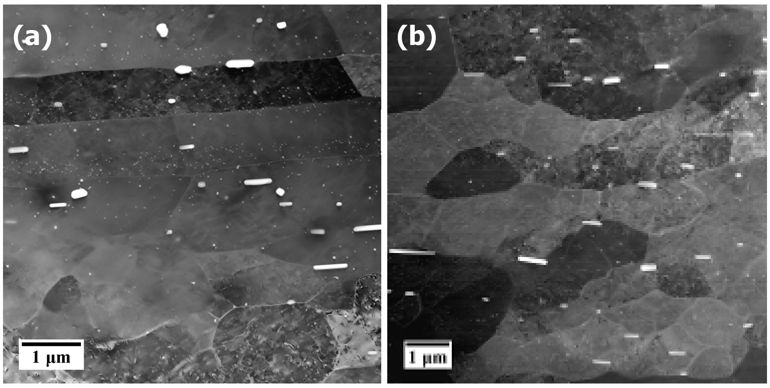

Fig. 6.2: Variation in subgrain size and morphology within the 0.1Zr-0.3Mn alloy in the T351 temper: **a)** elongated subgrains in areas of Al_3Zr bands, and **b)** more equiaxed subgrains in areas with a higher number of Mn-dispersoids.

As a final remark before studying the recrystallisation kinetics and mechanisms, it should be reminded that the subgrain size distribution in the rolled 0.1Zr-0.3Mn alloy was found to vary locally depending on the type of dispersoids present in that region. The alternating bands of Al_3Zr and $Al_{20}Cu_2Mn_3$ dispersoids led to a heterogeneous subgrain size distribution along the ND. The smaller average subgrain size in areas where Mn is in abundance brings a higher stored energy compared to bands of Al_3Zr dispersoids in the 0.1Zr-0.3Mn alloy. Thus recrystallisation would be more likely to initiate in Mn-containing areas.

6.3 Recrystallisation kinetics

All alloys in the F temper were annealed at 535°C for up to 144 h, to study the recrystallisation kinetics and identify the underlying mechanisms in each case. The annealing temperature was chosen to be within the solution treatment limits of Al-Cu-Li alloys according to Fig. 1.4 (between ~505-540°C), but also high enough to accelerate the recrystallisation kinetics of the alloys when there is strong particle pinning. The recrystallisation curves for samples annealed from both F and T351 tempers are presented in Figs. 6.3a,b respectively. The latter temper was used in order to observe the relative resistance of the standard 0.1Zr alloy compared to the 0.1Zr-D alloy, since it was only available in this condition.

Starting with the samples annealed from the F temper, the alloys containing less Zr and more Mn were clearly more prone to recrystallisation. The 0.4Mn alloy recrystallised completely after 5 min, while the 0.05Zr-0.3Mn alloy took 5 h. The 0.1Zr-0.3Mn alloy followed, but it did not recrystallise completely even after 144 h. Nevertheless, it reached a volume fraction of approximately 50% after prolonged heat treatment. Finally, the 0.1Zr-D alloy was the most resistant to recrystallisation with an almost constant recrystallised V_f of around 12%. It is clear even after prolonged annealing that the sequence of recrystallisation resistance observed here for the alloys, with respect to their dispersoid content, was the same as for the as-received T351 condition presented in §4.2.

The shape of each kinetics curve in Fig. 6.3 indicated differences in the controlling recrystallisation mechanism as a function of time and this subject will be discussed in more detail in §6.4. All four alloys in Fig. 6.3a were annealed from the F temper, where they had been hot-rolled only and the initial recrystallised V_f was zero. Since the individual addition of manganese was not so effective in restricting recrystallisation [132], the 0.4Mn alloy recrystallised very rapidly. The corresponding measured curve for this alloy could thus be described as the upper half of a classic JMAK curve for this material [14]. However, in the presence of stronger pinning by particles the shape of the curves deviated from this ideal form. In comparison, the curve of the 0.05Zr-0.3Mn alloy shifted towards longer times and did not increase so sharply due to the additional pinning effect of the Al_3Zr dispersoids. In the presence of a higher Al_3Zr number density, recrystallisation was suppressed more effectively, as shown for the 0.1Zr-0.3Mn alloy. In this case only a gradual increase was seen, with a steep rise at the end (pointed by the red arrow in Fig. 6.3a). The removal of Mn, in conjunction with an even higher pinning force, caused a complete halt of recrystallisation at a nearly constant volume fraction in the 0.1Zr-D alloy. I.e. again, the combined addition of Zr+Mn is seen to be less effective than Zr alone in preventing recrystallisation.

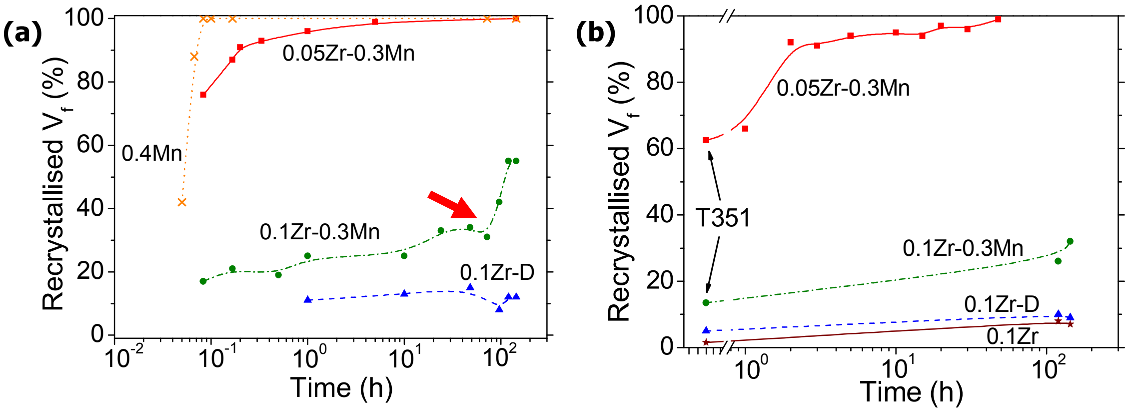

Fig. 6.3: Recrystallisation kinetics curves after annealing at 535°C from different tempers: **a)** F temper, and **b)** T351 temper.

The recrystallisation resistance of the different alloys indicated by the annealing curves from the T351 temper, showed exactly the same trend as in the F temper. The 0.4Mn alloy is absent from Fig. 6.1b, since it was fully recrystallised in T351 after solution-treatment. The 0.05Zr-0.3Mn alloy was affected by recovery that took place during the solution treatment and reduced the stored energy, thus a longer time was needed until complete recrystallisation (~48 h). The same phenomenon was observed for the 0.1Zr-0.3Mn alloy, where the recrystallised volume fraction after 144 h was still only 32%. However, the most interesting result revealed here was the difference between the 0.1Zr and 0.1Zr-D sheets; the former appeared to be ~2% less recrystallised than the latter even after extended annealing. Hence the 0.1Zr alloy in the standard homogenised condition would be expected to be slightly more resistant to recrystallisation than the 0.1Zr-D material in the F temper as well, if it was available in that condition.

The unforeseen phenomenon mentioned in §4.2, that combined Zr+Mn additions cannot prevent recrystallisation, but can still more effectively restrict the increase in grain size by recovery in unrecrystallised areas, was also observed during the annealing experiments. As Fig. 6.4a shows, the HAGB spacings in ND for the 0.1Zr-D and 0.1Zr-0.3Mn alloys were similar up to 48 h, but increased significantly after 96 h at 535°C, this rise being more pronounced for the former alloy. This difference was greatest after 144 h where the exact HAGB spacing values were 29.6 and 21.5 μm respectively (the grain structures are seen in Figs. 6.4b,c). Owing to the more substantial recrystallisation, the other two Mn-containing alloys exhibited a large increase in HAGB spacing with annealing time as seen in Fig. 6.4a.

The combined Zr+Mn addition only partly justified the rationale for the alloy design to include both Zr and Mn. The increase in grain size in unrercystallised areas was successfully suppressed since the pinning pressure was obviously higher than the driving force for grain growth. However, it was not higher than the driving force for recrystallisation and this is why a larger recrystallised V_f was observed. The reason for this is the large misorientation difference between the growing recrystallised grain and the surrounding substructure.

(a)

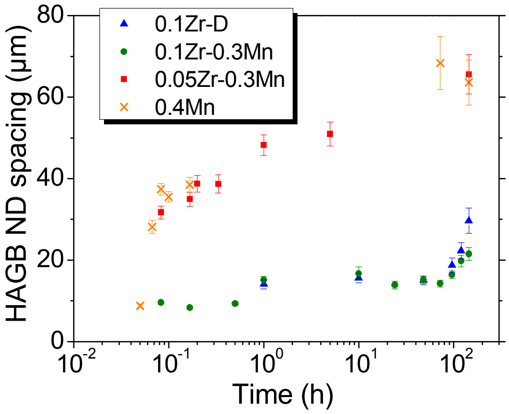

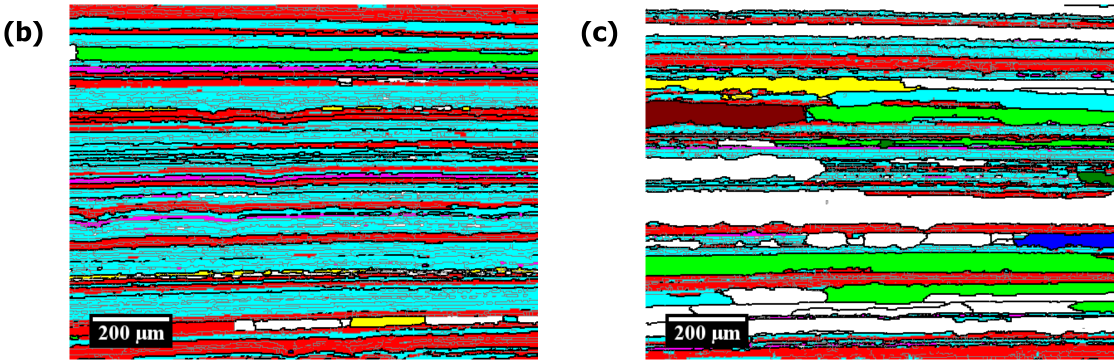

Fig. 6.4: HAGB spacing and microstructures during annealing at 535°C from the F temper: **a)** HAGB spacing, **b)** EBSD texture map for the 0.1Zr-D alloy after 144 h, and **c)** EBSD texture map for the 0.1Zr-0.3Mn alloy after 144 h.

6.4 Recrystallisation mechanisms

It is of importance to investigate how recrystallisation initiated in each alloy and how it was affected by the dispersoid content. In each case more than one mechanism was found to operate, but have different contributions to the overall kinetics. The alloys containing only Zr and only Mn are discussed first, before moving to the more interesting case of the 0.1Zr-0.3Mn alloy. The 0.05Zr-0.3Mn alloy is not reported here, since its recrystallisation behaviour was similar to the 0.4Mn alloy, due to the low Zr level.

6.4.1 Nucleation mechanisms in the 0.1Zr alloy

The current section contains a discussion of results from both the standard 0.1Zr material, as well as the 0.1Zr-D material subjected to the duplex homogenisation treatment, since the recrystallisation mechanisms were found to be identical in both. The longer homogenisation treatment of the latter affected only its resistance to recrystallisation and not the dominant mechanisms.

In the 0.1Zr alloy, strain induced boundary migration (SIBM) was found to be the dominant mechanism in each case. There was little evidence of any contribution from other processes of recrystallisation such as PSN. Regarding the nature of the SIBM process, multiple subgrain SIBM was more frequent than single subgrain SIBM due to the high pinning pressure from the Al_3Zr dispersoids [14].

Fig. 6.5 presents some examples of these processes. Grain A in Fig. 6.5a clearly originated from only one subgrain of S orientation at the lower side of the recrystallised grain, indicated by an arrow. Moving across Fig. 6.5a, the recrystallised grain B appeared to have initiated from at least two S subgrains, one on each side of the Brass island grain. The new grains grew laterally and merged when their migrating boundaries came into contact. This mechanism of lateral merging of new grains nucleated on GBs was also observed by

Somerday and Humphreys [196], but they also added that the new grains were connected by LAGBs. In general, the recrystallised grains can either form a LAGB or merge upon contact, depending on the misorientation between them. In the case of grain C, it was more difficult to predict if the grain grew from one or more subgrains since it had coarsened significantly.

The lateral merging of grains during the broad front SIBM mechanism can be clearly seen in Fig. 6.5b. The P-oriented grains that have nucleated from local bulges in a boundary have grown laterally and merged to form a very broad recrystallised grain.

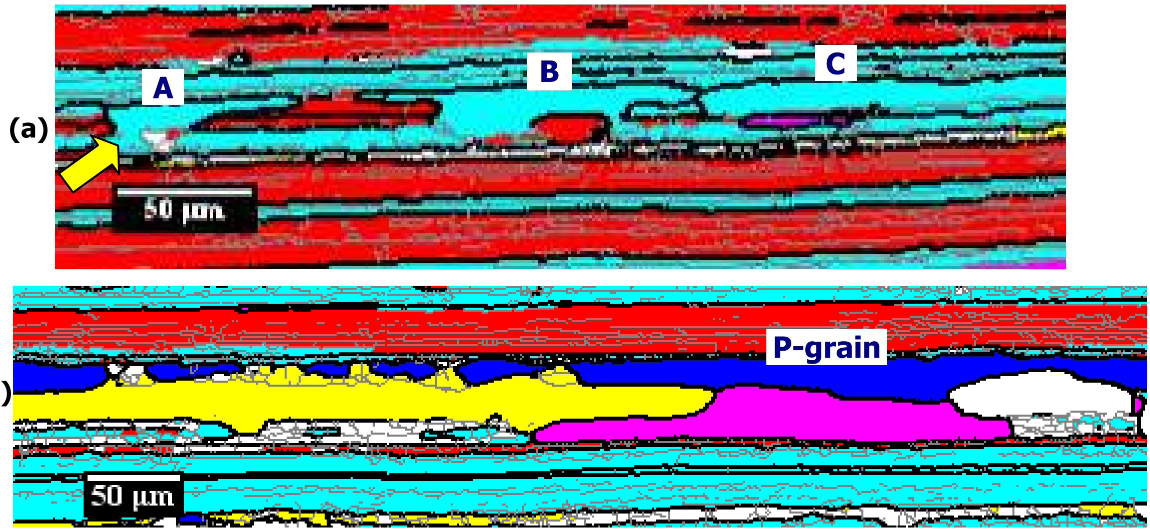

Fig. 6.5: EBSD texture maps showing evidence of single subgrain and multiple subgrain SIBM: **a)** 0.1Zr-D alloy in T351 (ST 20 min at 505°C), and **b)** lateral merging of P-oriented grains along a GB in the 0.1Zr-D alloy in T351 (at 2t/5 through-thickness position).

The presence of internal substructure within the bulging part of a grain growing by SIBM was supported by Higginson and Bate [217]. However, it was found in most cases in this work that the part of the recrystallised grain that was created by the passage of the migrating front via SIBM, exhibited only small misorientation gradients. This occurred irrespective of the grain orientation, since observations in this work were similar for grains of Brass, Cube and near-S texture components. The misorientation line scan A-B in Fig. 6.6 gives an example that proves that within a short distance in the bulge interior of approximately 6 µm, the misorientation hardly changes and a difference of only 1.3° was present.

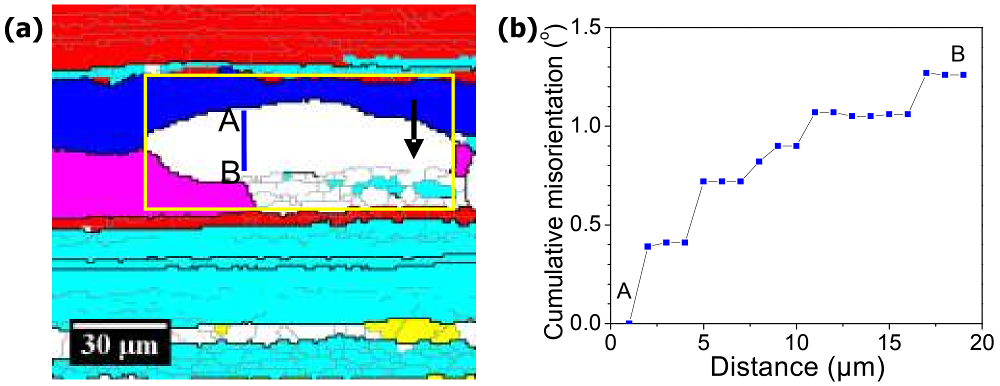

Fig. 6.6: Nucleation in the 0.1Zr-D alloy in T351 (at 2t/5 through-thickness position): **a)** EBSD texture map, and **b)** misorientation gradient within the recrystallised grain.

Nucleation of recrystallisation from a discrete subgrain in an orientation gradient, such as in a deformation band, is also possible in the alloys containing only Zr but it was more difficult to find any experimental evidence of such events. It can thus be concluded that this particular mechanism was very rare, if it occurred at all, in the Zr-containing alloys.

The same goes for the PSN mechanism which was not found with the aid of high resolution EBSD maps, but cannot be completely excluded as a possible mechanism. PSN is known to occur at high strains and high annealing temperatures [189], so it is possible in the current AA2198 alloy that was rolled to a true strain of 4.2 and subsequently annealed above 500°C. However, the lack of manganese reduces the amount of undissolved constituent phases in the microstructure of the alloys containing only Zr; thus PSN was not expected to have a major role in the nucleation events during annealing, as it would only be possible via the fewer, large Fe,Cu-constituent particles present. Further, high dispersoid densities can suppress PSN [14].

Grain boundaries are known as typical nucleation sites for recrystallised grains, as was also shown earlier for the SIBM mechanism. However, in cases where recrystallisation is at an advanced stage, it cannot be accurately concluded, where or how exactly the new grain initiated. Fig. 6.7 gives such an example, where the nucleation mechanism was not clear. Most possibly, the aligned pits shown in the band contrast map in Fig. 6.7b reveal the position where a GB used to be in the as-cast microstructure. The pits were formed by large particles falling out during the sample preparation by electropolishing. It is reasonable to assume that the recrystallised grain of random orientation (Fig. 6.7a) nucleated from the GB, but it is impossible to precisely conclude what was the exact mechanism. Either SIBM or PSN could be responsible.

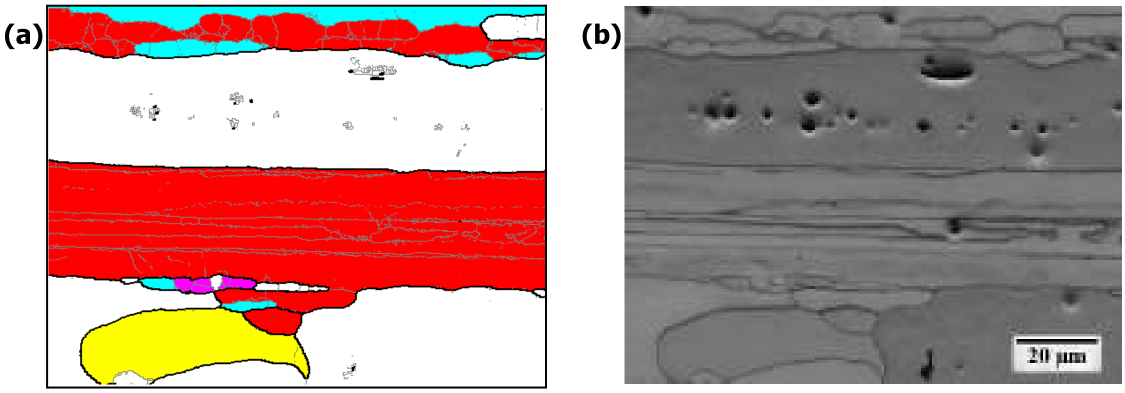

Fig. 6.7: Recrystallisation on a probable prior GB in the 0.1Zr-D alloy annealed 1 h at 535°C from the F temper: **a)** EBSD texture map, and **b)** EBSD band contrast map, showing aligned pits from large particles inherited from the as-cast microstructure.

To summarise, the main recrystallisation mechanism in the materials containing only Zr, was identified as broad front SIBM. All other mechanisms were suppressed by the pinning pressure of the Al_3Zr dispersoid bands. The vast majority of the recrystallised grains in the 0.1Zr and 0.1Zr-D alloys had rolling texture orientations. Only a small percentage of new grains with orientations other than the typical rolling components were found. Yet, these orientations most possibly pre-existed in the deformed microstructure. The retention of a rolling texture on recrystallisation is characteristic of the SIBM mechanism [14, 217]. Other nucleation mechanisms like PSN are also possible and cannot be entirely excluded, although it was hard to observe them via EBSD due to the low frequency with which they appeared.

6.4.2 Nucleation mechanisms in the 0.4Mn alloy

The recrystallisation of the 0.4Mn alloy at 535°C was seen to advance very rapidly and the whole deformed microstructure was eventually consumed by the new grains. It is interesting to determine what recrystallisation mechanisms acted in this alloy and make comparisons with the Zr-containing alloys discussed in the previous section. Due to the high Mn content in this alloy and the tendency for this element to be found in constituent particles, a higher number density of PSN sites were available in this case. Hence, the relative frequencies of the various recrystallisation mechanisms were expected to be different in the 0.4Mn alloy compared to the materials containing only Zr.

Fig. 6.8 presents an example of PSN in the 0.4Mn alloy. A factor that controls this mechanism is the density of pinning particles within the deformation zone that can prevent growth of the nucleus. A magnified view of a large constituent particle in Fig. 6.8a shows the effect of the distribution of dispersoids around it. There was a local reduction in the number of dispersoids below the right side of the particle, where the nucleated grain probably grew from. Some remnants of the deformation zone around the large particle were still evident from the orientation changes in the texture map in (b). The other recrystallised grain right above the particle, with a {111}<110> orientation, was also probably nucleated by PSN. It lay on a previous GB inherited from the as-cast condition, judging from the aligned large particles.

Since the PSN sites are related to GBs in that coarse particles lie on them, the high Mn content will increase the probability of nucleation on prior GBs inherited from the as-cast condition, due to the larger number of undissolved constituent phases in the microstructure of the 0.4Mn alloy. Grains recrystallised by PSN like in (c), were thus more frequent in this alloy compared to the alloys containing only Zr.

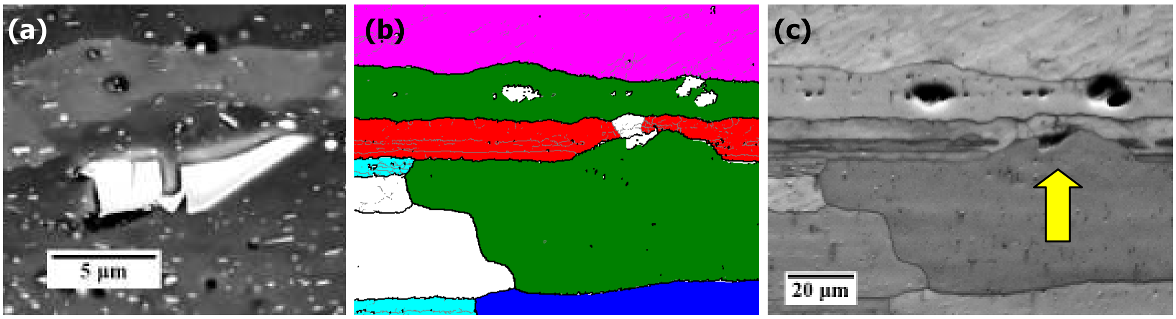

Fig. 6.8: Example of the PSN mechanism in the 0.4Mn alloy (3 min at 535°C): **a)** BSE image of a large constituent particle acting as a PSN nucleus as shown in the following pictures, **b)** EBSD texture map of the area containing the large particle of (a), and **c)** EBSD band contrast map of the same area. The position of the particle is pointed out by an arrow.

An assessment of the importance of PSN relative to the annealing time was carried out. The frequency of nucleation events occurring due to PSN was estimated at an early annealing stage, where the recrystallised volume fraction was only 13% for an area of 780 μm x 490 μm. The sample was from a 0.4Mn alloy in the F temper annealed for 3 min at 535°C. Figs. 6.9a,b illustrate a smaller part of the selected area. 16 recrystallised grains were counted in this area and 8 of them either contained, or were in contact with, one or more particles of several microns in size. This yielded a relative frequency of 0.5 for the association of large particles to recrystallised grains. Since these measurements were conducted from the ESBD band contrast map, it was quite difficult to detect some particles around 1 μm which were still potent nuclei and only the very large ones could be clearly seen. If one considers that the measured frequency was underestimated because of the 2-dimensional section, this renders the PSN mechanism dominant at the early stages of recrystallisation. On further annealing however, this frequency was reduced significantly. This implied that additional nucleation mechanisms became active later on.

Some of the recrystallised grains associated with very large particles are circled in Fig. 6.9b. It is unquestionable that grain A nucleated on a very large particle and, most possibly, also did grains B, C and D. PSN is known to yield orientations close to the existing ones in the prior deformed matrix around the large nucleus particle [14, 184]. The orientation of grain B ({111}<110>) was found to be close to that of some S and Brass subgrains located on its right side, but slightly rotated as the pole figure in (c) suggests. Similar results were found for the other recrystallised grains in the image.

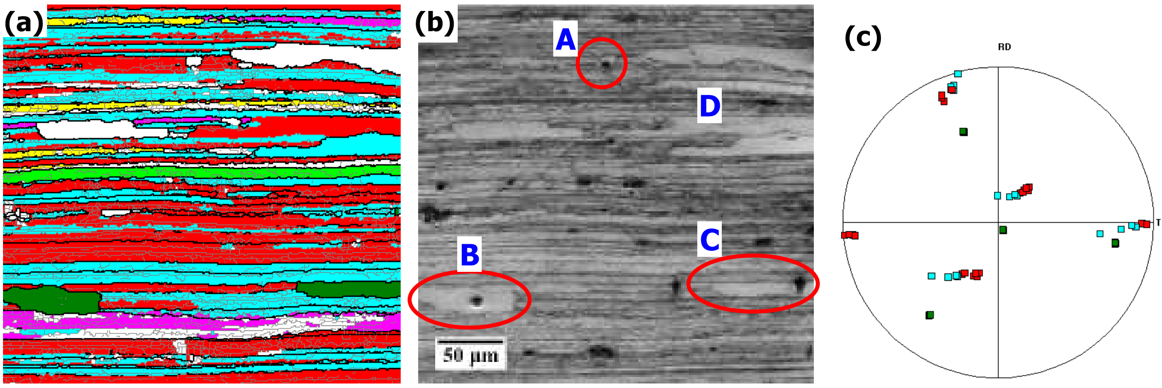

Fig. 6.9: Evidence of PSN in the 0.4Mn alloy after annealing for 3 min at 535°C from the F temper: **a)** EBSD texture map, **b)** EBSD band contrast map of the same area, and **c)** {111} pole figure showing the orientations of grain B and of several subgrains on its right side.

Regarding the broad front SIBM mechanism, this was also found to operate in the 0.4Mn alloy, but not to the same extent that it was encountered in the 0.1Zr and 0.1Zr-D alloys. An example of a grain recrystallised by broad front SIBM in this alloy can be seen in Fig. 6.10a, where a Cube grain has grown from the subgrains that appeared randomly textured on its top side.

The fact that the frequency of β-fibre orientations was quite low in the fully recrystallised microstructure also indicated that the broad front SIBM mechanism was not so strong in this alloy. Fig. 6.10b provides EBSD evidence supporting that only a low fraction of β-fibre orientations was observed after 5 min at 535°C and the {111} pole figure was quite randomised. This particular condition was chosen since it was the point where the recrystallised volume fraction reached 100% and ensured that no significant grain growth would affect the texture development.

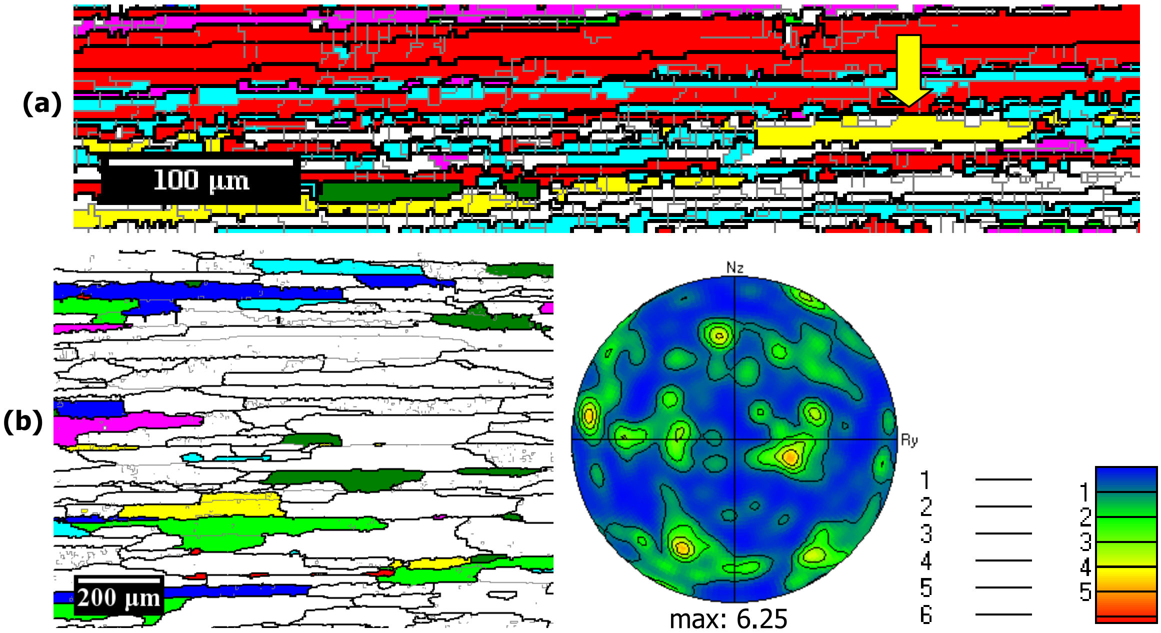

Fig. 6.10: Example of SIBM in the 0.4Mn alloy: **a)** a recrystallised Cube grain growing by broad front SIBM (2 min at 535°C from F temper), and **b)** EBSD texture map and {111} pole figure (5 min at 535°C from F temper).

In the 0.4Mn alloy, it was observed that some grains may have already recrystallised during the hot-rolling process and could have affected the static recrystallisation in the microstructure during the isothermal annealing at 535°C [295]. Some evidence of such grains, which were subsequently deformed during rolling, is presented in Fig. 6.11, where grains of various orientations are highlighted. It can be seen that the shape of some grains deviates significantly from the standard lamella structure and features curved protrusions into the surrounding matrix, similar to a typical recrystallisation front during annealing. In addition, their ND spacing is much larger than the average spacing in the rest of the microstructure.

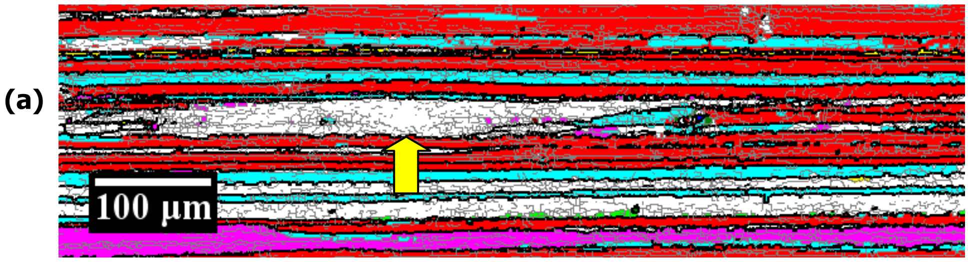

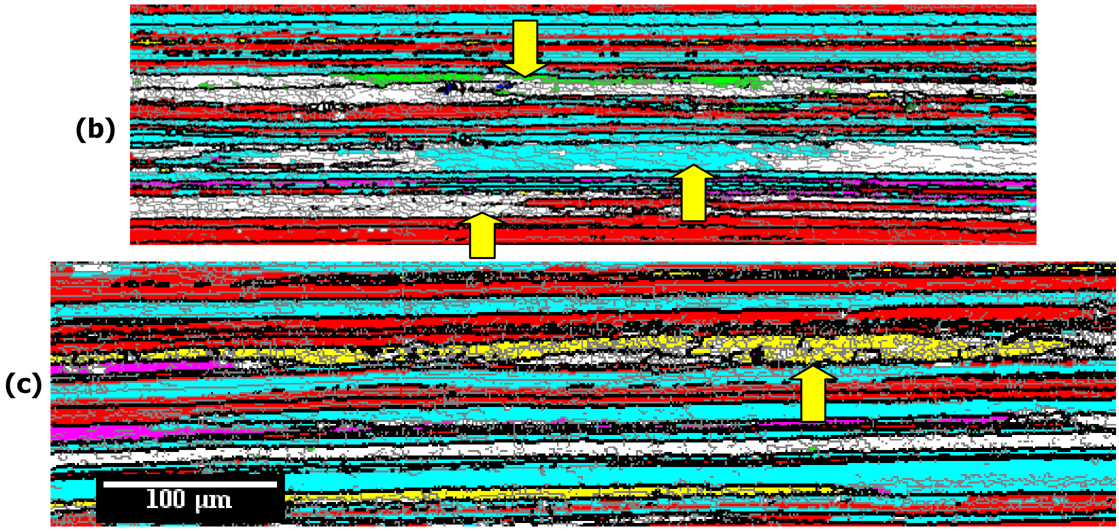

Fig. 6.11: Abnormally large grains of various orientations with a high density of LAGBs in their interior after hot-rolling (0.4Mn alloy, F temper).

Recrystallisation in the 0.4Mn alloy was also favoured in regions of high misorientation gradients, such as deformation or shear bands. The presence of these features within the randomly-oriented grain that was analysed in Fig. 6.12a, could lead to HAGB formation after appropriate subgrain coarsening events. The misorientation line scan across points A-B provides some solid proof of this possibility (Fig. 6.12b). After sufficient coarsening, the subgrain formed within the shear band, and having a misorientation of ~7° relative to point A, would be consumed and the resulting misorientation between the subgrain containing point A and the Cube subgrain at point B would be higher than 15°. The Cube-orientated grain could then obtain a more highly mobile HAGB and grow until it consumed the whole grain and the texture would change.

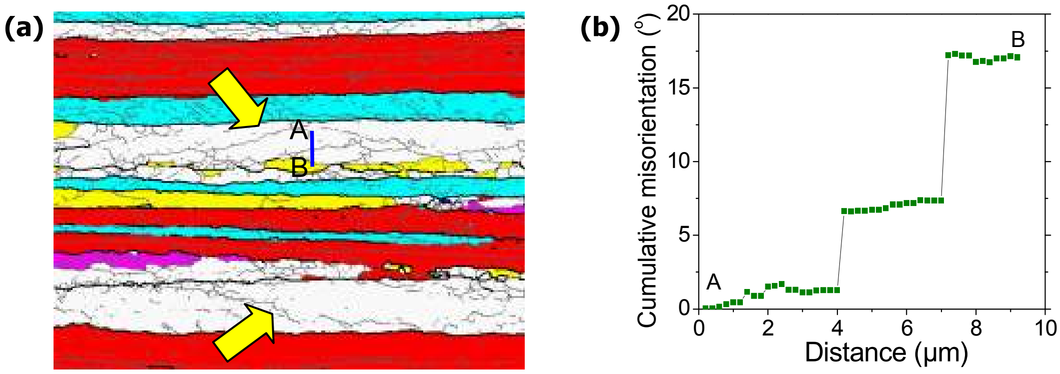

Fig. 6.12: Annealing behaviour of grains that probably had recrystallised during hot-rolling: **a)** EBSD texture map showing deformation or shear bands (150 sec at 535°C from F temper), and **b)** misorientation line scan from (a).

In summary, the main recrystallisation mechanisms in the 0.4Mn alloy were different than those encountered in the 0.1Zr alloy. PSN dominated at the initial stages of isothermal annealing. Recrystallisation was particularly favoured in areas of high misorientation gradients, such as deformation or shear bands.

6.4.3 Nucleation mechanisms in the 0.1Zr-0.3Mn alloy

The 0.1Zr-0.3Mn alloy exhibited the most noteworthy recrystallisation behaviour during annealing. Since it contained both Zr and Mn, which formed two very different types of dispersoids, it was of great interest to see how their combination would affect the recrystallisation mechanisms. At first, the reader is referred to the kinetics curves in Fig. 6.3a to remember the shape for this alloy as a function of annealing time. Recrystallisation initially occurred very rapidly and the new grains occupied 17% of the microstructure after 5 min at 535°C. Before that, there were no signs of new grains at 3 min, while after 4 min recrystallised grains were found sporadically. After 5 min the recrystallised V_f curve had an almost constant, very shallow slope up to 72 h and from 96 h it increased quite rapidly up to 144 h. This suggests that an initial rapid burst of recrystallisation occurred, which then stagnated until the microstructure changed sufficiently to allow for recrystallisation to resume.

Because of the heterogeneous dispersoid distribution in this alloy, it is of primary importance to investigate where recrystallisation initiated within the microstructure, relative to the segregation of Zr and Mn. Nucleation of recrystallisation in the 0.1Zr-0.3Mn alloy was observed primarily within bands of Mn-dispersoids as shown in Fig. 6.13. Three recrystallised grains are visible in this image and all of them were associated with a dispersoid band. In the areas between the Mn-dispersoid bands, few $Al_{20}Cu_2Mn_3$ particles were present together with bands containing high densities of Al_3Zr dispersoids. This correlation was observed regardless of the nucleation mechanism responsible for the recrystallised grain.

Fig. 6.13: Initiation of recrystallisation within bands of $Al_{20}Cu_2Mn_3$ dispersoids in the 0.1Zr-0.3Mn alloy (4 min at 535°C from F temper).

Several nucleation mechanisms could be responsible for the appearance of recrystallisation primarily in the Mn-dispersoid bands. These include all the mechanisms already mentioned in the previous two sections for the 0.1Zr and 0.4Mn alloys. Fig. 6.14 illustrates a possible example of PSN. The recrystallised grain shown most probably nucleated on the large constituent AlCuMn particle that was situated right on the HAGB. Its size (~2.5 μm) was large enough to cause a high distortion of the surrounding matrix and the deformation zone was visible with the STEM-HAADF detector, due to the different diffraction contrast of the adjacent subgrains. The sample was thick enough in this area to accommodate more than one subgrain around the particle through the specimen thickness. Thus the recrystallised grain might have resulted from a subgrain above or below the ones seen in the picture. It is interesting to note that the orientations of the subgrains varied depending on which side of the particle they were found. All three subgrains above the particle had orientations close to each other, but quite different than those on the right or left side. The same was observed for the subgrains at the bottom of the particle. These orientations obviously depended on the slip systems interacting with the particle during deformation. In any case, it was verified that the resulting orientations were not random, in agreement with the results of Humphreys [184].

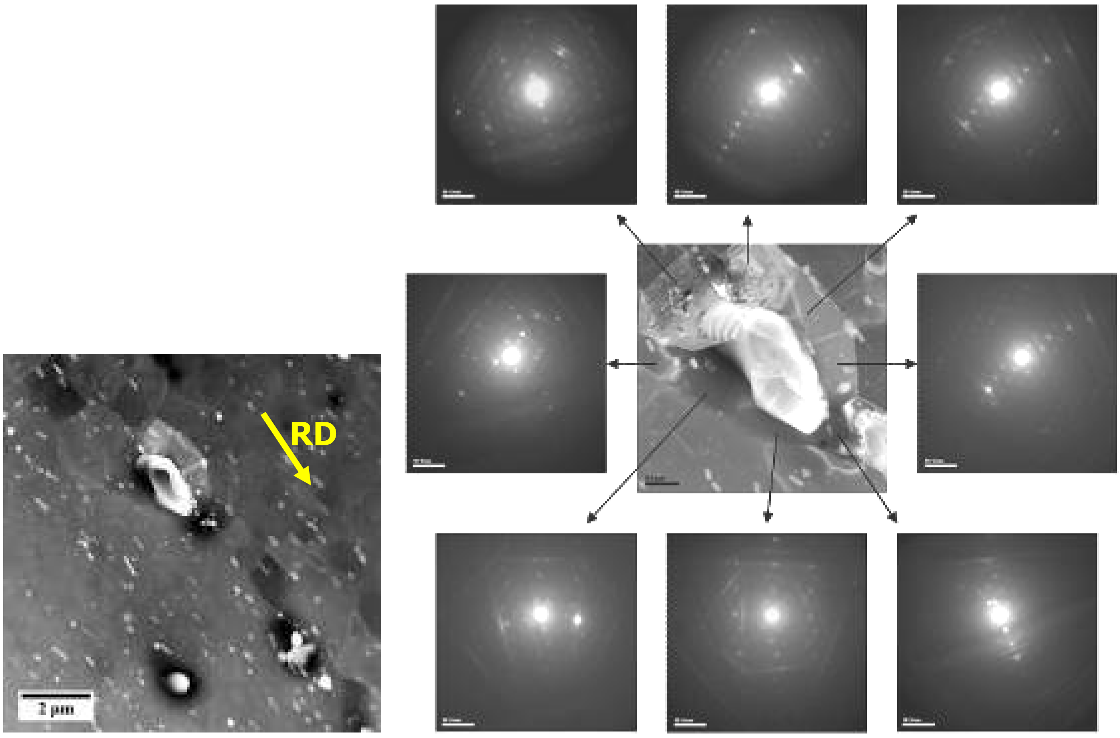

Fig. 6.14: STEM-HAADF showing possible PSN on a constituent particle on the HAGB of a recrystallised grain. The DPs of the surrounding subgrains are also shown (0.1Zr-0.3Mn alloy, 4 min at 535^{o}C).

SIBM could also be responsible for the initiation of recrystallisation within the Mn-dispersoids bands, but possibly did not have a very strong effect at the start of annealing. This mechanism was found to be present more frequently after 10 min at 535^{o}C. The frequency of recrystallised grains developed via this mechanism increased with annealing time, in agreement with the findings of the previous sections where PSN was dominant during the initial stages, while later on, other mechanisms also became active. Examples of SIBM and broad front SIBM in this alloy are shown in Fig. 6.15.

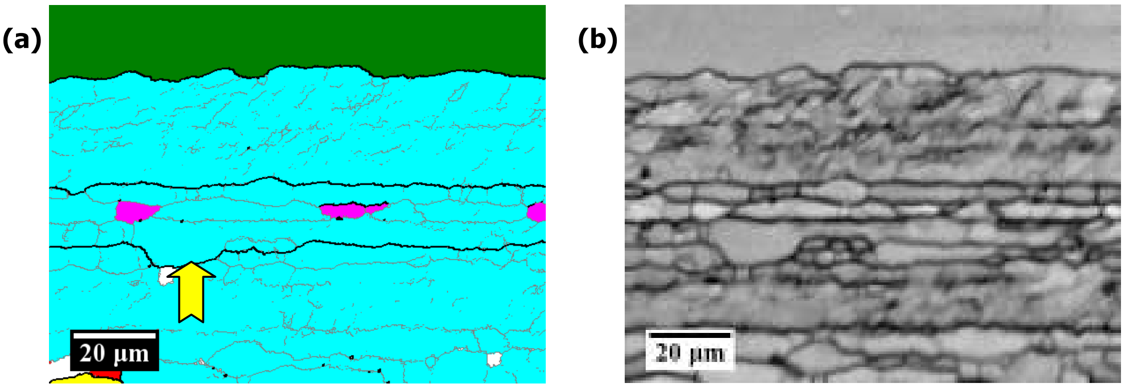

Fig. 6.15: EBSD maps showing evidence of the SIBM mechanism after annealing of the 0.1Zr-0.3Mn alloy for 24 h at 535°C: **a)** texture map, and **b)** band contrast map.

Regarding the broad front SIBM mechanism described by Somerday and Humphreys [196], it was only after longer annealing times that it became more wide-spread. Initially, the new grains developed by SIBM nucleated individually on the GBs, while after longer annealing there were more nuclei present which grew laterally and either merged, or a boundary was formed between them. Examples of these events are shown in Figs. 6.16a,b.

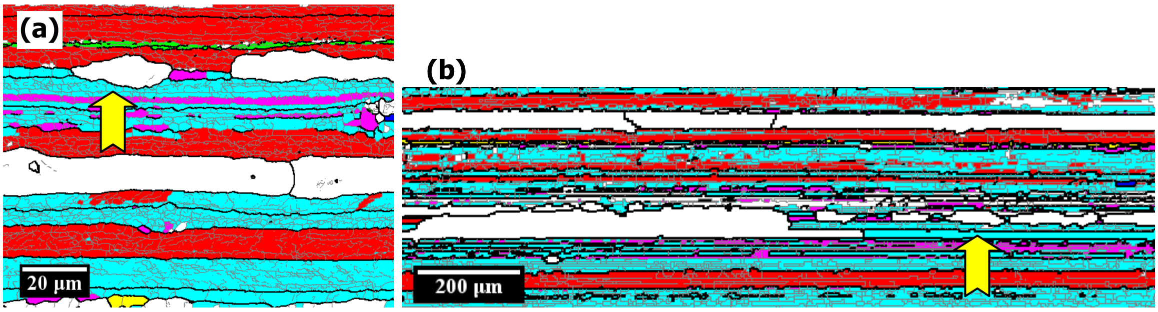

Fig. 6.16: EBSD texture maps showing SIBM with lateral encounter of the nucleated grains in the 0.1Zr-0.3Mn alloy: **a)** T351 condition, and **b)** 10 h at 535°C.

A further interesting observation is the static recrystallisation at the initial annealing stages within grains that were previously probably recrystallised during the hot-rolling process. These grains were also reported for the 0.4Mn alloy in §6.4.2. Fig. 6.17a shows a grain which exhibits different contrast to the surrounding subgrains and has a clearly different shape compared to its surroundings. Recrystallisation of this grain during hot-rolling most probably took place in between the rolling passes and not during deformation; hence it is not a case of dynamic recrystallisation. Dynamic recrystallisation is unusual for Al alloys, due to the strong recovery they exhibit [296]. This grain, which probably recrystallised during hot-rolling, underwent further deformation in the following rolling passes and thus developed internal substructure with a low average misorientation (Fig. 6.15c).

Recrystallisation during hot-rolling interpasses might initiate because of several mechanisms. As seen earlier, PSN is quite important in the 0.1Zr-0.3Mn alloy. Fig. 6.17a supports this statement by showing that during hot-rolling the recrystallised grain had nucleated in a region of aligned constituent particles remaining from the as-cast GBs. Upon further annealing, static recrystallisation appeared to occur more easily within such grains as seen in Fig. 6.17b. These regions of the microstructure may therefore be pre-selected by their low recrystallisation resistance, causing them to recrystallise during rolling passes and also first during static annealing after hot-rolling. The sudden recrystallisation of 17% of the microstructure after only 5 min at 535°C (Fig. 6.3a), compared to 0% at 3 min and a minor percentage at 4 min (not measured), was mainly attributed to recrystallisation of regions of low pinning pressure between bands of Al_3Zr dispersoids (as shown in §5.7.1). Static recrystallisation in previously recrystallised grains also contributed to the recrystallised V_f to a certain extent.

In order to study the substructure within grains that had appeared to recrystallise during the hot-rolling process, a high resolution EBSD map was obtained (Fig. 6.17c). The marked S grain exhibits subgrains, with no clearly defined boundaries in most cases, and also the presence of shear bands which is characteristic of a low deformation strain. The cut-off limit of 1.5° for LAGBs was higher than the actual misorientations between most of the subgrains and this was the reason why all boundaries did not appear clearly in the texture map. The misorientation line scan between points A and B verified that the misorientations between adjacent points were quite low (Fig. 6.17d).

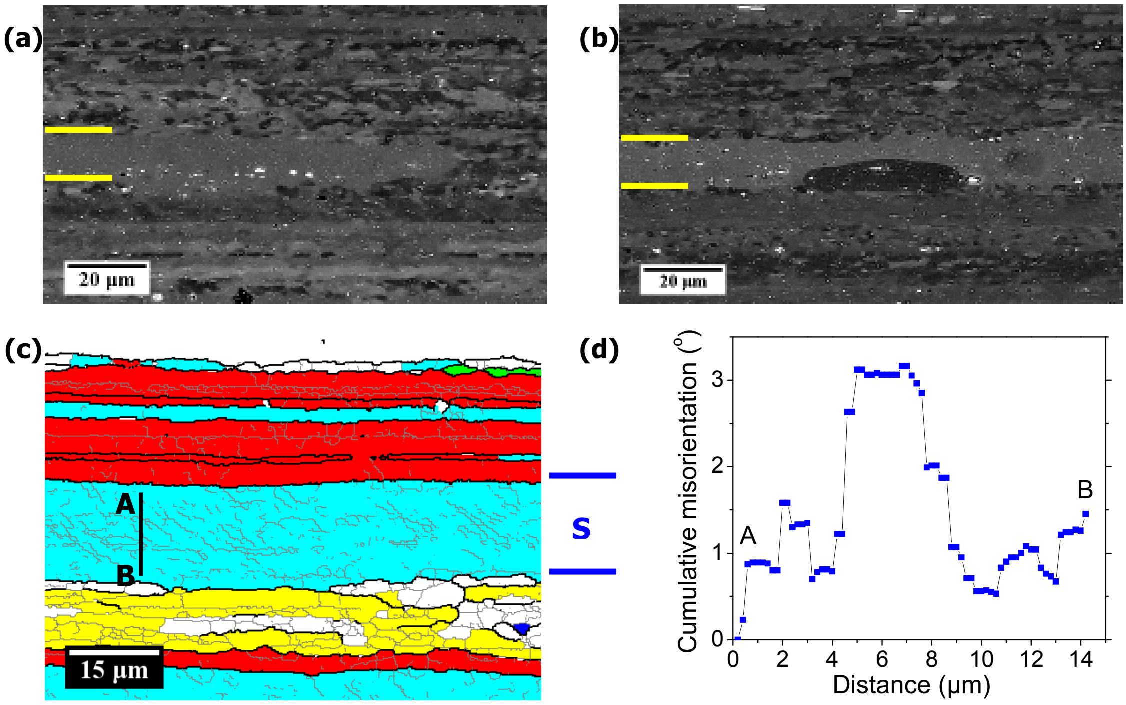

Fig. 6.17: Identification of previously recrystallised grains in the 0.1Zr-0.3Mn alloy during hot-rolling: **a)** BSE image of a previously recrystallised grain enclosing aligned large particles (4 min at 535°C), **b)** BSE image showing initiation of recrystallisation within a previously recrystallised grain (4 min at 535°C), **c)** EBSD texture map showing an S-oriented grain comprising of shear bands and subgrains of very low misorientations, and **d)** misorientation line scan from (c).

It is worth having a closer look at the annealing behaviour of a grain that had previously recrystallised during hot-rolling. Fig. 6.18 illustrates the striking differences in the substructure between such grains and the normal fibrous grains seen after rolling. In the former case (Fig.

6.18a) only two subgrains appeared to have strong diffraction contrast at the particular tilt angle in the TEM where this picture was taken. All the surrounding subgrains had other orientations similar to each other, as proved earlier by the EBSD map. On the other hand, the substructure of the normal unrecrystallised grain was quite different (Fig. 6.18b). In this case the subgrains exhibited several different orientations and the subgrain boundaries were defined more clearly without tilting the TEM sample. Moreover, the LAGB morphology was very different compared to the substructure in the previously recrystallised grains.

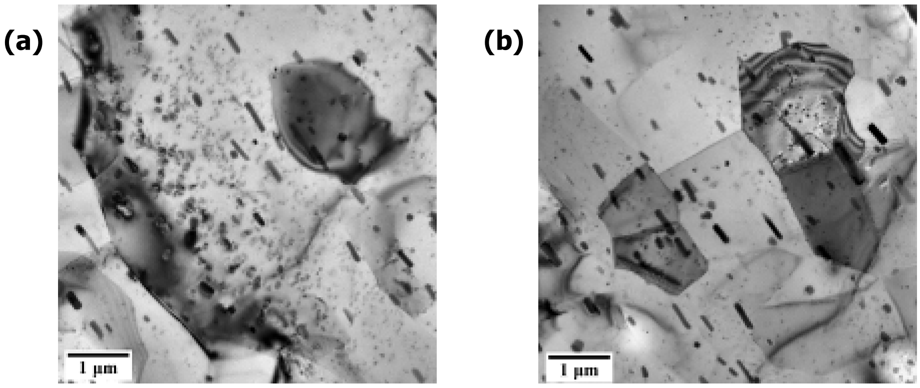

Fig. 6.18: Comparison between subgrains in Mn-bands in the 0.1Zr-0.3Mn alloy annealed for 4 min at 535°C: **a)** a grain that had recrystallised during hot-rolling, and **b)** an unrecrystallised grain.

As a final remark on the progress of recrystallisation in the 0.1Zr-0.3Mn alloy at 535°C, the important effect of Al_3Zr dispersoid coarsening has to be discussed. The growth of recrystallised grains was found to be inhibited by Al_3Zr bands (§5.7.1), thus limiting the extent of recrystallisation. During annealing, the recrystallised volume fraction increased very slowly after 5 min and up to 72 h. The gradual coarsening of the Al_3Zr dispersoids contributed towards this phenomenon, since the pinning pressure was reduced. Following this stage, the recrystallised volume fraction increased sharply in the interval between 72 h and 144 h. This occurred due to the combined increase in diameter and reduction in number density of the Al_3Zr dispersoids. After prolonged heat treatments, particles with smaller diameters were significantly fewer in number and the size distribution shifted towards higher values (Figs. 6.19a-c). Measurements showed that during this period the size bin of the minimum diameter in the particle distribution shifted from 10-15 nm to 25-30 nm and the maximum bin from 60-65 nm to 90-95 nm. The direct effect of this change was the drop of the average pinning pressure below a critical level which allowed further recrystallisation. The result was the extended growth of the existing recrystallised grains, as well as the nucleation of new ones due to the lower force to restrict subgrains from reaching the critical size for becoming recrystallisation nuclei. The microstructure after 120 h at 535°C (Fig. 6.19d) was indicative of both these effects.

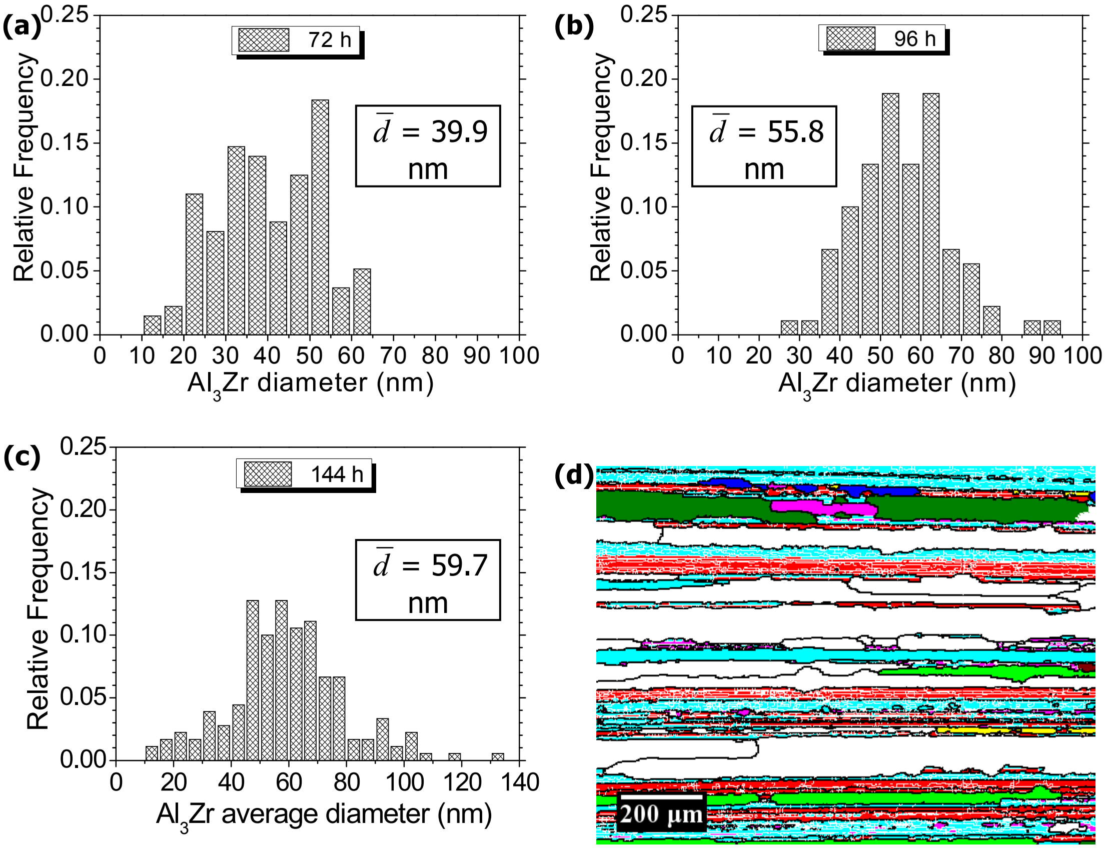

Fig. 6.19: Al_3Zr dispersoid coarsening in deformed areas of the 0.1Zr-0.3Mn alloy after annealing at 535°C and their effect on recrystallisation resistance: **a)** 72 h, **b)** 96 h, **c)** 144 h, and **d)** EBSD texture map after 120 h.

To sum up, the 0.1Zr-0.3Mn alloy exhibited an interesting recrystallisation kinetics curve, where it recrystallised abruptly to 17% after 5 min at 535°C and afterwards the increase was more gradual up to 72 h and then accelerated again. This increase after long annealing times was due to the reduction in the Al_3Zr number density along with a size increase, leading to a lower average pinning pressure. Recrystallisation was found to initiate within Mn-dispersoid bands, irrespective of the acting mechanism. Not all Mn-dispersoid bands recrystallised at the start of annealing, but all the recrystallised grains found at an early stage had grown within Mn-dispersoid bands. This initially rapid recrystallisation after the first 5 min was due to the growth of recrystallised grains in regions of low pinning pressure between bands of Al_3Zr dispersoids. It was apparent that some of these grains had probably previously recrystallised during hot-rolling passes.

6.5 Impact of dispersoids on recrystallisation

All the previous sections in the present chapter showed that the dispersoid content plays a major role in the extent and mechanisms of recrystallisation. The reasons behind this claim are analysed in more depth in the current section. Each type of dispersoid can have a different impact on the level and mechanisms of recrystallisation and the final textures after annealing. Additionally, variations in microstructural properties through the sheet thickness can result from differences in the behaviour of the two families of dispersoids. Finally, the relationship between the optimum amounts of Zr and Mn is discussed on a qualitative basis, in order to arrive at the ideal dispersoid content that would prevent recrystallisation.

6.5.1 Through-thickness heterogeneity

The through-thickness heterogeneity of the AA2198 sheet was studied in terms of the reasons for varying levels of recrystallisation seen at different depths in the sheet. Most of the studies in the literature (§2.4.4) refer to gradients of texture and yield stress. In the present work, the composition of the rolled alloys in the T351 condition was first analysed by means of electron probe microanalysis through the thickness of the sheet, from the surface to the mid-thickness plane. Alloying elements are known to segregate on casting, both within grains (microsegregation) and through the billet thickness (macrosegregation) [297].

The results shown in Figs. 6.20a-d illustrate that the concentration of Cu exhibited the most evident change throughout the sheet thickness. The Cu content was reduced in all the alloys from the surface to mid-thickness by approximately 0.3 wt%. The changes in the rest of the alloying elements were on a much finer scale and they are presented in separate graphs for the sake of clarity. Taken together, the data shows that the Mg and Ag levels also decreased slightly towards the mid-thickness, the drop being larger for the latter (Figs. 6.20e,f). However, this reduction was much lower compared to Cu. Regarding the dispersoid-forming elements, the Mn content also decreased towards the mid-thickness (Fig. 6.20g). All the afore-mentioned elements (Cu, Mg, Ag and Mn) are eutectic additions and were expected to segregate in this manner through the sheet thickness. In contrast, Zr is a peritectic addition and its concentration increased in the opposite direction (Fig. 6.20h). A similar opposing behaviour of Zr and Mn was observed for their microsegregation patterns in the cast grains (§5.3.1).

Further evidence is required before making precise conclusions on this, as the results here agree only partly with those of Robson and Prangnell [297]. They found that in an AA7050 plate the total alloying element content was lowest at mid-thickness, but they also claimed that a total alloying enrichment was observed at the t/4 position. Such solute enrichment at this position was not verified here. The standard 0.1Zr material was not available at the time when the EPMA measurements were carried out, but it is assumed that a similar behaviour would be observed in this case as different homogenising treatments do not affect macrosegregation.

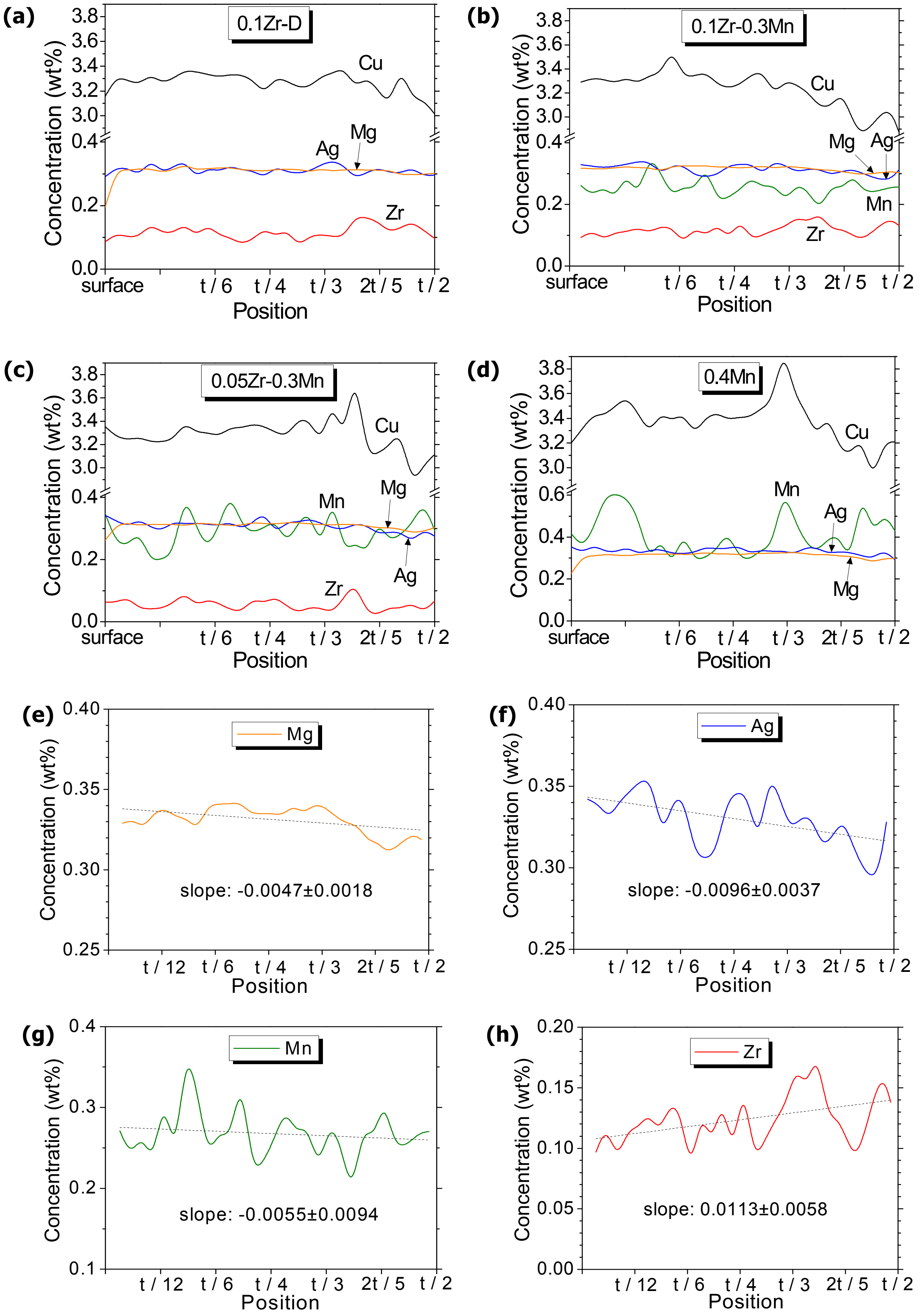

Fig. 6.20: Through-thickness electron microprobe measurements for alloys in the T351 temper: **a)** 0.1Zr-D, **b)** 0.1Zr-0.3Mn, **c)** 0.05Zr-0.3Mn, **d)** 0.4Mn, **e)** Mg profile in the 0.1Zr-0.3Mn alloy, **f)** Ag profile (0.1Zr-0.3Mn alloy), **g)** Mn profile (0.1Zr-0.3Mn alloy), and **h)** Zr profile (0.1Zr-0.3Mn alloy).

The extent of recrystallisation also varied through the sheet thickness. The 0.1Zr alloy exhibited a fairly uniform microstructure throughout the thickness, as it remained unrecrystallised until the t/2 position where a very low amount of recrystallisation was observed (Fig. 6.21a). This might be related to the lower amount of Cu (or solutes) in solid solution at mid-thickness, but opposes the trend for Zr segregation. The 0.1Zr-0.3Mn alloy behaved quite differently, showing a minimum recrystallised volume fraction at the t/4 position. Recrystallisation increased near the surface and at t/2, the surface volume fraction being much higher compared to that for the centre. The microstructure near the surface and at t/4 is shown in Fig. 6.21c and Fig. 6.21d respectively. A large number of wide, recrystallised grains appeared near the surface but they decreased in number and spacing towards larger depths. An even lower Zr content (0.05 wt%) together with Mn yielded an almost V-shaped curve with a minimum closer to the centre, at 2t/5. Since the 0.4Mn alloy was fully recrystallised everywhere, the same type of alloy was annealed from the F temper in order to observe the through-thickness variation as recrystallisation occurred, whereupon it showed a minimum at t/3.

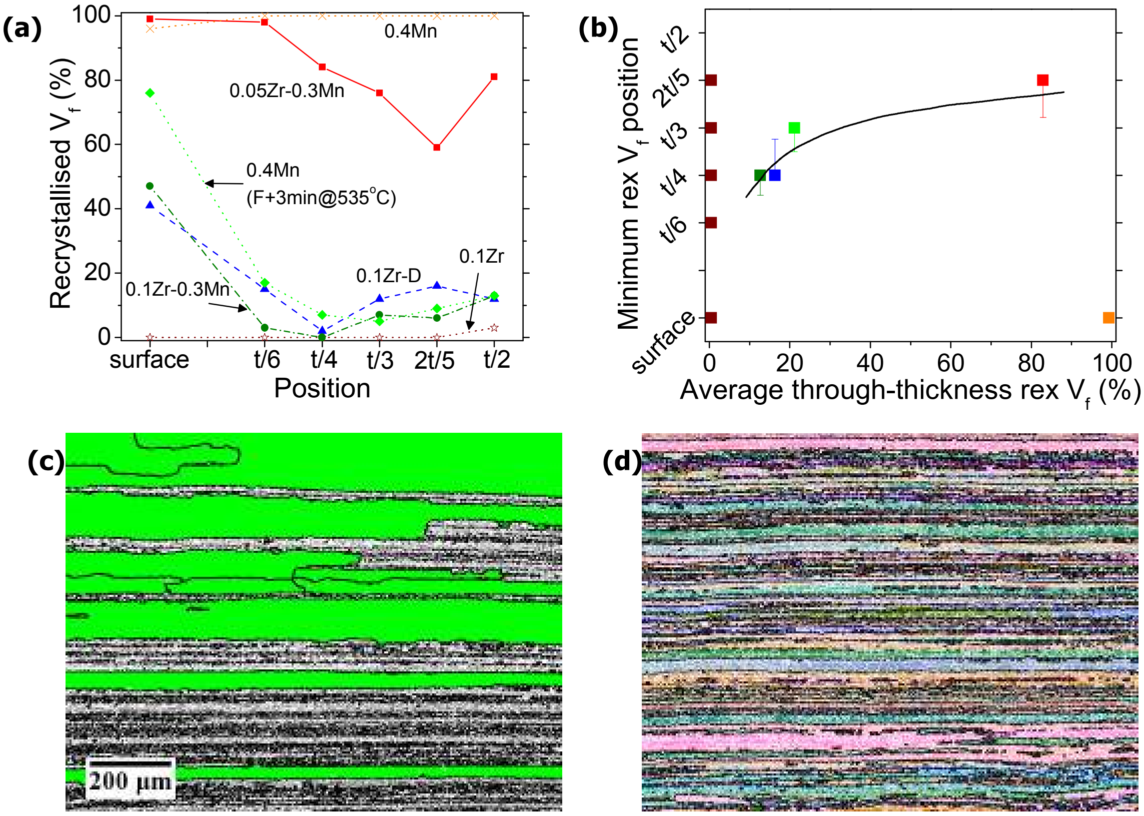

Fig. 6.21: Variation in through-thickness recrystallisation for all alloys in T351: **a)** recrystallised V_f at various depths from the sheet surface, **b)** position of the minimum recrystallised V_f through the sheet thickness, as a function of the average recrystallised V_f from all the through-thickness locations (all points correspond to the alloys in (a) and are denoted by the same colours), **c)** EBSD map near the surface of the 0.1Zr-0.3Mn sheet (recrystallised grains highlighted in green), and **d)** EBSD Euler colour map at t/4 (0.1Zr-0.3Mn alloy).

Although there is higher deformation and stored energy near the sheet surface due to the friction with the rolls and the roll chill, the pinning pressure exerted from the Al_3Zr dispersoids was still obviously high enough to restrict boundary motion and prevent recrystallisation throughout the depth of the 0.1Zr alloy. In contrast, the same did not happen for the 0.1Zr-

0.3Mn alloy. The lower Al_3Zr volume fraction in this alloy could not exert sufficient pinning pressure; therefore, recrystallisation was allowed to advance to a larger extent near the sheet surface, where the average Zr content was also slightly lower.

The 0.1Zr-D material exhibited a similar behaviour to the 0.1Zr-0.3Mn alloy, but for different reasons. Jia et al. [19] concluded that extended homogenisation is not beneficial for recrystallisation resistance because the Al_3Zr number density is reduced. Similarly in this work, the coarser Al_3Zr distribution measured in the 0.1Zr-D sheet, which underwent an extended homogenisation treatment, was not as effective in inhibiting recrystallisation as that in the 0.1Zr alloy with a shorter homogenisation treatment.

All the partially recrystallised alloys exhibited V-shaped curves through the half sheet thickness, but the position of the minimum recrystallised volume fraction varied according to the total amount of recrystallisation. This fact indicated that zones at different depths from the surface recrystallised at different rates. Magnusson and colleagues [298] made a similar observation; recrystallisation was found to proceed faster at t/4 than t/2, because of the subgrain nature and the corresponding higher stored energy in the former location.

With increasing levels of recrystallisation, the location of the minimum recrystallised V_f gradually shifted from areas near t/4 towards positions closer to the centre (Fig. 6.21b). The physical meaning of this change was linked to the faster recrystallisation kinetics in regions closer to the surface, as compared to the centre of the sheet. The data presented by Andersson and Johansson [299] also showed a similar trend for three AA7010 plates of different thicknesses, but unfortunately this effect was not noticed by the authors. A slight increase in the recrystallised V_f brought about a move of the position of minimum V_f from t/8 to t/4 (all three average volume fractions were lower than 10%).

The curve in the graph of Fig. 6.21b effectively describes the trend for almost the entire range of recrystallised volume fractions in the T3 sheet. However, it did not apply for very low or very high values, since the initiation and completion of recrystallisation are usually more complicated in terms of kinetics. At the preliminary stage, the incubation time required of recrystallisation was shorter for t/2 than for any other depth, but in subsequent stages the regions closer to the surface appeared to recrystallise faster. Thus the V_f regime up to approximately 10% was quite difficult to describe. The reason for the faster kinetics closer to the surface could be ascribed to the higher deformation and lower temperature experienced in rolling. Similarly, recrystallisation did not evolve regularly for volume fractions above 90%.

Apart from the recrystallised V_f, other significant parameters of the sheet microstructure were also affected through the thickness by rolling. Grain size measurements showed that the HAGB ND spacing exhibited a complicated pattern throughout the thickness, since it was evidently affected by the extent of local recovery and recrystallisation taking place (Fig. 6.22a). Recrystallised grains were much larger than the deformed fibrous ones, so this had a serious impact on the average value. Recovery and recrystallisation also affected the average

LAGB ND spacing (Fig.6.22b). This could explain the large decrease in the LAGB ND spacing of the 0.05Zr-0.3Mn alloy towards mid-thickness where the recrystallised V_f was lower than the surface. However, the LAGB aspect ratio showed an obvious tendency to increase towards the t/2 position for all alloys (Fig. 6.22c). Finally, the microhardness was found to decrease marginally towards mid-thickness in all the T351 alloys (Fig. 6.22d).

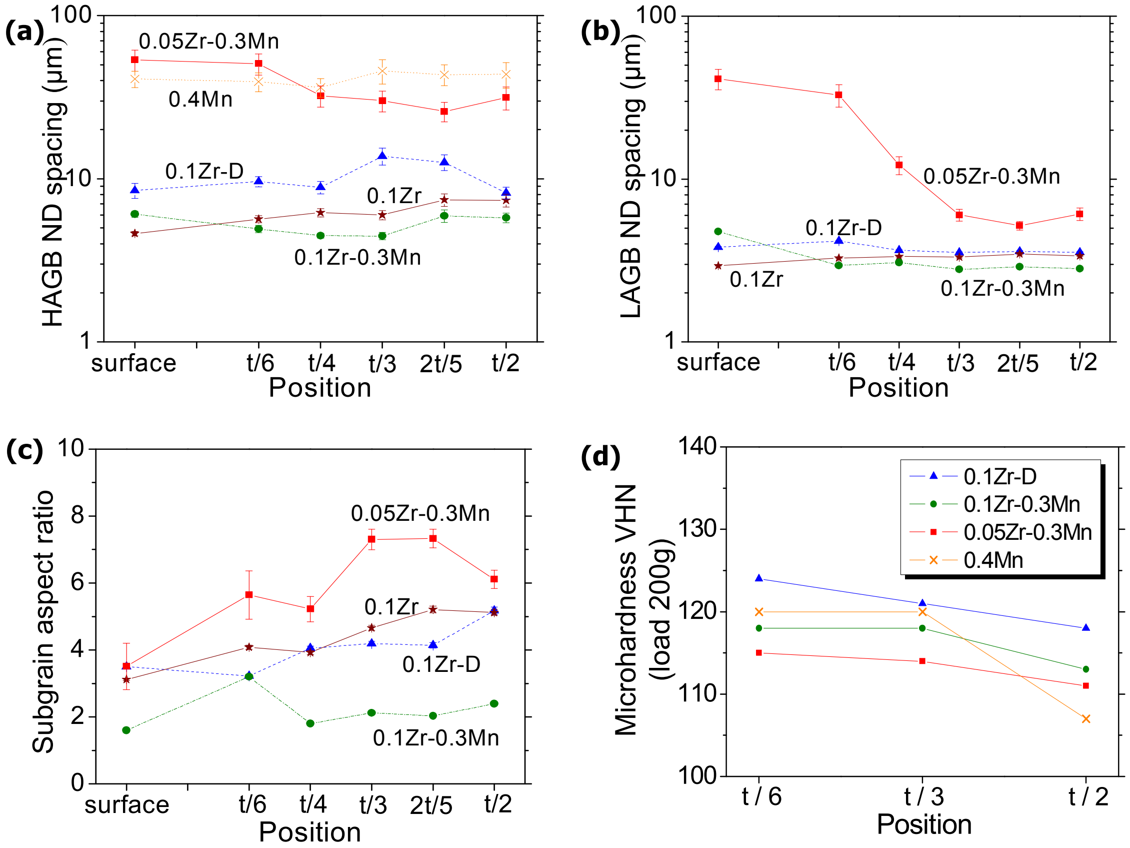

Fig. 6.22: EBSD data for all alloys at various positions through the sheet thickness in T351: **a)** HAGB ND spacing, **b)** LAGB ND spacing, **c)** subgrain aspect ratio, and **d)** microhardness.

Apart from the level of recrystallisation, the crystallographic texture is the next main parameter that can affect through-thickness anisotropy in the T3 condition [300]. However, variation of the individual deformation texture components through the sheet thickness was not found to be greatly affected by the addition of Mn together with Zr (Figs. 6.23a,b). S and Brass components prevailed in both the 0.1Zr and 0.1Zr-0.3Mn alloys, with a higher amount of the former almost everywhere in the microstructure. Brass only increased closer to the centre of the 0.1Zr sheet and exceeded the percentage of S at t/2. It is known from the literature that Brass is a typical hot-rolling texture component, in contrast to S [226]. The minimum S/Brass ratio in the two partially recrystallised alloys was observed close to the position of the minimum recrystallised volume fraction.

The combined Zr-Mn addition appeared to promote the Copper component, but suppressed the amount of Cube (Fig. 6.23a,b). This was a consequence of the weaker deformation texture in this alloy compared to the 0.1Zr one, as can be seen from Fig. 6.23c.

The sum of the main deformation components fluctuated for this alloy, but generally increased towards t/2. The curves of the 0.1Zr-0.3Mn and 0.1Zr-D alloys also correlated to the amount of recrystallisation with depth from the sheet surface.

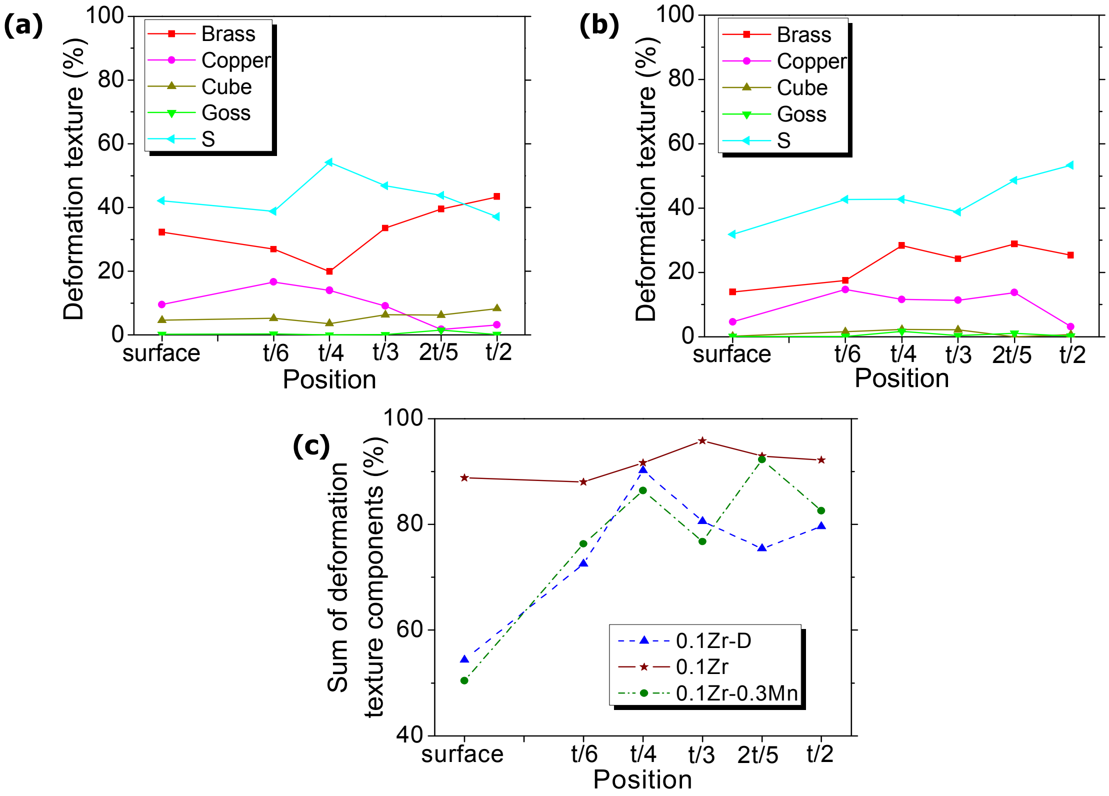

Fig. 6.23: Variation of the deformation texture through the sheet thickness in T351: **a)** deformation texture components of the 0.1Zr alloy, **b)** deformation texture components of the 0.1Zr-0.3Mn alloy, and **c)** sum of the main deformation texture components shown in (a) and (b).

6.5.2 Texture changes during annealing

The textures of the four alloys with different dispersoid contents were greatly affected by the extent of recrystallisation in each case. The main purpose of this section is to see if there was any kind of relationship between the dispersoid content and the deformation and recrystallisation textures, as a function of annealing time.

The change in the textures with annealing time is presented in Fig. 6.24. The textures at 0 h in each case correspond to the F temper microstructures. It is clear that prior to annealing, the S component had the highest volume fraction almost in every alloy. It was only in the 0.4Mn alloy where it was similar to the Brass content. In general, the S and Brass components were dominant also during annealing. There were only few grains that had orientations other than these two main β-fibre components. From the other orientations, Copper was the highest, but did not exceed 5% in any condition.

Looking closer at the graphs from (a) to (d), different rates of a drop in the actual amounts of S and Brass were evident, as well as in their relative amounts in the different alloys. This observation was due to the higher recrystallised V_f with increasing Mn concentration and lowering Zr level. Equally, longer annealing times had the same effect. Regarding the relative amounts of the two main texture components, S was seen to decrease faster than Brass for higher Mn contents and lower Zr. For example, the initially much higher S content in the 0.1Zr-D alloy (Fig. 6.24a) became nearly equal to Brass in the 0.05Zr-0.3Mn and 0.4Mn alloys (Figs. 6.24c,d). Thus, the Mn addition seemed to favour a preferential consumption of the S component after annealing at 535°C, which would be detrimental for mechanical properties if the Brass content prevailed [4]. On the other hand, the sole addition of Zr strongly promoted the retention of the S component in the less recrystallised sheet.

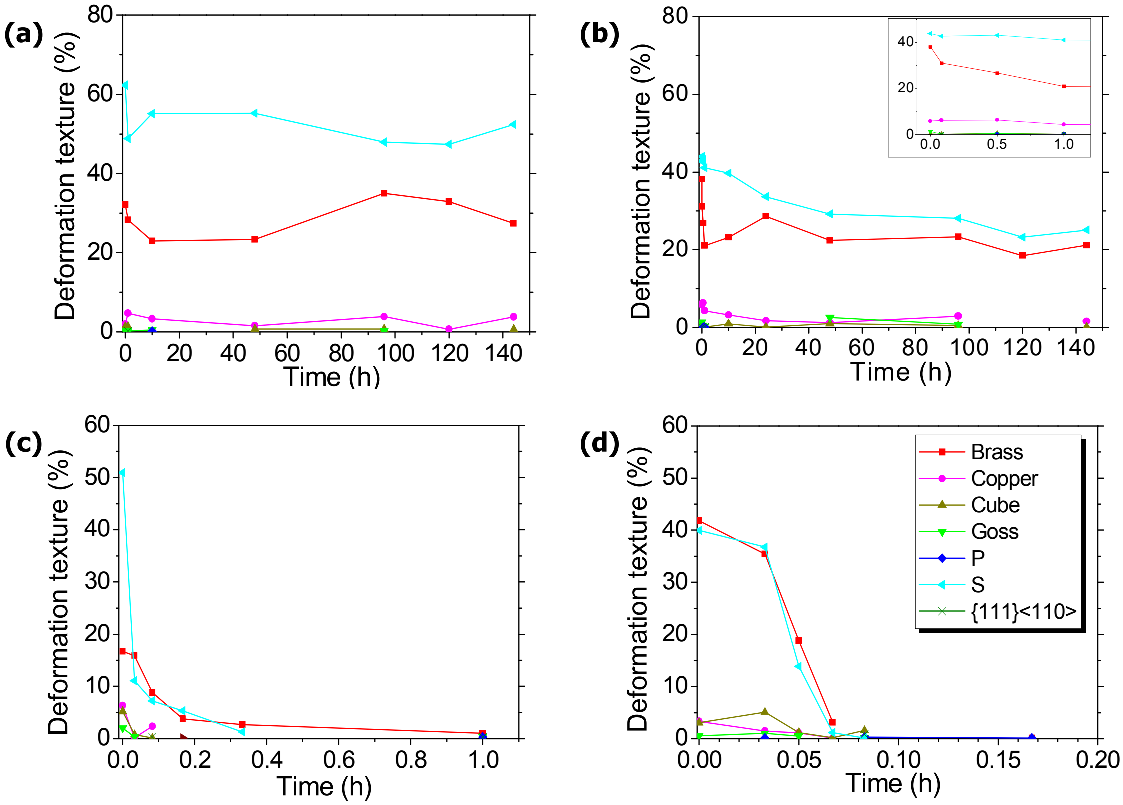

Fig. 6.24: Deformation textures as a function of annealing time at 535°C in alloys annealed from the F temper: **a)** 0.1Zr-D, **b)** 0.1Zr-0.3Mn, **c)** 0.05Zr-0.3Mn, and **d)** 0.4Mn.

Concerning the recrystallisation textures, lower magnification EBSD maps were obtained in order to include a larger number of grains and have more statistically accurate data. The recrystallisation textures of the four alloys are presented in Fig. 6.25. The orientations shown were derived from recrystallised grains only, but their percentage is given as the volume fraction in the whole microstructure. In all cases, the volume fractions of the grains with the defined orientations did not exceed 10%. The percentage of the recrystallisation texture components in the 0.1Zr-D alloy was fairly low due to the low recrystallised V_f. S and Brass were the dominant components. Goss was significant at all times in the 0.1Zr-0.3Mn alloy, while the shear component {111}<110> at the initial stages and P at the final stages were seen to prevail. The 0.05Zr-0.3Mn alloy showed similar results. Again, a stronger {111}<110> was observed initially, which was then reduced and Goss and P became dominant. The non-specified random orientations generally increased with annealing time. However, in the 0.1Zr-

D alloy, not many grains of random orientations were seen to have nucleated even after 144 h. Their percentage increased for higher Mn and lower Zr contents, in conjunction to the increasing recrystallised V_f. The texture changes after prolonged annealing depend on the growth rates of the various components. Certain components might nucleate later and others might stop growing at a certain stage. This may eventually lead to a change in the respective volume fractions of the orientations of the grains. This seemed to be happening in all the Mn-containing alloys.

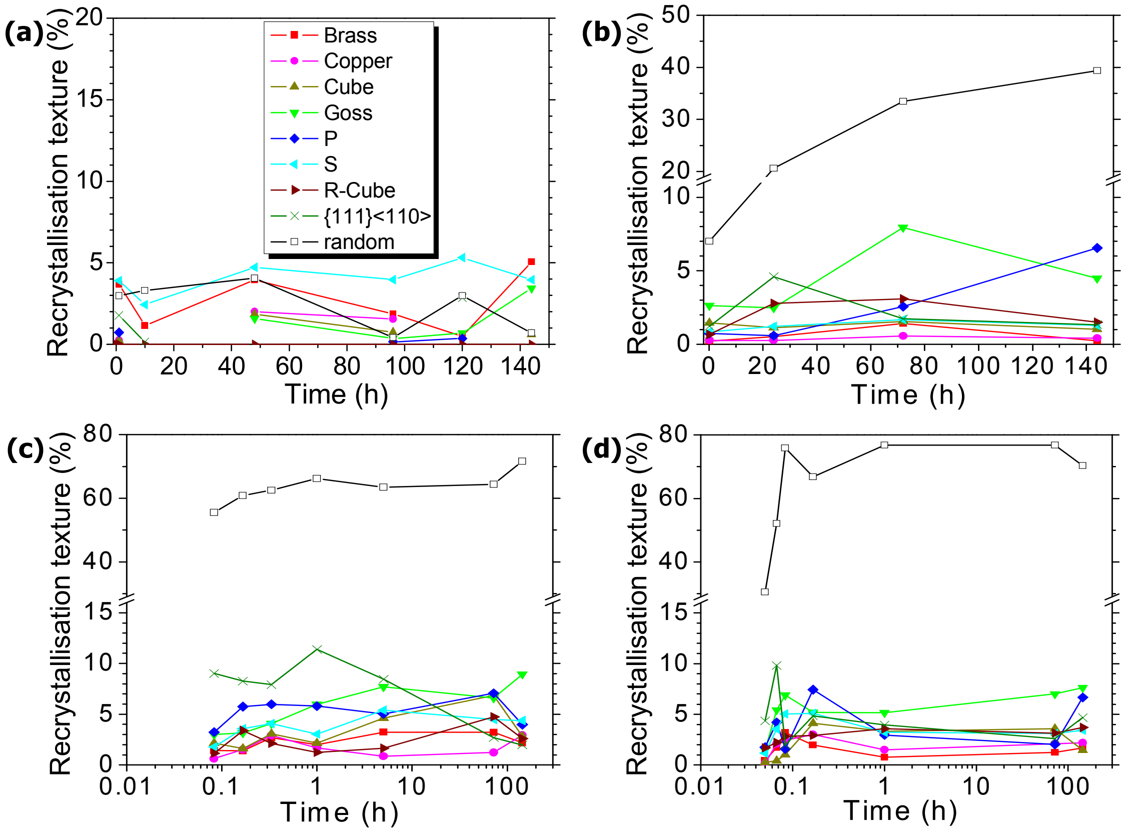

Fig. 6.25: Recrystallisation textures as a function of time in alloys annealed from the F temper at 535°C: **a)** 0.1Zr-D, **b)** 0.1Zr-0.3Mn, **c)** 0.05Zr-0.3Mn, and **d)** 0.4Mn.

The presence of the {111}<110> shear component, that was formed at a fairly large volume fraction at the start of annealing in the Mn-containing alloys, occurred concomitantly with the large reduction of the S component. A possible reason for this association might be the fact that it was slightly closer to the S than the Brass orientation. Hence, a smaller lattice rotation is required to produce this orientation from the existing S matrix. Regarding its nucleation mechanism, it was associated with PSN on large particles in the majority of the instances when such grains were detected in EBSD maps. The same nucleation pattern was also observed for the other shear component, R-Cube. However, the {111}<110> orientation was consumed after extended annealing. The reasons for this instability at long exposures at high temperatures could not be explained at this stage.

6.5.3 Predicting the optimum dispersoid content

In order to clarify the confusion in the literature regarding the effect of the combined Zr+Mn addition on recrystallisation resistance (e.g. [18, 164]), the plot of Fig. 6.26a was constructed. It presents published data for the Zr and Mn contents of alloys studied in terms of their reported recrystallisation behaviour. The compositions were taken from Table 2.3. The effect of adding Mn to the Zr-containing alloy was characterised in each case, as beneficial (green points) or detrimental (red and blue points), depending on the claimed change in recrystallisation resistance, compared to the starting alloy with Zr only. It is obvious that there is a clear interdependence between the Zr and Mn contents. Combined additions are found to deteriorate recrystallisation resistance compared to the alloys containing only Zr, when the Mn content is lower than a certain level. It is clear that for higher Zr contents, the Mn requirement was lower. In contrast, for lower Zr contents the Mn level should be much higher. This would be required in order to compensate for the reduction of the Al_3Zr particle densities, since they are more effective in GB pinning than Mn-dispersoids. Eschbach et al. [155] also suggested that the Zr and Mn levels should be adjusted relative to each other in order to obtain sufficient pinning pressure.

A logical question would be how is the Mn addition able to reduce recrystallisation resistance, since it offers higher dispersoid density in areas where Zr-particles are sparse and, hence, minimises dispersoid-free zones compared to the sole Zr addition. The answer to this critical question is two-fold. First, the Mn addition was found in this work to alter the Al_3Zr distribution by decreasing the number density of this phase and rendered it less effective in inhibiting migration of the recrystallisation front. Second, the stored energy increased locally within the bands of Mn-dispersoids, due to the smaller average subgrain size and possibly due to lattice distortion caused by the large intermetallic inclusions that also provide nucleation sites for PSN. Thus, both the Zr and Mn contents should exceed minimum values that lead to dispersoid distributions able to surpass the critical V_f/r ratio required to suppress recrystallisation. However, increasing the Mn content inevitably produces a higher frequency of large constituent particles that can act as PSN nuclei.

The next question would be which of the afore-mentioned effects of the Mn addition is more important. Starting with its effect on the Al_3Zr dispersoids, it is seen from Fig. 5.23 that the Al_3Zr distribution in the 0.1Zr-D alloy is worse than of the 0.1Zr-0.3Mn alloy; the Al_3Zr dispersoids are coarser, much fewer and more widely spaced in the former alloy. However, the 0.1Zr-D alloy has a much higher recrystallisation resistance than the 0.1Zr-0.3Mn. Hence it is reasonable to conclude that another effect of the Mn addition is the main reason for the reduction in recrystallisation resistance. This effect would then be the increase in local stored energy from the smaller subgrain size within bands of Mn-particles and from the large Mn-containing constituent particles during deformation and their ability to produce a higher density of PSN sites.

The reason why this interdependence between Zr and Mn levels was observed can be explained with the aid of Fig. 6.26b. When increasing the content of Zr and Mn, the grain interior can be filled more uniformly with a high density of dispersoids after homogenisation. When the volume fraction of either dispersoid family is low, the fraction of the other one should be high enough to compensate for their absence and fill up the vacant space with a particle distribution that exceeds the critical V_f/r ratio. Some examples illustrating this effect are given in Fig. 6.26a. The addition of 0.30 or 0.32 wt% Mn together with 0.11 wt% Zr (this work and [164] respectively) reduced the recrystallisation resistance, while the addition of 0.55 wt% Mn with the same amount of Zr was found to offer an improvement [157]. This means that the distribution of the Mn-dispersoids exceeded the critical V_f/r limit in the latter case.

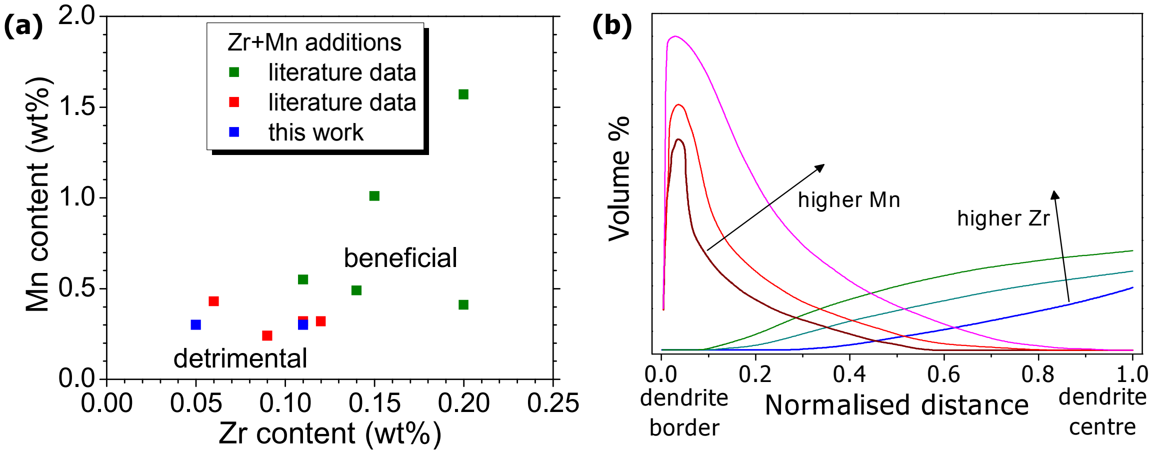

Fig. 6.26: Dependence of dispersoid distribution on the Zr and Mn levels and the related recrystallisation resistance: **a)** composition plot of alloys with combined Zr and Mn additions (data from Table 2.3), characterised as beneficial (green points) or detrimental (red and blue points) in comparison to the sole Zr addition, and **b)** illustration of how the grain interior is filled with dispersoids depending on the Zr and Mn levels. The curves of the lowest contents are those predicted with the Alcan Thermodynamic Package Prophase [277], while the rest are simply extrapolated.

It should be noted that the cut-off limit for the beneficial or detrimental effect of the combined Zr+Mn addition in Fig. 6.26a would depend on the rolling temperature and deformation strain during processing. A higher strain would compress the dispersoid-free zones and recrystallisation would not initiate in them as long as the pinning force of the dispersoids is high enough to offset the stored energy. PSN would also be less pronounced for lower strains and higher rolling temperatures [14] and hence a lower dispersoid density would be required. Unfortunately, not all the cited articles revealed details of the deformation process so no precise conclusion can be made on the effect of strain.

Regarding the curves in Fig. 6.26b, those corresponding to the lowest Zr and Mn contents were those predicted with the Alcan Thermodynamic Package Prophase [277], while the rest were schematically plotted in order to simply show a qualitative effect. The shape of the Zr curves was based on that predicted by Robson and Prangnell [113]. As suggested from this same work, the Zr and Mn curves strongly depend on the homogenisation conditions, such as temperature and time, apart from the solute content.

The level of both dispersoid-forming elements can be optimised by modelling the homogenisation process. The existing Alcan Thermodynamic Package Prophase [277] would be suitable for this purpose, after certain modifications to take into account the interaction between Zr and Mn when added together, and it could also be used to predict the minimum V_f/r ratio for each dispersoid family.

6.6 Summary of the effects of dispersoid content on recrystallisation behaviour

The most pronounced effect of the Zr and Mn content was on the recrystallisation resistance. Increasing the Mn level and decreasing the Zr level led to a higher recrystallised V_f during annealing at 535°C. In contrast, the grain size did not follow exactly the same trend. The 0.1Zr-0.3Mn alloy had a finer grain size than the 0.1Zr-D alloy after annealing for 144 h.

The observed discrepancy for the Mn-dispersoids, to restrict grain growth but in parallel favour recrystallisation, was reported by Lavernia et al. in their review [16] but unfortunately it was not explained further. In the present work, it is shown that in the Zr+Mn alloy the lower recrystallisation resistance was directly related to the higher stored energy offered by the Mn addition, which offers a smaller subgrain size locally within bands of Mn-dispersoids and produces a larger number of large Mn-constituent particles which can act as PSN nuclei, and to the interaction between Zr and Mn that lowered the Al_3Zr number density. This led to the formation of areas with fewer Al_3Zr dispersoids, which allowed new grains to nucleate in them and grow without meeting significant resistance. Regarding the probability of Mn-particles acting as PSN nuclei in the 0.1Zr-0.3Mn alloy, there is a very important difference compared to the 0.1Zr alloy since this mechanism could occur in the latter material only with the fewer Cu-containing constituent phases.

Another significant effect of the dispersoid type present was on the recrystallisation mechanism. The Zr addition favoured the broad front SIBM mechanism and the resulting recrystallisation textures were close to the β-fibre orientations, while the Mn addition promoted PSN on the large constituent Mn-phases leading to a texture dominated by more random orientations. These texture components were shown to be present in the deformation zones around the large particles. Finer Al_3Zr dispersoids also inhibited PSN.

In the 0.1Zr-0.3Mn alloy, recrystallisation was found to initiate within the Mn-containing zones, because they were regions of low pinning pressure between bands of Al_3Zr dispersoids, as shown earlier in §5.7.2. In addition, the lower subgrain size in these zones, as compared to Zr-containing ones, increased the local stored energy which is the driving force for recrystallisation. Not all Mn-dispersoid bands were associated with recrystallised grains at the start of annealing, but the recrystallised grains at this stage had all grown from such bands. The contribution from static recrystallisation of grains that probably recrystallised during hot-rolling and were subsequently deformed should not be excluded. For these two reasons recrystallisation appeared suddenly after 5 min and covered 17% of the microstructure, while for longer times the kinetics was controlled by the Al_3Zr coarsening and the increase was more gradual.

Finally, regarding the optimum dispersoid content in the AA2198 alloy, a strong interdependence between the Zr and Mn levels was observed from literature data for the combined addition of these elements. For higher Zr levels, a lower amount of Mn was required to effectively suppress recrystallisation and vice versa. For lower Zr and higher Mn levels, the dependence of Mn on the amount of Zr was much stronger and a much larger Mn content would be required when Zr would be reduced below a critical limit. Appropriate models could be used to predict the optimum dispersoid levels by taking into consideration the parameters that affect them.

CHAPTER 7: Effect of Dispersoids on Ageing Treatment and Mechanical Properties

7.1 Investigation of ageing and fracture toughness

The present chapter presents data on the mechanical properties of the AA2198 alloys as a function of the dispersoid content and ageing condition. These results were secondary observations of this thesis and they are not analysed in as much detail. However, they show that the dispersoid content is a crucial parameter that also affects other properties beyond recrystallisation resistance. Another point of focus is that the combined Zr+Mn addition deteriorates the alloys' overageing resistance at 200°C and fracture toughness compared to the sole Zr addition. The ageing behaviour was studied through Vickers hardness measurements and TEM, and the fracture toughness with Kahn tear tests and SEM.

7.2 Effect of dispersoids on ageing behaviour

The ageing response of the AA2198 alloy with various dispersoid contents was studied at room temperature, 155°C and 200°C. Hardness tests were employed to measure the change in strength of all alloys at each condition. The current section merely offers a brief description of the ageing behaviour, since it was not the main topic of this thesis. However, the overageing behaviour at 200°C showed some interesting results, which are worth looking at in more detail in the future.

7.2.1 Natural ageing

The hardening response of the AA2198 alloys at room temperature was examined after re-solution treating the T351 samples for 20 min at 505°C (Fig. 7.1). This was the only alloy temper available at the time of the experiments and this was the reason why the F temper was not chosen for these measurements.

After solution treatment the specimens were directly quenched in water. The Vickers hardness of the first samples was measured 1 h after the end of the heat treatment for times up to 1992 h (83 days) in the solution treated condition. All the alloys exhibited very low hardness values between VHN80 and VHN86 (Fig. 7.1). The vacancy concentration is known to be quite high right after annealing at a high temperature and water-quenching [108]. The strengthening kinetics were expected to be quite fast due to the faster diffusion of the solute atoms to form GP zones, which are responsible for room temperature strengthening in Al-Cu-Li alloys [65, 95]. After 24 h at RT, the Vickers hardness increased significantly for all alloys to values between VHN100 and VHN110. For longer times the increase was not so abrupt. In fact, all the hardness curves seemed to stabilise after 168 h. Prolonged RT ageing for 1992 h did not show any remarkable change. Of all the materials, the hardness values of the 0.1Zr-0.3Mn and 0.1Zr alloys were the highest throughout the whole time range covered, while that of the 0.4Mn alloy was the lowest.

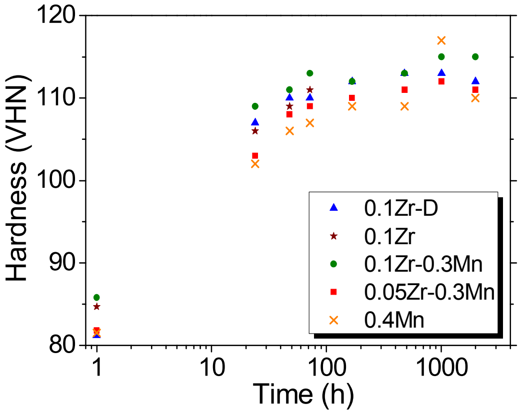

Fig. 7.1: Hardness curves for natural ageing after ST of the T351 sheet for 20 min at 505°C.

7.2.2 Artificial ageing at 155°C

The next step was to give the alloys an artificial ageing treatment which was carried out in an air furnace at 155°C. The temperature was increased from RT to 155°C at a rate of 75 K/h. The alloys used were initially in the T351 temper. During the very early stages of ageing, the alloys exhibited a significant drop in hardness of approximately VHN10-15 (Fig. 7.2). In some Al-Li alloys this hardness reversion is known to occur due to the dissolution of the GP zones and most or all of the δ' phase at the ageing temperature [42]. Since no δ' phase is formed in the AA2198 [12], the reversion trough in this case was due to the dissolution of GP zones. However, the alloys started to regain their strength after almost 2 h. Beyond this point there was a steep rise in hardness, due to the precipitation of the major strengthening phase T_1 and a minor volume fraction of θ' [12]. The hardness increased abruptly up to 14 h and after this point, only a marginal increase was observed up to 100 h. This was also the reason why the 14 h at 155°C condition was recommended as the optimum ageing treatment by Alcan CRV. The maximum hardness was approximately VHN170. The dispersoid type in each alloy did not seem to have any significant effect on the measured values. The 0.1Zr alloy showed a slightly lower hardness during the time interval 10-48 h, but eventually caught up with the rest. However, this variation was within the scatter range of the hardness data.

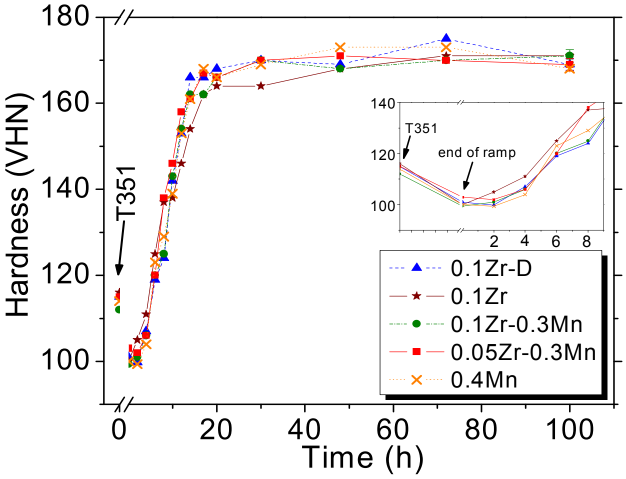

Fig. 7.2: Ageing curves at 155^{o}C from the T351 condition (ramp heating: 75 K/h). The inset shows the hardness reversion during the initial ageing stage.

From the hardness curves it is apparent that the strengthening precipitates in all the alloys here were not influenced by the dispersoid content. The diffraction patterns in Figs. 7.3a-c verified the presence of the major strengthening phase T_1 and a low volume fraction of θ', while no δ' was detected in agreement with expectations [12]. The presence of the T_1 phase was confirmed by the four spots around the $\{110\}_{Al}$ positions in the $<100>_{Al}$ zone axis in (a), by the streaks and the two spots in the $<110>_{Al}$ zone axis in (b) and by the six spots around the matrix reflections in the $<111>_{Al}$ zone axis, denoting hexagonal symmetry [70]. θ' was detected by the weak streaks seen in the $<100>_{Al}$ zone axis [70]. The fact that they were quite faint indicated their low volume fraction. The diffraction pattern in (e) shows the superlattice spots from the Al_3Zr phase which do not exist in the respective diffraction pattern of the 0.4Mn alloy in (b). Figs. 7.3d-g illustrate the size of T_1 plates at various stages of the ageing curve for the 0.1Zr-0.3Mn alloy. These pictures were taken at 8 h, 14 h and 100 h at 155^{o}C, near the $<110>_{Al}$ zone axis, in order to look at the T_1 plates edge-on because of their $\{111\}_{Al}$ habit plane. A large increase in the volume fraction of the plates was evident between 8 h and 14 h, which correlated well with the dramatic hardness increase in this interval. Between 14 h and 100 h the volume fraction did not change significantly, but undoubtedly precipitate coarsening took place [71]. The precipitate size was not measured experimentally since other references exist on this subject [12].

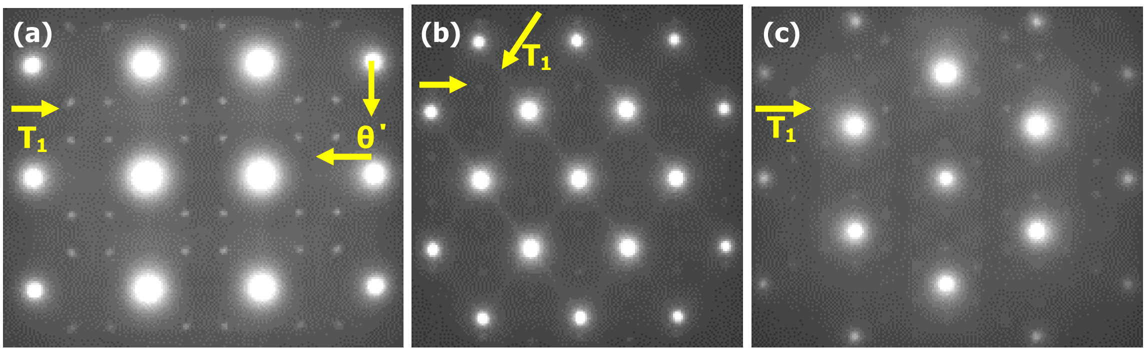

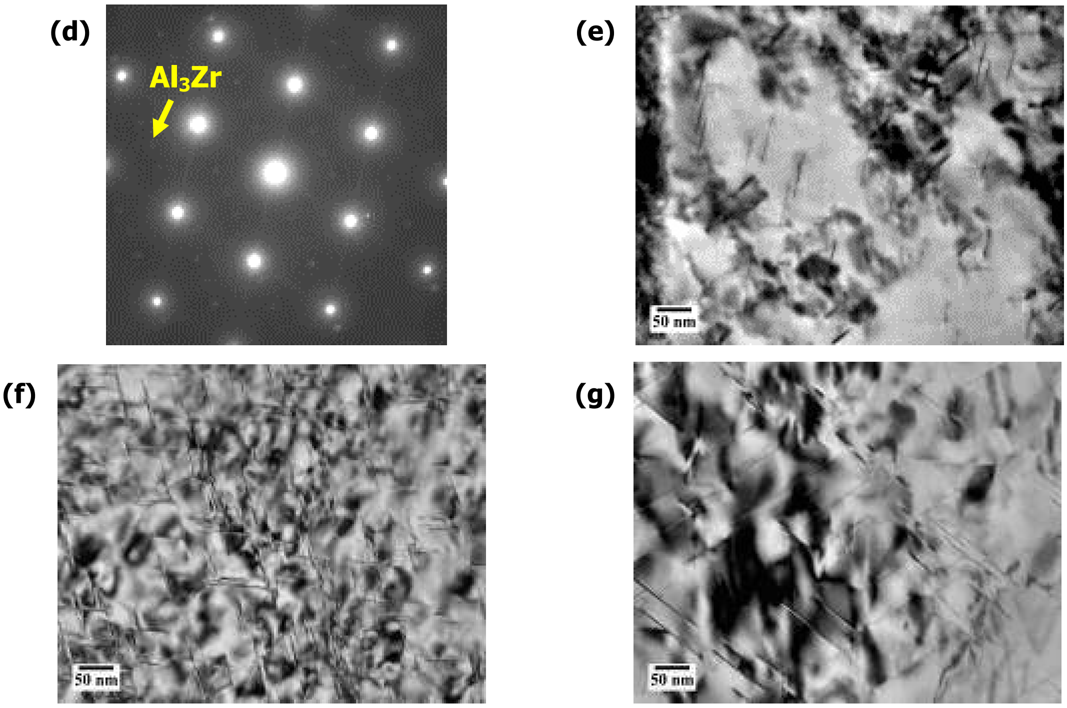

Fig. 7.3: Diffraction patterns (DPs) and T_1 distributions at different stages of the hardness curves at 155°C: **a)** DP of the $<100>_{Al}$ zone axis (35 h, 0.4Mn), **b)** DP of the $<110>_{Al}$ zone axis (35 h, 0.4Mn), **c)** DP of the $<111>_{Al}$ zone axis (35 h, 0.4Mn), **d)** DP of the $<110>_{Al}$ zone axis (8 h, 0.1Zr-0.3Mn), **e)** T_1 distribution (8 h, 0.1Zr-0.3Mn), **f)** T_1 distribution (14 h, 0.1Zr-0.3Mn), and **g)** T_1 distribution (100 h, 0.1Zr-0.3Mn).

7.2.3 Artificial ageing at 200°C

The artificial ageing response of the AA2198 alloys was also studied at 200°C, in order to determine if there was any effect of the dispersoids on the overageing behaviour. Hardness was measured for times up to 250 h. All the ageing curves in Fig. 7.4 exhibited a larger reduction at the end of the ramp heating stage, of approximately VHN15, compared to the initial T351 condition and around VHN40-50 compared to the peak hardness. The ageing response in this case was faster than at 155°C due to the accelerated kinetics at higher temperatures, so the hardness was much higher than for the T351 condition after only 30 min. The peak hardness was also achieved faster than at 155°C, after only 2 h, but it was slightly lower (VHN165). Overageing became apparent after 6 h. The dispersoid content did not seem to affect the alloy strength significantly throughout the interval up to 48 h. It was only for times longer than 72 h when some differences became evident. After 250 h the 0.1Zr-0.3Mn alloy exhibited the lowest hardness of all with a value of VHN110. The next lowest hardness was for the 0.1Zr-D alloy of VHN116 and then the sequence of the alloys was 0.1Zr, 0.05Zr-0.3Mn and 0.4Mn, with values of VHN120, VHN121 and VHN122 respectively. These results were not merely noise from the measurements, since the ageing treatments were repeated twice and gave the same sequence for the alloys both times. The reasons why these differences were observed are explained below.

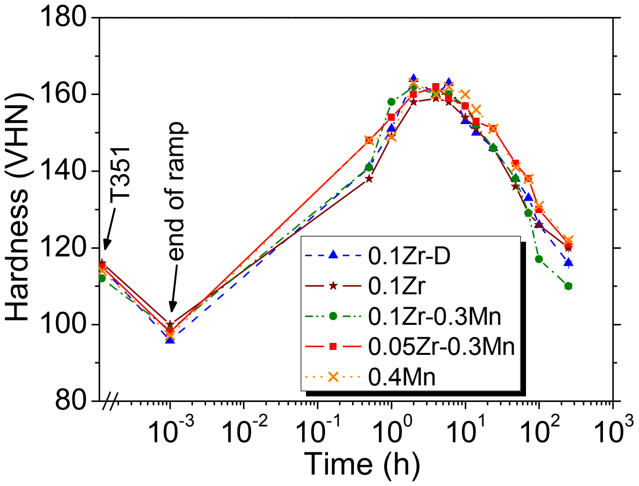

Fig. 7.4: Ageing curves at 200°C from the T351 condition (ramp heating: 75 K/h).

First of all, it has to be noted that the hardness drop after 6 h is caused by severe coarsening of the major strengthening phases (Fig. 7.5). Additionally, the nature of precipitation also affected the alloy strength. As it is generally known, heterogeneous precipitation is more intense at higher temperatures, while homogeneous nucleation is favoured at lower temperatures [107, 108]. The main reason for the reduced hardness of the 0.1Zr-0.3Mn alloy at 250 h, as compared to the rest of the alloys, was related to this parameter; the nature of precipitation. In the following paragraphs, all the cases of heterogeneous precipitation in the alloys are discussed.

The most important parameter of strength reduction was the coarsening of the main strengthening phases, especially of T_1. Fig. 7.5 shows the length of T_1 plates in the 0.4Mn alloy after 250 h at 200°C. The precipitates coarsened significantly, exceeding 150 nm in length in most cases. In the DF-TEM image in (a), they are shown tilted near a $<310>_{Al}$ zone axis in order to give a better view of their actual size in two-dimensions. Their thickness edge-on usually does not show a notable increase upon ageing [12].

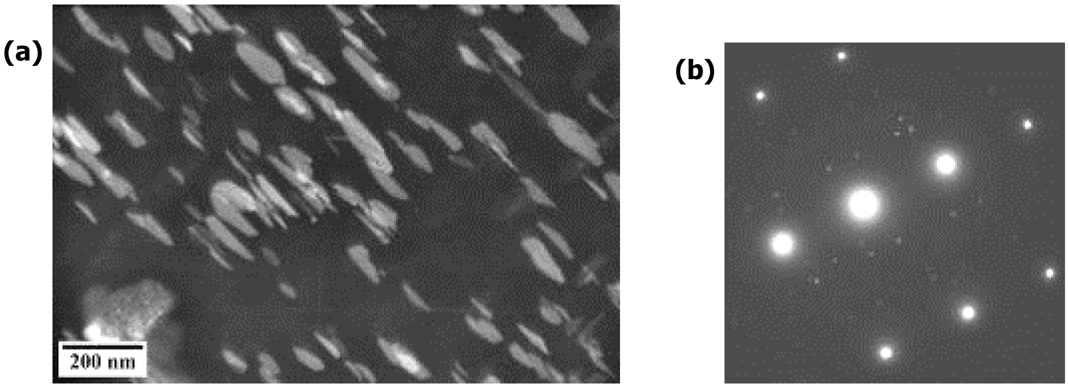

Fig. 7.5: Coarsening of T_1 plates (250 h at 200°C, 0.4Mn): **a)** dark field TEM image taken near the $<310>_{Al}$ zone axis, and **b)** DP from the $<310>_{Al}$ zone axis.

As mentioned earlier, a high density of heterogeneous precipitation was found on ageing at 200°C. Coarse phases were seen from SEM pictures to nucleate on HAGBs in all the alloys, although the density of the precipitates was slightly reduced at mid-thickness in comparison to the surface of the sheet. Evidence of this effect is provided for the 0.1Zr and 0.4Mn alloys in Figs. 7.6a-d. In addition, the GB phases appeared to be quite different in these two alloys. In the 0.1Zr-D alloy the coarse phases were individual particles, while in the 0.4Mn alloy a continuous GB layer was observed which covered the whole boundary (Fig. 7.6e). The composition of this phase remains unknown since it was not analysed by EDX.

Another important effect was that from the preferential precipitation of the T_1 phase on LAGBs. This was also known from the literature to occur at higher ageing temperatures [39, 40, 78]. Fig. 7.6g shows T_1 precipitates on a LAGB. Due to solute depletion in the regions adjacent to the GB, PFZs spanned over short distances from the boundary. Equally, PFZs were also created in the cases where individual particles nucleated (Fig. 7.6f). Thicker plates were also seen (Fig. 7.6h). All of these heterogeneities obviously affected the alloys' strength.

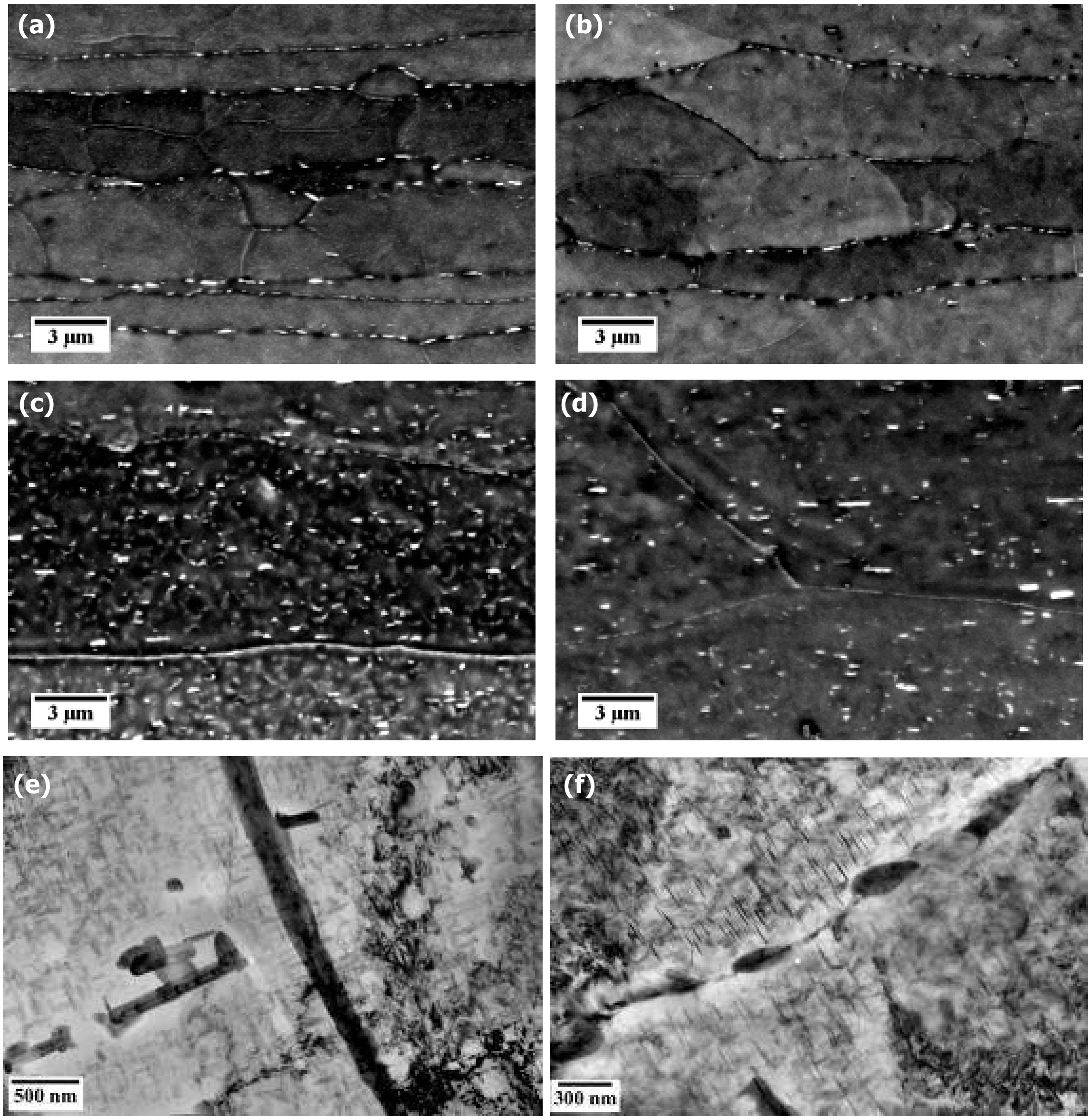

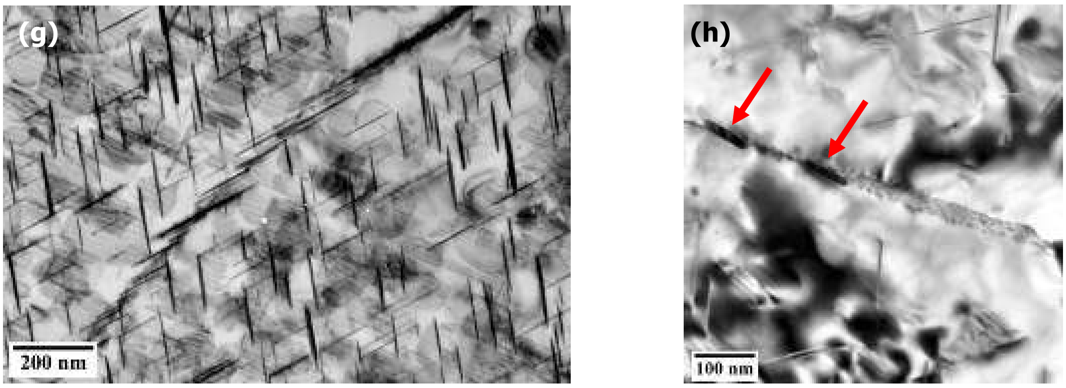

Fig. 7.6: GB precipitation after 250 h at 200°C: **a)** coarse HAGB particles in the 0.1Zr alloy near the surface, **b)** smaller HAGB particles in the 0.1Zr alloy at mid-thickness, **c)** a continuous HAGB phase in the 0.4Mn alloy near the surface, **d)** thinner HAGB phase in the 0.4Mn alloy at mid-thickness, **e)** unknown continuous phase on a GB (0.4Mn), **f)** individual particles precipitated on a LAGB (0.1Zr-0.3Mn), **g)** needle-like precipitates on a LAGB (0.1Zr-D), and **h)** thick plates on a LAGB (0.1Zr-0.3Mn).

The extent of recrystallisation was also found to hold an important role in the overageing behaviour of the alloys. Recrystallised grains contained coarse precipitates in their interior, in contrast to subgrains that did not appear to contain as many. This phenomenon was more intense near the sheet surface than at mid-thickness. Figs. 7.7a,b suggest that this happened irrespective of the dispersoid type present, since it was observed for both the 0.1Zr-D and 0.4Mn alloys. Coarser particles are less effective in inhibiting dislocation motion, so this behaviour was expected to deteriorate the alloy strength, irrespective of their features and composition. Differences between recovered and recrystallised grains have been reported in the past for an Al-Cu-Li-Zr alloy, where Kanno and Ou [83] noticed a difference in the nucleation pattern of the θ' phase on Al_3Zr dispersoids, but not for T_1. In recovered areas the flat coherent side of the θ' phase was attached to the Al_3Zr dispersoids, while in recrystallised grains the incoherent side of θ' was in contact with the Al_3Zr particles. Some similar phenomenon might be present here as well, i.e. in recrystallised grains the Al_3Zr dispersoids could have become incoherent encouraging nucleation of θ, T_2 and other equilibrium phases.

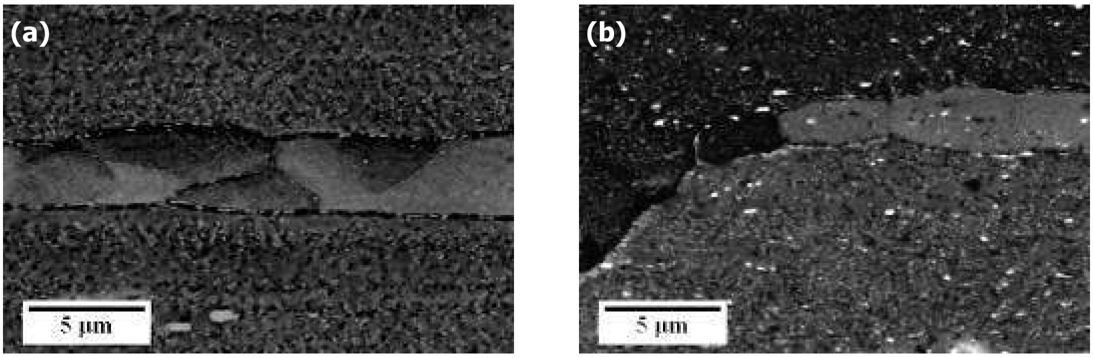

Fig. 7.7: Precipitation within recrystallised and recovered grains after 250 h at 200°C: **a)** near the surface of the 0.1Zr-D alloy, and **b)** near the surface of the 0.1Zr-0.3Mn alloy.

Several other signs of heterogeneous precipitation were found, some of them being directly related to dispersoids. Fig. 7.8 shows preferential nucleation of overaged phases on $Al_{20}Cu_2Mn_3$ dispersoids in the 0.4Mn alloy after 250 h. These phases had quite complicated morphologies and several types were noted. The most common morphology was lathes. In Al-Cu-Li alloys the overaged phases are mainly coarse T_1, with lower amounts of T_2, T_B and R [45]. Similarly to the GBs earlier, PFZs were observed around the dispersoids due to localised solute depletion. This obviously reduced the strength of the matrix locally. Hence, this phenomenon was expected more frequently in the alloy with the highest number density of Mn dispersoids (0.4Mn alloy), as shown in §5.5. However, since this alloy showed the highest hardness after 250 h, it was concluded that the preferential nucleation of second phases on dispersoids was not the most critical parameter that affected strength.

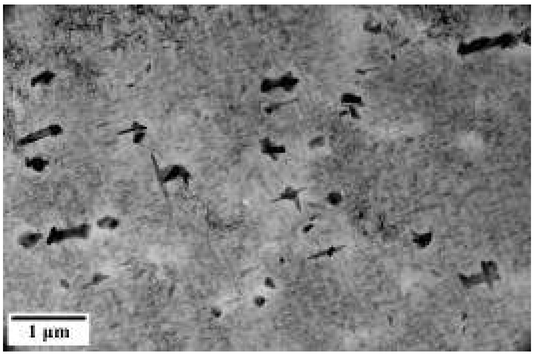

Fig. 7.8: PFZs around Mn-dispersoids due to solute depletion from the matrix, resulting from the heterogeneously precipitated phases in a recrystallised area (250 h at 200°C, 0.4Mn).

Heterogeneous distribution of second phases was generally quite intense in all alloys containing either type of dispersoid. Fig. 7.9 illustrates some examples. The $Al_{20}Cu_2Mn_3$ dispersoids were found to nucleate several types of particles at their interface, such as coarse plates or rod-like particles (Fig. 7.9a) or coarse T_1 plates (Fig. 7.9b). On the other hand, the Al_3Zr dispersoids were seen to be associated with large rod-like phases (Fig. 7.9c) or T_1 plates as well (Fig. 7.9d). The precipitates exhibited other types of interaction, either with each other or with other features in the matrix. On certain occasions, T_1 precipitates were seen to intersect other variants of the same type that formed on a different plane of the {111} family (Fig. 7.9e). Cross-linking was observed either in the main body of the plates (Fig. 7.9e) or at their edges (Fig. 7.9f). The T_1 plates were also found in one case to be connected to an unknown phase with an almost hexagonal morphology (Fig. 7.9g). Finally, second phases also nucleated on dislocations (Fig. 7.9h).

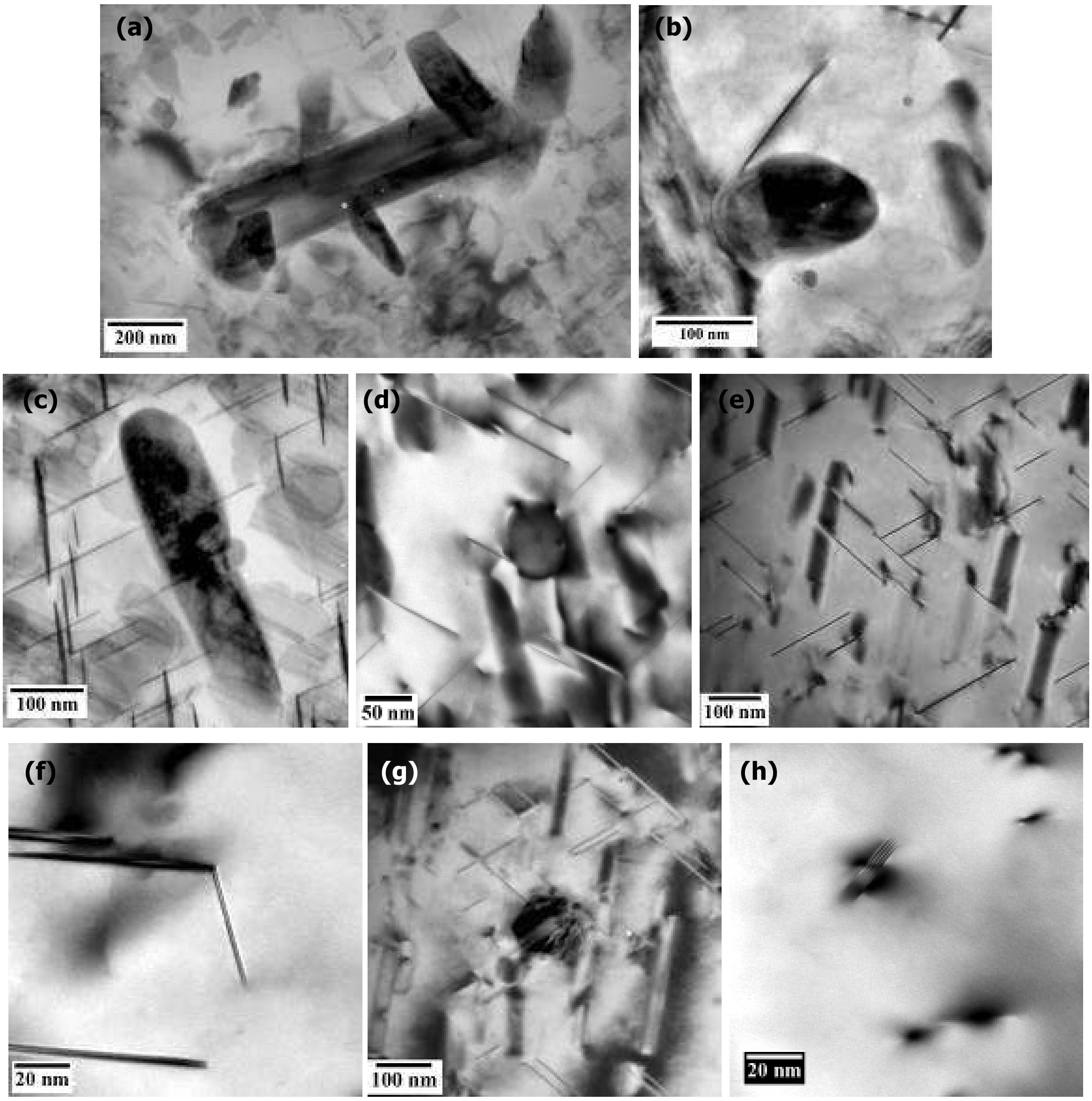

Fig. 7.9: Heterogeneous precipitation of second phases after 250 h at 200°C: **a)** phases nucleated on the incoherent interface of an $Al_{20}Cu_2Mn_3$ dispersoid (0.4Mn), **b)** T_1 plate nucleated on the incoherent interface of an $Al_{20}Cu_2Mn_3$ dispersoid (0.1Zr-0.3Mn), **c)** large rod-like particle nucleated on an Al_3Zr dispersoid (0.1Zr-D), **d)** T_1 precipitate nucleated on the interface of an Al_3Zr dispersoid (0.1Zr-D), **e)** association of T_1 precipitates with phases from a different plane (0.1Zr-D), **f)** two T_1 precipitates connected at their edges (0.1Zr-0.3Mn), **g)** a faceted phase associated with a needle-like precipitate (0.1Zr-D), and **h)** plate-like precipitate nucleated on a dislocation (0.1Zr-0.3Mn).

Table 7.1 summarises the measured values of the parameters that affect overageing resistance. A closer look at the measured values from the T351 temper of all alloys leads to the conclusion that a single parameter on its own cannot account for the hardness reduction upon overageing. This effect comes as a combination of all these parameters. For example, the 0.1Zr-0.3Mn alloy had a lower hardness than the 0.1Zr-D and 0.1Zr alloys due to its higher recrystallised V_f that promoted heterogeneous precipitation on large Al_3Zr dispersoids which had lost coherency and also on Mn-dispersoids. Hence, the addition of Mn causes the differences between these alloys. The net contribution from the PFZs around GBs is difficult to be determined due to the difference in the recrystallised V_f between these two alloys.

The reason why the 0.1Zr-D alloy had a slightly lower hardness on overageing than the 0.1Zr alloy, was most probably due to the higher recrystallised volume fraction of the former, especially near the surface of the sheet. This resulted in the heterogeneous precipitation of a higher volume fraction of coarse second phases which reduced strength. The Al_3Zr dispersoids were quite coarse in the 0.1Zr-D alloy and a larger number of them had lost coherency. Additionally, the hardness tests were carried out on the RD-TD plane at the sheet surface, hence the higher degree of recrystallisation of the 0.1Zr-D alloy in that area led to this observed discrepancy.

The 0.05Zr-0.3Mn and 0.4Mn alloys followed accordingly based on their recrystallised V_f and dispersoid number densities. The latter alloy contained the lowest total number of dispersoids (no Al_3Zr present). The detrimental effect of LAGB precipitation was removed by the fully recrystallised microstructure and only HAGB precipitation occurred. Hence the less severe heterogeneous precipitation in the 0.4Mn alloy was responsible for its higher strength.

In conclusion, the hardness drop after 250 h at 200°C resulted from a combination of all the previous factors. However, the most important ones are believed to be the recrystallised volume fraction, the number density of dispersoids that can act as heterogeneous nucleation sites and the subgrain size and grain size, as both are associated with PFZs around them. The lowest hardness observed for the 0.1Zr-0.3Mn alloy was due to the relatively high recrystallised volume (13.5% in the T351 temper) which led to a larger volume fraction of coarse phases nucleating on semi-coherent and incoherent particles within the recrystallised grains. On the other hand, the recrystallised V_f caused a reduction in the area of LAGBs in the locations where new grains have grown, moderating the negative effect of PFZs.

Table 7.1: Measured values in the T351 temper for all alloys, of parameters affecting the overageing resistance. The hardness values at the final ageing condition are also shown.

Alloy	**0.1Zr-D**	**0.1Zr**	**0.1Zr-0.3Mn**	**0.05Zr-0.3Mn**	**0.4Mn**
Recryst. V_f (%)	5.0	1.5	13.5	62.5	100
Al_3Zr num. density (μm^{-3})	102.0	251.9	174.5	N/M	—
Al_3Zr average diameter (nm)	33.9*	18.8*	21.3*	25.3*	—
$Al_{20}Cu_2Mn_3$ num. density (μm^{-3})	—	—	3.45	5.44	7.17
HAGB ND spacing (μm)	8.19	7.36	5.76	18.38	50.63
LAGB ND spacing (μm)	3.55	3.38	2.82	5.66	—
VHN 250h @ 200°C	116	120	110	121	122

* The average size is employed only to give an indication of the size distribution, since it is quite difficult to measure accurately the number density of only the semi-coherent and incoherent Al_3Zr dispersoids.

N/M: not measured

7.3 Fracture toughness

The effect of dispersoids on fracture toughness was assessed by means of the Kahn tear tests. The effects of several experimental parameters were investigated. Each alloy was tested in three conditions (T351, 14 h at 155°C, 100 h at 155°C) and for each of these conditions, samples were cut from the sheet in two different orientations (L-T and T-L). In addition to the two standard orientations, the two alloys of main interest (0.1Zr, 0.1Zr-0.3Mn) were also tested at a 45° angle to the RD. After presenting the results of the mechanical tests, the fracture mechanisms were analysed by SEM to determine the effect of the different dispersoids present on fracture resistance.

7.3.1 Measurements of fracture toughness

As mentioned in §3.3.3, four important properties can be determined by the Kahn tear tests; tear strength, unit initiation energy (UIE), unit propagation energy (UPE) and unit total energy (UTE). Fig. 7.10 illustrates how some of these properties change in all the alloys during ageing at 155°C. The alloys are compared to each other later in Figs. 7.11 and 7.12. All the numerical values are given in Appendix III.

The tear strength is proportional to the maximum force required to initiate a crack at the notch in the specimen (Fig. 7.10a) [260, 261]. The lowest values measured for all parameters corresponded to the T351 condition, with the benefit of ageing being obvious at the condition of the optimum ageing time (14 h). Overageing led to a tear strength reduction, since the coarser T_1 plates could not inhibit the dislocation motion as effectively. This was the case for both sample orientations, L-T and T-L. The UIE on the other hand, seemed to deteriorate with ageing for most alloys (Fig. 7.10b). However, the 0.4Mn alloy showed the lowest decrease upon ageing in both orientations. The severity of the effect of overageing could be seen from the fact that after 100 h the UIE was reduced to less than half of the T351 values for most alloys. The UPE was affected in a similar way, since precipitation on the GBs created an easier path for cracks to propagate (Fig. 7.10c). Only the 0.1Zr-0.3Mn alloy showed an increase in the L-T orientation at 14 h, but this could simply be an artefact. The UPE values in the T-L orientation at 100 h were zero, since all the alloys ruptured in a brittle manner due to cracking along GBs. Finally, the UTE values decreased with ageing according to the UIE and UPE (Fig. 7.10d).

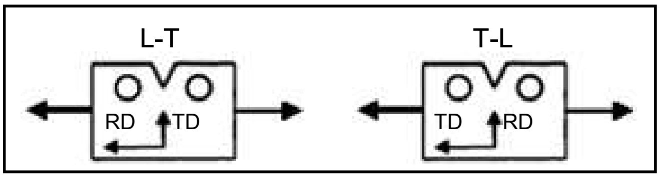

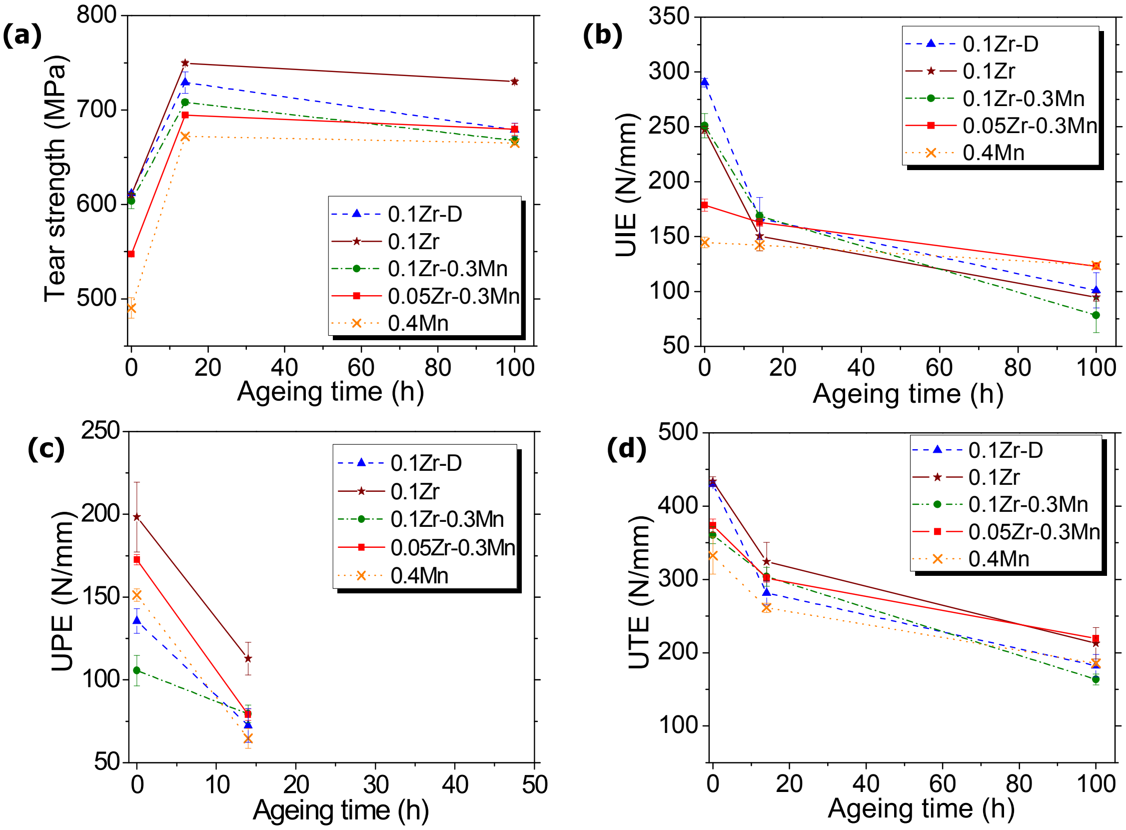

Fig. 7.10: Selected results obtained from Kahn tear test curves, showing the dependence on ageing time and sample orientation for all alloys: **a)** tear strength, L-T, **b)** unit initiation energy, L-T, **c)** unit propagation energy, T-L, and **d)** unit total energy, L-T.

The introduction of many experimental parameters in the Kahn tear tests rendered the presentation of the results difficult. The best method that allowed correlation of all these parameters was through radial plots, as shown in Fig. 7.11. They were constructed by using only ratios and not the measured values. The plots required the arbitrary assignment of the value 1 to one of the alloys and all the rest were expressed as the ratio over the measured value of the selected alloy. For the present results, the 0.4Mn alloy generally having the lowest values was allocated as the base alloy equal to 1.

The optimum dispersoid content should be determined by the best combination of all the measured properties in all conditions. Hence the alloy with the largest area outlined by the connecting points would be the best candidate. Fig. 7.11a shows that the 0.1Zr alloy exhibited the best combination of properties in the T351 condition. In this case, the slightly lower UIE values were outweighed by the very high UPE in both L-T and T-L, in contrast to the 0.1Zr-0.3Mn alloy which appeared to be the worst in these orientations. The situation was quite different upon peak ageing for 14 h at 155^{o}C (Fig. 7.11b), since the 0.1Zr-0.3Mn alloy was the most resistant to crack initiation, however, the 0.1Zr alloy was much more resistant in crack propagation. Finally, after 100 h the situation changed again (Fig. 7.11c). After overageing at 155^{o}C, the 0.1Zr alloy had better properties in the L-T orientation, while the 0.1Zr-0.3Mn alloy was best in T-L. Overall, these two alloys showed the best combination of properties in all ageing conditions and orientations.

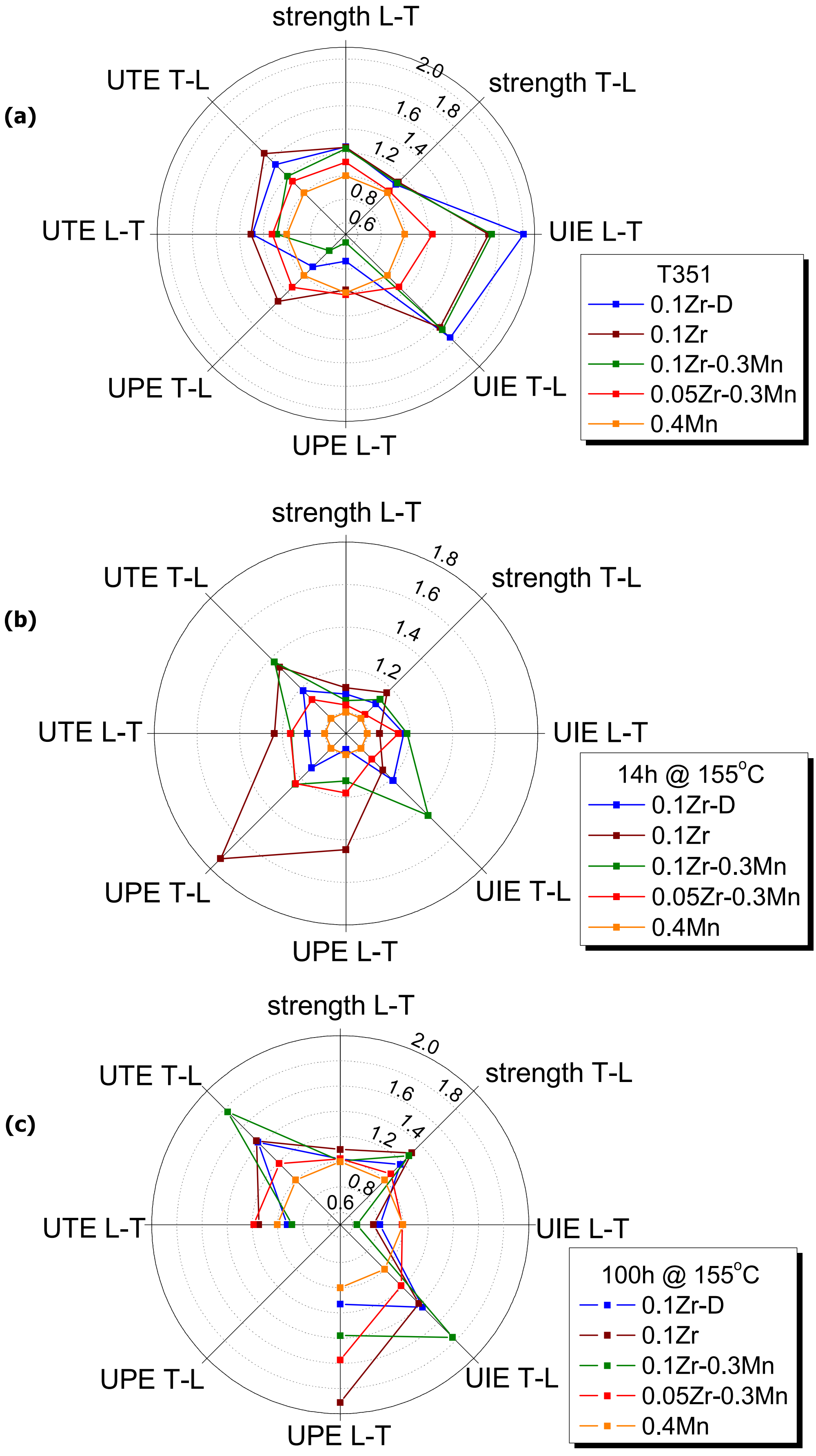

Fig. 7.11: Radial plots comparing the main Kahn tear test parameters for all alloys with varying conditions and sample orientations: **a)** T351 temper, **b)** aged for 14 h at 155°C, **c)** aged for 100 h at 155°C.

In order to have a better view of the properties in all orientations, the two alloys with the best properties were also tested at 45° to the RD in the optimum ageing condition (14 h at 155°C). The 0.1Zr alloy was in most cases superior to the 0.1Zr-0.3Mn in the 45° orientation, except for its lower UPE. In general, the 0.1Zr alloy prevailed in most of the properties shown on the comparison graph below (Fig. 7.12). Most important of all, in the cases where it exhibited higher values, the actual difference from the 0.1Zr-0.3Mn alloy was much greater than when the latter alloy prevailed.

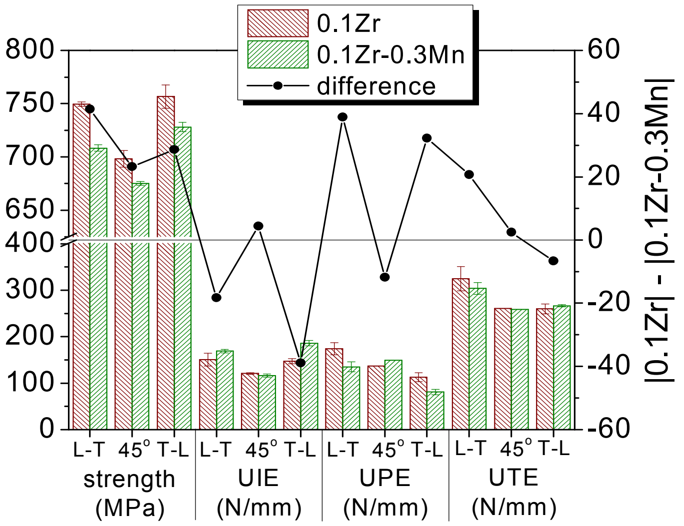

Fig. 7.12: Comparison of all Kahn tear test parameters between the two alloys exhibiting the best combination of mechanical properties; 0.1Zr and 0.1Zr-0.3Mn (aged for 14 h at 155°C).

The fact that the 0.4Mn alloy had the lowest properties, almost in every case, was not surprising since the Mn addition is known to significantly improve mechanical properties of Al alloys only for contents around 0.5-0.6 wt% or slightly higher [171, 245]. At such Mn contents, strength is not significantly affected, but ductility and toughness are generally improved.

7.3.2 Fracture dependence on the dispersoid content

By comparing the effect of the various dispersoid contents on the fracture surface morphology, one could observe striking differences between the individual Zr and Mn additions. The nature of the effect of the dispersoids was first compared in the T351 temper, in order to avoid effects from ageing precipitates in the other conditions. Fig. 7.13 illustrates differences between the 0.1Zr-D and 0.4Mn alloys. In the Zr-containing alloy in (a), large dimples were formed around constituent phases. Since the constituent phases were widely-spaced within the microstructure, the microvoids which nucleated on them grew to a large size before they coalesced and resulted in the large dimples observed eventually [239]. On the other hand, image (b) shows a combination of coarse and fine dimples resulting from large constituent phases and incoherent $Al_{20}Cu_2Mn_3$ dispersoids respectively. Since the dispersoids were relatively closely-spaced, the fine microvoids coalesced after growing to a small extent only. Figs. 7.13c,d show that indeed the particle size was relevant to the dimple size. In the case of the 0.4Mn alloy in Figs. 7.13e,f each dimple contained one Mn-dispersoid.

Dispersoids also have an indirect effect on fracture toughness, through their influence on the recrystallised V_f and texture. For example, the Brass texture component is known to deteriorate mechanical properties [4] and so do recrystallised grains [254].

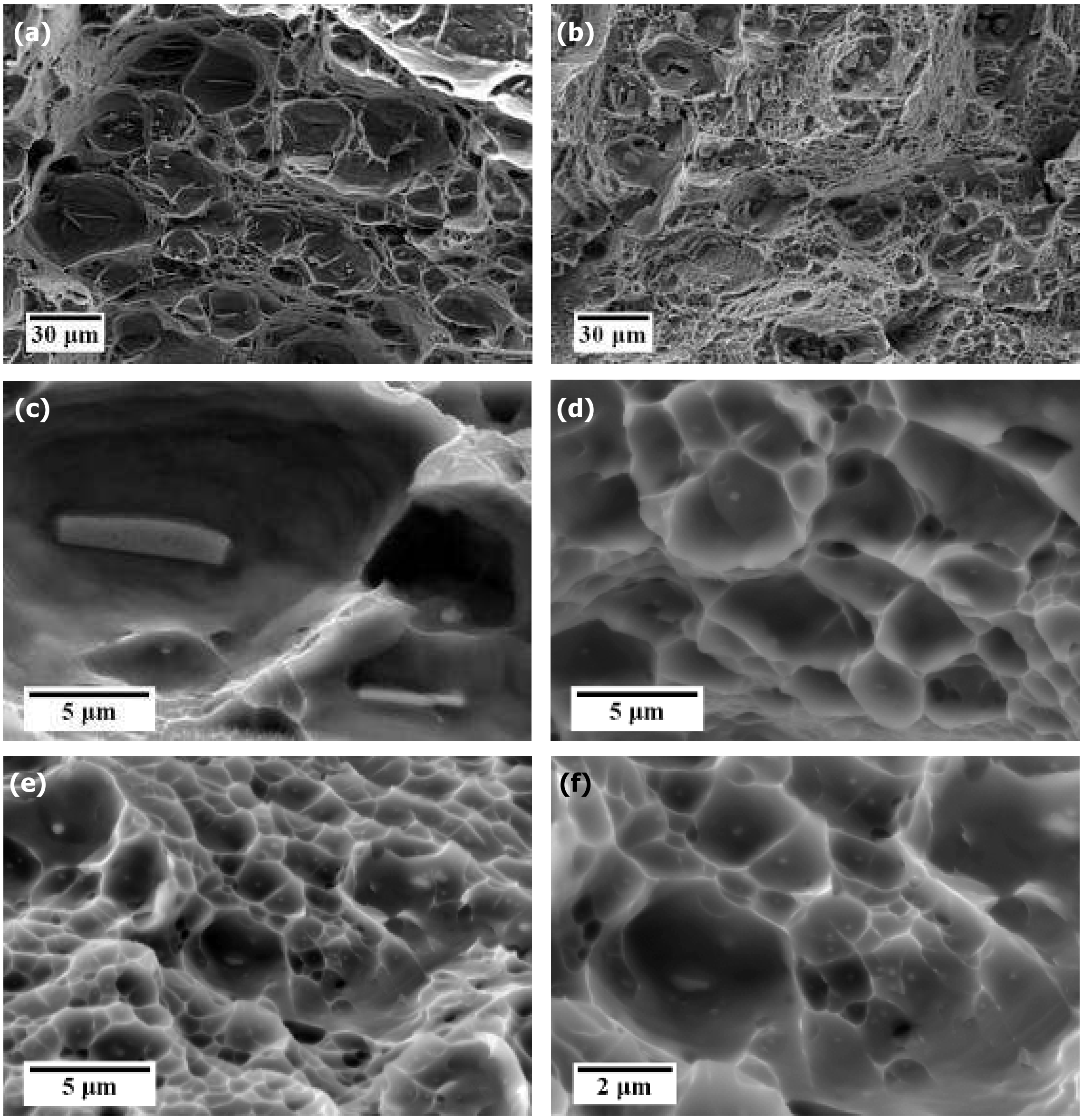

Fig. 7.13: Effect of Zr and Mn additions on the fracture surface morphology (T351, L-T): **a)** the 0.1Zr-D alloy having mainly large dimples, **b)** coarse and fine dimples in the 0.4Mn alloy, **c)** a large dimple around a constituent particle (0.1Zr-D), **d)** smaller dimples around smaller intermetallics (0.1Zr-D), **e)** fine dimples formed around $Al_{20}Cu_2Mn_3$ dispersoids (0.4Mn), and **f)** higher magnification of the same area showing the association of fine dimples with Mn-dispersoids.

The large constituent particles were analysed by EDX in the 0.1Zr-0.3Mn alloy to determine their composition. EDX mapping was employed in the SEM and the results are shown in Fig. 7.14. The large inclusions in this alloy contained Mn, Cu and Fe. No quantification was attempted here, since it was shown earlier in §5.2 that the GB phases in the as-cast material were mainly rich in Cu, with lower amounts of Fe principally and little Mn. In agreement to the previous findings in §5.2, the contrast of the particles relative to the background in the individual element maps below indicated the same ratio of Mn, Fe and Cu.

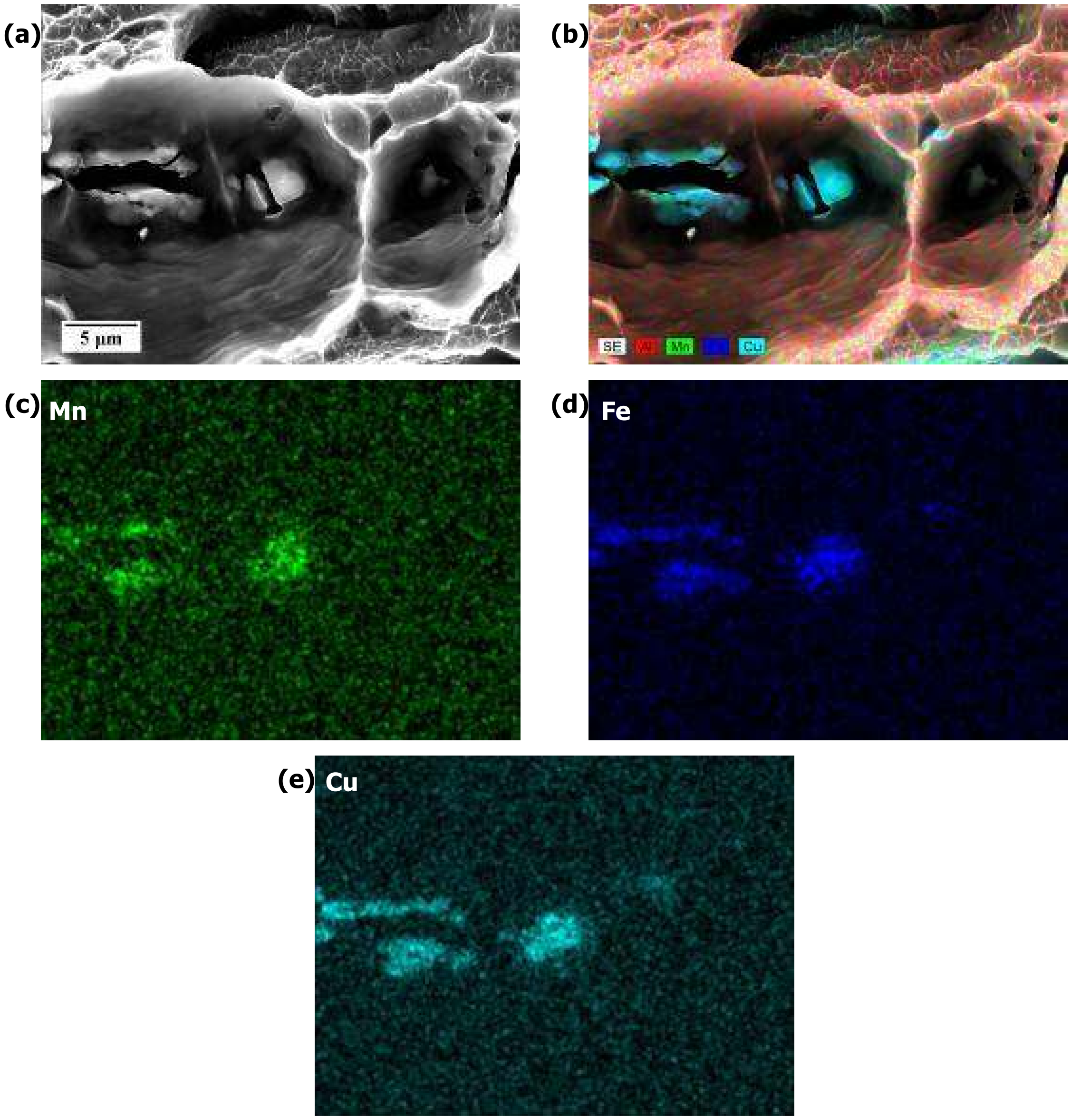

Fig. 7.14: EDX mapping on large constituent phases (0.1Zr-0.3Mn alloy, T351, L-T): **a)** SE image, **b)** EDX map, **c)** Mn map, **d)** Fe map, and **e)** Cu map.

7.3.3 Fracture dependence on the sample orientation

The effect of dispersoid content on anisotropy was quite significant, especially in the case of the Mn addition. In the L-T orientation, the crack initiates perpendicular to RD so it is more difficult to cut through the grains. On the other hand, cracks form parallel to RD and propagate along the GBs in the T-L orientation. Fig. 7.15 illustrates the most pronounced differences for the individual additions of Zr and Mn in the 0.1Zr-D and 0.4Mn alloys respectively. For both dispersoid types, mainly dimple fracture occurred again in the L-T, with some evidence of transgranular cleavage as well (Figs. 7.15a,c). In the T-L orientation, intergranular fracture was the principal mode, but again signs of cleavage were evident (Figs.

7.15b,d). The most significant difference came from the effect of the incoherent Mn-dispersoids, which again acted as sites for microvoid nucleation and resulted in large cracks initiating from the merging of these voids (Fig. 7.15e).

The fracture behaviour with the sample orientation 45° to the RD was more complicated than for L-T and T-L orientations. In this orientation, the 0.1Zr and 0.1Zr-0.3Mn alloys exhibited lower strength, lower UIE and intermediate UPE and UTE, as compared to the other two orientations, according to the graph in Fig. 7.12. In addition, the crack path showed a large deviation from a straight line connecting the notch tip to the opposite side of the specimen, resulting in some samples being discarded as outside the specifications for accurate tear test data.

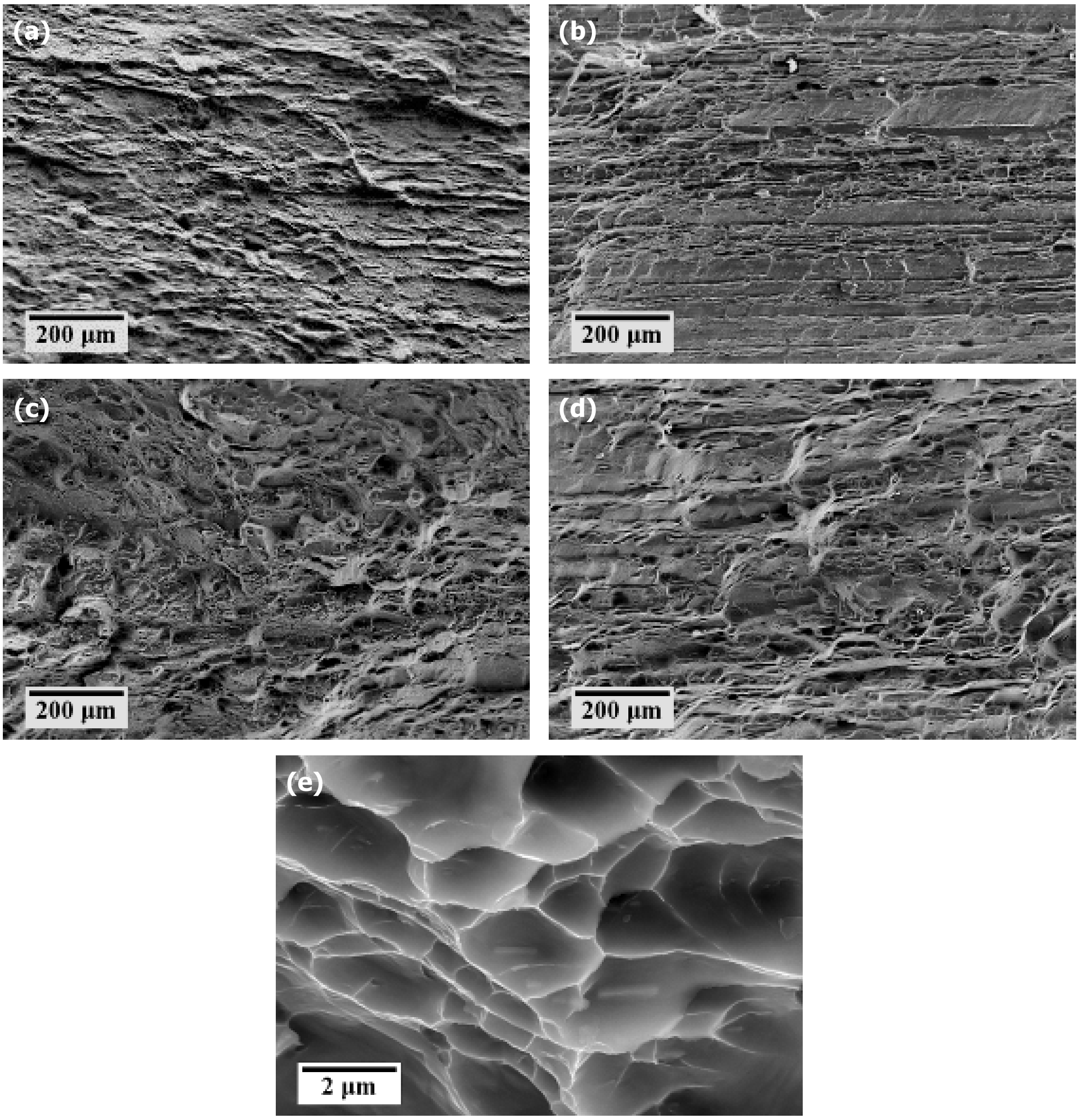

Fig. 7.15: Effect of sample orientation on the fracture surface morphology (propagation area, T351): **a)** L-T, 0.1Zr-D, **b)** T-L, 0.1Zr-D, **c)** L-T, 0.4Mn, **d)** T-L, 0.4Mn, and **e)** dimples originating from incoherent $Al_{20}Cu_2Mn_3$ dispersoids (T-L, 0.4Mn).

7.3.4 Fracture dependence on the ageing treatment

The peak-aged and overaged conditions clearly promoted intergranular fracture. This is evident when looking at Fig. 7.16 from (a) to (c). In the T351 temper dimple fracture was dominant. At the peak ageing condition, dimple fracture still existed (Fig. 7.16d) but intergranular fracture also occurred to a large extent. Eventually, after 100 h at 155°C the fracture mode was mixed with mainly transgranular cleavage and intergranular, as seen in (e). The cleavage steps in (f) are one characteristic sign of the former mode. The microstructural effects of ageing precipitates on fracture were mentioned briefly in §7.3.1 and several reviews analyse them in detail [16, 240, 301].

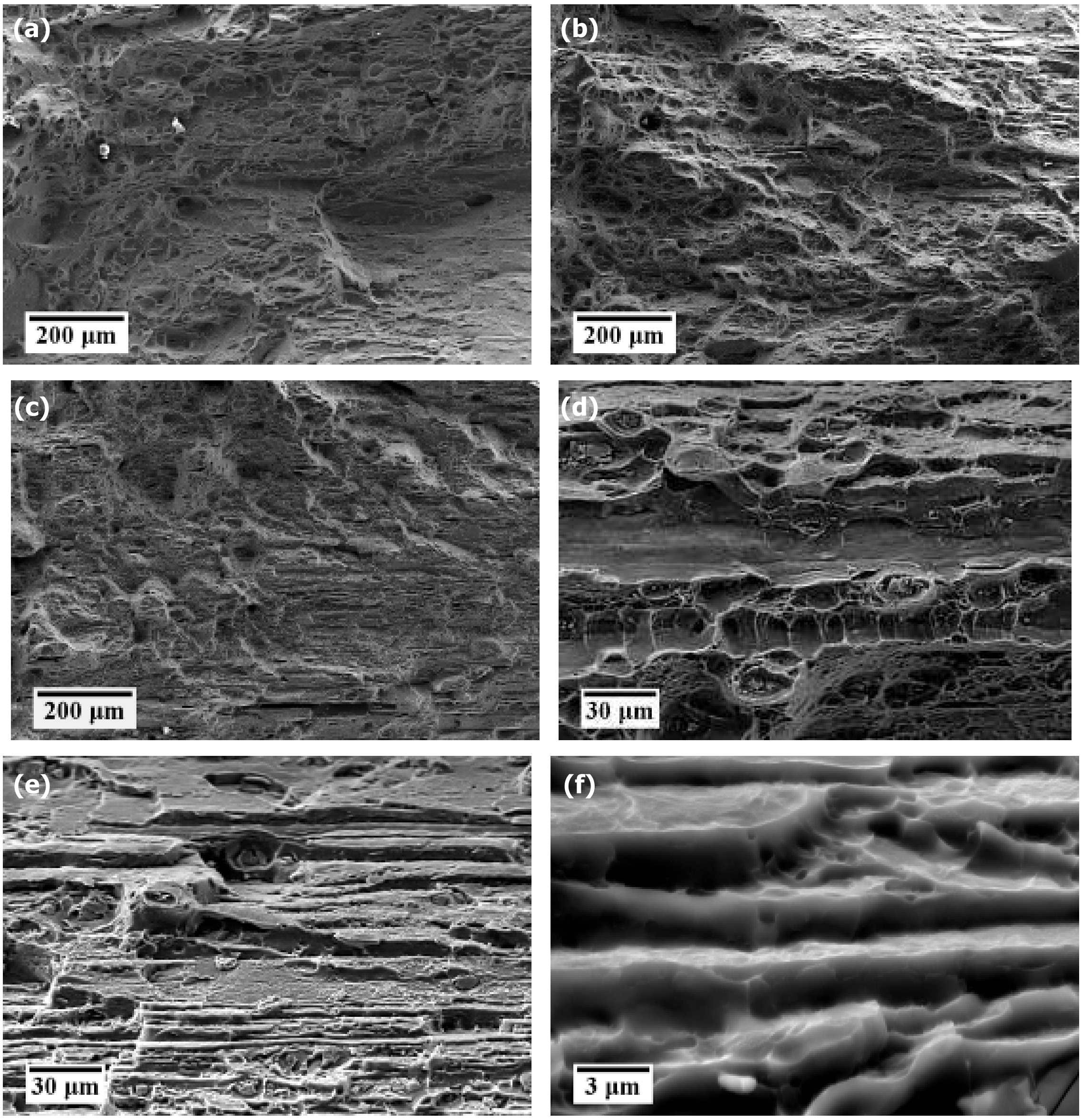

Fig. 7.16: Effect of ageing condition on the fracture surface morphology (0.1Zr-0.3Mn, T-L): **a)** T351, **b)** 14 h at 155°C, **c)** 100h at 155°C, **d)** intergranular dimple fracture after 14 h at 155°C, **e)** mixed transgranular cleavage and intergranular fracture after 100h at 155°C, and **f)** cleavage steps after 100 h at 155°C.

A final interesting observation was the presence of shallow dimples in some cases of intergranular fracture. Fig. 7.17 shows such an area in the overaged 0.4Mn alloy in the L-T orientation. The fine dimples were all linked to $Al_{20}Cu_2Mn_3$ dispersoids. As the magnified image indicates, decohesion took place at the incoherent interface of the particle since all of them could be seen protruding from the matrix. Such shallow dimples are reported to originate from microvoid coalescence by shear along slip planes [239].

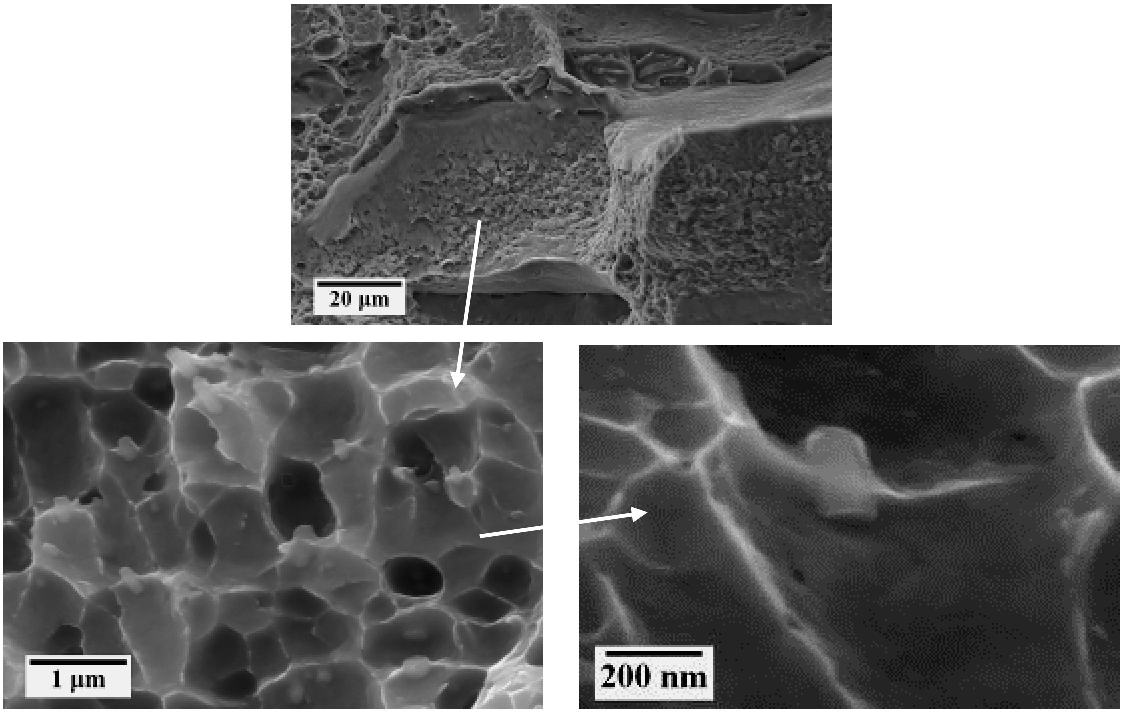

Fig. 7.17: Shallow dimples in the grain interior starting at a distance from the GBs (100 h at 155°C, 0.4Mn, L-T).

7.4 Summary of the effects of dispersoids on ageing and fracture behaviour

The natural ageing response of the AA2198 alloys was illustrated within 168 h after ST from the T351 temper. The differences between the alloys were small and varied within the range of the experimental error. The response to artificial ageing at 155°C on the other hand, was totally independent of the dispersoid content and only relied on the size and density of the major strengthening phase T_1.

The role of dispersoids on overageing was mainly determined by their coherency. When the Al_3Zr particles coarsened within recrystallised grains and lost coherency, preferential nucleation of second phases occurred on them and this led to a heterogeneous distribution of coarse equilibrium phases and to the creation of PFZs around the particles. Heterogeneous precipitation also occurred on all the Mn-dispersoids since they are incoherent. The overageing resistance was also affected by the grain size and subgrain size due to preferential nucleation of equilibrium phases on HAGBs and LAGBs. A smaller grain size yields a greater

GB length where precipitation can take place and form PFZs around them. However, the most important parameter was the level of recrystallisation since it promoted heterogeneous precipitation on semi-coherent and incoherent dispersoids. It also reduced the area of LAGBs and HAGBs due to the growth of recrystallised grains. The 0.1Zr-0.3Mn alloy with a high dispersoid density, recrystallised V_f of 13.5% and the lowest grain size, exhibited the lowest hardness after 250 h at 200°C. The order of decreasing hardness for the alloys was: 0.4Mn, 0.05Zr-0.3Mn, 0.1Zr, 0.1Zr-D, 0.1Zr-0.3Mn.

The fracture mode of the alloys was highly dependent on the experimental parameters examined here; i.e. dispersoid content, sample orientation, ageing condition. Other parameters that also affect fracture, such as texture and recrystallisation, were not discussed since it was difficult to separate them from the direct effects of the dispersoids. Overall, the 0.1Zr alloy was superior to the rest of the alloys since it exhibited the best combination of mechanical properties. Its unrecrystallised microstructure and strong texture also contributed towards this. In addition, the fine, coherent Al_3Zr dispersoids can pin the dislocation motion more effectively and do not nucleate microvoids around them in contrast to the $Al_{20}Cu_2Mn_3$ dispersoids. The 0.1Zr alloy had a better combination of properties compared to the 0.1Zr-0.3Mn alloy for the conditions studied. Their difference was mainly caused by the higher recrystallised volume fraction and weaker texture in the latter alloy and the ability of the Mn-dispersoids and constituent phases to nucleate voids. The alloy that exhibited the worst fracture resistance was the 0.4Mn alloy due to its fully recrystallised microstructure and the high volume fraction of Mn-particles.

Conclusions

- The main conclusion from this work is the interaction between Zr and Mn when these two elements are added together in an Al aerospace alloy. The most important effects of this interaction were on recrystallisation resistance, Al_3Zr dispersoid distributions, texture strength, fracture toughness and overageing resistance.

- Zr can inhibit more effectively recrystallisation and the increase in grain size compared to Mn. However, when both elements were present in the 0.1Zr-0.3Mn alloy, the grain size was lower compared to the 0.1Zr alloy, but recrystallisation resistance was worse. The lower grain size resulted from the opposite microsegregation patterns of Zr and Mn during casting, which helps fill up the grain with dispersoids and minimise dispersoid-free zones. A further reduction of the Zr content to 0.05 wt% deteriorated the recrystallisation resistance even more and a fully recrystallised microstructure was found in the 0.4Mn alloy in the T351 rolled sheet.

- The interaction between Zr and Mn is visible from the effect on the distributions of both types of dispersoids. The 0.1Zr-0.3Mn alloy had a lower number density and volume fraction of Al_3Zr dispersoids compared to the 0.1Zr alloy. On the other hand, the $Al_{20}Cu_2Mn_3$ dispersoids were also reduced in density and volume fraction in the 0.1Zr-0.3Mn alloy compared to the 0.05-0.3Mn alloy. Hence, the interaction works in both directions for these two elements.

- The larger size, lower number density and lower volume fraction of the Al_3Zr dispersoids in the 0.1Zr-0.3Mn alloy compared to the 0.1Zr alloy was proven not to result from the inclusion of Zr within Mn-containing constituent phases on GBs and $Al_{20}Cu_2Mn_3$ dispersoids in the grain interior. The reasons for these effects remain unclear at this stage. The Al_3Zr volume fraction was especially low within bands of $Al_{20}Cu_2Mn_3$ dispersoids. Zr was also found dissolved in a number of other phases, such as Al_2Cu after hot-rolling. However, Al_3Zr dispersoids were shown not to nucleate at the interfaces of $Al_{20}Cu_2Mn_3$ particles and such signs in the TEM are merely due to overlapping through the specimen thickness.

- The lower recrystallisation resistance in the 0.1Zr-0.3Mn alloy compared to the 0.1Zr alloy was explained to result from the heterogeneous distribution of stored energy within the microstructure due to the smaller subgrain size within Mn-dispersoid bands compared to bands of Al_3Zr dispersoids, combined with the higher density of PSN sites stemming from the large Mn-constituent particles and, finally, the lower pinning pressure of the Al_3Zr dispersoids due to their interaction with Mn.

- The 0.1Zr-0.3Mn alloy suddenly recrystallised by 17% after 5 min at 535°C and then this volume fraction increased more gradually up to 144 h. The initial abrupt rise was owing to the static recrystallisation of dispersoid-depleted areas with a low pinning pressure, but there was also a contribution from grains that had recrystallised during the hot-rolling process and then slightly deformed during the following rolling passes. At longer times the kinetics were controlled by the Al_3Zr coarsening.

- Recrystallisation was found to initiate within bands of Mn-dispersoids. Not all the Mn-bands recrystallised at the start of annealing, but all the recrystallised grains after 5 min at 535°C were found around Mn-dispersoid bands.

- The recrystallisation mechanisms strongly depend on the dispersoid addition. Al_3Zr dispersoids favour the broad front SIBM mechanism, while the Mn addition promotes PSN due to the higher density of Mn-constituent phases and the formation of dispersoids with lower density and larger size.

- The Zr and Mn contents required to achieve sufficient pinning and prevent recrystallisation are related to each other and the effect of Zr is much stronger than of Mn. A higher Zr content would require the addition of a lower Mn content and vice versa.

- Texture strength in the T351 temper was highest for the 0.1Zr alloy due to the lowest amount of recrystallisation. S and Brass were the dominant components in the unrecrystallised microstructure. The Mn addition seemed to preferentially consume the S component upon annealing at 535°C. Recrystallisation textures were quite randomised.

- The effect of dispersoids on ageing at room temperature or 155°C is insignificant, but the overageing resistance is clearly influenced. The 0.1Zr-0.3Mn alloy showed the lowest hardness after 250 h at 200°C. This was owing to several effects; second phases nucleating on incoherent dispersoids, preferential precipitation of second phases on GBs, taking into account the smallest grain size of this alloy, and the extent of recrystallisation which cause more rapid overageing of dispersoids that lose coherency in these regions.

- The fracture mode and fracture toughness are clearly affected by the dispersoid content. The Mn addition is detrimental due to the higher recrystallised V_f it produces and also due to the $Al_{20}Cu_2Mn_3$ dispersoids that nucleate microvoids at their incoherent interface and facilitate void link-up and early fracture. The large Mn-particles also increase the number density of constituent phases that nucleate large voids. Hence, the 0.1Zr alloy with an unrecrystallised microstructure and the fine Al_3Zr dispersoids had the best combination of mechanical properties amongst all alloys.

- An overall comparison of the properties of all AA2198 alloys studied in this work thus shows the superiority of the 0.1 wt%Zr addition over the 0.1 wt%Zr-0.3 wt%Mn for damage tolerant applications of the 6 mm thick sheet.

Further Work

- An AA2198 alloy containing Zr and less than 0.3 wt% Mn could be cast to verify if the anticipated benefits will appear in the sheet material. The proposed alloy is expected to have better combination of properties than the 0.1Zr-0.3Mn alloy, but this has yet to be compared to the 0.1Zr alloy. The recommended composition of the dispersoid-forming elements is 0.1 wt% Zr together with 0.05-0.10 wt% Mn. Such a composition is expected to yield the following advantages over the 0.1Zr-0.3Mn alloy.
    - Formation of a lower volume fraction of Mn-dispersoids and with a smaller size. Since the solid solubility limit of the $Al_{20}Cu_2Mn_3$ phase at 508^{o}C is known to be approximately 0.12 wt% [302], dispersoids will mainly form during the ramp and only a few at the ST temperature (505^{o}C). So most of the Mn will remain in SS, where it is known to be more effective than Mn-dispersoids in terms of GB pinning [161].
    - The lower amount of Mn will impose a smaller interaction between Zr and Mn and consequently a higher volume fraction of Al_3Zr will precipitate.
    - Less randomised texture due to the lower recrystallised V_f.
    - A lower amount of undissolved constituent phases will remain in the microstructure, giving the benefit of fewer PSN sites and higher fracture toughness.
    - The lower number density of constituent phases can allow for a lower homogenisation temperature (~490^{o}C) which will be closer to the nose of the Al_3Zr TTT diagram and will result in an optimum dispersoid distribution (higher volume fraction and smaller size, due to the higher nucleation rate and lower growth rate at that temperature [116]).
    - Even higher deformation strains might be possible without any signs of recrystallisation with such a dispersoid distribution.
    - The smaller grain size due to the presence of Mn-dispersoids together with Al_3Zr will remain unaffected.

- Perform EDX in the as-cast material to see if any Zr or Mn is dissolved in any of the Cu-containing phases. Compare to the hot-rolled F temper where Zr was found within a Cu-containing phase.

- Create a model that will predict at which true strain the combined Zr-Mn addition becomes beneficial/detrimental for recrystallisation resistance. It should predict at what size the

PFZs become sites for preferential nucleation of recrystallised grains and should also incorporate the Zr-Mn interaction which modifies the Al_3Zr distribution.

- Analyse textures in more detail with the aid of ODFs. There is a lack of texture analyses on the latest variants of 3rd generation Al-Li alloys in the literature. The latest variants of these alloys have lower Brass contents, which significantly affects their mechanical properties and especially anisotropy [4]. A texture study throughout the whole processing route to the final T351 temper would be ideal.

- Perform orientation imaging in the TEM to calculate the stored energy by measuring the subgrain size and misorientation. EBSD in the SEM might be a more standard process, but it is very difficult to detect the Mn-dispersoid bands in the bulk specimen. TEM has the ability to detect these bands, but the disadvantage that EBSD detectors are not readily available in these microscopes and manual, time-consuming measurements from diffraction patterns might be required.

- Correlate the dispersoid pinning effect with certain grain orientations/misorientations. Dispersoids do not affect grain rotations during deformation, but they may have influenced the texture during previous processing stages [303].

- Determine the effect of the amount of Li in solid solution on the deformation textures, by preparing alloys of similar composition but with less than 1 wt% Li, so as not to exceed the δ' solvus boundary.

- Study recrystallisation kinetics at lower annealing temperatures and observe if there is any difference in the role of the combined Zr and Mn addition compared to the results at 535°C.

Appendix I: Dispersoid Volume Fraction Calculations

In order to measure second phase particle volume fractions in the TEM, an accurate measurement of the foil thickness is required. EELS is considered to be the simplest and most accurate way of measuring the foil thickness in the TEM [263]. In the same reference, several techniques for thickness determination were analysed. Recently EELS has started being employed by several research groups in order to measure sample thickness and subsequently calculate particle volume fractions [115, 160, 304, 305]. Another accurate, yet more complicated, method reported in the literature for particle volume fraction measurements is the conversion of 2-dimensional data to 3-dimensional by using appropriate mathematical equations [128], also in combination with EELS measurement of the sample thickness [306]. A similar method of 2-D to 3-D data conversion was also reported, where the sample thickness was calculated from GB contrast fringes of TEM samples and the dispersoid volume fraction was calculated from the size distribution instead of the average value [307]. However, other methods have also been reported in the past where no account of the foil thickness was taken, such as extracting volume fraction values from interparticle spacing measurements [141]. Also, taking volume fraction values from the phase diagram of the studied system is not an ideal option, since it only gives equilibrium values which do not correspond to the exact thermal treatment time at the condition of interest [131, 132, 284]. There have also been references where no justification was provided at all regarding the method used to calculate the particle volume fractions (e.g. [308]). Lately, some efforts have been made to quantify volume fractions of fine, ageing precipitates by using state-of-the-art techniques such as small angle x-ray scattering (SAXS), but this method is only useful as means of comparison for the volume fractions between different conditions and not for obtaining the exact numerical values [12]. DSC measurements have also been employed by some researchers for volume fraction calculation of ageing precipitates and intermetallics [309] and so have electrical resistivity measurements [306].

A) Al_3Zr volume fraction calculation from their particle size distributions

The calculations were simplified by making the following two assumptions:

- the Al_3Zr particles are considered spherical;

- all particles allocated in the same size bin have the same radius r_b, equal to the value corresponding to the bin's middle.

If x particles are allocated in the same bin, then it is assumed that they are all equal to the value at the bin's middle:

$$r_1 = r_2 = \ldots = r_x = r_b \tag{I-1}$$

The overall dispersoid volume in the i^{th} bin becomes:

$$V_i = x_i \cdot V_{bi} = x_i \cdot \frac{4}{3} \cdot \pi \cdot r_{bi}^3 \tag{I-2}$$

where V_{bi} and r_{bi} are the dispersoid volume and radius respectively for the i^{th} bin.

The total dispersoid volume in the material/all bins is given from the relationship:

$$V_T = \sum_{i=1}^{m} V_i = \sum_{i=1}^{m} x_i \cdot V_{bi} \tag{I-3}$$

The total number of particles (x_i) in the i^{th} bin, calculated from a size distribution, is:

$$x_i = a_i \cdot N \tag{I-4}$$

where a_i is the percentage of dispersoids allocated to the i^{th} bin and N is the total number of particles in all the bins.

Substituting Eq. I-4 into Eq. I-3, the total dispersoid volume is found to be:

$$V_T = \sum_{i=1}^{m} a_i \cdot N \cdot \frac{4}{3} \cdot \pi \cdot r_{bi}^3 \tag{I-5}$$

and the dispersoid volume fraction in the matrix is equal to:

$$V_f = \frac{V_T}{V_S} \cdot 100\% \tag{I-6}$$

where V_s is the sample's volume in which the dispersoids were counted. The sample volume was calculated by multiplying the area of the STEM image times the thickness of the area which was measured with EELS (see §3.4.4).

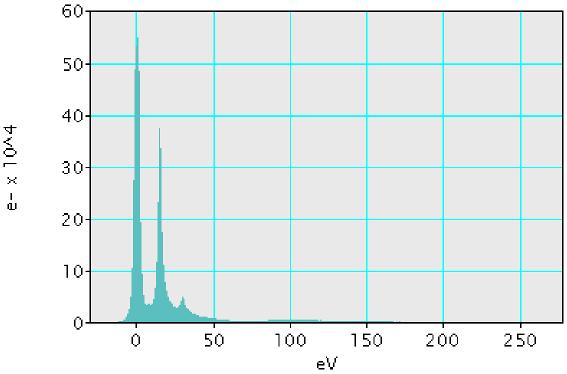

Fig. I.1: Typical EELS spectrum obtained with the FEI Tecnai F30 for specimen thickness measurements. The calculated thickness for the spectrum shown here was 142 nm.

To summarise, the steps followed in this method were the following.

- Calculate the sample thickness using EELS, for the area where the STEM picture of the particles was taken. A spectrum like the one in Fig. I.1 is obtained.
- Calculate the sample volume corresponding to the area of the STEM image by multiplying the image area times the thickness.
- Count the number of particles from the STEM image.
- Calculate the total particle volume by multiplying the total number of particles times the frequency with which each radius appears according to the size distribution that was measured in advance.
- Divide the total particle volume over the sample volume for that area to calculate the V_f.
- Average the V_f calculated from 10 iterations of all the following steps, from different areas on the specimen in order to obtain more statistically reliable results.

— Error in the equal size (r_b) assumption

The measured radius of the j^{th} particle in every bin of size y follows the relationship:

$$r_b - \frac{y}{2} \leq r_j \leq r_b + \frac{y}{2} \qquad \text{(I-7)}$$

The error for the calculation of a single value r_j within each bin is given by the equation:

$$\sigma(i) = \frac{|\, r_j - r_b \,|}{r_b} \cdot 100\% \qquad \text{(I-8)}$$

Hence, a smaller bin size y results in a smaller difference between r_j and r_b and consequently a smaller error as calculated from Eq. I-8. However, it should be large enough to contain a statistically acceptable number of particles. For the calculations in this work, the bin size was taken equal to 5 nm.

B) $Al_{20}Cu_2Mn_3$ volume fraction calculation

The volume fraction of the Mn-containing dispersoids was calculated by following exactly the same steps as earlier for the Al_3Zr particles. The size distribution was again employed to calculate the volume in each size bin and the following simplification was made:

- all Mn-dispersoids were considered to be cylinders with a diameter equal to their width and their volume is given by the equation: $V = \pi R^2 L$

where R is half the dispersoid width and L the length.

C) Al_3Zr volume fraction variation across the ND

The graphs in Figs. 5.27a,b were plotted by calculating the Al_3Zr volume fraction within a certain distance along the ND, for the 0.1Zr and 0.1Zr-0.3Mn alloys. At least one dispersoid band existed in each of the chosen areas, so as to assess the difference in pinning pressure between the Al_3Zr bands and the sparsely distributed dispersoids in the surrounding areas. For the 0.1Zr-0.3Mn alloy, a recrystallised grain was selected in order to study the distribution of the finer dispersoids in areas where the $Al_{20}Cu_2Mn_3$ phase is predominant (Fig. I.2a).

First of all, the sample thickness had to be measured at several points across the chosen area, so as to calculate the dispersoid V_f. It was then easy to construct thickness maps such as those depicted in Figs. I.3b,c, where the thickness at every point of the analysed distance can be found. The selected area was divided into narrow zones of up to 1.5 μm spacing along ND and the number of Al_3Zr dispersoids was measured within them. The average size of the contained particles was also measured for each zone and it was used for the volume fraction calculations. Thus, the volume fraction in each zone was found by dividing the dispersoid volume over the corresponding sample volume in that zone, as found with the aid of the thickness maps.

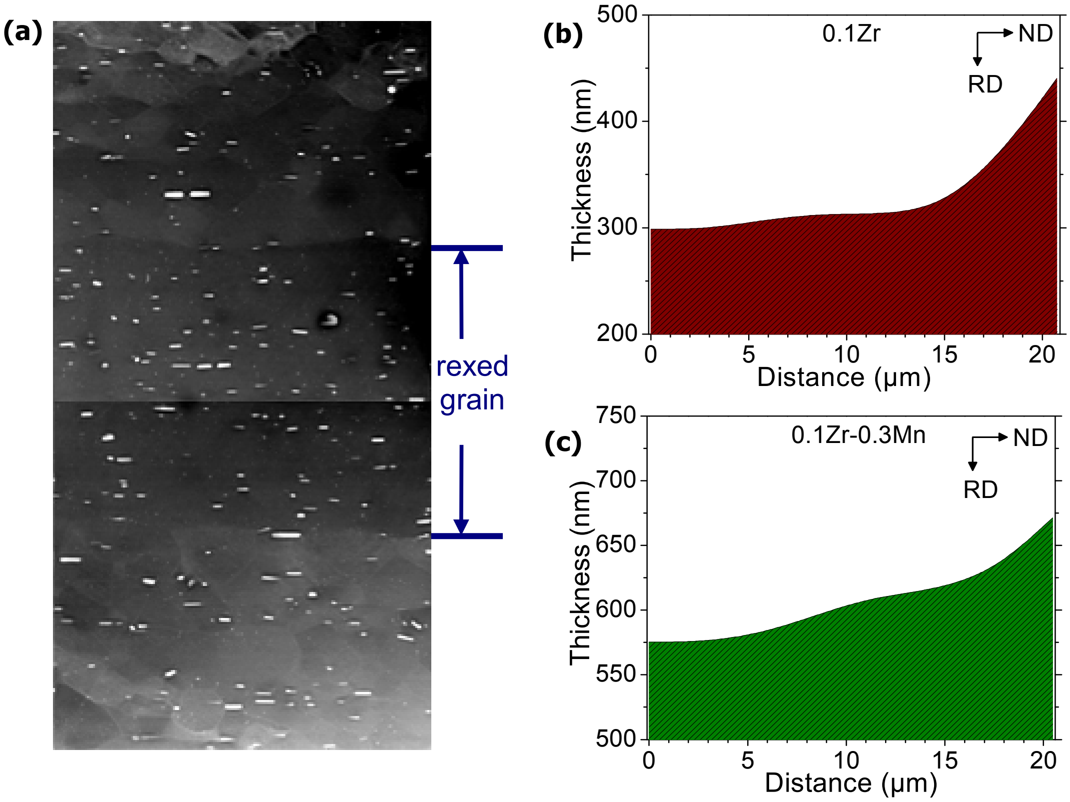

Fig. I.2: a) STEM image of the area corresponding to the graph in (c). **b)** Thickness map for the area analysed in the 0.1Zr alloy. **c)** Thickness map for the area analysed in the 0.1Zr-0.3Mn alloy.

Appendix II: Microstructural observations not directly relevant to the main topic of the thesis

A) Fine, Ag-containing globular particles

A very low volume fraction of a fine, spherical phase was detected in the microstructure at all conditions, irrespectively of the dispersoid content (Figs. II.1a-c). It contained Al and Ag as determined from the EDX spectrum in Fig. II.1d. The Cu peak was produced by the surrounding matrix. EDX line scans showed that no additional Cu was present in these particles. The particles were not analysed further due to their insignificance to the recrystallisation process. A list of Al-Ag phases can be found in the literature [310]. According to the Al-Ag phase diagram, the 0.3 wt% Ag content of the AA2198 corresponds to the area of Al in solid solution between 500-535^{o}C and no second phases are formed (Fig. II.2). Eventually, it was concluded that this phase was simply an artefact from the electropolishing of TEM samples. According to Lee et al. [311], Ag segregates to the free surfaces of Al samples during electropolishing.

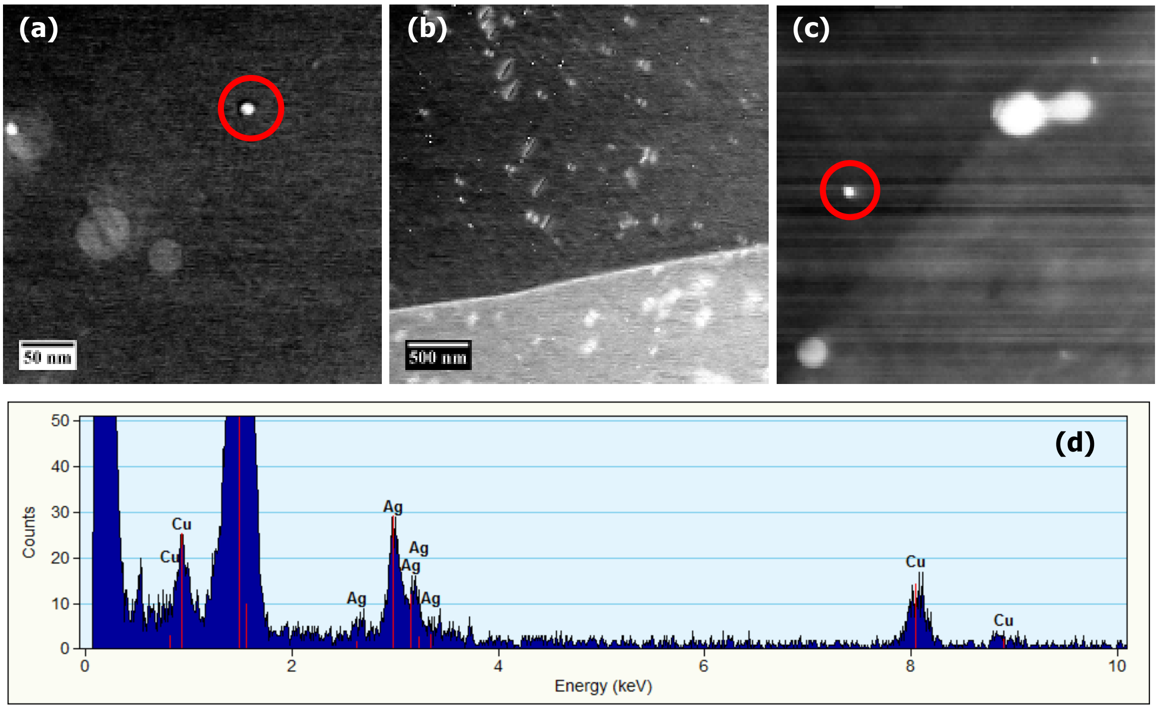

Fig. II.1: TEM distributions of a fine, spherical Al-Ag phase: **a)** morphology of the Al-Ag phase, also showing coarser Al$_3$Zr dispersoids (0.1Zr-0.3Mn alloy annealed for 72 h at 535^{o}C from the F temper), **b)** STEM-HAADF image showing the increased number density of the small particles after long annealing, **c)** an Al-Ag-particle in the 0.1Zr-D alloy in T351, and **d)** EDX spectrum of the particle in (a).

The particle morphology is shown clearly in Fig. II.1a. These particles appeared brighter than the Al_3Zr phase with the HAADF detector in the STEM mode, due to the higher atomic number of Ag compared to Zr. It is evident that they were much smaller than the Al_3Zr dispersoids and they were typically less than 10 nm in diameter.

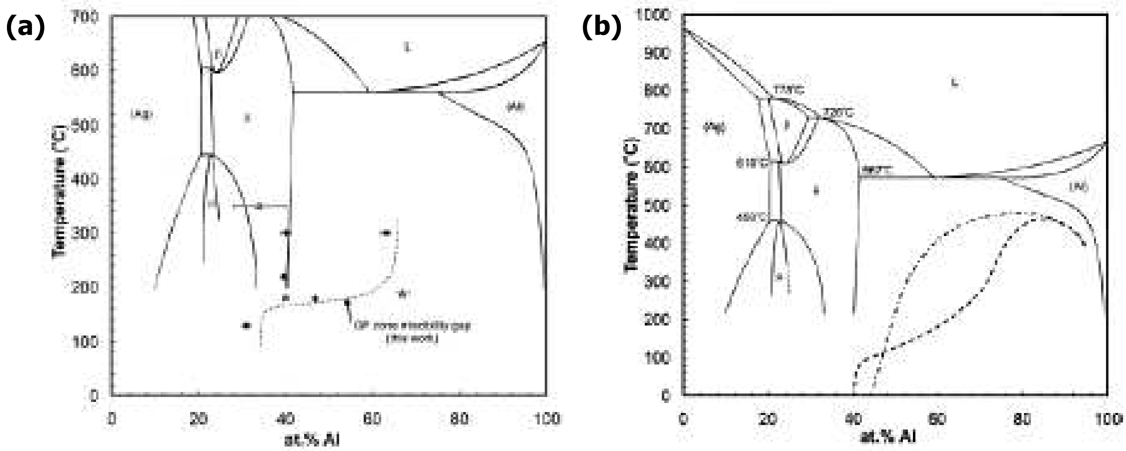

Fig. II.2: Metastable miscibility gap for GP zones in the Al-Ag system [312]: **a)** boundary defined by Marquis, and **b)** boundaries defined by other researchers.

B) Faceted voids

A very interesting phenomenon that also appeared during annealing at 535°C was the presence of voids in the microstructure. Their distribution and number density can be seen in Fig. II.3a, where the 0.1Zr-0.3Mn sample was annealed for 144 h at 535°C. The voids appeared brighter than the matrix, since the lower mass in that location gives a lower atomic number compared to the surrounding area. They were faceted with the facets oriented in the same direction for all the voids within a certain grain. A typical morphology is seen in Fig. II.3b. The origin of these voids was difficult to be determined. However, there is a possibility that they resulted from faceted particles that fell off during the sample preparation. Fig. II.3c shows an area where the voids (highlighted in yellow) coexisted with faceted particles (highlighted in red) of the same size and with their facets having identical orientations with the facets of the pits. The fact that the particles were present after 72 h but disappeared after 144 h, supports the argument that they may have coarsened beyond a critical size and fell out during the sample preparation. The composition or structure of these precipitates is not known.

Pits also formed at the interfaces of coarse Al_3Zr dispersoids Fig. II.3d. This might have occurred due to loss of coherency after these dispersoids reached a certain size. The orientations of the facets of the pits were again identical in all the cases where they appeared. It should be noted that the interfacial pits were significantly larger in size than those formed in the matrix (Fig. II.3e).

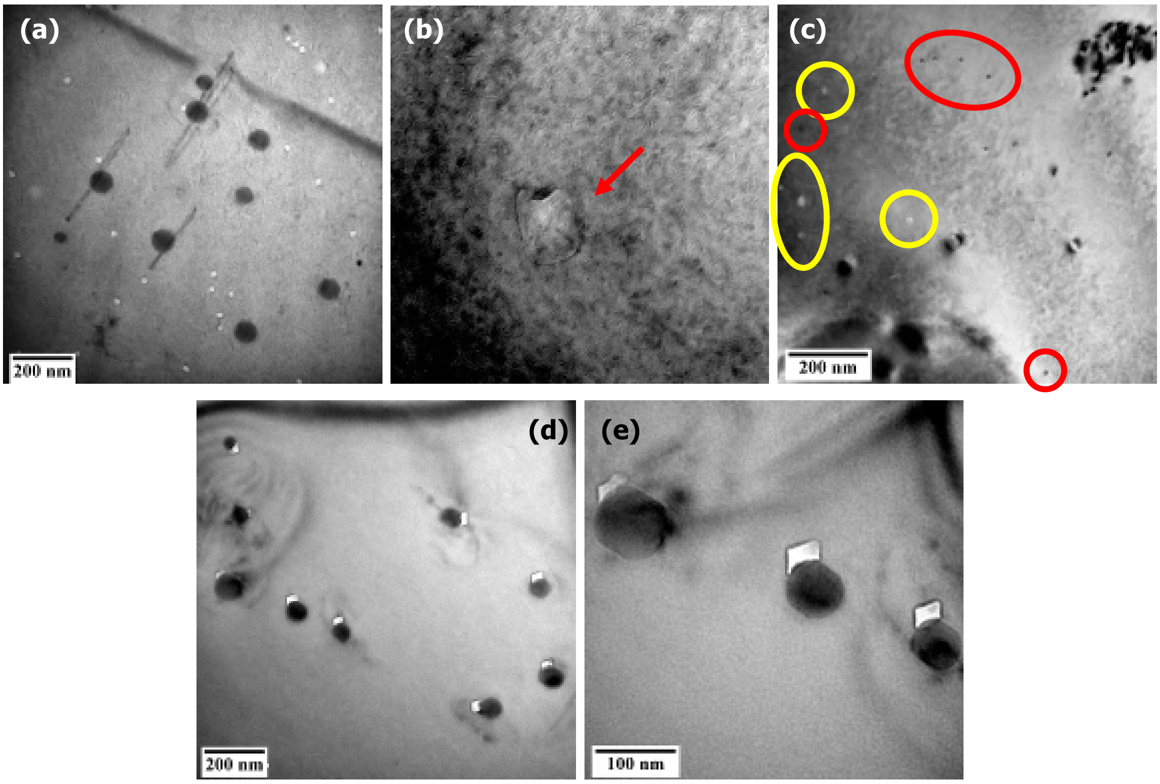

Fig. II.3: Annealing pits in the 0.1Zr-0.3Mn alloy: **a)** faceted pits among coarse Al_3Zr dispersoids (144 h at 535°C), **b)** high magnification BF image of a faceted pit, **c)** yellow circles: faceted pits, red circles: faceted particles (72 h at 535°C), **d)** faceted pits at the interfaces of coarse Al_3Zr dispersoids (144 h at 535°C), and **e)** higher magnification of the area in (d).

C) Dislocations

Several interesting dislocation structures were observed after prolonged annealing. Dislocation helices were formed in the matrix, especially within recrystallised grains, and they were not necessarily associated with either type of dispersoids (Fig. II.4a). Dislocation loops formed at the interface of semi-coherent or incoherent Al_3Zr dispersoids, after they coarsened considerably (Fig. II.4b). These dislocation loops can also be seen edge-on in Figs. II.4c,d.

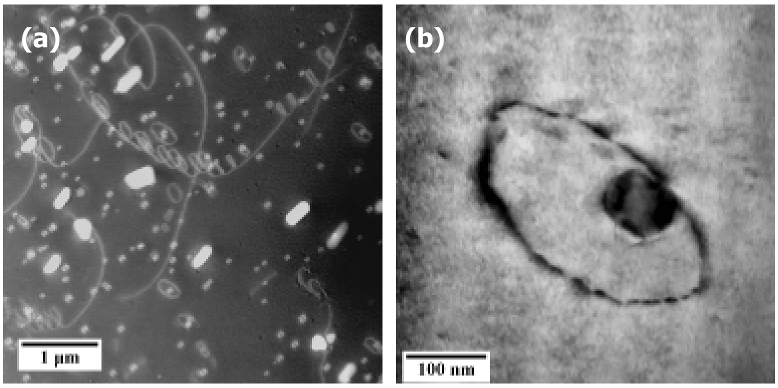

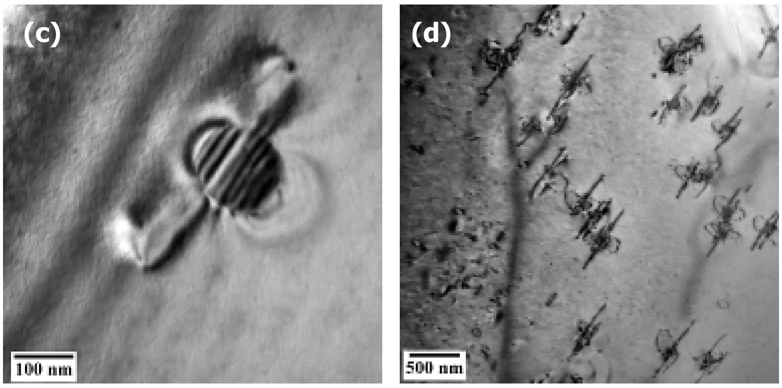

Fig. II.4: Dislocations structures after long annealing times (0.1Zr-0.3Mn alloy, 72 h at 535°C from the F temper): **a)** dislocation loops around Al_3Zr dispersoids and free dislocation helices, **b)** dislocation loop protruding from an Al_3Zr interface, **c)** dislocation loop seen edge-on at the interface of a semi-coherent Al_3Zr dispersoid, and **d)** dislocations loops seen at two different planes at the interfaces of incoherent Al_3Zr dispersoids.

As a final comment, some rare dislocation arrays were observed after long annealing times. An example is seen in Fig. II.5, where a wave-like dislocation array was seen protruding from a HAGB next to a recrystallised grain. The boundary of this array was characterised as low-angle twist type relative to the surrounding grain.

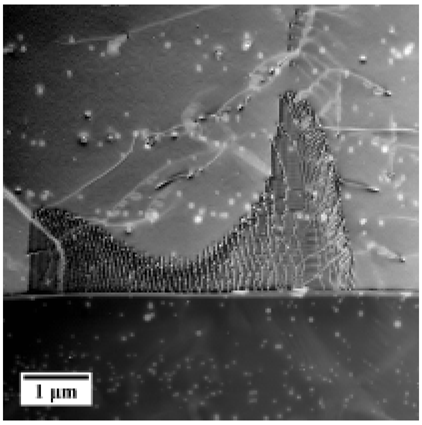

Fig. II.5: Dislocation array protruding from a HAGB in the 0.1Zr-D alloy after annealing for 72 h at 535°C.

Appendix III: Kahn tear test measurements

Measured values of all the alloys and conditions tested

The exact values of some of the mechanical properties were presented in §7.3, but the main focus was the comparative study of all the different alloys and conditions. All the measured values of strength, unit initiation energy (UIE), unit propagation energy (UPE) and unit total energy (UTE) are presented in Table III.1 as a reference.

Table III.1: Measured values from the Kahn tear tests for all the alloys and conditions tested.

Alloy	Temper/ Orientation	Strength (MPa)	UIE (N/mm)	UPE (N/mm)	UTE (N/mm)
0.1Zr-D	T351/ L-T	611.8±1.9	290.3±3.9	139.7±5.0	430.0±3.2
0.1Zr		609.9±2.5	247.3±3.1	186.5±3.3	433.8±6.2
0.1Zr-0.3Mn		603.7±8.3	251.1±11.1	109.3±2.5	360.4±11.6
0.05Zr-0.3Mn		547.4±1.7	178.7±5.7	194.7±12.3	373.4±9.2
0.4Mn		490.3±11.0	144.7±4.7	191.1±27.7	332.6±25.4
0.1Zr-D	14h@155°C/ L-T	729.2±7.0	166.5±19.2	115.1±21.6	281.6±16.2
0.1Zr		749.7±2.1	150.5±13.6	173.8±13.3	324.2±26.2
0.1Zr-0.3Mn		708.3±3.0	168.8±3.4	136.5±17.3	303.8±12.9
0.05Zr-0.3Mn		694.7±1.1	162.9±3.5	138.8±8.2	301.7±5.1
0.4Mn		672.1±2.1	142.2±4.9	119.1±4.5	261.3±6.3
0.1Zr-D	100h@155°C/ L-T	679.0±7.0	101.0±15.9	81.2±2.8	182.3±15.4
0.1Zr		730±2.5	94.7±3.6	117.9±18.1	212.6±21.4
0.1Zr-0.3Mn		667.8±4.4	78.4±16.0	85.1±12.5	163.5±7.4
0.05Zr-0.3Mn		679.6±6.3	123.1±2.3	96.3±4.3	219.4±3.7
0.4Mn		665.1±2.1	123.8±2.5	61.5±2.1	185.3±2.8
0.1Zr-D	T351/ T-L	598.3±2.8	289.4±3.0	135.5±7.4	424.9±6.4
0.1Zr		615.0±2.2	268.9±6.3	198.3±21.1	467.2±15.2
0.1Zr-0.3Mn		608.0±2.5	273.8±7.6	105.6±9.2	379.4±2.4
0.05Zr-0.3Mn		556.1±3.4	188.0±8.3	172.6±3.0	360.6±7.5
0.4Mn		543.5±1.3	165.3±3.2	151.2±3.7	316.5±
0.1Zr-D	14h@155°C/ T-L	709.5±2.6	155.8±2.9	72.5±10.1	228.3±11.7
0.1Zr		756.7±11.0	146.9±5.7	112.8±9.9	259.7±10.6
0.1Zr-0.3Mn		728.1±4.5	185.8±6.0	79.4±5.3	265.1±2.4
0.05Zr-0.3Mn		663.7±4.8	137.6±4.4	79.0±3.5	216.7±1.7
0.4Mn		646.5±5.1	128.5±3.0	64.6±6.0	193.7±3.1
0.1Zr-D	100h@155°C/ T-L	615.0±6.4	90.3±3.1	—	90.3±3.1
0.1Zr		683.6±8.8	87.8±3.5	—	87.8±3.5
0.1Zr-0.3Mn		667.0±8.1	111.8±3.9	—	111.8±3.9
0.05Zr-0.3Mn		559.9±7.8	75.1±2.3	—	75.1±2.3
0.4Mn		523.6±12.5	63.4±5.3	—	63.4±5.3
0.1Zr	14h@155°C/ 45°	698.2±7.8	120.7±1.8	136.9*	260.7*
0.1Zr-0.3Mn		675.0±1.7	116.3±3.4	148.7*	258.3*

* only 1 sample was found to comply with the guidelines of the ASTM B 871-01.

References

1. *ASM Specialty Handbook: Aluminium and Aluminium Alloys* / edited by J.R. Davis, ASM International, Materials Park, Ohio, USA (1993)
2. J.W. Martin, *Annual Review of Materials Science*, **18** (1988) 101-119
3. R.J.H. Wanhill, *International Journal of Fatigue*, **16** (1994) 3-20
4. R.J. Rioja, *Materials Science and Engineering: A*, **257** (1998) 100-107
5. I.J. Polmear, *Light Alloys: Metallurgy of the Light Metals 3rd Ed.*, Butterworth-Heinemann, Oxford (1995)
6. R.C. Dorward, T.R. Pritchett, *Materials & Design*, **9** (1988) 63-69
7. T.H. Sanders Jr., E.A. Starke Jr., *Proceedings of the Fifth International Conference on Al-Li alloys*, Birmingham, UK (1989) 1-37
8. T. Warner, *Materials Science Forum*, **519-521** (2006) 1271-1278
9. E.A. Starke Jr., K.H.J. Buschow, R.W. Cahn, M.C. Flemings, B. Ilschner, E.J. Kramer, S. Mahajan, P. Veyssière, Aluminum: Alloying, in: *Encyclopedia of Materials: Science and Technology*, (Ed.), Elsevier Oxford (2001) 101-106
10. C. Le Port-Samzun, PhD thesis, University of Bimingham (2004)
11. P. Lequeu, *Advanced Materials and Processes*, **166** (2008) 47-49
12. B. Decreus, F. Bley, A. Deschamps, P. Donnadieu, *ICAA-11: 11th International Conference on Aluminium Alloys*, Aachen, Germany (2008) 1040-1046
13. Materials Science International Team Msit®, Al-Cu-Li (Aluminium-Copper-Lithium), in: *Non-Ferrous Metal Systems. Part 2*, G. Effenberg, S. Ilyenko (Ed.), Springer Berlin (2007) 1-42
14. F.J. Humphreys, M. Hatherly, *Recrystallization and Related Annealing Phenomena (2nd ed.)*, Elsevier, Oxford (2004)
15. X.H. Zeng, T. Ericsson, *Acta Materialia*, **44** (1996) 1801-1812
16. E.J. Lavernia, T.S. Srivatsan, F.A. Mohamed, *Journal of Materials Science*, **25** (1990) 1137-1158
17. H. Yoshida, H. Tanaka, S. Tsuchida, T. Tsuzuku, A. Takahashi, *Proceedings of the Fifth International Conference on Al-Li alloys*, Birmingham, UK (1989) 179-188
18. B. Forbord, H. Hallem, K. Marthinsen, *ICAA-9: 9th International Conference on Aluminium Alloys*, Brisbane, Australia (2004) 1179-1185
19. Z. Jia, G. Hu, B. Forbord, J.K. Solberg, *Materials Science and Engineering: A*, **444** (2007) 284-290
20. E.J. Lavernia, N.J. Grant, *Journal of Materials Science*, **22** (1987) 1521-1529
21. B. Noble, S.J. Harris, S. Katsikis, K. Dinsdale, *ICAA-11: 11th International Conference on Aluminium Alloys*, Aachen, Germany (2008) 215-221
22. C. Giummarra, R.J. Rioja, G.H. Bray, J.P. Moran, *ICAA-11: 11th International Conference on Aluminium Alloys*, Aachen, Germany (2008) 176-188
23. E.A. Starke Jr., J.T. Staley, *Progress in Aerospace Sciences*, **32** (1996) 131-172
24. J.C. Williams, E.A. Starke, *Acta Materialia*, **51** (2003) 5775-5799
25. J.P. Immarigeon, R.T. Holt, A.K. Koul, L. Zhao, W. Wallace, J.C. Beddoes, *Materials Characterization*, **35** (1995) 41-67
26. R. Boyer, K.H.J. Buschow, R.W. Cahn, M.C. Flemings, B. Ilschner, E.J. Kramer, S. Mahajan, P. Veyssière, Aircraft Materials, in: *Encyclopedia of Materials: Science and Technology*, (Ed.), Elsevier Oxford (2001) 66-73
27. E.A. Starke Jr., K.H.J. Buschow, R.W. Cahn, M.C. Flemings, B. Ilschner, E.J. Kramer, S. Mahajan, P. Veyssière, Aluminum Alloys: Properties and Applications, in: *Encyclopedia of Materials: Science and Technology*, (Ed.), Elsevier Oxford (2001) 114-116
28. L. Meng, X.L. Zheng, *Materials Science and Engineering: A*, **237** (1997) 109-118
29. J.J. Lewandowski, N.J.H. Holroyd, *Materials Science and Engineering: A*, **123** (1990) 219-227
30. W.R. Wilson, J. Worth, E.P. Short, C.F. Pygall, *Journal de Physique III*, **48** (1987) C3 75-83
31. Summaries of Alcan papers at AeroMat 2006-Seattle USA, *Advanced Materials and*

Processes, **164** (2006)
32. P. Lequeu, P. Lassince, T. Warner, *Advanced Materials and Processes*, **165** (July 2007) 41-44
33. D.L. Chen, M.C. Chaturvedi, N. Goel, N.L. Richards, *International Journal of Fatigue*, **21** (1999) 1079-1086
34. P. Lequeu, F. Eberl, S. Jambu, T. Warner, A. Danielou, B. Bés, *19th AeroMat Conference & Exposition*, Austin, Texas, USA (2008)
35. M. Knuewer, J. Schumacher, H. Ribes, F. Eberl, B. Bés, *17th AeroMat Conference & Exposition*, Seattle, Washington, USA (2006)
36. J.R. Pickens, F.H. Heubaum, L.S. Kramer, *Scripta Metallurgica et Materialia*, **24** (1990) 457-462
37. A. Cho, US patent 7229509 (2007)
38. P.S. Chen, A.K. Kuruvilla, T.W. Malone, W.P. Stanton, *Journal of Materials Engineering and Performance*, **7** (1998) 682-690
39. P.S. Chen, W.P. Stanton, NASA Technical Memorandum, 211546 (2002)
40. P.S. Chen, W.P. Stanton, NASA Technical Memorandum, 211547 (2002)
41. N.J. Kim, E.W. Lee, *Acta Metallurgica et Materialia*, **41** (1993) 941-948
42. K.S. Kumar, S.A. Brown, J.R. Pickens, *Acta Materialia*, **44** (1996) 1899-1915
43. A.K. Mukhopadhyay, V.V. Rama Rao, P. Ghosal, N. Ramachandra Rao, *Zeitschrift fur Metallkunde*, **91** (2000) 483-488
44. N. Boukos, E. Flouda, C. Papastaikoudis, *Journal of Materials Science*, **33** (1998) 3213-3218
45. Y.-S. Lee, *Journal of Materials Science Letters*, **17** (1998) 1161-1164
46. A.K. Mukhopadhyay, *Metallurgical and Materials Transactions A*, **30** (1999) 1693-1704
47. Y. Mou, J.M. Howe, E.A. Jr Starke, *Metallurgical and Materials Transactions A*, **26** (1995) 1591-1595
48. Z.Q. Zheng, S.Q. Liang, H. Xu, C.Y. Tan, D.F. Yun, *Journal of Materials Science Letters*, **12** (1993) 1111-1113
49. K. Satya Prasad, A.K. Mukhopadhyay, A.A. Gokhale, D. Banerjee, D.B. Goel, *Scripta Metallurgica et Materialia*, **30** (1994) 1299-1304
50. K.S. Vecchio, D.B. Williams, *Metallurgical Transactions A*, **19** (1988) 2875-2884
51. E.A. Ludwiczak, R.J. Rioja, *Scripta Metallurgica et Materialia*, **25** (1991) 1415-1419
52. P. Donnadieu, *ICAA-4: 4th International Conference on Aluminium Alloys*, Atlanta, USA (1994) 222-229
53. K.S. Vecchio, D.B. Williams, *Philosophical Magazine B*, **57** (1988) 535-546
54. C.W. Bartges, E. Ryba, *Proceedings of the Fifth International Conference on Al-Li alloys*, Birmingham, UK (1989) 711-720
55. R. Yoshimura, T.J. Konno, E. Abe, K. Hiraga, *Acta Materialia*, **51** (2003) 4251-4266
56. K.M. Knowles, W.M. Stobbs, *Acta Crystallographica B*, **44** (1988) 207-227
57. K.H. Lee, Y.J. Lee, K. Hiraga, *Journal of Materials Research*, **14** (1999) 384-389
58. R.A. Herring, F.W. Gayle, J.R. Pickens, *Journal of Materials Science*, **28** (1993) 69-73
59. J.C. Huang, *Scripta Metallurgica et Materialia*, **27** (1992) 755-760
60. J.K. Park, A.J. Ardell, *Scripta Metallurgica et Materialia*, **26** (1992) 1759-1762
61. Y.-S. Lee, S.P. Ringer, B.C. Muddle, I.J. Polmear, *ICAA-4: 4th International Conference on Aluminium Alloys*, Atlanta, USA (1994) 582-589
62. M. Murayama, K. Hono, *Scripta Materialia*, **44** (2001) 701-706
63. F. De Geuser, B. Gault, M. Weyland, L. Bourgeois, B.M. Gable, S.P. Ringer, B.C. Muddle, *ICAA-11: 11th International Conference on Aluminium Alloys*, Aachen, Germany (2008) 724-731
64. B.M. Gable, A.W. Zhu, A.A. Csontos, E.A. Starke, *Journal of Light Metals*, **1** (2001) 1-14
65. F.W. Gayle, F.H. Heubaum, J.R. Pickens, *Proceedings of the Fifth International Conference on Al-Li alloys*, Birmingham, UK (1989) 701-710
66. S.P. Ringer, K. Hono, I.J. Polmear, *ICAA-4: 4th International Conference on Aluminium Alloys*, Atlanta, USA (1994) 574-581
67. L. Reich, M. Murayama, K. Hono, *ICAA-6: 6th International Conference on Aluminium Alloys*, Toyohashi, Japan (1998) 645-650
68. F.W. Gayle, W.T. Tack, G. Swanson, F.H. Heubaum, J.R. Pickens, *Scripta Metallurgica et Materialia*, **30** (1994) 761-766
69. I.J. Polmear, R.J. Chester, *Scripta Metallurgica*, **23** (1989) 1213-1218
70. Z.M. Wang, R.N. Shenoy, NASA Contractor Report, 206914 (1998)
71. W.S. Jung, J.K. Park, *Scripta Metallurgica et Materialia*, **26** (1992) 831-836

72. M. Ahmad, T. Erricsson, *Proceedings of the Third International Conference on Al-Li alloys*, Oxford, UK (1986) 509-515
73. K.S. Kumar, S.A. Brown, J.R. Pickens, *Scripta Metallurgica et Materialia*, **24** (1990) 1245-1250
74. G. Itoh, Q. Cui, M. Kanno, *Materials Science and Engineering: A*, **211** (1996) 128-137
75. B. Noble, G.E. Thompson, *Metal Science Journal*, **6** (1972) 167-174
76. B.P. Huang, Z.Q. Zheng, *Acta Materialia*, **46** (1998) 4381-4393
77. S. Hirosawa, T. Sato, A. Kamio, K. Kobayashi, T. Sakamoto, *ICAA-4: 4th International Conference on Aluminium Alloys*, Atlanta, USA (1994) 199-206
78. B.P. Huang, Z.Q. Zheng, *Scripta Materialia*, **38** (1998) 357-362
79. P.S. Chen, B.N. Bhat, NASA Technical Memorandum, 211548 (2002)
80. B.P. Huang, Z.Q. Zheng, *Acta Metallurgica Sinica (English Letters)*, **11** (1998) 45-50
81. M.H. Tosten, A.K. Vasudévan, P.R. Howell, *Proceedings of the Third International Conference on Al-Li alloys*, Oxford, UK (1986) 490-495
82. P.S. Chen, W.P. Stanton, NASA Technical Memorandum, 108524 (1996)
83. M. Kanno, B.-L. Ou, *JIM Materials Transactions*, **32** (1991) 445-450
84. T. Honma, S. Yanagita, K. Hono, Y. Nagai, M. Hasegawa, *Acta Materialia*, **52** (2004) 1997-2003
85. T. Ahrens, E.A.J. Starke *Proceedings of the Fifth International Conference on Al-Li alloys*, Birmingham, UK (1989) 385-396
86. F. Donkor, M.R. Edwards, D.C. Wicks, *Proceedings of the Fifth International Conference on Al-Li alloys*, Birmingham, UK (1989) 397-405
87. E.W. Lee, W.E. Frazier, *Scripta Metallurgica*, **22** (1988) 53-57
88. S.P. Ringer, B.C. Muddle, I.J. Polmear, *Metallurgical and Materials Transactions A*, **26** (1995) 1659-1671
89. W.T. Tack, F.H. Heubaum, J.R. Pickens, *Scripta Metallurgica et Materialia*, **24** (1990) 1685-1690
90. Z. Li, R. Mirshams, *Materials Science Forum*, **217-222** (1996) 1233-1238
91. B.M. Gable, M.A. Pana, G.J. Shiflet, E.A. Starke, *Materials Science Forum*, **396-402** (2002) 699-704
92. J.K. Kim, D.S. Chung, H.S. Park, M. Enoki, *Materials Science Forum*, **475-479** (2005) 381-384
93. J.S. Robinson, R.L. Cudd, *Materials Science Forum*, **331-337** (2000) 971-976
94. S. Hirosawa, T. Sato, A. Kamio, K. Kobayashi, T. Sakamoto, *Materials Science Forum*, **217-222** (1996) 839-844
95. K.S. Kumar, F.H. Heubaum, *Acta Materialia*, **45** (1997) 2317-2327
96. C.P. Blankenship, E.A. Starke, *Acta Metallurgica et Materialia*, **42** (1994) 845-855
97. Q. Contrepois, C. Maurice, J.H. Driver, *ICAA-11: 11th International Conference on Aluminium Alloys*, Aachen, Germany (2008) 1085-1090
98. Z.Q. Zheng, X.Z. Chen, Z.G. Chen, S.C. Li, X.Y. Wei, *Materials Science Forum*, **519-521** (2006) 1931-1936
99. A.W. Bowen, *Materials Science and Technology*, **6** (1990) 1058-1071
100. W. Schneider, D. Granger, *Aluminium*, **83** (2007) 74-79
101. A. Cho, Z. Long, B. Lisagor, T. Bales, M. Domack, J. Wagner, *Materials Science Forum*, **519-521** (2006) 1585-1590
102. S.H. Kim, H.G. Kang, M.Y. Huh, O. Engler, *Materials Science and Engineering: A*, **508** (2009) 121-128
103. A.K. Vasudévan, M.A. Przystupa, W.G. Fricke Jr, *Materials Science and Engineering: A*, **208** (1996) 172-180
104. A.K. Vasudévan, W.G. Fricke Jr, R.C. Malcolm, R.J. Bucci, M.A. Przystupa, F. Barlat, *Metallurgical Transactions A*, **19** (1988) 731-732
105. M. Crumbach, M. Goerdeler, G. Gottstein, *Acta Materialia*, **54** (2006) 3291-3306
106. J. Hirsch, K. Lücke, *Acta Metallurgica*, **36** (1988) 2863-2882
107. J.D. Robson, M.J. Jones, P.B. Prangnell, *Acta Materialia*, **51** (2003) 1453-1468
108. D.A. Porter, K.E. Easterling, *Phase Transformations in Metals and Alloys (2nd Ed.)*, CRC Press, (2004)
109. R.W. Hyland Jr., *Metallurgical Transactions A*, **23** (1992) 1947-1955
110. J.D. Robson, P.B. Prangnell, *Materials Science and Engineering A*, **352** (2003) 240-250
111. Z.J. Lok, A. Miroux, S. van der Zwaag, *Materials Science Forum*, **519-521** (2006) 443-448
112. J.W. Martin, R.D. Doherty, B. Cantor, *Stability of microstructure in metallic systems*,

Cambridge University Press, Cambridge, UK (1997)
113. J.D. Robson, P.B. Prangnell, *Acta Materialia*, **49** (2001) 599-613
114. A. Miroux, Z.J. Lok, K. Marthinsen, S. van der Zwaag, *Materials Science Forum*, **539-543** (2007) 281-286
115. Y. Li, T. Furu, A.L. Dons, K. Marthinsen, L. Arnberg, *ICAA-11: 11th International Conference on Aluminium Alloys*, Aachen, Germany (2008) 929-935
116. J.D. Robson, *Materials Science and Engineering: A*, **338** (2002) 219-229
117. P.C.M. de Haan, J. van Rijkom, J.A.H. Söntgerath, *Materials Science Forum*, **217-222** (1996) 765-770
118. T.L. Zoeller, T.H. Sanders Jr., *Journal de Physique IV*, **120** (2004) 61-68
119. L. Lodgaard, N. Ryum, *Materials Science and Engineering A*, **283** (2000) 144-152
120. K.E. Knipling, D.C. Dunand, D.N. Seidman, *Acta Materialia*, **56** (2008) 114-127
121. J.Q. Guo, K. Ohtera, *Materials Letters*, **27** (1996) 343-347
122. K.S. Vecchio, D.B. Williams, *Acta Metallurgica*, **35** (1987) 2959-2970
123. K. Satya Prasad, A.A. Gokhale, A.K. Mukhopadhyay, D. Banerjee, D.B. Goel, *Acta Materialia*, **47** (1999) 2581-2592
124. N. Ryum, *Acta Metallurgica*, **17** (1969) 269-278
125. S. Rystad, N. Ryum, *Aluminium*, **53** (1977) 193-195
126. C. Li, S.C. Wang, Y. Jin, M. Hua, M. Yan, *Aluminium Alloys '90. Second International Conference on Aluminium Alloys-Their Physical and Mechanical Properties*, Beijing, China (1990) 504-507
127. P. Ratchev, B. Verlinden, P. Van Houtte, *Acta Metallurgica et Materialia*, **43** (1995) 621-629
128. E. Anselmino, A. Miroux, S. van der Zwaag, *Aluminium*, **80** (2004) 680-685
129. M. Dehmas, P. Archambault, M. Serriere, E. Gautier, C.-A. Gandin, *Aluminium*, **80** (2004) 619-623
130. T.S. Srivatsan, *Journal of Materials Science Letters*, **7** (1988) 940-943
131. N. Gao, M.J. Starink, L. Davin, A. Cerezo, S.C. Wang, P.J. Gregson, *Materials Science and Technology*, **21** (2005) 1010-1018
132. K. Kannan, J.S. Vetrano, C.H. Hamilton, *Metallurgical and Materials Transactions A*, **27** (1996) 2947-2957
133. R.D. Doherty, *Metal Science*, **16** (1982) 1-13
134. E. Nes, N. Ryum, O. Hunderi, *Acta Metallurgica*, **33** (1985) 11-22
135. P.M. Hazzledine, *Czech Journal of Physics*, **38** (1988) 431-443
136. L. Winberg, M. Dahlén, *Journal of Materials Science*, **13** (1978) 2365-2372
137. E. Nes, *Journal of Materials Science*, **13** (1978) 2052-2055
138. Y. Himuro, K. Koyama, Y. Bekki, *Materials Science Forum*, **519-521** (2006) 501-506
139. S.J. Lillywhite, P.B. Prangnell, F.J. Humphreys, *Materials Science and Technology*, **16** (2000) 1112-1120
140. H. Ahlborn, E. Hornbogen, U. Köster, *Journal of Materials Science*, **4** (1969) 944-950
141. V. Randle, B. Ralph, *Acta Metallurgica*, **34** (1986) 891-898
142. B. Forbord, O. Daaland, E. Nes, *ICAA-6: 6th International Conference on Aluminium Alloys*, Toyohashi, Japan (1998) 189-194
143. M.J. Jones, F.J. Humphreys, *Acta Materialia*, **51** (2003) 2149
144. F.A. Costello, J.D. Robson, P.B. Prangnell, *Materials Science Forum*, **396-402** (2002) 757-762
145. F.W. Gayle, J.B. Vander Sande, *Scripta Metallurgica*, **18** (1984) 473-478
146. M.S. Zedalis, M.E. Fine, *Metallurgical and Materials Transactions A*, **17** (1986) 2187-2198
147. K.E. Knipling, D.C. Dunand, D.N. Seidman, *Acta Materialia*, **56** (2008) 1182-1195
148. H. Hallem, B. Forbord, K. Marthinsen, *ICAA-9: 9th International Conference on Aluminium Alloys*, Brisbane, Australia (2004) 240-245
149. F. Nakamura, S. Hirosawa, T. Sato, *ICAA-9: 9th International Conference on Aluminium Alloys*, Brisbane, Australia (2004) 582-587
150. M. Conserva, M. Leoni, *Metallurgical Transactions A*, **6** (1975) 189-195
151. R. Kaibyshev, F. Musin, D.R. Lesuer, T.G. Nieh, *Materials Science and Engineering: A*, **342** (2003) 169-177
152. B. Forbord, H. Hallem, K. Marthinsen, *Materials Science Forum*, **467-470** (2004) 369-374
153. M.S. Chuang, G.C. Tu, *Scripta Metallurgica et Materialia*, **31** (1994) 1259-1264
154. H. Hallem, B. Forbord, K. Marthinsen, *Materials Science Forum*, **539-543** (2007) 167-172
155. L. Eschbach, P.J. Uggowitzer, M.O. Speidel, *Materials Science and Engineering: A*, **248** (1998) 1-8

156. S.-W. Lee, J.-W. Yeh, *Materials Science and Engineering: A*, **460-461** (2007) 409-419
157. S. Cheong, H. Weiland, *Materials Science Forum*, **558-559** (2007) 153-158
158. T.S. Srivatsan, E.J. Coyne Jr, E.A. Starke Jr, *Journal of Materials Science*, **21** (1986) 1553-1560
159. M.J. Starink, N. Gao, N. Kamp, S.C. Wang, P.D. Pitcher, I. Sinclair, *Materials Science and Engineering: A*, **418** (2006) 241-249
160. B. Forbord, L. Auran, W. Lefebvre, H. Hallem, K. Marthinsen, *Materials Science and Engineering: A*, **424** (2006) 174-180
161. H. Westengen, L. Auran, O. Reiso, *Aluminium*, **57** (1981) 797-803
162. H. Westengen, O. Reiso, L. Auran, *Aluminium*, **56** (1980) 768-775
163. T. Pettersen, Y. Li, T. Furu, K. Marthinsen, *Materials Science Forum*, **558-559** (2007) 301-306
164. E.S. Balmuth, A. Cho, *Materials Science Forum*, **217-222** (1996) 1365-1370
165. C. Sigli, *ICAA-9: 9th International Conference on Aluminium Alloys*, Brisbane, Australia (2004) 1353-1358
166. R. Kaibyshev, F. Musin, E. Avtokratova, Y. Motohashi, *Materials Science and Engineering: A*, **392** (2005) 373-379
167. T. Ohashi, L. Dai, N. Fukatsu, *Metallurgical and Materials Transactions A*, **17** (1986) 799-806
168. A. Johansen, Ø. Bauger, J.D. Embury, N. Ryum, *Aluminium*, **82** (2006) 980-985
169. A. Johansen, Ø. Bauger, J.D. Embury, N. Ryum, *Aluminium*, **82** (2006) 868-872
170. Y.B. Kim, Y.H. Chung, K.K. Cho, M.C. Shin, *Scripta Materialia*, **36** (1997) 111-116
171. D.S. Chung, C.W. Jea, J.H. Yoon, J.K. Kim, *Materials Science Forum*, **539-543** (2007) 481-486
172. H.T. Kim, S.W. Nam, *Scripta Materialia*, **34** (1996) 1139-1145
173. K. Delijić , V. Asanović, D. Radonjić, *Materiali in Technologije*, **39** (2005) 101-106
174. J. Chang, I. Moon, C. Choi, *Metallurgical and Materials Transactions A*, **29** (1998) 1873-1882
175. X. Feng, A.M. Kumar, J.P. Hirth, *Acta Metallurgica et Materialia*, **41** (1993) 2755-2764
176. D.S. Park, S.W. Nam, *Journal of Materials Science*, **30** (1995) 1313-1320
177. A. Cho, B. Bès, *Materials Science Forum*, **519-521** (2006) 603-608
178. F.J. Humphreys, *Acta Materialia*, **45** (1997) 4231-4240
179. H. Jazaeri, F.J. Humphreys, *Acta Materialia*, **52** (2004) 3251-3262
180. P.B. Prangnell, J.S. Hayes, J.R. Bowen, P.J. Apps, P.S. Bate, *Acta Materialia*, **52** (2004) 3193-3206
181. Q. Xing, X. Huang, N. Hansen, *Metallurgical and Materials Transactions A*, **37** (2006) 1311-1322
182. R.D. Doherty, D.A. Hughes, F.J. Humphreys, J.J. Jonas, D.J. Jensen, M.E. Kassner, W.E. King, T.R. McNelley, H.J. McQueen, A.D. Rollett, *Materials Science and Engineering: A*, **238** (1997) 219-274
183. M.J. Luton, R.A. Petkovic, J.J. Jonas, *Acta Metallurgica*, **28** (1980) 729-743
184. F.J. Humphreys, *Materials Science Forum*, **467-470** (2004) 107-116
185. A. Duckham, O. Engler, R.D. Knutsen, *Acta Materialia*, **50** (2002) 2881-2893
186. H. Paul, J.H. Driver, C. Maurice, Z. Jasieński, *Acta Materialia*, **50** (2002) 4339-4355
187. Y. Huang, F.J. Humphreys, M. Ferry, *Materials Science and Technology*, **16** (2000) 1367-1371
188. F.J. Humphreys, *Acta Metallurgica*, **25** (1977) 1323-1344
189. O. Engler, K. Lücke, *Scripta Metallurgica et Materialia*, **27** (1992) 1527-1532
190. J.R. Porter, F.J. Humphreys, *Metal Science*, **13** (1979) 83-88
191. D.J. Lloyd, *Metal Science*, **16** (1982) 304-308
192. K. Kashihara, F. Inoko, *Acta Materialia*, **49** (2001) 3051-3061
193. M.C. Theyssier, J.H. Driver, *Materials Science and Engineering A*, **272** (1999) 73-82
194. M. Winning, *Scripta Materialia*, **58** (2008) 85-88
195. P. Bate, B. Hutchinson, *Scripta Materialia*, **36** (1997) 195-198
196. M. Somerday, F.J. Humphreys, *Materials Science and Technology*, **19** (2003) 20-29
197. O. Engler, *Acta Materialia*, **46** (1998) 1555-1568
198. P.A. Manohar, M. Ferry, T. Chandra, *ISIJ International*, **38** (1998) 913-924
199. S.P. Ringer, R.P. Kuziak, K.E. Easterling, *Materials Science and Technology*, **7** (1991) 193-200
200. S.P. Ringer, W.B. Li, K.E. Easterling, *Acta Metallurgica*, **37** (1989) 831-841
201. J.R. Hirsch, *Recrystallization '90: International Conference on Recrystallization in Metallic Materials: Conference Proceedings*, Wollongong, Australia (1990) 759-768

202. K.V. Jata, A. Hopkins, R.J. Rioja, *Materials Science Forum*, **217-222** (1996) 647-652
203. Y.S. Liu, L. Delannay, P. Van Houtte, *Acta Materialia*, **50** (2002) 1849-1856
204. P. Van Houtte, S. Li, M. Seefeldt, L. Delannay, *International Journal of Plasticity*, **21** (2005) 589-624
205. A.K. Kanjarla, P. Van Houtte, L. Delannay, *International Journal of Plasticity*, **In Press, Corrected Proof**
206. J.R. Hirsch, *Materials Science and Technology*, **6** (1990) 1048-1057
207. M. Hatherly, A.S. Malin, C.M. Carmichael, F.J. Humphreys, J. Hirsch, *Acta Metallurgica*, **34** (1986) 2247-2257
208. A.K. Vasudévan, M.A. Przystupa, W.G. Fricke Jr, *Materials Science and Engineering: A*, **196** (1995) 1-8
209. H. Jin, S. Saimoto, *Scripta Materialia*, **46** (2002) 275-279
210. O. Engler, J. Hirsch, K. Lücke, *Acta Metallurgica*, **37** (1989) 2743-2753
211. O. Engler, J. Hirsch, K. Lücke, *Acta Metallurgica et Materialia*, **43** (1995) 121-138
212. K. Lücke, O. Engler, *Materials Science and Technology*, **6** (1990) 1113-1130
213. G. Guiglionda, A. Borbély, J.H. Driver, *Acta Materialia*, **52** (2004) 3413-3423
214. E. Nes, H.E. Vatne, *Zeitschrift fur Metallkunde*, **87** (1996) 448-453
215. G.H. Zahid, Y. Huang, P.B. Prangnell, *Acta Materialia*, **57** (2009) 3509-3521
216. P.A. Hollinshead, *Materials Science and Technology*, **8** (1992) 57-62
217. R. Higginson, P. Bate, *Acta Materialia*, **47** (1999) 1079-1090
218. O. Engler, *Metallurgical and Materials Transactions A*, **30** (1999) 1517-1527
219. J. Liu, S.W. Banovic, F.S. Biancaniello, R.D. Jiggets, *Metallurgical and Materials Transactions A*, **36** (2005) 869-874
220. X.H. Zeng, M. Ahmad, O. Engler, *Materials Science and Technology*, **10** (1994) 581-591
221. R. Crooks, Z. Wang, V.I. Levit, R.N. Shenoy, *Materials Science and Engineering: A*, **257** (1998) 145-152
222. E. Romhanji, D. Mitlin, V. Radmilovic, *Materials Science and Engineering A*, **291** (2000) 160-167
223. K.E. Crosby, R.A. Mirshams, S.S. Pang, *Journal of Materials Science*, **35** (2000) 3189-3195
224. S.J. Hales, R.A. Hafley, *Materials Science and Engineering: A*, **257** (1998) 153-164
225. O. Brun, T. Chauveau, B. Bacroix, *Materials Science and Technology*, **7** (1991) 167-175
226. P.S. Bate, Y. Huang, F.J. Humphreys, *Acta Materialia*, **52** (2004) 4281-4289
227. C. Maurice, J.H. Driver, *Acta Materialia*, **45** (1997) 4627-4638
228. O. Engler, P. Wagner, J. Savoie, D. Ponge, G. Gottstein, *Scripta Metallurgica et Materialia*, **28** (1993) 1317-1322
229. P. Bate, A. Oscarsson, *Materials Science and Technology*, **6** (1990) 520-527
230. T. Leffers, R.K. Ray, *Progress in Materials Science*, **54** (2009) 351-396
231. C. Maurice, J.H. Driver, *Acta Materialia*, **45** (1997) 4639-4649
232. B. Davis, F.J. Humphreys, K.M. Gatenby, C.P. Johnson, *ICAA-6: 6th International Conference on Aluminium Alloys*, Toyohashi, Japan (1998) 1275-1280
233. O. Daaland, E. Nes, *Acta Materialia*, **44** (1996) 1413-1435
234. O. Daaland, E. Nes, *ICAA-4: 4th International Conference on Aluminium Alloys*, Atlanta, USA (1994) 275-282
235. G. Burger, P. Wycliffe, C. Gabryel, D.J. Lloyd, *Materials Science Forum*, **242** (1997) 101-110
236. H.E. Vatne, O. Engler, E. Nes, *Materials Science Forum*, **157-162** (1994) 1501-1506
237. D. Tsivoulas, P.B. Prangnell, C. Sigli, B. Bès, *Advanced Materials Research*, **89-91** (2009) 568-573
238. D. Dumont, A. Deschamps, Y. Brechet, *Materials Science and Engineering: A*, **356** (2003) 326-336
239. *ASM Handbook: Fractography, vol. 12*, ASM International, USA (1987)
240. A.K. Vasudévan, R.D. Doherty, *Acta Metallurgica*, **35** (1987) 1193-1219
241. P. Kenny, J.D. Campbell, *Progress in Materials Science*, **13** (1968) 135-181
242. J.A. Walsh, K.V. Jata, E.A. Starke Jr, *Acta Metallurgica*, **37** (1989) 2861-2871
243. M. Nakai, T. Eto, *Materials Science and Engineering A*, **285** (2000) 62-68
244. E.P. Butler, N.J. Owen, D.J. Field, *Materials Science and Technology*, **1** (1985) 531-536
245. S. Nam, D. Lee, *Metals and Materials International*, **6** (2000) 13-16
246. T.S. Srivatsan, D. Lanning Jr, K.K. Soni, *Journal of Materials Science*, **28** (1993)
247. J.A. Blind, J.W. Martin, *Materials Science and Engineering*, **57** (1983) 49-54
248. K.V. Jata, A.K. Vasudévan, *Materials Science and Engineering: A*, **241** (1998) 104-113
249. S.C. Jha, T.H. Sanders Jr, M.A. Dayananda, *Acta Metallurgica*, **35** (1987) 473-482

250. T.S. Srivatsan, *Journal of Materials Science Letters*, **5** (1986) 589-591
251. A.M. Gokhale, N.U. Deshpande, D.K. Denzer, *ICAA-4: 4th International Conference on Aluminium Alloys*, Atlanta, USA (1994) 685-692
252. K.M. Gatenby, M.A. Reynolds, J. White, I.G. Palmer, *Proceedings of the Fifth International Conference on Al-Li alloys*, Birmingham, UK (1989) 909-919
253. L. Zhen, Y.X. Cui, W.Z. Shao, D.Z. Yang, *Materials Science and Engineering A*, **336** (2002) 135-142
254. E.A. Starke Jr., F.S. Lin, *Metallurgical and Materials Transactions A*, **13** (1982) 2259-2269
255. H.X. Li, C.Q. Chen, *Materials Science and Technology*, **6** (1990) 850-856
256. Y. Minamino, T. Yamane, H. Araki, *Metallurgical and Materials Transactions A*, **18** (1987) 1536-1538
257. K.K. Soni, D.B. Williams, D.E. Newbury, P. Chi, R.G. Downing, G. Lamaza, *Corrosion*, **49** (1993) 31-41
258. ASTM E 92(2003)$^{\varepsilon 2}$: Standard test method for Vickers hardness of metallic materials
259. ASTM E 384-99$^{\varepsilon 1}$: Standard test method for microindentation hardness of materials
260. ASTM B 871-01: Standard test method for tear testing of aluminium alloy products
261. J.G. Kaufman, A.H. Knoll, *Materials Research and Standards*, **4** (1964) 151-155
262. R.W. Hertzberg, *Deformation and fracture mechanics of engineering materials*, John Wiley & Sons, New York, USA (1976)
263. D.B. Williams, C.B. Carter, *Transmission Electron Microscopy (A Textbook for Materials Science)*, Springer, New York (1996)
264. G. Thomas, M.J. Goringe, *Transmission Electron Microscopy of Materials*, Wiley, New York (1979)
265. R.F. Egerton, M. Malac, *Journal of Electron Spectroscopy and Related Phenomena*, **143** (2005) 43-50
266. P.A. Midgley, M. Weyland, *Ultramicroscopy*, **96** (2003) 413-431
267. P.A. Midgley, E.P.W. Ward, A.B. Hungría, J.M. Thomas, *Chemical Society Reviews*, **36** (2007) 1477-1494
268. M. Weyland, P.A. Midgley, *Materials Today*, **7** (2004) 32-40
269. P.J. Goodhew, F.J. Humphreys, *Electron Microscopy and Analysis (2nd ed.)*, Taylor & Francis, London (1988)
270. V. Randle, *Microtexture Determination and its Applications (2nd ed.)*, Maney, London (2003)
271. F.J. Humphreys, *Journal of Materials Science*, **36** (2001) 3833-3854
272. V.D. Scott, G. Love, S.J.B. Reed, *Quantitative Electron-Probe Microanalysis (2nd ed.)*, Ellis Horwood, London (1995)
273. J. Murray, A. Peruzzi, J.P. Abriata, *Journal of Phase Equilibria*, **13** (1992) 277-291
274. J.-T. Beauchesne, D. Caillard, F. Mompiou, P. Ochin, M. Quiquandon, D. Gratias, *Zeitschrift fur Kristallographie*, **223** (2008) 823-826
275. J. Idrac, G. Mankowski, G. Thompson, P. Skeldon, Y. Kihn, C. Blanc, *Electrochimica Acta*, **52** (2007) 7626-7633
276. Y. Du, Y.A. Chang, B. Huang, W. Gong, Z. Jin, H. Xu, Z. Yuan, Y. Liu, Y. He, F.Y. Xie, *Materials Science and Engineering A*, **363** (2003) 140-151
277. C. Sigli, L. Maenner, C. Sztur, R. Shahani, *ICAA-6: 6th International Conference on Aluminium Alloys*, Toyohashi, Japan (1998) 87-98
278. R. Nadella, D.G. Eskin, Q. Du, L. Katgerman, *Progress in Materials Science*, **53** (2008) 421-480
279. K.P. Mingard, B. Cantor, I.G. Palmer, I.R. Hughes, P.W. Alexander, T.C. Willis, J. White, *Acta Materialia*, **48** (2000) 2435-2449
280. L. Chunzhi, W. Shuncai, J. Yan, H. Mingjian, Y. Minggao, *ICAA-2: 2nd International Conference on Aluminium Alloys*, Beijing, China (1990) 504-507
281. J. Røyset, N. Ryum, *Scripta Materialia*, **52** (2005) 1275-1279
282. S. Srinivasan, P.B. Desch, R.B. Schwarz, *Scripta Metallurgica et Materialia*, **25** (1991) 2513-2516
283. N. Louat, *Philosophical Magazine A*, **47** (1983) 903-912
284. E.A. Marquis, D.N. Seidman, *Acta Materialia*, **49** (2001) 1909-1919
285. Z. Suo, *Acta Metallurgica et Materialia*, **42** (1994) 3581-3588
286. G. Bruno, G. Schumacher, H. Pinto, C. Schulze, *Metallurgical and Materials Transactions A*, **34** (2003) 193-197
287. S. Iwamura, Y. Miura, *Acta Materialia*, **52** (2004) 591-600
288. D. Tsivoulas, J.D. Robson, *Materials Science Forum*, **519-521** (2006) 473-478

289. P.B. Hirsch, A. Howie, R.B. Nicholson, D.W. Pashley, M.J. Whelan, *Electron microscopy of thin crystals*, Butterworths, London (1965)
290. M.F. Ashby, L.M. Brown, *Philosophical Magazine*, **8** (1963) 1083 - 1103
291. N. Ryum, *Journal of Materials Science*, **10** (1975) 2075-2081
292. B. Forbord, W. Lefebvre, F. Danoix, H. Hallem, K. Marthinsen, *Scripta Materialia*, **51** (2004) 333-337
293. P. Vermaut, P. Ruterana, *Acta Materialia*, **44** (1996) 2445-2455
294. J.D. Robson, P.B. Prangnell, B.J. McKay, C.P. Heason, *Materials Science Forum*, **550** (2007) 45-54
295. S. Serajzadeh, *Materials Science and Engineering: A*, **448** (2007) 146-153
296. W.G. Jiang, G.C. Wang, S.Q. Lu, J.W. Li, *Journal of Materials Processing Technology*, **182** (2007) 274-280
297. J.D. Robson, P.B. Prangnell, *Materials Science Forum*, **396-402** (2002) 545-550
298. H. Magnusson, B. Hutchinson, L. Ryde, *The Fourth International Conference on Recrystallization and Related Phenomena*, Tsukuba, Japan (1999) 191-196
299. N.-E. Andersson, S. Johansson, *ICAA-6: 6th International Conference on Aluminium Alloys*, Toyohashi, Japan (1998) 1191-1196
300. F. Barlat, S.M. Miyasato, J. Liu, J.C. Brem, *ICAA-4: 4th International Conference on Aluminium Alloys*, Atlanta, USA (1994) 389-396
301. T. Kobayashi, *Materials Science and Engineering A*, **280** (2000) 8-16
302. D.J. Chellman, NASA Contractor report, 172521 (1985)
303. F.J. Humphreys, M.G. Ardakani, *Acta Materialia*, **44** (1996) 2717-2727
304. H. Hallem, W. Lefebvre, B. Forbord, F. Danoix, K. Marthinsen, *Materials Science and Engineering: A*, **421** (2006) 154-160
305. Y. Li, L. Arnberg, *Materials Science Forum*, **396-402** (2002) 875-880
306. Y.J. Li, L. Arnberg, *Acta Materialia*, **51** (2003) 3415-3428
307. H.-E. Ekström, J. Hagström, L. Östensson, *Materials Science Forum*, **331-337** (2000) 179-184
308. V. Radmilovic, A. Tolley, E.A. Marquis, M.D. Rossell, Z. Lee, U. Dahmen, *Scripta Materialia*, **58** (2008) 529-532
309. M.J. Starink, *International Materials Reviews*, **49** (2004) 191-226
310. N.A. Zarkevich, D.D. Johnson, *Physical Review B: Condensed Matter*, **67** (2003) 064104
311. H.K. Lee, R.W. Hyland, H.I. Aaronson, P.P. Wynblatt, *Surface Science*, **408** (1998) 288-299
312. E.A. Marquis, *Microscopy and Microanalysis*, **13** (2007) 484-492